Laser induced molecular motion in strong nonresonant laser fields

Simon Mark Purcell

Submitted for the degree of Doctor of Philosophy

Department of Physics and Astronomy

University College London

November 2009

Declaration

I, Simon Mark Purcell confirm that the work presented in this thesis is my own. Where information has been derived from other sources, I confirm that this has been indicated in the thesis.

Simon Mark Purcell ____________________________________

Abstract

The optical dipole force from a singe focussed laser beam was used to study the role of laser-induced molecular alignment on the centre-of-mass motion of carbon disulphide molecules in a molecular beam. The translational, rotational and vibrational temperatures of the CS_2 molecules were measured to be 3.4±0.2 K, 35±10 K and 250±14 K respectively. The velocity of the beam was measured to be 542±22 m s^{-1}. Time-of-flight mass spectroscopy was used to measure the acceleration and deceleration of the molecules. Maximum velocity changes of 7.5 m s^{-1} and 10 m s^{-1} were recorded for linearly and circularly polarised light respectively. These results showed that the dipole force, $F \propto \nabla[\alpha_{eff}(I)I(r)]$, where α_{eff} is the effective polarisability and determined through laser-induced alignment, can be modified by changing the laser polarisation. For linearly and circularly polarised light, a 12 % difference in effective polarisability was measured to produce a 20 % difference in dipole force.

The dipole force from a single focussed laser beam produces a molecular optical lens and the downstream density of the molecular focus was probed by measuring the ion signal for both laser polarisations. The focal lengths for linearly and circularly polarised light were found to be separated by ≈100 μm. By altering the laser polarisation from linearly through elliptically to circularly polarised light, the focal length of the molecular optical lens could be smoothly altered over the ≈100 μm focal range.

The role of the effective polarisability of each rotational state was also studied numerically. Separate rotational states were found to significantly alter the focal properties of a molecular optical lens. In CS_2, higher rotational states ($J > 10$), exhibit less molecular alignment and when occupied, the focal length of the molecular optical lens for these states was increased by 60 % compared to the ground state.

Acknowledgements

I would like to thank my supervisor Professor Peter Barker, for his guidance and support. His enthusiasm, encouragement and light hearted sense of humor have had a significant and positive effect on my studies. I also thank my secondary supervisor Dr. Jonathan Underwood for useful discussions which have undoubtedly added to this work, and for also being very generous with his time and patience.

Publications

1. S. M. Purcell and P. F. Barker, *"Tailoring the optical dipole force for molecules by field-induced alignment"*, Phys. Rev. Lett. **103**, 153001 (2009).
2. P. F. Barker, S. M. Purcell, P. Douglas, P. Barletta, N. Coppendale, C. Maher-McWilliams and J. Tennyson, *"Sympathetic cooling by collisions with ultracold rare gas atoms, and recent progress in optical Stark deceleration"*, Faraday Discuss., **143**, 175, (2009).
3. P. F. Barker, S. M. Purcell and M. N. Schneider *"Spectra of molecular gases trapped in deep optical lattices"*, Phys. Rev. A, **77**, 063409, (2008).

Contents

Chapter 1

Background

1.1 Motivation

The goal of this thesis is to investigate the effects of nonresonant optical fields which induce centre-of-mass motion and molecular alignment. A nonresonant laser beam can be used to induce a dipole moment in a molecule, which in turn, interacts with the field to create a force on the molecule. This interaction creates both molecular alignment and centre-of-mass motion. In this thesis, a molecular lens created by a nonresonant laser field is studied because it enables both alignment and centre-of-mass motion to be examined simultaneously. The main goal of this thesis is to answer three questions:

1. *'Is it possible to use the properties of molecular alignment in dipole force experiments to enhance or alter the magnitude of the dipole force?'* Firstly, a review of the theory of molecular alignment is presented by developing an alignment-dependent dipole force equation. To measure the alignment-dependent dipole force, molecules created in a molecular beam are accelerated and decelerated using the dipole force provided by a single focussed nonresonant laser beam. This force is measured using time-of-flight mass spectroscopy and the experimental data is then fitted using the alignment-dependent dipole force equation, validating the model of this process.

2. *'What is the influence of individual rotational states and how will they affect the focus produced by a molecular lens?'* By simulating a cold molecular beam of CS_2 and N_2 molecules focussed by a molecular lens, the different orientations of separate rotational states will cause the molecules to focus at different positions along the molecular beam axis. The presence of these rotational states in the molecular lens is explored and characterized.

3. *'How useful are these techniques and what will they lead to?'* Using the experiments and simulations we wish to show that the alignment-dependent dipole

force could be used in other dipole force experiments to control or enhance molecular interactions.

The bulk of this thesis is dedicated to answering these questions, whilst this current introductory chapter consists of a brief review of the forces applied to atoms or molecules by light.

1.2 Introduction

Understanding physical or chemical interactions can often be a complex and difficult task with many variables and parameters. By artificially creating an environment with reduced dimensions or simplified dynamics, researchers stand a much better chance of being able to explain their observations. For example, recently a Bose-Einstein condensate confined to one dimension was used to experimentally demonstrate the physics of a Tonk-Girardeau gas[1], a one dimensional gas with special properties where bosons act like fermions. Other examples include using optically trapped atoms to enhance metrology measurements[2], and the use of BEC's to probe chaos in systems which have many colliding particles[3].

In molecular physics there is much work being done to create stationary low temperature molecular gases[4, 5, 6], which offer properties different to cold atomic gases. Cold molecules with dipole moments offer the opportunity to measure the electron electric dipole moment[7]. Additionally, cold molecules promise new limits of spectroscopy. Microwave spectroscopy on the hydroxyl molecule at cold temperatures (5 mK), has been combined with astrophysical measurements of the same transition in hydroxyl. This has improved the accuracy of the variation of the fine structure constant on cosmological time scales[8]. Much interest is also generated by the chemical physics community where precise control over chemical reactions or collisions[9, 10] would provide an ideal test bed for theoretical models[11]. In order to create such molecules and control how they interact with their surroundings, new methods of molecular and atomic manipulation have been developed using optical, electrostatic and magnetic fields. This thesis concentrates on the optical manipulation of molecules through nonresonant optical fields, where control over the translational and rotational dynamics is achievable.

The following sections outline some of the modern atomic and molecular manipulation techniques and their applications.

1.3 Mechanical light forces

1.3.1 Optical tweezers

Optical fields are a well established method of controlling the motion of atoms and molecules. Radiation pressure, where linear momentum is transferred from incident photons to a molecule, atom or surface can be used in the micron scale to control the motion of microscopic particles. Controlling particles in this way is termed optical tweezers and was initially demonstrated through the manipulation of dielectric particles[12, 13] in the early 1970s. Manipulation of small sized particles is possible through the refraction of a large number of photons[14] by the particle which creates a force in the pico-Newton range. In a single focussed beam, the particles are pushed toward the high field region and along the laser beam axis. By adding a second counter-propagating laser beam, the motion along the laser beam axis is canceled and only a net inward force toward the high field region is created, forming a trap at the centre of the beams. The polarisation of the laser light can be used to add angular momentum to trapped particles by using circularly polarised light to induce a torque on the particles. Measuring the applied torque can yield the physical properties of the particle[15] (torsion of coiled DNA molecules[16]), the surrounding medium (viscosity[17]), and the trapping potential[18].

Optical tweezers have been used extensively in biology by controlling the motion of single molecules of DNA[19, 20] and other biomolecules[21, 22, 23]. Optical tweezers can be also be used to hold biomolecules in the focus of a microscope, or used to stretch out and unravel coiled molecules for study. Another important application is the use of single flurosphores which are luminescent tags placed onto biomolecules held in tweezer traps. By monitoring the tags, the step by step bonding and dissociation processes in biological molecules[24] can be observed.

1.3.2 Laser cooling

Forces on atoms can be divided into either dissipative and conservative. Dissipative forces are used in laser cooling[25, 26, 27, 28] where two or more counter propagating laser beams are red detuned from an atomic resonance. As an atom moves towards the light source, it absorbs a photon and receives a quanta of momenta $\hbar\hat{\mathbf{k}}$ in the opposite direction. The atom subsequently re-emits the photon in a random direction. Through repeated absorption-emission cycles, the effect of absorbing photon momenta in the direction opposite to which the atoms are traveling removes kinetic energy from the atom. As the photons are re-emitted in a random direction, the net effect of emitting the absorbed photons is zero. This process reduces the temperature of the atoms into the $10^{-3} - 10^{-6}$ K range. The efficiency of the process is highly dependent on the frequency of the red detuned laser, which must also be tuned as the velocity of the atoms is decreased. Eventually a limit is reached where the atomic velocity is small, and the reduction in momentum is negligible compared to the heating that is induced as the red detuned light is tuned closer and closer to the atomic frequency. Additional heating of the slowed atoms may also occur from noise in the frequency of the red detuned light. To cool further and reach BEC temperatures in the nano Kelvin regime, evaporative cooling[29] is used.

Essential to laser cooling is the availability of a closed cycle of atomic transitions. This means that when the atom re-emits its photon, the atom returns to its initial state and does not end up in a state which will no longer absorb the "cooling photons". If the transition cycle is not fully closed, repumper lasers can sometimes be used to excite atoms back into an upper state so it will re-emit into its initial state. This requirement of a closed scattering cycle or at least a cycle which involves only one or two repumper lasers is what limits the technique of laser cooling to a small set of atoms[30]. Several diatomic molecules which approximately satisfy this criteria have been identified[31], but the majority of molecules cannot be laser cooled in this way.

1.4 Conservative forces

1.4.1 Atoms

Near-resonant dipole force

Conservative forces in atoms refer to a reversible transfer of energy, one such process is the dipole force[32, 33], which is caused by Stark shifting the atomic eigenvalues with an optical field below or above an electronic resonance. Using a focussed laser beam with red detuned light, the spatial gradient of the atomic Stark shift attracts atoms to the central high field region of the focus. This interaction forms the basis for a dipole trap for atoms[34]. A typical trap is formed using a $\sim$100 mW continuous wave laser which is tuned below an atomic resonance. Such traps are shallow ($\sim$ 1 mK), and are restricted to trapping laser cooled atoms. The dipole force in atoms also depends on the sign of detuning from resonance, which can make the atoms high or low field seeking. The force is inversely proportional to the detunings from resonance, however, large detunings are often desirable as this reduces the scattering rate from the atoms which can heat the trap.

Nonresonant dipole force

The dipole force can also be created by using strong nonresonant optical fields. Intensities in the range $10^{11} - 10^{12}$ W cm^{-2} can provide significant attractive forces in the 100 K range for atoms. In the far-off resonant regime, the interaction between the atom and field is well approximated by the atom's ground state polarisability[35]. This removes the spectral restrictions found in the near-resonant dipole force, making the nonresonant dipole force completely general to all atoms and molecules. The main difference between the methods is that although the near-resonant dipole force requires laser frequencies specific to each atom, it needs much less intensity, and so continuous wave lasers maybe used. By contrast, the interaction between the field and atomic polarisability is weak in the nonresonant case and so pulsed lasers are used to create the dipole force. The large well depth and generality of the nonresonant dipole force means strong nonresonant fields can induce a significant dipole force in any atom without laser cooling. The generality of the nonresonant dipole force makes it suitable for manipulating inert atoms[36], and it has potential uses in helium microscopy[37]. The nonresonant technique when used with continuous wave lasers in optical cavities could be used to trap both atoms and molecules. Optical cavities can combine a large mode volume (in comparison to a single focussed laser beam of the same intensity) and provide an intensity in the $10^7 - 10^9$ W cm^{-2} range, which would be sufficient to trap slowed atoms and molecules[38, 39].

1.4.2 Molecules

Small sized molecules lie between the microscopic (atoms) and macroscopic (biomolecules, micron spheres and particles) regimes and are too small to be controlled using optical tweezer methods. They cannot be controlled using radiation pressure either because their complex energy structure mean there are no closed transition cycles for laser cooling. Only from the mid 90s onward have methods to coherently control molecular motion become available. Modern methods of manipulation include electrostatic Stark control of polar molecules, magnetic control of paramagnetic molecules and optical Stark control of polar and nonpolar molecules.

Stark deceleration

For collision, trapping or cold molecule experiments[11] it is often advantageous to bring molecules to rest. Polar molecules possess a permanent dipole moment and if it is sufficiently large the molecule can be slowed using arrays of electrodes[40]. The interaction of the dipole with an electrostatic field in the kV range causes molecules in low field seeking states to climb a potential hill or do work against the field as it moves toward the electrode. This uses up kinetic energy, slowing the molecule. A single electrode arrangement however, only marginally reduces the molecular velocity and long arrays of electrode stages are constructed over a metre long[40]. Each stage must be carefully controlled such that each electrode turns on at the correct time to match the decreasing velocity of the beam. High field seeking states are dispersed by the high fields around the electrodes but can be slowed using alternate gradient focussing[41]. These processes are called Stark deceleration[42] and was first demonstrated in 1999[43]. The process is well characterized[44, 45] and offers velocity tunability and control over the external and internal degrees of freedom of polar molecules. This amount of control is ideal for studies in molecular trapping[46, 47], molecular collisions[48, 49] and molecular state-selectivity[50, 51].

Magnetic control

Magnetic control of molecules is also a viable alternative to electric field methods. The interaction of paramagnetic atoms or molecules with pulsed magnetic fields allows kinetic energy to be removed by using magnetic field coils in a linear array. In a setup similar to the Stark decelerator, the amount of kinetic energy removed is equal to the Zeeman shift in the molecule when the magnetic field is turned off. This technique relies on the presence of a permanent magnetic moment in the molecule. By using water cooled coils and a pulsed high current (750 A), magnetic fields of the order 5 T are produced. The resulting reduction in kinetic energy is similar to the Stark decelerator and many separate coil stages (~ 60) are required to slow the molecular species sufficiently. Another feature similar to the Stark decelerator is that the Zeeman shift is quantum state dependent so quantum state selection is intrinsic to the magnetic slowing of species. Recently, oxygen molecules were slowed from 389 m s^{-1} to 83 m s^{-1}, using a 64 stage decelerator[52]. The efficiency of this method was calculated by dividing the area of the unperturbed time-of-flight signal by the area of the slowed molecules' time-of-flight, a value 0.8 % was recorded. In an earlier experiment by the same group, Neon atoms were slowed from 446 m s^{-1} to 55.8 m s^{-1} with a 2 % efficiency[53], demonstrating the applicability of the technique to atoms.

Dipole force

In placing any molecule in a Stark decelerator, a dipole moment is induced from the electrostatic field. The induced dipole is however too small to reduce the kinetic energy by any reasonable amount as it passes through the electrode assembly. Stronger fields provided by pulsed lasers can induce a significant dipole moment which will interact with the field which produced it. At laser frequencies below all electronic resonances (infra-red), the response of the molecule is well approximated by the static polarisability and the square of the electric field. The rapid oscillations of the laser field are averaged and the molecule follows the envelope of the field. A more detailed analysis is provided in section 1.7. The ground state eigenvalues are shifted negatively providing an attractive force in the laser field. Studies by Seideman[54], Friedrich and Herachbach[55] show the effective Hamiltonian of the AC Stark shift is

$$V(t) = -\frac{1}{4}\varepsilon^{*}(t)\boldsymbol{\alpha}\varepsilon(t), \tag{1.1}$$

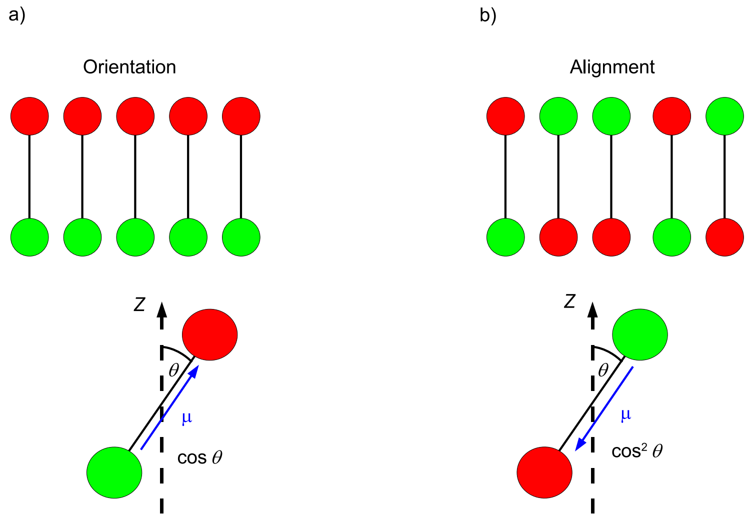

Figure 1.1: We distinguish between orientation and alignment. a) Shows complete orientation of polar molecules where a directional axis, defined by the dipole moment, is aligned with the laser polarisation vector (dashed line). The value $\cos\theta$, quantifies the directional properties of the molecules. b) When only the molecular axis is confined, the dipole moment of the polar molecules can point in any direction and is randomly oriented. This process is termed alignment. The alignment dynamics in this circumstance are quantified by the directionless parameter $\cos^2\theta$.

where $\boldsymbol{\alpha}$ is the polarisability tensor of the molecule and $\varepsilon(t) = \mathbf{e}\varepsilon_0 g(t)$ is the electric field containing the magnitude of the field ε_0. The field polarisation vector is given by $\mathbf{e}$, and the pulse envelope of the field is given by $g(t)$. Using low frequency infra-red lasers will always lower the eigenvalues[56] of ground state molecules which means they are always high field seeking. The spatial gradient of the Stark shift creates a force $F(r, t) = -\nabla V(r, t)$, attracting all ground state atoms and molecules to the high field regions of the electric field. The size of the Stark shift is large $\sim 10 - 200$ K and can manipulate molecules without laser cooling. Low field seeking states can also be created through near resonance excitation[57] between the vibronic states of the molecule. However, this technique is limited by accessible spectral regions. The principle advantage of this technique is that the Stark shift is general and applicable to all species of atoms and molecules because they are all polarisable.

In addition to controlling the centre-of-mass motion, molecules can have an anisotropic polarisability which induces molecular rotation, confining the axis of highest polarisability to the electric field vector. Depending on the technique used to create the angular confinement, molecular orientation or alignment will ensue. Figure 1.1 shows examples of the orientation and alignment of diatomic polar molecules. The confinement of the molecular axis in both cases to the Z direction, which is defined in the lab frame, serves to bring the molecular axis into the lab frame. In figure 1.1 a), the permanent dipole moment of the polar molecules, along the molecular axis, can be used to define a unique direction in space. This allows us to distinguish between the atoms, and when they all point the same way, this is termed orientation. In molecular alignment, figure 1.1 b), only the molecular axis of each molecule is confined to the Z axis, the dipole moment is not confined in a particular direction. The confinement of the molecular axis but with a randomly oriented dipole moment is termed molecular alignment. We use the parameter $\cos^2\theta$, which is insensitive to the sign of θ, to characterize the molecular alignment with a lab fixed axis (Z). Whilst $\cos\theta$, which is sensitive to the direction of the dipole moment is used to measure orientation.

Thus the dynamic Stark effect serves to push molecules into high field regions and also to align or orient the principle polarisability axis with the laser polarisation vector[58]. This angular confinement serves to enhance the centre-of-mass motion. Rotational motion responds much faster than centre-of-mass motion, typically picoseconds compared to μs. Frequently the phenomena are studied separately as the confinement of each type of motion has its own particular applications. Two research fields governed by the same potential in equation 1.1 have been created, “molecular optics” involved in manipulating centre-of-mass motion[59, 60, 61] and molecular alignment[62, 63], which uses the polarisability anisotropy of molecules. This thesis brings these two areas together.

1.5 Dipole force experiments

1.5.1 Deflection and focussing of atomic or molecular species

The spatial gradient of equation 1.1 provides an attractive force $F(r,t) = -\nabla V(r,t)$, acting in the radial direction of a single focussed laser beam. This creates an “optical” lens for molecules and atoms and is illustrated in figure 1.2. Using pulsed free jet sources, the species of interest is seeded at a few percent in a carrier gas, which is typically a noble gas. The expansion provides molecules or atoms with a translational temperature of a few Kelvin. Typical values are given in the figure for the laser intensity I_0, translational temperature T_t, wavelength λ and molecular density n. Molecules traveling along the x axis are accelerated along the y axis toward the centre of the focussed beam. The potential well is not deep enough to trap the molecules but perturbs their motion so they focus downstream from the lens. This is illustrated by molecules A and B in figure 1.2. The waist radius of the focussing laser and intensity determine the focal length of the lens which is of the order $\approx 200 - 800$ μm. In order to achieve the required intensity to form a lens, pulsed lasers are used with ns duration. A duration $\tau_{FWHM} = 15$ ns ensures a long interaction time, increasing the acceleration along the y axis. The time dependence of the field gives the lens a special property different from conventional optical lenses because the molecules only

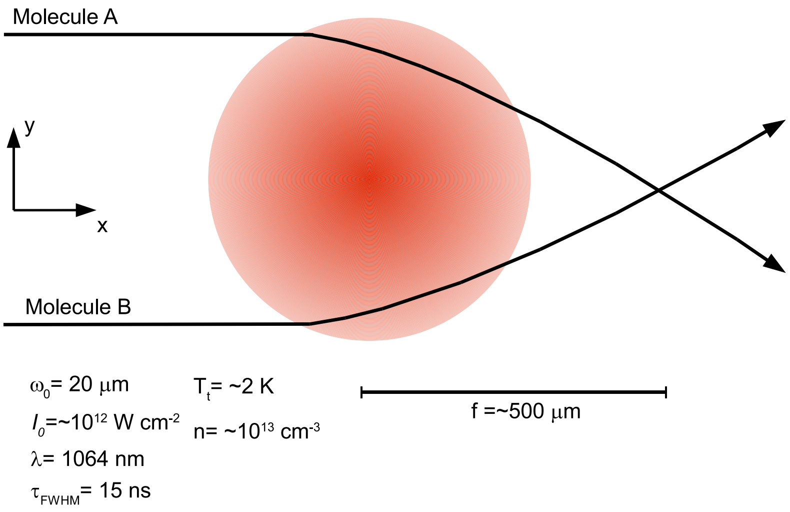

Figure 1.2: A schematic of molecular focussing using a nonresonant laser beam. A Gaussian focussed beam with a e^{-2} radius of 20 μm creates a radial force which pushes incident molecules A & B toward the centre of the lens. Molecules traveling in the x direction are given a "kick" along the y axis, altering the trajectory and forming a focus downstream. Typical experimental parameters are also given.

travel partly through the lens whilst it is on. Molecules traveling toward the lens are accelerated by being pulled into the potential well, and molecules moving away from the lens are decelerated as they are pulled into the potential well.

The size of the molecular or atomic focus is important in applications such as surface probes or lithography. Theoretical studies have shown that a molecular lens could produce nanometre sized structures on substrates[54]. Experimentally, the smallest focus formed using an intense pulsed optical field was with xenon atoms. The focus was measured using time-of-flight mass spectroscopy to spatially probe the density of the atoms within the focus. The full-width-half-maximum of the focus was measured to be 7 μm[64]. Achieving nanometre sized atomic foci was prevented by the laser pointing stability in the laser which formed the lens. The temperature of the molecular beam also affects the focussing properties. Translational temperature acts to spread out the focus along the molecular beam axis as different molecules with different velocities arrive at different positions in the focal plane. The size and density of the focal spot is determined by the perpendicular velocity kick given to the molecules by the lens, $\Delta v_y \propto \alpha I_0/m$.

1.5.2 Lithography

Atoms

Nanometre atomic sized structures have been created on substrates using the dipole force. In such experiments, the dipole force was applied by using weak, near-resonant light[65] to form a standing wave above a substrate. The detuning of the standing wave laser above or below an electronic resonance will determine the attractive or repulsive nature of the dipole force. Consider a well collimated laser-cooled atomic beam traveling perpendicular to the optical standing wave, the interference pattern will act like a series of cylindrical lenses for the atoms. The standing wave will minimise the atomic eigenvalues in the high field or low field regions, channeling the atoms into parallel lines which are deposited onto the surface.

The first demonstration of atomic submicron lithography was by Timp *et al.*[66] using sodium atoms. The atoms were deposited in a series of parallel lines onto a silicon substrate with a periodicity of 294 nm. Later, in 1993 McClelland *et al.*[67] deposited chromium onto a 0.4 mm x 1 mm silicon substrate. Analysis in an atomic force microscope showed a series of parallel Cr lines with a linewidth of 65 nm, separation between the adjacent lines was 213 nm. The lines took twenty minutes to form. Other atomic species have been focussed using the standing wave method, aluminium[68], caesium[69], ytterbium[70], and iron[71]. Obtaining such small nm features requires a well collimated atomic beam obtained using laser cooling which limits the applicability of this scheme to simple level structure atoms.

Molecules

Molecules and atoms can be manipulated without laser cooling[72, 39, 73]. Standard molecular beam techniques[74] can generate molecules in the ∼1-10 K range which is low enough to be manipulated using the dynamic Stark effect and standard pulsed laboratory lasers (e.g intense, pulsed, nanosecond Nd:YAG λ =1064 nm).

Although no experimental demonstrations of deposited molecules using the dipole force have been presented, there have been many theoretical studies on the subject and its applications[14, 75, 76, 57, 54]. The dipole force can be applied to all polarisable species and could be used to deposit metals, semiconductors and biomolecules. As the dipole force also confines the angular motion of molecules with anisotropic polarisability, the prospect of depositing aligned molecules onto a surface stimulates much interest. Deposited, aligned molecules could be used to form structures with new electric, magnetic and optical properties. Numerical simulations of a single focussed Gaussian laser beam have shown features of width <50 nm[14] could be produced using the dipole force, suggesting possible applications in creating nanowires or quantum dots[77].

1.5.3 Optical lattice: slowing of molecules

The optical Stark effect maybe used to create an optical lattice. By crossing two nonresonant laser beams at a shallow angle, a standing wave, also termed an optical lattice is created[40, 11]. For slowing jet cooled molecules, the lattice is constructed to be along the molecular beam direction. This periodic potential is deep enough to trap molecules in a molecular beam and manipulate them by changing the speed of the lattice. The optical lattice velocity is proportional to the difference in frequency of the laser beams. By using a constant frequency offset, a lattice with a constant velocity has been used to slow NO molecules[78] from 400 m s^{-1} to 242 m s^{-1} and benzene molecules from 380 m s^{-1} to 191 m s^{-1}[79]. Similarly, by creating a positive lattice velocity, the molecules maybe accelerated.

Work toward ultracold molecules[39] shows a decelerating lattice velocity, created by a frequency chirp in one of the lattice lasers offers the prospect of bringing jet cooled molecules entirely to rest. In such a scheme the optical lattice velocity is decreased as the molecules are decelerated producing a higher yield of slowed molecules. Once at rest, the molecules can be trapped and sympathetically cooled by using laser cooled atoms[80].

1.5.4 Optical prism: for separation of molecules

A single focussed nonresonant laser, identical to the setup in figure 1.2, can be used to disperse mixed gases in a molecular beam. The force applied to the molecule along the y direction is $F \propto \alpha I_0/m$, where α, m, and I_0, are the polarisability, mass and intensity respectively. Hence, molecules with different polarisabilities or mass can be spatially separated. This was demonstrated in 2003 by Zhao *et al.*[59] using NO and benzene molecules. Benzene is more polarisable than NO, and despite its heavier mass experiences a greater force allowing the species to be spatially separated downstream from the molecular lens.

1.6 Aligned molecules

Spectroscopic or collision studies on gaseous molecules are sensitive to the internal motion of the molecule[81]. Molecules which rotate freely in space are represented by an average over the Euler rotation angles, smearing out dynamics which depend on rotational motion. This limits the level to which molecular dynamics can be probed. Much modern physics now depends on the rotational states to be well known in a gas sample. Examples include high harmonic generation[82], spectroscopy[83], chemical branching ratios[84] and tomographic imaging of molecular orbitals[85].

Solutions to orientational averaging were sought in the early 1970s through collisions in molecular beams which can preferentially align species with its angular momentum vector perpendicular to the direction of propagation[86]. Diatomic sodium molecules[87], and other alkali-metal dimers[88], were demonstrated to be aligned this way. Beyond the alkali metals, by using pure iodine expansions it was found the molecules could not be significantly aligned[89]. Alignment of I_2 was obtained with a seeded beam of CO_2, but only at lower pressures, and the alignment all but vanishes as one approaches typical pressures used in seeded molecular beams[90].

Alternative methods of aligning molecules in molecular beams have been explored such as electrostatic hexapole focussing of polar molecules. This method can produce state selected linear[91] and symmetric top molecules[92]. Electrostatic focussing works by using the first order Stark effect in symmetric top molecules (or the weaker, second order Stark effect in linear molecules) to deflect quantum states. The quantum states which interact more strongly with the field are spatially separated at the end of the focuser. However, implementing such schemes is challenging as long interactions times[93] and very cold molecular beams are required. Additionally, quantum states which interact weakly with the field or have an opposite sign depending on the KM product of the symmetric top wave function $|J, K, M\rangle$, can be dispersed by the hexapole[94].

Other electrostatic techniques have used strong DC fields to orient molecules[86, 95] creating pendular states. These are directional hybrids of field-free states, which confine the molecular axis to the field polarisation. This technique is limited to polar molecules which have sufficiently large dipole moments that when combined with available DC fields, the confinement energy can overcome the thermal energy.

Near-resonant optical methods can be used to align nonpolar molecules[96, 97, 58, 98, 56] but cannot be generally extended to other molecules because of the molecule specific spectroscopic requirements. By far the most commonly used and well developed method is the use of strong nonresonant optical fields to orient or align nonpolar or polar molecules. Work by Friedrich and Herschbach[55, 99] showed a strong nonresonant laser induces a dipole moment in the molecule which interacts with the field to lower the eigenvalues creating centre-of-mass motion. At the same time rotational motion is confined to the laser polarisation axis. The rotational motion is induced because of the polarisation anisotropy in molecules where the stronger polarisation component seeks to align with the laser polarisation axis. This means the laser polarisation can be used to bring the highest polarisability axis in the molecular frame into the lab frame.

In a quantum mechanical explanation, the vibronic state is given angular momentum from the optical field, increasing the rotational population in the ground state. Resonant and nonresonant alignment in optical fields transfer angular momentum in a similar way, by scattering from an excited or virtual state. At near electronic resonances, the laser field induces Rabi-type cycles between the electronic ground state and an excited vibronic state, each cycle transfers a unit of angular momentum from the field to the ground state, the rotational selectional rules are $\Delta J = 0, \pm 1$. By repeated Rabi cycling between the levels, a rotational wave packet is generated in the ground state producing rotational motion. The interaction is proportional to the electric field strength. In the nonresonant case, the selection rules arise from Raman-type transitions, sequential nonresonant photons connect a virtual manifold above the ground state and transfer angular momentum creating a rotational wave packet. The nonresonant selection rules are $\Delta J = 0, \pm 2$ and the interaction is proportional to the square of the optical intensity due to the requirement that two photons are used to connect the rotational states. More detail on both near resonant and nonresonant techniques is provided in reviews of molecular alignment[100, 101].

Experimental observations of molecular alignment created by a nonresonant optical field in a room temperature gas cell containing CS_2 molecules were recorded in 1975[102] and attributed to the creation of a rotational wave packet. To the author's knowledge, this is the earliest observation of nonadiabatic molecular alignment. A theoretical description was provided in 1986[103]. Later, more experiments began to show that molecular alignment could occur with intense laser fields. In 1992 and 1993, experiments on dissociative ionisation of CO (Normand *et al.*[104]) using an aligning 30 ps pulse and a second, identical pulse to ionise the molecules, showed that the ions were ejected along the aligning pulse's laser polarisation axis, indicating the molecules were being aligned before being ionised. Dietrich *et el.*[105] used two 70 fs optical pulses with linear polarisations orthogonal and parallel to a time-of-flight axis. A decrease in signal was produced when both laser pulses were used compared to used individually. It was proposed some of the molecules were being aligned away from the probe pulse laser polarisation, decreasing the ionisation probability and the ion signal. Direct evidence was reported in 1996, in Raman spectroscopy on naphthalene trimers[105]. In the experiment, the Raman spectra was significantly enhanced by the presence of pendular states[83] created by a nonresonant external electric field.

1.6.1 Adiabatic alignment

In 1999 important observations of adiabatic alignment induced by a strong nanosecond laser field were reported by Sakai *et al.*[62] and Larsen *et al.*[63]. Under adiabatic conditions, the alignment dynamics change slowly compared to the rotational period of the molecule and the alignment follows the electric field envelope. In these experiments, an optical field which was below the ionisation threshold for the molecules was used to align the molecules. The molecules were then probed using a femtosecond laser to coulomb explode the molecules. These experiments were able to visually show angular confinement through the use of velocity map imaging[106], which records a 2D picture of the alignment distribution. The image can subsequently be converted into $\langle \cos^2 \theta \rangle$ to measure the alignment. Significant alignment of I_2[62] was achieved via this method. In ref [63], this technique was extended further to include ICl, CS_2, CH_3I and C_6H_5I molecules, proving the generality of the scheme. Generally speaking, the amount of alignment is proportional to the anisotropic polarisability, field strength and inversely proportional to the rotational constant B and the rotational temperature of the molecules.

1.6.2 Nonadiabatic alignment: field-free alignment

After the exploration of adiabatic alignment, short pulsed (femtosecond-picosecond) lasers were used to induce nonadiabatic alignment, where the rotational dynamics of the molecule change on the scale of the rotational period of the molecule. In essence, a short pulsed laser quickly transfers a large amount of angular momentum to the molecule, creating a rotational wave packet which keeps the molecule rotating in space even after the aligning pulse has passed. This is a purely quantum mechanical effect, the persistence of alignment after the alignment pulse is caused by the rotational wave packet, which de-phases and re-phases[98]. In adiabatic alignment, even though the field is changing, the molecule's field-free eigenfunctions dressed by the field will satisfy the stationary Schrödinger equation at all times. This assumption is no longer valid in the nonadiabatic regime and the full time-dependent Schrödinger equation must be used to quantify the dynamics. Field-free alignment has created much interest as it allows researchers to study molecules with well quantified internal motion without any perturbing background fields, this is in contrast to adiabatic alignment.

Through the use of polarised laser beams, laser induced alignment has been used to align molecules both adiabatically and nonadiabatically in one[62, 63, 107] and three dimensions[108, 101, 109, 110, 111]. Aligned molecules have also been a tool in studying high harmonic generation[82, 85, 112], chemical reaction dynamics [84, 113, 114], thermal motion[115], photodissociation[116, 117], molecular collisions[118] and molecular manipulation[119]. Nonadiabatic alignment has also been used to determine the polarisability anisotropy of molecules[120] and has been used in strong field ionisation studies of molecules[121, 122]. Only a few applications of aligned molecules have been discussed here and there will undoubtedly be many more in the future.

1.7 Effective Hamiltonian of the AC Stark effect

The dipole operator produced by an optical field may induce direct dipole transitions in a molecule, but the applied field can also spatially distort the molecular wave function and modify the stationary states of the molecule. This distortion creates an induced dipole moment which in turn can induce transitions between the molecular states by interacting with the same field that induced the dipole. These processes are generally termed multiphoton, specifically for the nonresonant AC Stark effect, the transitions require two photons to connect the ground and virtual states.

To evaluate the effect of nonresonant radiation on the energy levels of the molecule, we first note dipole force experiments use high intensity nonresonant fields $\approx 10^{11-12}$ W cm^{-2}. This means conventional perturbation methods cannot be used[123]. Conventional perturbation techniques require a small perturbation to the total energy of the system in order express small energy corrections to the unperturbed field-free energy. With strong fields, the wave function is being significantly distorted as the well depths are in the region ~ 100 K which is much larger than the field-free low lying J state energy levels. For example, the field-free energy with $J = 10$ for carbon disulphide is 17 K compared to a Stark shift of ~ 100 K.

In order to characterize a strong field interacting with a molecule, we proceed by splitting the dynamics of the molecule into two parts by forming separate equations of motion for the ground and virtual states. An effective Hamiltonian is formed which consists of a dipole and Raman interaction. The optical dipole force arises from the Raman Hamiltonian, it describes the nature of indirect transitions within the electronic ground state induced by a nonresonant field. The dipole interaction describes all transitions in the ground state caused by resonant single photon excitation.

In this section a brief derivation following the work of Shore[124] is shown to illustrate the key points and approximations in developing the effective Hamiltonian. More thorough treatments are available elsewhere[125, 35, 126, 127]. In the following section, the molecular alignment is shown to be written as an effective polarisability for linearly and circularly polarised light.

1.7.1 P and Q basis states

Figure 1.3 shows a molecular energy diagram. The ground state manifold P, consists of rotational quantum states p and p'. The label, p', refers to a rotational state with a different energy to p in the ground state. As the laser is nonresonant, all other excited states are collected into the Q manifold, which is a virtual state with sublevels q and q'. The goal is to describe the effect of the Q states as a whole on the ground states p and p'. Figure 1.3 shows the states are connected by two photons of the laser frequency ω. A state p, absorbs a photon and the molecule is excited to the virtual q state. From the same q state, a photon is emitted, and the molecule returns to the P manifold, but to a different sub level p' (the molecule may also return to its initial state p). The energy of the sub level p', plus the emitted photon will equal the energy of the absorbed photon. Thus the two photons connect the P and Q states through sequential Raman transitions[128], the re-emitted photons return to the P manifold, but can leave the molecule in the same or different rotational state

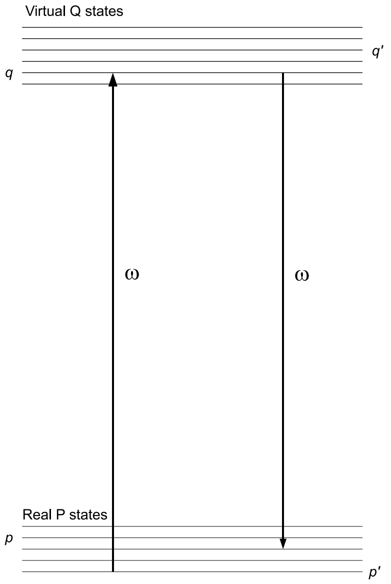

Figure 1.3: The dynamics of the ground state and virtual levels can be separated into a Q and P manifold, connected by two nonresonant photons. The Q manifold contains the virtual rotational levels q, whilst the P manifold contains rotational levels p and p'.

by absorbing angular momentum from the field. Mathematically, the electric field is

$$\mathbf{E}(t) = \frac{1}{2}\boldsymbol{\varepsilon}(t)\exp^{-i\omega t} + \frac{1}{2}\boldsymbol{\varepsilon}^*(t)\exp^{i\omega t}, \tag{1.2}$$

where $\boldsymbol{\varepsilon}(t)$ contains the field amplitude, ε_0, polarisation vector, $\mathbf{e}$, and pulse envelope, $g(t)$, such that $\boldsymbol{\varepsilon}(t) = \mathbf{e}\varepsilon_0 g(t)$. The time-dependent Schrödinger equation is used to describe molecular excitations through

$$i\hbar\frac{\partial}{\partial t}\Psi(t) = H(t)\Psi(t), \tag{1.3}$$

where $H(t)$ is the Hamiltonian of the system with $H(t) = H_0 + V(t)$. The perturbation $V(t)$, is $V(t) = -\boldsymbol{\mu}\cdot\mathbf{E}(t)$ and H_0 is the field-free Hamiltonian of the molecule. The Schrödinger equation in the Dirac picture is

$$i\hbar\frac{\partial}{\partial t}\Psi(t) = V(t)\Psi(t). \tag{1.4}$$

With time varying fields the equation $H(t)\Psi = E\Psi$ cannot be satisfied with constant energy E. Rather than trying to calculate the absolute energy of the molecule, the Dirac picture is used to define energy shifts $V(t)$, in the eigenvalues. By using an initial wave function multiplied by the phase difference of the field free energy, we will obtain an equation of the form 1.4. We use the dipole approximation which states that the molecular dimensions are small compared to the wavelength of the electric field. A superposition of orthogonal field-free P and Q states ($\langle\psi_p|\psi_q\rangle = 0$) is used to express the total wave function as

$$\Psi(t) = \sum_p \psi_p C_p \exp(-iW_p t) + \sum_q \psi_q C_q(t) \exp(-iW_q t). \tag{1.5}$$

The eigenvalue $W_{p,q}$, is in units of frequency and relates to a particular stationary state. The complex amplitudes for each stationary state are $C_{p,q}(t)$ and contain the subscripts p, q which run over all quantum numbers relating to the two manifolds. Substitution of equation 1.5 into equation 1.3 produces the equations of motion for the P and Q states. For the P states we find

$$i\hbar\frac{\partial}{\partial t}C_p(t) = \sum_{p'} \boldsymbol{\mu}_{pp'} \cdot \mathbf{E}(t) C_{\acute{p}} \exp[-i(W_{\acute{p}} - W_p)t] + \sum_q \boldsymbol{\mu}_{pq} \cdot \mathbf{E}(t) C_q \exp[-i(W_q - W_p)t], \tag{1.6}$$

and for the Q states we find

$$i\hbar\frac{\partial}{\partial t}C_q(t) = \sum_p \boldsymbol{\mu}_{qp} \cdot \mathbf{E}(t) C_p \exp[-i(W_p - W_q)t]. \tag{1.7}$$

Where $\boldsymbol{\mu}_{qp}$ is defined as $\langle q|\boldsymbol{\mu}|p\rangle$. This separation of molecular dynamics into two different basis sets is the essential states approximation[124].

1.7.2 Effective Hamiltonian

In most practical applications of the dipole force, the laser field is tuned below electronic resonances. This nonresonant approximation assumes negligible population reaches the Q states. Additionally, provided the laser wavelength has a bandwidth which is much smaller than the separation of the rotational levels in the ground state, a pulsed laser field of multiple frequencies can be represented by a single central frequency. Under these approximations the solution to equation 1.7 is

$$C_q(t) = \frac{1}{2i\hbar}\sum_p \left[\frac{\boldsymbol{\mu}_{qp} \cdot \boldsymbol{\varepsilon}(t)}{W_q - W_p - \omega} + \frac{\boldsymbol{\mu}_{qp} \cdot \boldsymbol{\varepsilon}^*(t)}{W_q - W_p + \omega}\right] C_p(t) \exp[-i(W_p - W_q)t]. \tag{1.8}$$

Equation 1.8 describes the probability amplitudes in the Q states purely in terms of the P state amplitudes. The interaction between the p and q sub-levels is mediated by the matrix elements between the electric field vector and the induced dipole moment of the molecule. It is also inversely proportional to the separation between the p and q levels $W_q - W_p$. Equation 1.6, describing the p state time evolution, is rewritten using the solution for the q state amplitudes in equation 1.8. We then eliminate the fast oscillating phase terms using the rotating wave approximation. The phase terms containing the laser frequency ω and the upper state levels W_q are neglected because these frequencies are large compared to phase terms with only p and p'. Thus

$$\begin{aligned}&(W_q - W_p) \pm \omega \\ &(W_p - W_{p'}) \pm 2\omega\end{aligned} \tag{1.9}$$

are eliminated, whilst the energy differences

$$W_p - W_{p'} \tag{1.10}$$

are retained. The only remaining term from insertion of 1.8 into 1.6 is

$$i\hbar\frac{\partial}{\partial t}C_p(t) = \sum_{p'} V_{pp'}^{eff}(t)C_{p'}(t)\exp\left[-i(W_{p'} - W_p)t\right], \tag{1.11}$$

where $V_{pp'}^{eff}(t) = V_{pp'}^{dip}(t) + V_{pp'}^{Ram}(t)$ is an effective Hamiltonian[129, 124] which contains the direct dipole transitions within the ground P state and the Raman transitions which interact with the Q state manifold. The dipole Hamiltonian is

$$V_{pp'}^{dip}(t) = -\boldsymbol{\mu}_{pp'} \cdot \mathbf{E}(t). \tag{1.12}$$

The Raman part is

$$V_{pp'}^{Ram}(t) = -\frac{1}{4}\sum_q \left[\frac{\boldsymbol{\mu}_{pq} \cdot \boldsymbol{\varepsilon}^*(t)\boldsymbol{\mu}_{qp'} \cdot \boldsymbol{\varepsilon}(t)}{W_q - W_p + \omega} + \frac{\boldsymbol{\mu}_{pq} \cdot \boldsymbol{\varepsilon}(t)\boldsymbol{\mu}_{qp'} \cdot \boldsymbol{\varepsilon}^*(t)}{W_q - W_{p'} - \omega}\right] \tag{1.13}$$

which can be written as

$$V_{pp'}^{Ram}(t) = -\frac{1}{4}\,\boldsymbol{\varepsilon}^*(t) \cdot \boldsymbol{\alpha}_{\boldsymbol{pp'}} \cdot \boldsymbol{\varepsilon}(t). \tag{1.14}$$

The Placzek approximation has been used in the denominators of equation 1.13 to approximate the scattered light to be equal to the incident light which allows the use of $\boldsymbol{\alpha}_{\boldsymbol{pp'}}$, which is the frequency dependent Raman polarisability tensor between the transitions p and p' expressed in the molecular axis frame[130]. In the ground state, and with nonresonant fields, the polarisability varies very little within the P manifold and the denominators of 1.13 are replaced by the average difference between the P and Q states, $W_q - W_p = W_q - W_{p'} = W_{qp}^{ave}$. This final assumption means the Raman polarisability tensor is well approximated by the static polarisability. Since we are concerned with the shift in the ground state we find

$$V(t) = -\frac{1}{4}\,\boldsymbol{\varepsilon}^*(t) \cdot \boldsymbol{\alpha} \cdot \boldsymbol{\varepsilon}(t). \tag{1.15}$$

In the two limits of the molecular interaction, the dipole Hamiltonian is used to represent resonant transitions and the dynamics follow the instantaneous electric field. When far from resonance, the Raman Hamiltonian dominates and the dynamics follow the electric field envelope.

1.8 Effective polarisability

Once the polarisation of the AC field is known, the general expression

$$V(t) = -\frac{1}{4}\mathbf{e}^* \cdot \boldsymbol{\alpha} \cdot \mathbf{e}\, \varepsilon^2(t), \tag{1.16}$$

can be further evaluated to yield the effective polarisability, which describes the rotation of the body fixed polarisability components in $\boldsymbol{\alpha}$ into the lab frame where the laser polarisation vectors $\mathbf{e}$ are defined. Thus

$$\begin{aligned} V(t) &= -\frac{1}{4}\alpha_{eff}\varepsilon^2(t) \\ \alpha_{eff} &= \mathbf{e}^* \cdot \boldsymbol{\alpha} \cdot \mathbf{e}. \end{aligned} \tag{1.17}$$

Firstly the lab axes are defined and the lab direction Z is chosen to lie parallel with the polarisation vector for linearly polarised light. For circularly polarised light the propagation direction is chosen for the Z axis, which is perpendicular to the plane of radiation. The alignment in both cases is quantified by θ. Figure 1.4 shows both cases of molecular alignment for CS_2 molecules. Figure 1.4 a) shows that the linearly polarised light polarisation vector is parallel to the Z axis, and θ_l forms the angle between the molecular bond axis and the Z axis. For circularly polarised light in figure 1.4 b), the Z axis (blue) is perpendicular to the polarisation plane (green), and θ_c forms the angle between the bond axis and the Z direction. One can see maximum alignment is obtained for $\theta_l = 0°$ and $\theta_c = 90°$ for linearly and circularly polarised light respectively.

1.8.1 α_{eff} for linearly polarised light

The polarisability tensor of a molecule is

$$\boldsymbol{\alpha} = \begin{pmatrix} \alpha_{xx} & 0 & 0 \\ 0 & \alpha_{yy} & 0 \\ 0 & 0 & \alpha_{zz} \end{pmatrix}$$

where α_{xx} is the static polarisability along the molecular axis x due to an electric field applied along x in the molecular frame. The average polarisability is calculated from $\alpha_{ave} = \frac{1}{3}(\alpha_{xx} + \alpha_{yy} + \alpha_{zz})$. When the molecule's rotational motion cannot be

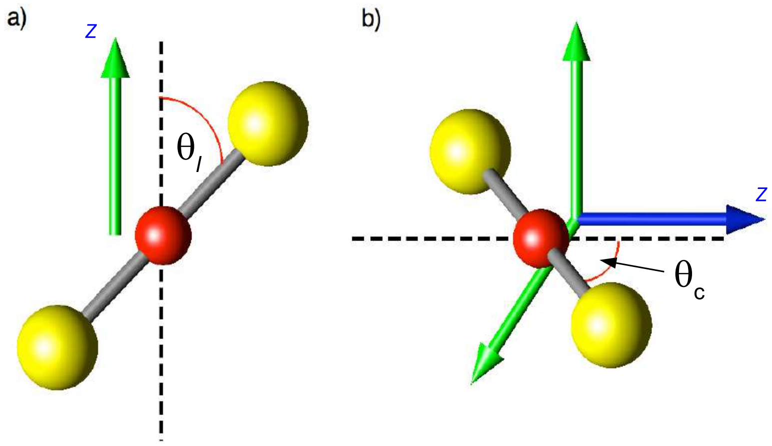

Figure 1.4: The alignment of CS_2 with linearly and circularly polarised light is shown. Linearly polarised light a), has its polarisation vector parallel to the electric field (green) in the space fixed direction Z. b) The Z direction for circularly polarised light is chosen to be parallel to the propagation direction (blue), but perpendicular to the plane of the radiation (green).

averaged, the induced dipole moment in the lab frame is

$$\boldsymbol{\mu} = \mu_{IX}\hat{\mathbf{i}} + \mu_{IY}\hat{\mathbf{y}} + \mu_{IZ}\hat{\mathbf{k}}. \tag{1.18}$$

By only considering the dipole moment in the Z direction the expression becomes

$$\mu_{IZ} = \mu_{Ix}\Phi_{Zx} + \mu_{Iy}\Phi_{Zy} + \mu_{Ix}\Phi_{Zz} \tag{1.19}$$

where Φ_{Gg} are Euler rotation angles for the lab fixed axis G and the body fixed axis g. The induced dipole moment in the molecular frame is $\mu_{Ig} = \alpha_{gg}E_g$, which can be inserted into the above equation yielding

$$\mu_{IZ} = \alpha_{xx}E_x\Phi_{Zx} + \alpha_{yy}E_y\Phi_{Zy} + \alpha_{zz}E_z\Phi_{Zz}. \tag{1.20}$$

The electric field along a particular molecular axis g due to an electric field along any lab fixed axis XYZ is

$$E_g = E_X\Phi_{Xg} + E_Y\Phi_{Yg} + E_Z\Phi_{Zg}. \tag{1.21}$$

Since the field is only being applied along the Z direction, the expression reduces to $E_g = E_Z\Phi_{Zg}$ along all three molecular axis xyz. The induced dipole moment is

$$\mu_{IZ} = \alpha_{xx}E_Z\Phi_{Zx}^2 + \alpha_{yy}E_Z\Phi_{Zy}^2 + \alpha_{zz}E_Z\Phi_{Zz}^2. \tag{1.22}$$

At this point equation 1.22 is completely general for any shape molecule. By limiting the case to linear molecules which are symmetrical about the bond axis, the polarisability components are simplified becoming $\alpha_{yy} = \alpha_{xx} = \alpha_{\perp}$, where $\alpha_{\perp}$ is the polarisability perpendicular to the molecular axis and $\alpha_{zz} = \alpha_{||}$ is the polarisability parallel to the molecular axis. The induced dipole moment becomes

$$\mu_{IZ} = \left[\alpha_{\perp}\left(\Phi_{Zx}^2 + \Phi_{Zy}^2\right) + \alpha_{||}\Phi_{Zz^2}\right] E_Z, \tag{1.23}$$

by using the identity $\sum_g \Phi_{Zg}^2 = 1$ we find

$$\mu_{IZ} = \left(\alpha_{||}\cos^2\theta_l + \alpha_{\perp}\sin^2\theta_l\right) E_Z \tag{1.24}$$

or

$$\mu_{IZ} = \left(\Delta\alpha\cos^2\theta_l + \alpha_{\perp}\right) E_Z = \alpha_{eff} E_Z \tag{1.25}$$

where $\Delta\alpha = \alpha_{||} - \alpha_{\perp}$, which is the polarisability anisotropy of the molecule. The complete expression for the AC Stark shift of the molecule in a linearly polarised field along the Z axis is

$$V(t) = -\frac{1}{4}\left[\Delta\alpha\cos^2\theta_l + \alpha_{\perp}\right] E^2(t). \tag{1.26}$$

1.8.2 α_{eff} for circularly polarised light

A similar procedure is followed except the nonzero components are

$$\boldsymbol{\mu} = \mu_{IX}\hat{\mathbf{i}} + \mu_{IY}\hat{\mathbf{j}} \tag{1.27}$$

with

$$\begin{aligned} \mu_{IX} &= \left(\alpha_{xx}\Phi_{Xx}^2 + \alpha_{yy}\Phi_{Xy}^2 + \alpha_{zz}\Phi_{Xz}^2\right) E_X \\ \mu_{IY} &= \left(\alpha_{xx}\Phi_{Yx}^2 + \alpha_{yy}\Phi_{Yy}^2 + \alpha_{zz}\Phi_{Yz}^2\right) E_Y \end{aligned} \tag{1.28}$$

we note $|E_X| = |E_Y| = E$, yielding the lab frame effective polarisability

$$\frac{\mu_{IX} + \mu_{IY}}{E} = \alpha_{\perp}\left(\Phi_{Xx}^2 + \Phi_{Xy}^2 + \Phi_{Yx}^2 + \Phi_{Yy}^2\right) + \alpha_{||}\left(\Phi_{Xz}^2 + \Phi_{Yz}^2\right), \tag{1.29}$$

the identities $\sum_g \Phi_{Zg}^2 = 1$ and $\sum_G \Phi_{Gz}^2 = 1$ are used to yield the expression for the effective polarisability

$$\alpha_{eff} = \frac{1}{2}\left[\alpha_{\perp}\left(1 + \cos^2\theta_c\right) + \alpha_{||}\sin^2\theta_c\right]. \tag{1.30}$$

The factor of $\frac{1}{2}$ is introduced from the definition of circularly polarised light $\mathbf{e}^* \cdot \mathbf{e} = \frac{x+y}{2}$, thus the total Stark shift due to circularly polarised light is

$$V(t) = -\frac{1}{8}\left[\alpha_{||} + \alpha_{\perp} - \Delta\alpha \cos^2\theta_c\right] E^2(t). \tag{1.31}$$

1.8.3 Units of polarisability

Polarisability is used frequently throughout this thesis and can sometimes be found in the literature in units of Å^3, with Å^3=10^{-24} cm^3. Most recent scientific papers which use the dipole force quote the units in C m^2 V^{-1}, this convention is maintained in this thesis. The formula to convert between the units is[131]

$$\alpha(\mathrm{cm}^3) = \frac{10^6}{4\pi\epsilon_0}\alpha(\mathrm{C\ m}^2\ \mathrm{V}^{-1}), \tag{1.32}$$

where ϵ_0 is the permittivity of free space.

1.9 Conclusion

A brief review of the applications of the dipole force and molecular alignment was presented. The AC Stark effect causes centre-of-mass motion by negatively shifting the eigenvalues of the molecules. Molecular alignment is caused by angular confinement of the molecular axis due to polarisation anisotropy. Both interactions were shown to be produced by an effective Raman Hamiltonian which was derived in the nonperturbative, nonresonant limit of the AC Stark effect. The cases of linearly and circularly polarised light were considered. Both interactions were quantified by $\cos^2\theta_{l,c}$, which is the angle between the molecular axis and the laser polarisation vector for linearly polarised light and the angle between the molecular axis and the propagation vector for circularly polarised light. We have also defined an effective polarisability, which expresses the molecular polarisability in the lab frame where the laser polarisation is best expressed. The complete lab frame effective Hamiltonian for each laser polarisation, which describes the centre-of-mass motion and molecular alignment, is given by equations 1.26 and 1.31.

Chapter 2

Experimental apparatus

2.1 Introduction

Strong molecular alignment only occurs when a few rotational states of a molecule are occupied. To study the role of molecular alignment on the dipole force it is necessary to have either cold molecules or a state-selected beam. In this work we use a cold molecular beam created via a supersonic expansion. In this chapter, we describe the apparatus used to create a molecular beam of CS_2 and characterize the beam in terms of temperature and velocity. Also, the laser systems for detecting the molecules and for creating the dipole force are described.

2.2 Vacuum systems

The experiments to investigate the dipole force and the role of molecular alignment were carried out in the experimental setup shown in figure 2.1. A molecular beam of carbon disulphide (CS_2) is formed by expanding carbon disulphide in argon through a pulsed valve into a vacuum chamber containing a skimmer (source chamber). The skimmed molecules then enter a second differentially pumped vacuum chamber (main chamber) where the molecules fly into a time-of-flight mass spectrometer (TOFMS) and are ionised by a probe laser beam ($\lambda = 478$ nm) at a right angle to the molecular beam. The ionized molecules impact onto a micro channel plate detector (MCP) where their time-of-flight (TOF) is recorded on an oscilloscope and later converted into a molecular velocity spectrum. The effects of molecular alignment and its influence on the centre-of-mass motion of molecules is studied by focussing a seeded, nonresonant, infra-red ($\lambda = 1064$ nm) laser onto the molecular beam before the molecules encounter the probe laser. Molecules which have interacted with the IR field are ionized by the probe laser and their perturbed TOF is recorded and compared against molecules unperturbed by the IR laser field.

The skimmer is made from nickel whilst the main and source vacuum chambers

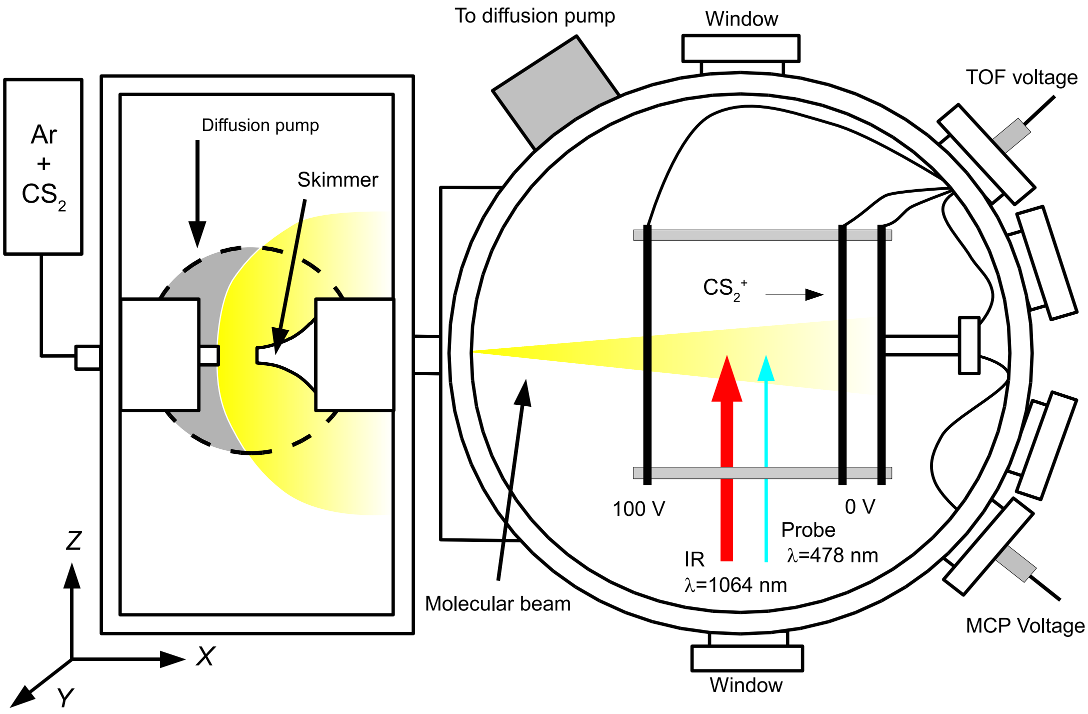

Figure 2.1: A top-down schematic of the apparatus shows the creation of the molecular beam in the source chamber. The molecules then enter into the main chamber and are intersected at 90° by the probe (blue) and IR (red) laser beams inside a TOFMS. Ionised molecules are repelled by the 100 V plate of the TOFMS and are collected at the MCP which is connected to an oscilloscope. Diffusion pumps are connected to the bottom of the source chamber and to the side of main chamber. The separation between the skimmer and valve is approximately 30 mm whilst the distance from the valve to the probe laser beam is 300 mm.

are made from stainless steel. Each chamber is cylindrical with a diameter of 30 cm and a height of 15 cm giving an approximate volume of 11 litres. The source chamber is separated from the main chamber by a skimmer with a 2 mm circular aperture. This selects the central on-axis molecules of the molecular beam whilst all other molecules are reflected and pumped away in the source chamber. The source chamber is connected to a Varian diffusion pump (600 ls^{-1}) which has an Edwards rotary vane RV12 backing pump. An Edwards E02K diffusion pump (150 ls^{-1}) is connected to an Edwards E2M8 backing pump, providing the vacuum in the main chamber. Both diffusion pumps are water cooled and use Dow Corning 705 silicone pump oil. The pump rates of the rotary pumps are 3.9 ls^{-1} and 2.5 ls^{-1} for the RV12 and E2M8 respectively. The backing pumps both provide pressures of approximately 5×10^{-2} mbar when the diffusion pumps are switched off. The quality of the vacuum is determined by the leaks and contaminants in the system arising from seals, oils, windows, welds and dust. When the diffusion pumps are activated, a vacuum of 8×10^{-8} mbar is measured in the main chamber, which is sufficiently low to create a molecular beam. The molecular beam signal could not be detected when the pressure was above 6×10^{-7} mbar. Low vacuum pressure measurements are obtained using two Edwards APG-M Pirani gauges attached to each chamber. When a high vacuum is achieved ($< 10^{-7}$ mbar) and the molecular beam is operating, an Edwards Active Ion gauge (AIGX-S) is used to monitor the pressure in the main chamber. No high vacuum gauge is attached to the source chamber as during operation of the pulsed valve the pressure rapidly rises to a level which may damage the vacuum gauge. A Parker Instrumentation pulsed solenoid valve has a circular orifice of 500 μm and is controlled by an Iota One pulsed valve driver. Through the valve, a mixture of 4 % or 25 % of carbon disulphide is expanded into 1.8 bar of argon. When the pulsed valve is operating, the pressure in the main chamber increases by approximately 0.8×10^{-8} mbar.

2.2.1 Molecular detection

The time-of-flight mass spectrometer

A home made time-of-flight mass spectrometer[132], which was built by Alexis Bishop, occupies the centre of the main chamber in figure 2.1, where the molecules are ionised by the probe laser. A more detailed schematic of the TOF apparatus is shown in figure 2.2.

For an ion in an electric field $\mathbf{E}$, the force on the ion is given by $\mathbf{F} = m\mathbf{a} = q\mathbf{E}$. The resulting acceleration is

$$\frac{d\mathbf{v}}{dt} = \frac{q\mathbf{E}}{m} \tag{2.1}$$

where m is the mass of the ion, $\mathbf{E}$ is the electric field vector, $\mathbf{v}$ is the molecular velocity

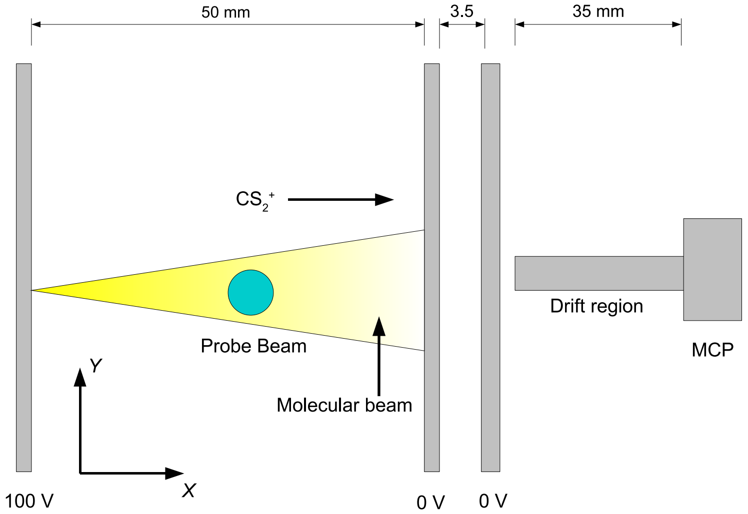

Figure 2.2: A side schematic (XY plane) of the time-of-flight mass spectrometer. After the ions are created, the 100 V electrode accelerates the ions toward the field-free drift region. After the drift region the ions impinge onto the surface of the MCP which is held at a DC voltage of -2.5 kV. A lower voltage on the repeller plate will mean the ions spend longer in the drift region, increasing the TOF separation between ions of differing velocity, increasing the dispersion ratio (see text).

vector and q is the charge of the ion. Equation 2.1 describes the motion of the ion through the electric field. To solve this equation and the electrostatic equations that govern the electric field distribution around the electrodes in the TOF mass spectrometer, Simion[133] software was used. Simion calculates the electric field for a given geometry of electrodes. It can also calculate the properties of charged particles in the electric field such as position, velocity and total TOF. Using the geometry in figure 2.2 together with Simion, the TOF of a singly charged CS_2 molecule was calculated to be 9.3 μs. This value of predicted TOF for the apparatus agrees within ± 1 % of the measured TOF. This corresponds to a difference in TOF of ± 100 ns. An error of ± 100 ns in TOF is too large to be used to directly measure the velocity of ions in the TOF mass spectrometer. Consequently, changes in molecular velocity are measured. By comparing time-of-flight spectra, the difference in arrival time of the ions can be used to calculate the difference in velocity. Simion can be used to simulate the differences in arrival time between the molecules around a central velocity. This velocity is determined theoretically from the terminal velocity of a supersonic expansion. The difference in arrival time as shown by Simion is linear over the range of velocities simulated (540 ± 50 m s^{-1}). Thus, although Simion is not accurate enough to measure velocities directly, we are still able to extract information about the dipole force through the induced velocity changes by determining the slope of TOF to velocity. We term the ratio of TOF to velocity the dispersion and its value depends on the TOF voltages and the length of the field-free region. In most of the experiments described in this thesis the dispersion is 0.4 ns/(m s^{-1}), which is for the 100 V setting on the TOFMS repeller plate. For a given shift in TOF measured in ns, dividing by the dispersion yields the corresponding velocity change. The error in the dispersion ratio is determined by the experimental measurement of the TOF compared to Simion of ±1 %. Using Simion, if each simulated molecular velocity has an error of ±1 % in its TOF, the error in the dispersion is approximately ±2 %. This error is systematic and so each measured velocity shift will be increased or decreased by the same amount.

The dispersion ratio is imperative to measuring the dipole force imparted onto the molecules. The value provided by Simion agrees well with the measured TOF in our apparatus but ideally an experimental determination is more preferable. Although not carried out here, a way to determine this value would be to use different seed gases. The differing terminal velocity of the gases would provide a series of TOF points which would be used to create a best fit plot, the gradient of which at each velocity is the ratio of TOF to m s^{-1}.

Micro channel plate detector (MCP)

The MCP[134] is produced by El-Mul[135] and consists of many glass tubes (channels) coated with carbon. The tubes lie parallel to each other have an approximate diameter of 10 μm. A large negative voltage is applied across the tubes. An impact from a charged molecule or particle starts an avalanche process inside the channels releasing electrons. The production of electrons is measured by a circuit[136] connected to an oscilloscope to measure when the ions are collected. The MCP typically requires a voltage of -2.5 kV producing a gain of 10^6. Ion collection is typically a series of discrete events and in order to build up a smooth TOF spectrum, the data is averaged over 1200 shots of the probe laser, corresponding to 120 seconds of averaging from the 10 Hz probe laser.

The isotopes of CS_2

Shown in figure 2.3 is a time-of-flight spectrum for carbon disulphide and its sulphur isotopes when ionised by the probe beam at a wavelength of 478.63 nm. The dominant isotopes of sulphur are ^{34}S which has an abundance of 4.2 %[137] and ^{33}S which has an abundance of 0.75 %[138]. The strength of the signal due to the presence of isotopes is calculated using tables 2.1 and 2.2

Table 2.1 lists the atomic abundances of the atoms in the CS_2 molecule. Table 2.2 shows the permutations of the carbon disulphide molecule with the isotopes and the probability of detecting each molecule. By summing the contribution from all molecules with the same mass, the fourth column in table 2.2 shows the contribution

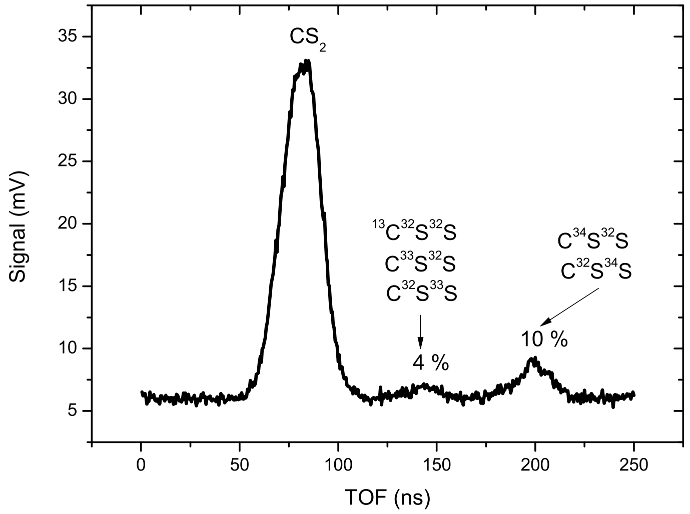

Figure 2.3: The TOF spectrum of CS$_2$ at a probe laser wavelength of 478.63 nm is shown. The heavier isotopes of CS$_2$ are resolved and arrive later in time at the MCP. The presence of the isotopes with respect to the CS$_2$ signal is indicated by the percentage labels. The mass resolution is better than 1 amu as each mass peak corresponds to a separation of 1 amu. The mass and temporal resolution depend on the voltage to the repeller plate. The x axis is offset by 9.3 μs.

Table 2.1: Atomic abundances (%)

Atom	^{12}C	^{13}C	^{32}S	^{33}S	^{34}S
% Abundance	98.9	1.10	95.02	0.750	4.22

Table 2.2: Strength of molecule signal in mass spectra

Molecule	Mass	Abundance (%)	% of main CS$_2$ peak
^{12}C^{32}S^{32}S	76	89.2	100
^{12}C^{33}S^{32}S	77	0.704	2.7
^{12}C^{32}S^{33}S	77	0.704	
^{13}C^{32}S^{32}S	77	0.993	
^{12}C^{34}S^{32}S	78	3.96	8.9
^{12}C^{32}S^{34}S	78	3.96	
^{13}C^{32}S^{33}S	78	0.0157	

to the mass spectra in figure 2.3, as a proportion of the main CS_2 signal. In figure 2.3 the measured strengths of the peaks are 10 % and 4 % respectively, with an error of approximately ±1% arising from determining the height of each peak. This allows the mass peaks to be labelled from table 2.2. We label the larger sub-peak as mainly $^{12}C^{34}S^{32}S$ and $^{12}C^{32}S^{34}S$ molecules. The smallest peak is labelled as a mixture of $^{13}C^{32}S^{32}S$, $^{12}C^{33}S^{32}S$ and $^{12}C^{32}S^{33}S$ molecules. This means the peaks are separated by approximately 1 amu and as they are clearly resolved, this gives a mass resolution in our mass spectrometer of better than 1 amu.

Due to their heavier mass, the isotope-molecules arrive later at the MCP even though they will have had the same velocity in the molecular beam. It is important to identify the isotopes and keep track of them so they are not mistaken for a velocity change. Since the isotope peaks are small in comparison to the CS_2^+ signal and are sufficiently separated from the main CS_2 signal, they play no further role in the experiments.

In addition to the isotopes of CS_2, dissociation of CS_2^+ can create other detectable ions by absorption of further photons[139] after the initial ionisation process. Typically CS^+ and S^+ ions are produced in this way. This process occurs mainly at wavelengths of higher energy than 478 nm and also at higher intensities[140, 141, 137]. The presence of these ions becomes important in spectroscopy as the dissociation paths can be wavelength dependent. In order to assess the strength of a transition in comparison to others, all of the ions produced in ionisation would need to be recorded and added together to create a total TOF signal. Using the wavelengths and intensity provided by the probe laser ($\sim 10^{10}$ W cm^{-2}), the complete TOF signal was monitored and only CS_2^+ ions and its isotopes were observed.

2.3 Laser systems

2.3.1 The dye laser

Two Nd:YAG laser systems were used, the first was used to pump a tunable dye laser which generated the probe beam which resonantly ionised the molecules. The second laser system provided the strong nonresonant optical field. Both lasers were operated at 10 Hz. An unseeded Q-switched Continuum Precision II 8000 Nd:YAG laser had its fundamental output frequency tripled to produce a wavelength of 355 nm. The tripled output had an energy of 110 mJ per pulse measured using a Spectra Physics Model 407A power meter. This laser was used to pump a Continuum ND6000 tunable dye laser. Using an Exciton coumarin 102 laser dye (also known as coumarin 480) the wavelength of the dye laser had a tuning range from 460-500 nm. The maximum energy output for this dye occurs at 475 nm[142]. The output energy from the dye laser is 1.8±0.2 mJ per pulse. Before being directed into the vacuum chamber, the

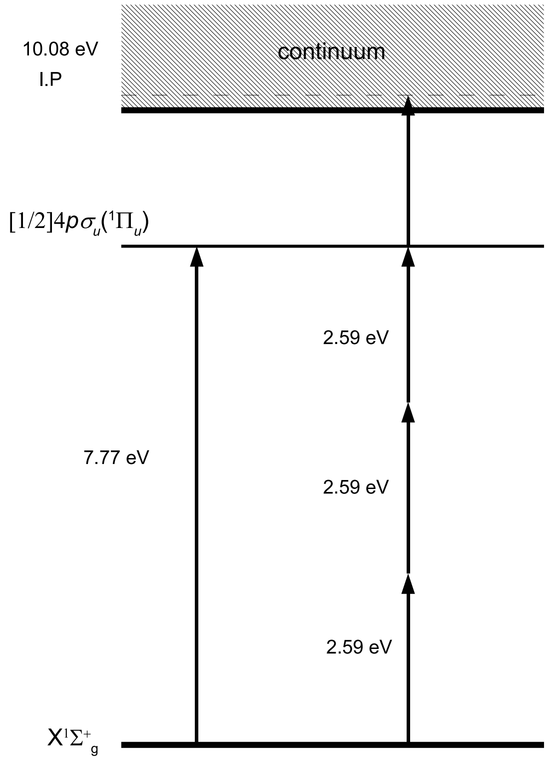

Figure 2.4: An energy diagram showing the sequential absorption of three photons to reach the resonant one photon level $\left[\frac{1}{2}\right] 4p\sigma_u(^1\prod_u)$ from the ground state $\tilde{X}^1\sum_g^+$. The wavelength of this transition is 159.32 nm for one photon or 477.95 nm for three photons. An additional single photon is required to ionise the molecule by exciting the electron into the continuum. The additional kinetic energy of 0.28 eV is spread between the molecule and the ejected electron.

output from the dye laser was spatially filtered by focussing the dye beam using a $f = 500$ mm plano-convex lens onto a 200 μm pinhole producing a spatial Gaussian intensity profile. This was necessary to improve the initial poor spatial quality of the dye laser beam. A pulse energy of 0.2±0.05 mJ was measured entering the vacuum chamber. The temporal profile of the laser pulse is near Gaussian shaped with a full width half maximum (FWHM) of 7 ns. This was measured on InGaAs photodiode with a rise time of <1 ns. After spatial filtering, the dye laser beam was expanded to a diameter of 25 mm filling a one inch plano-convex lens of focal length 20 cm. This optic focuses the dye laser into the vacuum chamber and intersects the molecular beam. The 20 cm plano-convex lens produces a Gaussian focus with an e^{-2} waist radius of approximately 5 μm. This was measured on a CCD with square pixels, where each pixel was 5.6 μm wide. This yields an intensity of approximately 2×10^{10} W cm^{-2}. This intensity and spot size produces a very small dipole force inducing a velocity change in the molecules of less than 1 m s^{-1}. The carbon disulphide is ionised from its electronic ground state in a (3+1) resonance enhanced multiphoton ionisation[140] (REMPI) process at a laser wavelength of 478.63 nm, corresponding to a $\left[\frac{1}{2}\right] np\sigma_u(^1\prod_u) \leftarrow \tilde{X}^1 \sum_g^+$ transition. The wavelength of this transition from other studies is 477.90 nm[141, 143], indicating our dye laser has an offset of -0.73 nm. The ionisation process creates predominantly CS_2^+ ions, only at shorter wavelengths and higher intensities does molecular dissociation occur. Due to the high intensities required in a (3+1) multiphoton absorption process, only the central region of the probe focus will actually ionise the molecules and so we estimate the spatial resolution of the probe beam will be better than that given by the waist radius of 5 μm.

Figure 2.4 shows an energy diagram of a REMPI process. Resonance enhanced multiphoton ionisation adds the energy of subsequent photons in order to excite to a resonant level allowed by the symmetry selection rules of the laser polarisation and molecular states. By adding three 477.95 nm photons, an equivalent 159.32 nm photon is produced and excites the molecule into a resonant p shell state, further absorption of a single 477.95 nm photon ionises the molecule. We record the velocity of the neutral molecules by assuming the ion velocity is close to that of the neutrals

$$v(\mathrm{CS_2}) \simeq v(\mathrm{CS_2^+}). \tag{2.2}$$

The excess energy above the 10.08 eV[143] ionisation potential of CS_2 is 0.28 eV, this excess energy is spread between the ejected electron and the ion. As the mass of the electron is much less than that of the CS_2^+ ion, the recoil effects from the electron ejection will be small. Equating the excess kinetic energy and using the conservation of momentum between the ion and electron, a maximum recoil velocity of 2.2 m s^{-1} is calculated. During ionization, electrons are preferentially ejected along the probe laser polarisation axis, which is vertical (Y in the lab axis) and perpendicular to the molecular beam axis. In the experimental setup shown in figure 2.2, the TOFMS is only sensitive to velocity changes along the molecular beam axis, and so any recoil effects from the ejection of an electron along the laser polarisation axis should not significantly alter the measured molecular velocity.

Laser saturation

When a laser which is resonant with a transition of a two level system is of sufficient intensity that the pumping rate of population into the upper state is larger than the relaxation rate of the upper state, the system is said to be saturated[144]. This means fewer and fewer atoms or molecules will be in a state which can absorb the radiation, leading to a decrease in absorption signal. This is particularly important in spectroscopy where measuring the temperature of the gas is dependent on the initial state population. For a given transition and laser wavelength, the signal created in TOF mass spectroscopy is proportional to the density of the molecules and the laser intensity (or the cube of the intensity for three photon transitions). For pulsed lasers,

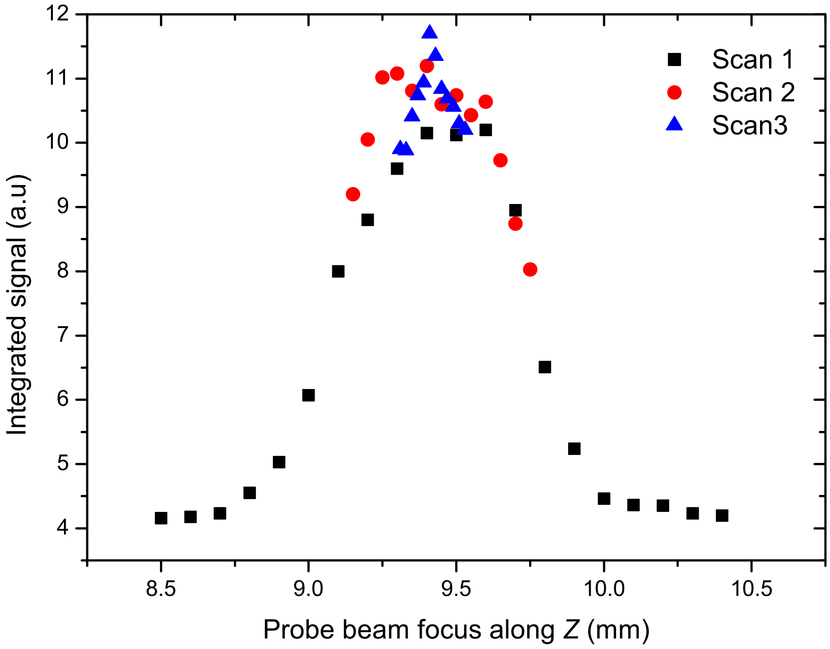

Figure 2.5: The integrated ion signal as the probe beam focus is changed along the Z axis is shown. The different data sets correspond to smaller step sizes to locate the optimum probe beam focus.

steady state conditions might not be reached as the interaction time is limited to the pulse length of the laser. For this reason, a pulsed laser's saturation intensity is generally much higher when compared to a continuous wave laser.

In the REMPI detection scheme used in the experiments of this thesis, three-photons are used to reach a resonant level and a subsequent photon ionises the molecule. The saturation process is much more complicated in REMPI schemes. Saturation of the intermediate state will change the ionisation rate, also rotational levels can be severely perturbed due to the high fields and an increased density of electronic states at the three-photon resonance may occur[145]. This can greatly affect the rotational line strength factors. Fluorescence and collisional energy transfer of the intermediate state may also compete with the ionisation. These complications make extracting information about the internal population of molecular states using REMPI difficult and often unreliable.

Figure 2.5 shows the integrated ion signal of the probe beam operated at the energy used in the experiments. The probe beam focus is traversed through the interaction region along the Z axis. As the size of the focus is decreased, the ion signal is also increased due to increasing intensity, reaching a maximum at a well defined Z position. The different data sets on figure 2.5 show several scans with reduced step sizes to refine the optimum probe beam focus. By scanning the laser focus along the Z axis, the intensity is being increased but the focal volume is also being decreased. The estimated focal volume given by the $e^{-2} = 5$ μm probe beam width and the Rayleigh range is $\sim 2 \times 10^{-8}$ cm^3. If the three-photon intermediate transition were fully saturated, the integrated ion signal would decrease at the focus as the focal volume would be at a minimum, lowering the number of molecules available to be ionised. This would result in the signal increasing before and after the focus along Z, with a drop in signal at the optimum focus, creating a saddle shape along the Z axis. Figure 2.5 shows the three-photon transition is not fully saturated as no such shape is observed. Unfortunately, although we may conclude the transition is not fully saturated, figure 2.5 cannot be used to quantify or indicate if there is any partial saturation occurring.

2.3.2 Infra-red laser

To irradiate the molecules with a nonresonant optical field we use an injection seeded Spectra Physics Quanta Ray Nd:YAG laser, which is Q-switched and provides an output energy of 175 mJ per pulse at 10 Hz. Injection seeding[146] in pulsed lasers can be used to force the laser to operate in a single longitudinal mode which will stabilize the output energy. The seeder laser provides a small intensity I_L, of frequency ω_L, which is directed into the host laser cavity which seeds operation at a chosen frequency. The advantage of this technique is that rather than allowing laser emission to build up from spontaneous emission within the gain medium, the seeder laser provides control over the initial excitation of the laser modes by creating an intensity I_L for amplification much larger than that arising from the build up of spontaneous emission. As the intensity of the amplified seeder mode, ω_L, increases, it will use most of the gain in the medium, therefore suppressing the build up and emission of other longitudinal modes. Pulsed lasers will always revert to their resonant frequency ω_0 as this frequency has the highest gain. The cavity length of the pulsed laser is peizo controlled in an active feedback system which alters the cavity resonant frequency ω_0, to match the seed resonant frequency ω_L. This allows the host laser to emit a single mode at the centre of the gain curve, maximizing the output energy.

The pulse shape from the Spectra Physics laser is shown in figure 2.6, the FWHM is 15 ns. The black and red traces show seeded and unseeded temporal profiles. The data was taken using a 3 GHz Tektronix Wavepro 7300 oscilloscope sampling at 20 GS/s and using an InGaAs fast photodiode with a rise time of < 1 ns. A good indication of seeded operation is the reduction in build up time compared to unseeded operation. Unseeded lasing takes longer because the laser is waiting to build longitudinal modes from spontaneous emission. This can clearly be seen in figure 2.6 where the seeded trace (black) is reduced in build up time by 27 ns compared to the unseeded trace in red. The black trace is temporally smooth, indicating only one longitudinal mode is

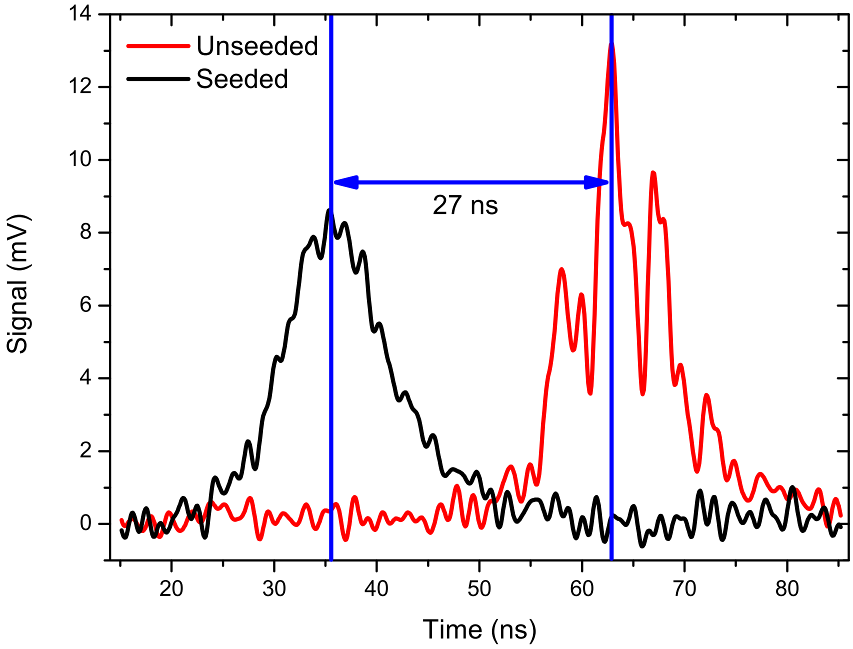

Figure 2.6: The temporal profile of the IR pulse is recorded in seeded (black) and unseeded operation (red). Multiple longitudinal modes are clearly seen when compared to the seeded laser pulse.

present. In contrast, the red trace clearly shows mode beating on the diode due to the presence of multiple longitudinal modes.

A Fourier transform of the seeded and unseeded pulses is shown in figures 2.7 a) and b). The transforms show the longitudinal modes are completely suppressed in seeded operation a), compared with unseeded operation b). The theoretical longitudinal mode separation in a laser cavity is given by[147]

$$\Delta\nu = \frac{c}{2L} = 200 \text{ MHz}, \tag{2.3}$$

where $\Delta\nu$, is the separation between longitudinal cavity modes, L is the length of the cavity and c is the speed of light in the cavity. Figure 2.7 shows the separation between the longitudinal modes is 195±7 MHz. A slightly lower value than calculated is expected as the gain medium has a higher refractive index than air, increasing the optical path length in the cavity, which would decrease the mode spacings.

Suppressing the longitudinal modes in the laser cavity is important because although for an unseeded pulse, the average intensity maybe high enough to induce translational motion, the mode beats typically have a short duration causing their intensity to be very high compared to the average intensity of the pulse. The unseeded pulse in figure 2.6 shows the individual longitudinal mode beats have rise times of <1

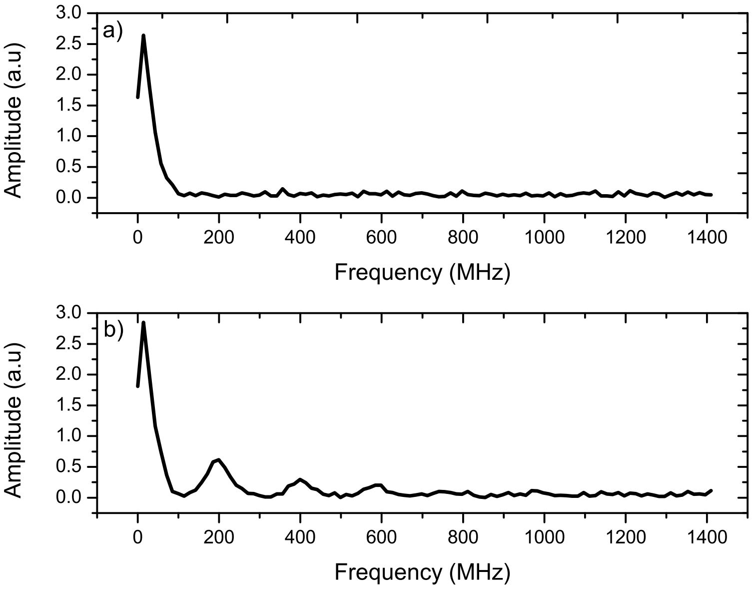

Figure 2.7: a) A Fourier transform of the seeded pulse shows no longitudinal modes. b) Regularly spaced longitudinal modes in the Fourier transform of the seeded beam are clearly visible. The measured mode spacing is 195±7 MHz.

ns, and lengths of $\sim$ 2 ns. This short temporal duration increases the peak intensity for that part of the pulse, which can cause unwanted ionisation of the molecules and prevent adiabatic alignment. This limits the maximum intensity the laser can provide before loss of molecules due to ionisation. This was verified by operating the laser with no probe beam present, at an unseeded intensity just above the ionization threshold, for the molecules, creating an ion signal. When the seeding was switched on, the ion signal was observed to disappear and the intensity of the laser was increased further until it was just below the seeded threshold ionisation intensity. This intensity gives the strongest dipole force without molecular ionisation. In addition to causing unwanted ionization of molecular species, unseeded operation produces ps rise times in the electric field which is on the time scale of the rotational dynamics of many molecules. The random nature of the longitudinal modes, combined with their short rise times, prevent coherent molecular alignment. This is shown in other studies[60, 77, 148] of the dipole force where unseeded lasers are used and only centre-of-mass motion is observed.

2.4 Molecular beam characterization

2.4.1 Cooling molecules with a molecular jet

In order to observe the effect of nonresonant optical fields on molecules, a stable well characterized molecular beam is required. The dynamics of molecular beams are complex and heavily dependent on the apparatus used, such as nozzle shape, diameter, source pressure, temperature and the species used. Molecular beams have been, and are, still the subject of much study[149, 74, 150, 40]. The goal of these studies is often to provide a high density of molecules with a high degree of cooling in the translational and rotational motions.

A supersonic expansion involves molecules at a stagnation pressure P_0, and temperature T_0, in a reservoir which is expanded through an orifice into a vacuum typically $< 10^{-6}$ mbar. Under these conditions the velocity of the gas is increased as it exits the valve orifice. As the gas expands it cools, the resulting velocity distribution is converted from a wide room temperature (295 K) distribution to a cold (≈ 3 K) narrow velocity distribution. This conversion process also increases the mean velocity from the mean room temperature velocity. The flow is termed supersonic because the speed of the molecular beam velocity rapidly reaches a terminal velocity, with a Mach number greater than 1. During the expansion process the gas undergoes adiabatic cooling of all degrees of freedom. Molecular or atomic collisions during the expansion act to bring the beam into thermal equilibrium. This thermalization process is rarely completed with the translational energy being the most efficiently cooled, followed by the rotational and vibrational energy[149]. The cooling process is characterized by the temperature of the motions

$$T_v \gg T_R > T_t, \tag{2.4}$$

where T_v, T_R and T_t are the vibrational, rotational and translational temperatures. The cooling of each type of energy depends on the number of collisions during the cooling process, each type of energy requires a certain number of collisions in order to thermalize. Typically, for diatomic and small polyatomic molecules, the translational and rotational energies require collisions in the $10 - 10^2$ range, whilst vibrational equilibrium requires significantly more collisions of order $10^3 - 10^5$. As such, the rotational temperature is almost always higher than the translational but generally still of the same order. The vibrational temperature however, can remain uncooled and may still have a room temperature distribution.

The flow of molecules is often treated by a non-rigorous separation of the gas flow into three regimes[151]. Close to the source where cooling occurs, where there is high molecular density and a large collision frequency, the expansion is approximated to be isentropic and thermodynamic equilibrium is maintained. Here, the flow is accurately modeled by equilibrium thermodynamics and the properties of ideal gases[74]. The next flow regime is a transition region where molecular densities and collision frequencies decrease, thermodynamic equilibrium is not maintained and cooling can decouple between the molecular degrees of freedom. With further expansion the density decreases and the collisions eventually stop. This final regime is said to be free-molecular flow or "frozen" as the gas is now sufficiently rarefied each molecule no longer interacts with the surrounding molecules. In the initial expansion stage where the flow is isentropic, it can be described using the first law of thermodynamics, which can be used to find the equations which describe the velocity (equation 2.5) and density (equation 2.7) of the molecular beam. Although these equations are formulated in the isentropic region, they can be used to describe the beam properties in the frozen region many nozzle diameters away, where the molecular beam will encounter the IR and probe lasers. The maximum or terminal velocity of the molecular beam is quickly achieved during the expansion, typically within a few nozzle diameters[74]. However, the process of internal cooling takes much longer as it is dependent on molecular collisions, whilst the velocity depends mainly on source temperature and mass of the species. Changing the source conditions P_0, T_0 and nozzle diameter do not greatly alter the velocity of the beam, but can be used to change the cooling properties since P_0 and T_0 are related to the number of molecular collisions during the expansion.

Seeding molecular beams

The obvious choice in wanting to achieve the coldest beams and maximum molecular flux for experimentation is to significantly increase P_0 and so obtain the maximum number of collisions possible. In this situation, molecular clusters can form. The formation of clusters can occur when the temperature of the molecules drops below the boiling point for the species and also when the density is sufficiently high three body collisions may occur[152]. The type of collisions within the gas determine its properties, two body collisions are necessary in order to thermalize the gas whilst three body collisions will allow the formation of clusters. Although cluster formation is important in other aspects of physical chemistry[153], they are undesirable in molecular optics experiments, where a stable well characterized molecular beam is important. Dimers, trimers and large clusters will release their heat of formation into the local gas increasing the translational, rotational or vibrational temperature. A way to solve this problem is to dilute the species of interest into an inert monatomic gas. Because of the dilution (typically below 5 %) the molecular beam has the properties of a monatomic expansion and clusters are less likely to occur. Secondly, a monatomic gas has the least degrees of freedom and so molecular cooling is more efficient. Molecules have more total energy (through rotational, translational and vibrational degrees of freedom), whilst an atom has only the translational velocity[154]. All of the work done by the atomic gas in expanding into a vacuum chamber is taken from the gas's temperature, cooling the atoms and the seeded molecules more efficiently. This was demonstrated by Byer *et al.*[152] in 1981, whom determined the rotational temperature of a pure acetylene (C_2H_2) beam and then repeated the experiment but with a diluted beam consisting 1:3 of helium of acetylene. Using laser spectroscopy to calculate rotational populations, the experiments showed the rotational temperature was 37-45 K and 25-30 K respectively, indicating monatomic gases could further cool molecular species. Experiments in 2003 (Hillenkamp *et al.*[155]) have shown aniline seeded in helium produced a rotational temperature of 200 mK and a translational temperature of 200 mK, indicating that thermal equilibrium between the translational and rotational degrees of freedom had been achieved. Results by Kumarappan *et al.*[156], where a specially designed valve had a stagnation pressure of 60 bar of helium, into which 2-9 mbar of iodobenzene was seeded, produced a rotational temperature of 1.5 K.

The ratio of the molecules in a seeded beam is not the only area of control in producing a cold molecular beam. Experimental parameters (nozzle shape, nozzle width) in pulsed valves can be just as critical as the stagnation pressure, carrier gas and temperature as they determine the boundary conditions of the expansion in the initial high density, thermodynamic equilibrium stage.

Seeding molecules can also be used to accelerate or decelerate molecular species because of the difference in molecular weights, heavier molecules in the beam will decrease the overall beam speed as they are harder to accelerate. Mixtures of molecules and an atomic carrier gas will have a fractional weight based on the mixing ratio of the gases.

Pulsed molecular beam

A pulsed jet has economical advantages over a continuous jet because the minimum vacuum pump speed is reduced and the amount of gas used by the jet decreased. In the experiment, a pulsed solenoid valve operated at 10 Hz was controlled by an Iota One pulse valve controller. A square wave pulse of width 180 μs is used to trigger the valve. The valve is slow to respond, and the length of gas pulse actually detected by the probe laser (see section 2.4.3, figure 2.11) is approximately 500 μs. By sampling molecules at the front, middle, or rear of the pulse, the temperature, density and speed of the beam can be fine tuned.

Table 2.3: Supersonic velocities of ideal noble gases

Gas	molar mass (kg)	velocity (m s^{-1})
Helium	0.004	1750
Neon	0.02	783
Argon	0.04	553
Krypton	0.084	381
Xenon	0.132	305

2.4.2 Molecular velocity

Theoretical Value

The increased molecular beam velocity is due to the molecules being forced through a small orifice into a chamber with low pressure. In the supersonic flow regime the molecular velocity does not depend on the orifice diameter, shape, or background pressure it is being expanded into (in the subsonic regime these properties are important). The terminal velocity shown below in equation 2.5 is rapidly reached and can be determined from the entropy along a streamline[74].

$$v = \sqrt{\frac{2R}{\bar{M}}\left(\frac{\gamma}{1-\gamma}\right)T_0}, \tag{2.5}$$

where R is the molar specific heat capacity, 8.314 K mol^{-1} K^{-1}, $\bar{M}$ is the fractional average molar mass of the species, $\bar{M} = \sum_i C_i W_i$ where C_i is the fraction of the species i and W_i is the molecular weight of the species i. T_0 is the temperature at the source and $\gamma = 1.667$ for a monatomic species. Shown in table 2.3 are the theoretical velocities for the noble gases.

Table 2.3 shows how different carrier gases produce different molecular beam speeds, also, the introduction of the molecular species itself will change the speed of the carrier gas as it modifies the total mass of the gas. In our experiments we utilize two modes of operation of the molecular beam. The first is the coldest where carbon disulphide with a vapour pressure of 7 mbar is expanded into 1.8 bar of argon, the second mode uses 450 mbar in 1.8 bar of argon. These pressures correspond to 4 % and 25 % mixtures with the carrier gas. To achieve 4 % concentration, the argon was bubbled through liquid carbon disulphide held in a reservoir which was in thermal contact with a Peltier cooler. This arrangement provided a temperature inside the reservoir of -20° C. The second mode of operation used no cooling and the room temperature vapour pressure of carbon disulphide was used. Under these less cold operating conditions, the velocity of the molecular beam is decreased due to the higher presence of the heavier CS_2 in the beam. Using the fractional mass of the beam and equation 2.5, this produces theoretical molecular beam speeds of 544 m s^{-1} and 500 m s^{-1} for mixtures of 4 % and 25 % respectively.

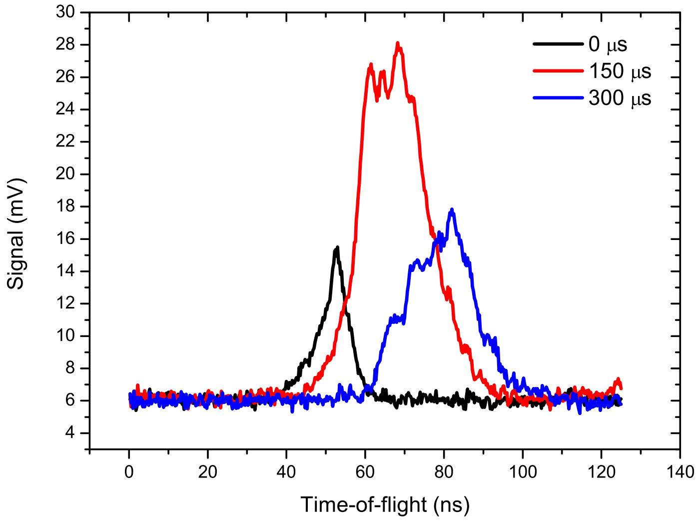

Figure 2.8: Time-of-flight spectra for various time delays between the pulsed valve and probe laser. Earlier delays (0 μs) show molecules at the start of the pulse travel faster and arrive at the MCP earlier than molecules at the centre of the pulse (150 μs). Molecules at later delays (300 μs) arrive later at the MCP as they have a lower velocity.

Experimental measurement

The molecular beam speed operating with 4 % CS_2 was measured by using the dipole force to create a molecular lens (see chapter 1 figure 1.2) and then track temporally and spatially the group of molecules focussed downstream by the lens. The time measured ΔT, between the IR pulse and the probe pulse is the time for the molecules, after interacting with the molecular lens to reach the molecular focus. The molecular focus is where the molecules converge along the molecular beam axis after being deflected by the dipole force. The distance between the molecular lens to the molecular focus is ΔX. At the molecular focus, the signal from the probe beam increases by approximately three times compared to the background signal, indicating that the molecules are being focussed. The background signal is the value recorded by the probe laser when there is no IR beam present. The time delay ΔT between the two laser pulses is found by optimising the delay of the IR beam so that the largest possible signal is obtained for a given IR probe beam separation ΔX. A single IR beam produces a cylindrical molecular lens with a molecular focal spot in the plane perpendicular to the molecular beam. This molecular focus is of the order 10 μm FHWM[36] with a focal length of around 500 μm. Consequently it is easy to miss the molecular focus when moving the probe beam downstream along the molecular beam axis by around 500 μm, and so one must tune the perpendicular direction of the probe beam in addition to the timing to ensure the focus is found and good signal to noise ratio is achieved. Using this method, $\Delta X = 650 \pm 25$ μm and $\Delta T = 1.211 \pm 0.016$ μs yielding a velocity of 537±22 m s^{-1}. This is in good agreement with the theoretical value of 544 m s^{-1}. The velocity of the molecular beam under the room temperature CS_2 condition was not measured because the focussing experiment was not performed using the molecular beam in this mode. However, it can be approximated by scaling the theoretical value compared to the cold beam mode, doing so produces a beam speed of 492 m s^{-1}. The error in measurement is from determining the overlap of the IR and probe beams at the $\Delta X = 0$ point and in finding the peak signal produced when at the molecular focus by adjusting the timing of the lasers. These were small sources of error and can easily be reduced by repeated measurements. The main source of error arises from detecting molecules which will have originated from different points in the lens. We are detecting molecules which have arrived at the same point in the molecular focus, but due to the Gaussian intensity distribution of the IR laser, the molecules may have originated from different positions in the molecular lens. This ambiguity as to where the molecules originated from is quantified by the assumption that the molecules within ±10 μm of the centre of the IR beam defined by a waist of radius $e^{-2} = 20$ μm, are most likely to converge at the same point, because within this region the Gaussian spatial profile closely resembles a parabolic profile and is analogous to a conventional lens. The additional error in ΔX of ±15 μm arises from finding the molecular focus. A similar problem exists with regard determining in time when the molecules actually begin to focus. The laser pulse has a FWHM of 15 ns and so is assigned an error of ±8 ns in determining ΔT.

The measured velocity of 537±22 m s^{-1} represents the average speed of the molecules. The properties of a pulsed supersonic expansion mean molecules at the start of the molecular pulse move faster than those at the tail of the pulse. This is shown in figure 2.8 where the time delay between the probe laser and the firing of the molecular pulse is changed and the resulting TOF profile is shown. The delay times are referenced to the start of the molecular pulse and for the three profiles shown, the delays 0 μs, 150 μs and 300 μs correspond to molecules probed at the front (black), centre (red) and at the rear (blue) of the molecular pulse. This allows additional control over the molecular velocity and the translational temperature which in turn is coupled to the rotational temperature. The range over which the velocity can be altered by changing the probe delay is 85 m s^{-1}. This is limited by the signal quality as the density of the molecules decreases at the start and end of the molecular pulse. The measured velocity of 537 m s^{-1} was recorded at a delay of 300 μs. This is near the end of the molecular pulse as shown in figure 2.11, and so the tuning range from this velocity is -67.5 m s^{-1} and + 17.5 m s^{-1}.

2.4.3 Translational temperature

A translational temperature can be assigned to a velocity profile recorded at the time-of-flight mass spectrometer. The TOF shape is well approximated by a Gaussian distribution[157]. A fit to the TOF profile can be used to calculate the spread of velocities in the molecular beam. Shown in figure 2.9 is the TOF velocity profile for the 4 % beam at the delay of 300 μs. A Gaussian fit to this profile shows a spread of velocities with a FWHM of 45 m s^{-1}. This spread is converted into a temperature by re-arranging the 1D Maxwell-Boltzmann[154] velocity distribution to yield

$$T_t = \frac{m\Delta v_{FWHM}}{8k_b \ln 2}, \tag{2.6}$$

where Δv_{FWHM} is the full width half maximum of the velocity distribution, k_b is Boltzmann's constant, and m is the mass of the CS_2 molecule, which is 76 amu. The translational temperature of these molecules is T_t=3.4±0.2 K. Although not shown in figure 2.9 is the translational temperature of the hot molecular beam at this delay, with T_t =9.4±0.2 K. The rotational temperature is typically close to T_t, and serves as a rough starting rotational temperature for simulations of molecular alignment. Shown in figure 2.10 are the TOF spectra for both 4 % and 25 % modes of the jet near the end of the molecular pulse at a delay of ∼450 μs. The translational temperatures are 6.9 K and 0.9 K. This shows the variable degree of cooling obtained by using different parts of the molecular beam. What is clear from figure 2.10 is that molecules which have been seeded with a higher vapour pressure have a higher translational temperature and density, increasing the ion signal.

The molecular beam densities for both molecular beam modes is shown in figure 2.11. This was obtained by integrating the TOF signals shown in figure 2.10 for several probe-molecular beam delay times. Marked by an arrow on figure 2.11 is the delay of 300 μs, where the experiments were carried out. This setting provided the best compromise between a cold beam and molecular ion signal. The relationship between the molecular beam density and translational temperature for the 4 % CS_2 beam is shown in figure 2.12. From the graph it can be seen that where the signal is the highest, so too is the translational temperature. Figure 2.12 shows the coldest temperatures are found at the start and end of the pulse, and the shape approximately follows the molecular density of figure 2.11.

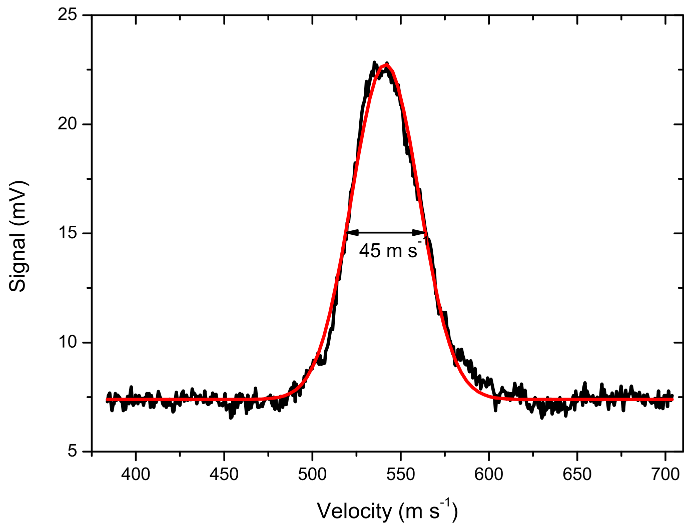

Figure 2.9: A velocity profile of 4 % CS_2 seeded in 1.8 bar of argon. This trace was averaged over 1200 laser shots. The width of 45 m s^{-1}, corresponds to a translational temperature of T_t=3.4±0.2 K.

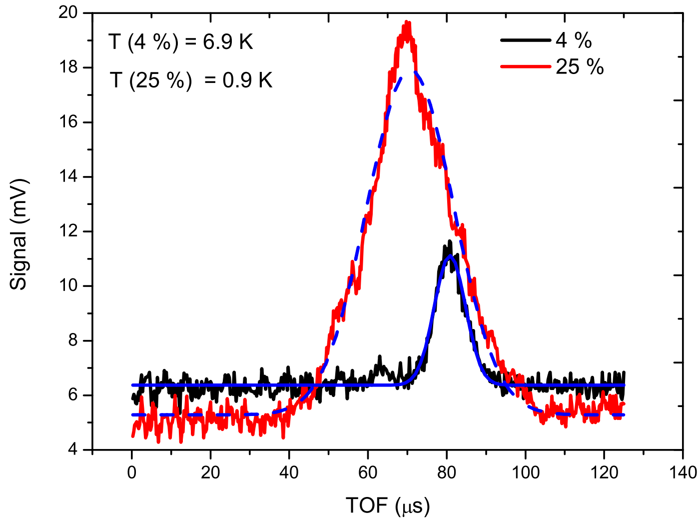

Figure 2.10: A delay of 450 μs between the start of the molecular pulse and the probe laser samples molecules at the rear of the pulse. The 4 % CS_2 (black) beam has a temperature of T_t=0.9 K. The 25 % molecular beam (red) at a similar delay has a stronger signal but a higher temperature of T_t=6.9 K.

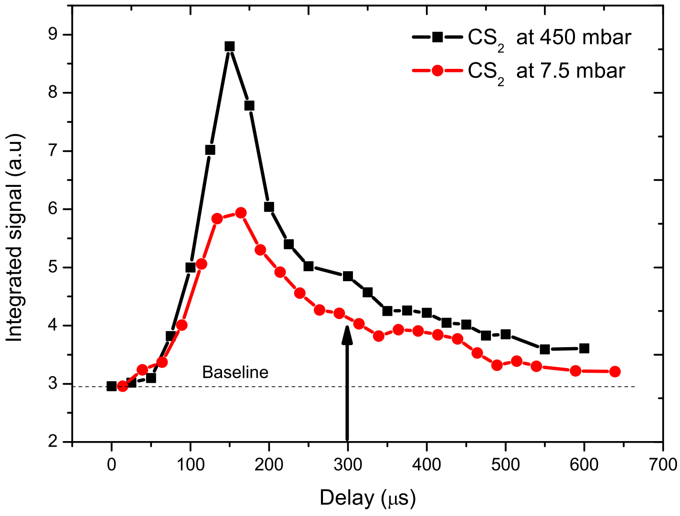

Figure 2.11: The integrated TOF signal is plotted as the time delay between the probe and the molecular pulse is varied. The hot molecular beam (black) has a higher signal compared to the cold beam (red) due to the greater number of CS$_2$ molecules in the beam. The dashed line indicates the signal with no probe beam present and the black arrow is the time delay where the experiments were carried out.

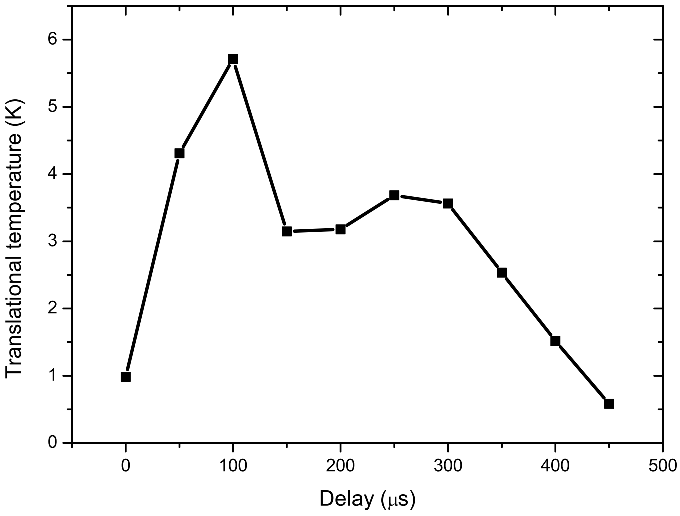

Figure 2.12: The translational temperature from several TOF profiles in the cold molecular beam has been plotted as the time delay to the pulsed valve is increased. The lowest temperatures are at the front and tail of the pulse.

2.4.4 Molecular beam density

The density of the molecular beam can be estimated using the theoretical equation[74] in which the on axis downstream density of the molecular beam is given by

$$I(y) = \frac{k_p N}{\pi v_b y^2}, \tag{2.7}$$

where N is the nozzle flow rate and k_p is the peaking factor, which is 1.98 for a monatomic gas, y is the downstream distance from the nozzle and v_b is the molecular beam speed. The nozzle flow rate is given by

$$N = \left(\frac{\gamma}{\gamma + a}\right)^{1/2} \left(\frac{2}{\gamma + 1}\right) n_0 \sqrt{\frac{2k_b T_0}{m}}\ \frac{\pi d^2}{4}, \tag{2.8}$$

with $\gamma = 1.67$ and k_b is Boltzmann's constant, m the mass of CS_2 and d is the nozzle diameter. The density calculated from equation 2.7 is 2.0×10^{13} cm^{-3}, but since there is only 4 % and 25 % of CS_2 in the beam this yields a theoretical density of 8.0×10^{11} cm^{-3} and 5.0×10^{12} cm^{-3} respectively.

2.4.5 Vibrational temperature

Vibrational spectra

Figure 2.13 shows the apparatus used to record the vibrational spectra. The ion signal and photodiode voltage were recorded using three Stanford Research Systems modules. A SR240 fast preamp was connected to a SR250 gated integrator and boxcar averager, the averaged data was then sent to a PC using the SR245 computer interface module. At the PC, the data acquisition software program SR272 was used to record the integrated signal as a function of probe beam wavelength. The boxcar integration window was set to a time delay in the total time-of-flight spectrum to record the arrival of CS_2^+ ions only. Negligible ion signal was produced for the dissociated ion species (CS^+, S^+) as discussed in section 2.2.1. When recording the vibrational spectra care was taken to use as little laser intensity as possible in an attempt to avoid saturation which would artificially populate the molecular levels. The probe laser intensity during the wavelength scan was monitored by integrating the laser pulse signal from a photodiode. Over the 10 nm scan range the signal was found to be constant. The integrated ion signal for the 25 % CS_2 molecular beam in the three-photon spectrum as function of probe laser wavelength is shown in figure 2.14. This scan over 10 nm shows two electronic and three vibrational excitations. The electronic transitions are from the ground state $\tilde{X}^1\sum_g^+$ to $\left[\frac{1}{2}\right] np\sigma_u(^1\prod_u)$, which is a p shell orbital, and is a singlet state with spin $S = 0$, corresponding to a laser wavelength of 478.630 nm. At a lower energy and longer wavelength there is also a $\left[\frac{3}{2}\right] np\sigma_u(^3\prod_u)$

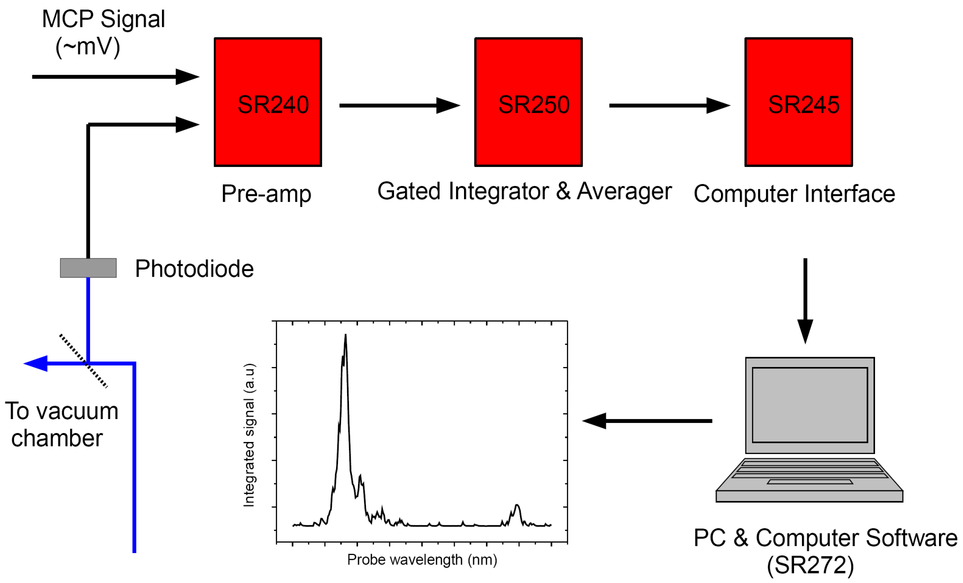

Figure 2.13: A block diagram of the apparatus and electronics used to record the vibrational spectra of CS_2 around 480 nm. A small portion of the probe beam was focussed onto a photodiode and the signal was integrated along with the MCP signal in order to monitor the pulse energy of the probe beam as the wavelength was varied.

transition with $S = 1$, but this transition is spin forbidden because of the selection rule $\Delta S = 0$. However, the ${}^3\prod_u$ state is observed because it is made up of the individual spin states ${}^3\prod_1$, ${}^3\prod_2$ and ${}^3\prod_3$, and it is through the mixing[158] of the triplet ${}^3\prod_1$ state with the spin S=0 ${}^1\prod_1$ state via Renner-Teller coupling[159], which allows the triplet state to gain intensity, although with much less strength than the ${}^1\prod_1$ transition.

By measuring the position of the band centre of the ${}^1\prod_u \leftarrow \tilde{X}^1\sum_g^+$ transition in figure 2.14 and the separation to the smaller vibrational peaks, they can be identified by comparison with other studies by Baker *et al.*[140] and Morgan *et al.*[141] on the (3+1) REMPI spectrum of CS_2. Table 2.4 shows the measured separation in wavenumbers (cm^{-1}) of the vibrational transitions compared to [140, 141]. The peaks are identified and labelled as the transitions; 2^1_1, 2^2_2, 2^3_3, where the integer 2 corresponds to the vibrational mode being excited, which for a triatomic molecule is the bending mode (1 is symmetric stretch and 3 is the asymmetric stretch)[160]. The subscript and superscript are the vibrational quantum numbers from which the molecule is being excited from and to respectively. For the transitions in figure 2.14 the molecule is already in a vibrational mode, and after absorption of three photons, remains in the same vibrational mode but is electronically excited into the $4p$ shell. The bending mode has the lowest excitation energy[161, 162] of ν_2=396.7 cm^{-1}, compared

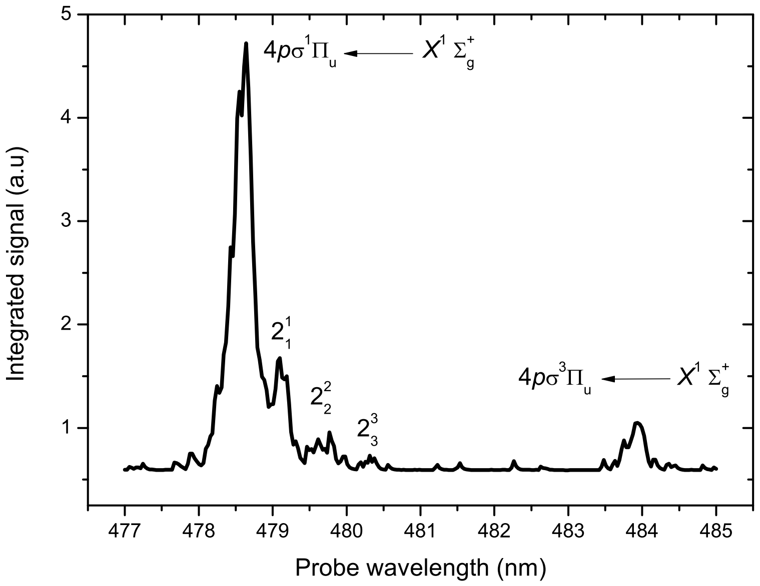

Figure 2.14: An average of three scans where the wavelength of the probe laser is changed whilst the ion yield is recorded. The resonances correspond to the singlet and triplet spin states of the $\left[\frac{1}{2}\right] np\sigma_u({}^{1,3}\prod_u) \leftarrow \tilde{X}^1\sum_g^+$ transition. Also shown are the vibrational excitations associated with the singlet excitation.

Table 2.4: Separation of vibrational transitions from band centre

Transition	Measured (cm^{-1})	Baker (cm^{-1})	Morgan(cm^{-1})
2_1^1	65±2	64	60
2_2^2	132±5	141	133
2_3^3	218±2	218	217

to the symmetric stretch ν_1=658 cm^{-1} and asymmetric stretch with ν_3= 1535 cm^{-1}. Consequently we do not detect the other vibrational modes at room temperature.

Calibration of the dye laser

By comparing the band centre as recorded by Morgan[141] and Baker[140] with the band centre measured in figure 2.14 for the $\left[\frac{1}{2}\right] 4p\sigma_u({}^1\prod_u) \leftarrow \tilde{X}^1\sum_g^+$ transition the laser wavelength can be calibrated. The measured value from figure 2.14 is 62 678±2 cm^{-1} or 478.63±0.02 nm. The averaged value from Morgan and Baker is 62 744±6 cm^{-1} or 477.90±0.05 nm giving a one photon offset of +96±6cm^{-1} or a wavelength offset for our dye laser of -0.73 nm.

Vibrational temperature

Figure 2.15 shows the normalized ion signal in the 477 nm to 480 nm region. This data was taken for both 25 % (red line) and 4 % (black line) mixtures of CS_2 in argon.

Due to the lower density of CS_2 of the 4 % beam, the laser intensity was four times the laser intensity used for the 25 % molecular beam. The width of the band head is almost identical in both cases suggesting the population of the rotational levels was not altered significantly by quadrupling the intensity or increased power broadening has compensated for a reduced rotational temperature in the 4 % beam. Figure 2.15 as expected, shows that the higher density 25 % beam has vibrational transitions which are stronger than for the 4 % molecular beam. This suggests that some vibrational cooling is taking place in the 4 % beam. We now proceed to determine a vibrational temperature for both modes of operation of the molecular beam.

For a constant intensity and wavelength, the strength of any molecular transition depends on the transition probabilities from each of the electronic, vibrational and rotational motions and the initial population of the levels. To approximate the vibrational temperature, four assumptions are made[140]:

1. The vibrational levels are populated according to a Boltzmann distribution.
2. The rotational line strengths are not dependent on the electronic or vibrational transition probabilities and are the same for the band head and for the vibrational transitions.
3. The electronic transition moment is the same for the ground state transition and for the vibrational transitions.
4. The potential surfaces of the $4p\sigma_u({}^1\prod_u)$ and $\tilde{X}^1\sum_g^+$ state are assumed to be the same in the region of the energy minima. This means the Frank-Condon factors of the $\Delta\nu = 0$ transitions will be ≈ 1.

The first assumption is made because of the properties of molecular jets[74], where by the gas starts with a room temperature Boltzmann distribution and because of expansion into the vacuum chamber the temperature is lowered but is approximated to remain in a Boltzmann distribution. The second assumption is the Born-Oppenheimer approximation which states the rotational motion is uncoupled from the vibronic motion allowing their wave-functions to be separated. The third assumption is made because the vibrational transitions are all being excited to the same electronic state and the electronic transition probability is approximately the same. The final assumption assumes because the vibrational quantum number does not change $\Delta\nu = 0$, the potential surfaces which depend on the separation of the nuclei, about the equilibrium position, will be similar. This allows us to approximate the Frank-Condon factors to ≈ 1. These assumptions mean the strength of each vibrational transition will only be proportional to the number of molecules in each vibrational state and this is given by a Boltzmann fraction. The Boltzmann fraction can be measured from the height of each peak in figure 2.15.

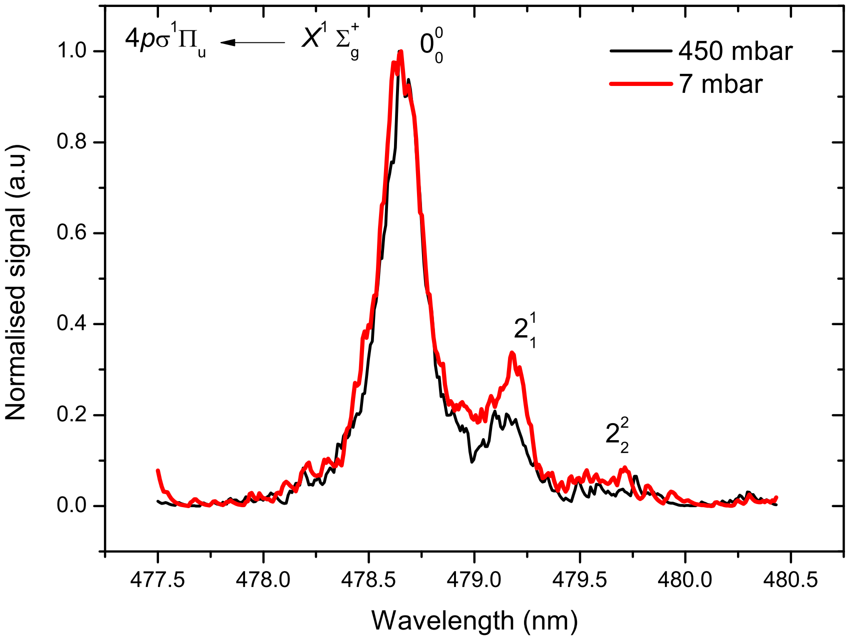

Figure 2.15: For each operational mode of the molecular beam, three scans were averaged to obtain the ion signal as a function of laser wavelength over the 477 nm to 480 nm range.

From Herzberg[161], the vibrational population in any vibrational state is dependent on temperature and on the vibrational energy.

$$\frac{N_v}{N} = \frac{\exp^{[-G(\nu_2)hc/k_bT_v]}}{1+\exp^{[-G(1)hc/k_bT_v]}+\exp^{[-G(2)hc/k_bT_v]}+\ldots} \tag{2.9}$$

Equation 2.9 describes the fraction of molecules that will be in each vibrational quantum state, ν_2 is the vibrational quantum number of the bending mode, T_v is vibrational temperature and k_b is Boltzmann's constant. The total vibrational energy of the populated mode is the energy of the harmonic oscillator with $G(\nu_2) = (\nu_2+1)f_2(\nu_2+\frac{1}{2})$, where f_2 is the vibrational constant of the bending mode. The bracketed term (ν_2+1), accounts for the degeneracy of the bending mode[161]. It is also possible to remove the factor of $\frac{1}{2}$ in the expression to simplify the maths, this simply shifts the energy zero as all the vibrational levels are shifted by the same amount. The denominator in equation 2.9 is a normalization constant summing the probabilities from all states. Figure 2.15 is normalized so the temperature is calculated using

$$H = (\nu_2+1)\exp\left(-G(\nu_2)hc/k_bT_v\right), \tag{2.10}$$

where H is the height of a vibrational feature in figure 2.15. The heights of the

Table 2.5: Height of vibrational transitions and corresponding temperature

Transition	Height (25 %)	Height (4 %)
2^1_1	0.31	0.19
2^2_2	0.06	0.04
Temperature, T_v	298±7 K	250±14 K

transitions for the 25 % and 4 % molecular beams in figure 2.15 have been recorded, and an average temperature is calculated from the 2^1_1 and 2^2_2 transitions. The results are shown in table 2.5.

The results suggest with a 25 % CS_2 molecular beam there is no vibrational cooling and the vibrational population remains at room temperature. The temperature in the lab was measured to be 294±2 K. At 4 %, the molecular beam has a modestly lower vibrational temperature of 250±14 K, which is also the temperature of the CS_2 reservoir at 253 K. These results suggest there is actually no vibrational cooling in the jet. This analysis has also been carried out on CS_2 by Baker *et al.*[140] and in different spectral regions by Liu *et al.* [163] and Fischer *et al.*[164]. Each recorded a room temperature vibrational distribution for their molecular jets, Baker used CS_2 in helium whilst Liu and Fischer used CS_2 seeded in argon. These results are in contrast to those obtained by McDiarmid *et al.*[165] whom performed one photon spectroscopy of the $4p\sigma_u(^1\prod_u)$ band in a room temperature gas cell and with a jet cooled sample. The temperatures recorded were 420 K and 371 K respectively. Different results were also obtained by Morgan *et al.*[141] who measured a jet cooled temperature of 413±41 K (from inspection of fig. 1 in [141]). It is worth noting that these studies are concerned principally with identifying and locating the wavelength where the transitions in CS_2 occur. It seems no particular precaution was taken to avoid saturation of the transitions which would artificially populate the levels.

2.4.6 Rotational temperature

The use of molecular jets to determine molecular structure has a significant advantage because of the large amount of rotational relaxation which simplifies the molecular spectra[166, 167, 168, 169, 170]. Detection of molecules by REMPI can allow access to states which are not allowed in the one-photon spectrum because of the electric-dipole selection rules[171]. Consequently, REMPI spectra is often more complicated compared to a one photon spectrum. The multiphoton spectrum for three photons has been treated theoretically and experimentally in the past and has been used to determine rotational temperatures for acetaldehyde[172] and ammonia[173].

The rotational temperature can be difficult to determine because of spectroscopic and laser properties such as overlapping bands, saturation of levels, power broadening and laser linewidth. A model of the rotational contours must be produced which can be used to fit the data to give a rotational temperature. CS_2 has a small rotational constant, $B = 0.109$ cm^{-1} which is of the order of the probe laser line width (0.1 cm^{-1} as measured by Ray Fulton[174]). Carbon disulphide is a centro-symmetric molecule with zero nuclear spin on the sulphur atoms[175] meaning the wave function is unchanged upon exchanging the sulphur nuclei[176]. This means the wave function can only be even or odd in the ground state. CS_2 in the electronic ground state has Σ_g^+ structure so only even rotational[175, 177] levels, or only + levels in spectroscopic notation (odd levels have - sign) are observed[163, 178]. Even with the odd lines missing, no rotational contours are observed in the spectra in figure 2.15. They are however, clearly observed by Cramb *et al.*[178] and Liu *et al.*[163] in the spectral region ≈350 nm through the use of fluorescence spectroscopy. The detection method used in this thesis is ion detection which is very sensitive as single ions can be detected. This however, means that the molecule has to be irradiated by a field of sufficient intensity to absorb four photons sequentially to ionise the molecule. It is possible to construct a model based on the three photon line strengths and selection rules to model the REMPI spectrum as shown below.

Three photon absorption model

To determine the rotational spectra of a rovibronic transition, Fermi's golden rule states the probability per unit time of absorbing three photons is[179]

$$\Gamma_{21} = \left(\frac{16\pi^4}{c^3\hbar}\right) I_a I_b I_c \rho_2(E) |R_{21}|^2, \tag{2.11}$$

where $\rho(E)$, is the density of states and contains upper-state relaxation information, c is the speed of light, I_a, I_b and I_c are the intensities of each photon with polarisation a, b and c, $|R_{21}|^2$ is the squared matrix element of the transition. The first approximation is to assume the density of states is constant for all of the rotational transitions and $|I_a| = |I_b| = |I_c|$ which is the case where the molecule absorbs three identical photons. As all of the terms to the left of $|R_{21}|^2$ in equation 2.11 are now constants we need only consider the transition matrix elements to determine the rotational contours. At a constant laser intensity, the strength S, of a rotational transition is the product of the transition probability, a population distribution describing the initial population in the original state, and the degeneracy of that state. The line strength is given by

$$\begin{aligned} S &= |R_{21}|^2 g_J \exp\left(\frac{-E_r}{k_b T_r}\right), \\ &\text{or} \\ S &= |R_{21}|^2 \frac{2J+1}{Q_r} \exp\left(\frac{-BJ(J+1)}{k_b\, T_r}\right), \end{aligned} \tag{2.12}$$

where $g_J = (2J + 1)$ is the degeneracy of the rotational states. The rotational energy is $E_r = BJ(J + 1)$. Q_r is a normalizing factor for the rotational populations, and is equal to the sum of the Boltzmann fraction $\exp\left(\frac{-E_r}{k_b T_r}\right)$ over all rotational states including degeneracies. This is shown later in equation 2.22. Considering first the transition matrix element of the rovibronic transition R_{21}, the absorption of three photons from a ground state $\mid 1 \rangle$ to an upper state $\mid 2 \rangle$ is[180]

$$R_{21} = \sum_j \sum_i \frac{\langle\, 2\, |\mathbf{e_a} \cdot \mathbf{r_a}|\, j \,\rangle\langle\, j\, |\mathbf{e_b} \cdot \mathbf{r_b}|\, i \,\rangle\langle\, i\, |\mathbf{e_c} \cdot \mathbf{r_c}|\, 1 \,\rangle}{(\Delta E_{1j} - 2h\nu + i\Gamma_j)(\Delta E_{1i} - h\nu + i\Gamma_i)}, \tag{2.13}$$

where R_{21} contains the rovibronic line strength factors, and $\mathbf{e_{a,b,c}}$ are the electric field polarisation vectors along the axes a, b, and c in the molecular axis coordinate system. The energy separations between the intermediate states $\mid i \,\rangle$ and $\mid j \,\rangle$ are ΔE_{1j} and ΔE_{1i}, with half-widths Γ_i and Γ_j. Equation 2.13 is extended from the one-photon transition matrix element given by perturbation theory to three photons. A more general case to n photons[181] is also possible. It is also assumed there are no single or two photon resonances in between the ground and excited state. In this notation the transition probability is in Cartesian coordinates and in the molecular frame. Equation 2.13 can be separated into two third rank Cartesian tensors, one containing the information about the polarisation of the photons and another detailing the transition probability between the states

$$R_{21} = \mathbf{T}(\mathbf{e_a}, \mathbf{e_b}, \mathbf{e_c}) \cdot \mathbf{T}(\mathbf{B})_{21}. \tag{2.14}$$

$\mathbf{T}(\mathbf{e_a}, \mathbf{e_b}, \mathbf{e_c})$ is the tensor relating to the polarisation of the photons, and $\mathbf{T}(\mathbf{B})_{21}$ is the vibronic molecular transition tensor, where $\mathbf{B}$ is used because it is analogous to the first molecular transition hyperpolarisability which has the symbol β. Equation 2.14 is also in the molecular frame and may be expressed in an irreducible basis of spherical tensors[182, 183] to allow the rotation of the molecular axis system into the laboratory axis system where the polarisation tensor is best expressed. The symmetry of $\mathbf{T}(\mathbf{B})$ is dictated by the energies of the photons and determines the symmetry of the electronic levels that are accessible. The reduction into spherical tensors for three photons of different energies is shown in equation 2.15.

$$\mathbf{T}(\mathbf{B}) \equiv \mathbf{T}^0(\mathbf{B}) + 3\mathbf{T}^1(\mathbf{B}) + 2\mathbf{T}^2(\mathbf{B}) + \mathbf{T}^3(\mathbf{B}) \tag{2.15}$$

The general case of equation 2.15 is simplified when three identical photons are used. The molecular transition tensor is now split into two components, one first rank tensor and one third rank tensor[180, 184] as shown below

$$\mathbf{T}(\mathbf{B}) \equiv \mathbf{T}^1(\mathbf{B}) + \mathbf{T}^{\mathbf{3}}(\mathbf{B}), \tag{2.16}$$

where $\mathbf{T}^k_q(\mathbf{B})$ are the components of the spherical tensor $\mathbf{T}^k$ of rank k with $2k{+}1$ components. In terms of rovibronic transitions, k refers to the number of photons and hence its symmetry type. The label q, is the component of the spherical tensor and runs from $-k$ to k, it refers to the change in electronic angular momentum and hence dictates what electronic states are accessible. Thus the selection rules for three photons can obtained through the symmetry properties of the tensors. Since three photons are used producing $k = 1, 3$ tensors, from a s state it is possible to access states with electronic angular momentum via $\Delta l = 1, 3$ corresponding to a p and f state orbital. With one photon from a s state it is only possible to access a p state. These electronic selection rules are obtained from sequential addition of the electric dipole selection rules $\Delta l = \pm 1$. The rotational selection rules remain the same for the one-photon component $\Delta J = 0, \pm 1$ giving P, Q and R branches, whilst for the three-photon transitions[185] we have $\Delta J = 0, \pm 1, \pm 2 \pm 3$ giving seven branches of N, O, P, Q, R, S and T. The vibronic transition considered is a s to p state transition ${}^1\prod_u \leftarrow \tilde{X}^1\sum_g^+$, so the only parts of the rovibronic tensor, $\mathbf{T}(\mathbf{B})$ which need to be considered are the $q = +1$ components, $\mathbf{T}^1_1$ and $\mathbf{T}^3_1$. At this point through the Born-Oppenheimer approximation the molecular transition tensor can be split into the vibronic and rotational contributions, yielding $\mathbf{T}(\mathbf{B}) = \mathbf{E}^k_q R_{k,q}$. Where $\mathbf{E}^k_q$ is the vibronic component of the molecular transition tensor and $R_{k,q}$, which is the rotational line strength for k photons with a change in electronic angular momentum of q. The full expression for $|R_{21}|^2$ which is required by equation 2.12 to calculate the transition strength S, is

$$|R_{21}|^2 = |\mathbf{T}(\mathbf{e_a}, \mathbf{e_b}, \mathbf{e_c})|^2 \cdot |\mathbf{E}^1_{+1}(\mathbf{B})|^2 R_{1,+1} + |\mathbf{T}(\mathbf{e_a}, \mathbf{e_b}, \mathbf{e_c})|^2 \cdot |\mathbf{E}^3_{+1}(\mathbf{B})|^2 R_{3,+1}. \quad (2.17)$$

The components $|\mathbf{T}^k_p(\mathbf{e}_a, \mathbf{e}_b, \mathbf{e}_c)|^2$ depend on the beam geometry and on the polarisation of each of the three photons, and not the properties of the molecule. These values are rotated into the lab frame so laser polarisation is easily definable and can be found in Table 2 of [179] or in [173] or through a more general approach[186]. The square of the vibronic molecular transition component $|\mathbf{E}^k_q|^2$, is transition and molecule dependent and for a s to p transition, the matrix elements are identical[143]. Applying these simplifications, where the mean squared polarisation tensor values given by Nieman[173] have been used, the only remaining factors required are the one and three-photon rotational line strength factors $R_{1,+1}, R_{3,+1}$ which are also given by Nieman. Equation 2.17 becomes

$$|R_{21}|^2 = \frac{21}{175} R_{1,+1} + \frac{10}{175} R_{3,+1}. \quad (2.18)$$

Selection rules

Equation 2.18 shows the absorption spectra can be split into one and three-photon contributions. What is required are the selection rules and positions of each transition. The rotational selectional rules are derived from the symmetry constraints placed on the molecular transition tensor as discussed above, in a more succinct form they are

Orbital momentum rules

one photon : $\Delta J = 0, \pm 1$

three photon : $\Delta J = 0, \pm 1, \pm 2, \pm 3$

(2.19)

Electric dipole symmetry rules

$+ \leftrightarrow -$ and $g \leftrightarrow u$.

Shown in figure 2.16 are the allowed transitions from the ${}^1\sum_g^+$ state to the ${}^1\prod_u$ state. The excited ${}^1\prod_u$ state is lambda doubled and has both + and - levels[161]. Due to the nuclear spin on the sulphur atoms in the CS_2 ground state, only the + states are allowed. The upper state ${}^1\prod_u$ has both even and odd J since each J contains both + and $-$ levels, and so transitions of all seven branches are allowed. The total angular momentum quantum number of the ${}^1\prod_u$ level is the end over end rotational contribution plus the electronic angular momentum, $J{+}\Omega$. This means the first level in the excited state has non zero total angular momentum because $\Omega = 1$ (dashed line on figure 2.16). Rotational transitions from $J = 0$ and $J = 2$ will have limited branches because they cannot access the rotational states via the selection rules $\Delta J = -3, -2, -1, 0$ and $\Delta J = -3, -2$ respectively. Consequently they only have R, S and T and P, Q, R, S and T branches respectively.

The change of angular momentum of $\Delta\Omega = +1$ from $\Omega = 0$ is represented by the quantum number Ω which is the projection of angular momentum along the molecule axis. This electronic angular momentum is coupled to the angular momentum of molecular rotation through Hund's cases a) to e). At low rotational quantum numbers the electronic angular momentum will remain strongly coupled to the molecular axis and one would expect Hund's case a). In this situation the additional electronic angular momentum vector is along the molecular symmetry axis which is perpendicular to the rotational angular momentum vector. The addition of these two vectors turns the linear rotor into a symmetric top rotor. The upper state energy is modified accordingly to $F(J') = B'[J'(J'+1) - \Omega'^2]$. The frequency positions of the rotational transitions from the ground state J to upper J' state are

$$F(J, J') = B' \left[J'(J'+1) - \Omega'^2\right] - BJ(J+1), \tag{2.20}$$

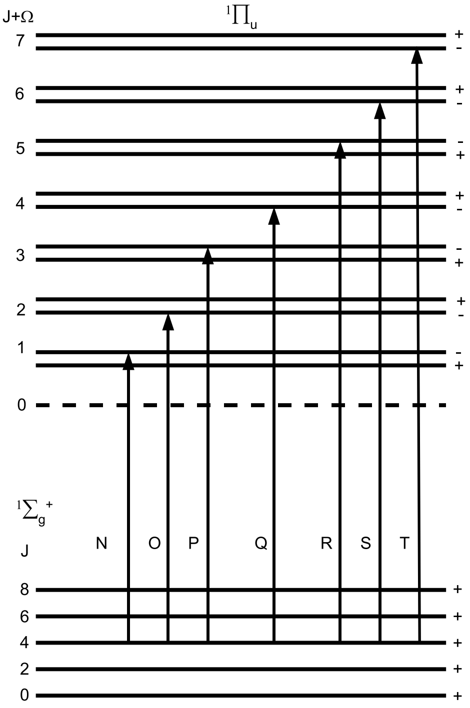

Figure 2.16: An energy diagram for three-photon rotational selection rules. The upper $^1\prod_u$ has both + and - levels which allows all seven branches N, O, P, Q, R, S and T. The $^1\prod_u$ state does not have a $J = 0$ level because $\Omega = 1$.

where Ω is the electronic angular momentum quantum number taking values 0 and 1 for the ground and upper states respectively. B' and J' refer to the upper state rotational constant and angular momentum quantum number. By inserting the angular momentum selection rules listed in equation 2.19 into equation 2.20 the frequency position of each of the allowed rotational transitions can be calculated.

Rotational line strength

The one photon line strengths in equation 2.18 are well known as the Honl-London factors[161] and the three photon line strengths have been calculated analytically by Nieman [173] or can be expressed by the Wigner 3j symbols[179]. Other factors which are required for the calculation of the rotational spectrum are the populations of the rotational levels in the electronic ground state. This is assumed to be given by a Boltzmann distribution but is not known, in certain circumstances, this assumption is not always valid[187]. The fraction of molecules in a certain rotational level J is given by

$$\frac{N_J}{N} = \frac{(2J+1)}{Q_r} \exp\left(\frac{-BJ(J+1)}{k_b T_R}\right) \tag{2.21}$$

where B, k_b and Q_r are the rotational constant, Boltzmann constant and the rotational partition function, which is simply a normalization constant summing populations in all states as shown in equation 2.22. The $2J + 1$ term accounts for the degeneracy of the rotational levels as each J state has $2J + 1$ M states. M is the projection of angular momentum onto a designated space fixed axis and can take values from $-J$ to J, the sum of which is $2J + 1$. The rotational partition function is

$$Q_r = \sum_J (2J+1) \exp \frac{-BJ(J+1)}{k_b T_R}. \tag{2.22}$$

Equation 2.18 is now substituted in equation 2.23 to give the strength of a rotational transition,

$$S = \left[\frac{21}{175} R_{1,+1} + \frac{10}{175} R_{3,+1}\right] \frac{2J+1}{Q_r} \exp\left(\frac{-BJ(J+1)}{k_b\, T_R}\right). \tag{2.23}$$

Equation 2.23 shows explicitly how the strength of the rotational lines will depend on T_R for the approximations considered.

Width of the rotational lines

The laser linewidth in the one-photon spectrum is 0.3 cm^{-1}. There is additional broadening from the instrument linewidth, this depends on the averaging used on the SR250 and laser scan speed. Slower, more detailed scans were carried out over the $^1\prod_u \leftarrow \tilde{X}^1\sum_g^+$ transition and did not yield any resolvable rotational lines or features. Based on the scan speed of the laser and the averaging at the Boxcar, the instrument linewidth is approximately 1.3 cm^{-1}. The separation between the rotational lines in the upper state is $2B'$, and since the instrument line width is large in comparison, B' is assumed to be equal to B in equation 2.20. The ground state rotational constant is B=0.109100 cm^{-1}, for comparison the rotational constant of the CS_2^+ ion is B'=0.109126 cm^{-1}. The effects of Doppler broadening of the rotational lines is also neglected, as at the rotational temperatures expected <100 K, the width is 513 MHz calculated from equation 2.24. This value is much less than the linewidth of the laser at 8.7 GHz or 0.3 cm^{-1}.

$$f_D = \frac{2}{\lambda}\sqrt{\frac{2k_b T_R \ln 2}{m}} \tag{2.24}$$

The effects of power broadening are difficult to measure but through examination of figure 2.15 the widths of the $^1\prod_u \leftarrow \tilde{X}^1\sum_g^+ 0_0^0$ transition for the 4 % and 25 % seeded molecular beam are very similar despite using four times the intensity to record the 4 % spectrum. This suggests either the power broadening between the data sets is the roughly the same, or the expected decrease in the width of the 0_0^0 transition due to a lower rotational temperature, has been compensated for by an increase in the power broadening. Unfortunately, it is difficult to disentangle these effects.

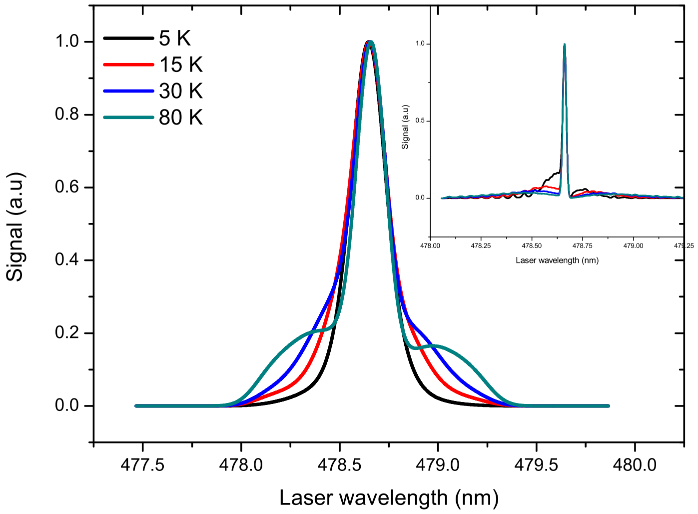

Figure 2.17: The simulated rotational contour is convolved with the instrument linewidth of 2.5 cm^{-1} at 80 K and 10 K. The Q-branch depends heavily on the linewidth but not T$_R$, only the wings of the feature are affected by T$_R$. The inset graph shows the simulated spectra without the instrument linewidth for comparison.

Results

All of the factors that contribute to the shape of the rotational spectrum; the positions of the rotational lines in equation 2.20; the selection rules in equation 2.19; the rotational line strengths $R_{3,+1}$ and $R_{1,+1}$; a Boltzmann population of the rotational levels; and the Gaussian laser and instrument line widths were incorporated into a program written in Matlab. The program is shown in the Appendix, it produces the rotational contour in the three photon spectrum (477 to 480 nm). To calculate the experimentally measured spectrum the calculated contour using only the Gaussian linewidth of 0.3 cm^{-1} is convolved with the instrument linewidth of 1.3 cm^{-1}. The results are shown in figures 2.18 and 2.19.

The averaging of the SR250 Boxcar integrators and the speed of the scan from the dye laser which was used to record the spectra in figures 2.18 and 2.19 had a resolution of approximately 1.3 cm^{-1}. This provided the correct balance between laser scan time and noise levels. Simulating features with the instrumental linewidth of 1.3 cm^{-1} produced an inaccurate fit much too narrow for figures 2.18 and 2.19. In an attempt to correct for this, it is noted the Q branch of the $^1\prod_u \leftarrow \tilde{X}^1\sum_g^+$ transition is very strong and not heavily dependent on rotational temperature. The temperature behavior is predominantly in the wings of the features as shown in figure 2.17, where simulations of the spectrum show the upper part of Q-branch has effectively the same width for a range of temperatures from 10 K to 80 K. The inset in figure 2.17 shows the simulated spectra with no instrument linewidth for comparison. This is confirmed

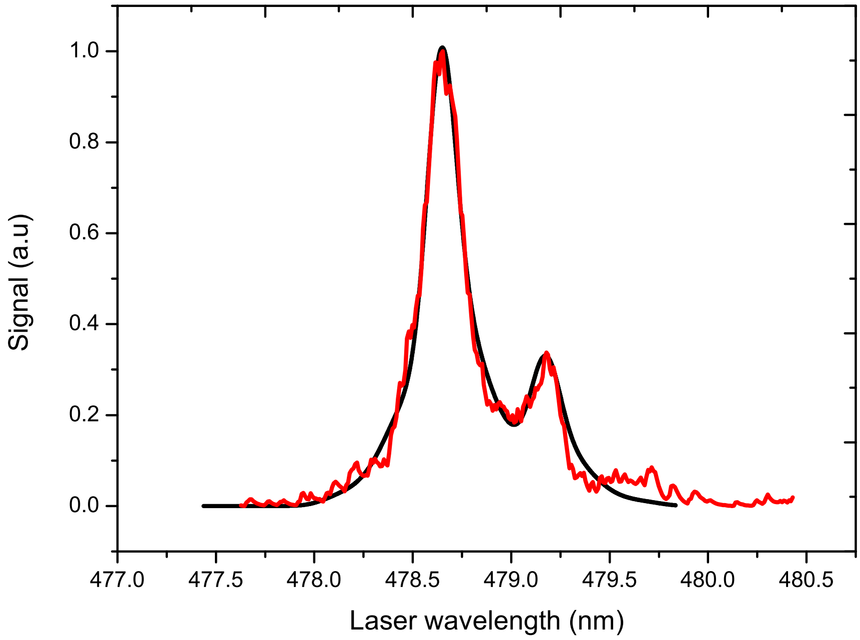

Figure 2.18: The simulated rotational contour is fitted to the experimental data with 25 % CS_2 in the beam yielding a temperature of 20 K.

through the experimental data in figure 2.15, where the central part of the 0^0_0 feature with the 4 % beam has the same width as the hotter 25 % beam, suggesting its width is not strongly temperature dependent. This weak coupling of the rotational temperature and instrument linewidth is used to increase the instrument linewidth to fit the data around the centre of the 0^0_0 transition, and the rotational temperature is then varied to fit the data in the wings of the spectrum, and in the overlap between the vibrational peak 2^1_1. Using this approach the fitted instrument linewidth is 2.5 cm^{-1}. Figures 2.18 and 2.19 show the best fit of the rotational contour model with the new instrument linewidth of 2.5 cm^{-1} with rotational temperatures of 20 K and 10 K for the 25 % and 4 % CS_2 seeded molecular beams.

Discussion

For the assumptions made, the temperatures of 10 K and 20 K represent very approximate values. Figure 2.20 shows a diagram of the (3+1) REMPI process, the ion signal will be affected by stimulated emission, spontaneous emission and quenching, which can be caused by collisions with other molecules (although at the distance from the molecular jet where the laser interacts with the molecular beam, molecular collisions are not expected). These processes were not taken into account in the model of the three photon spectra primarily because information such as upper state life time and

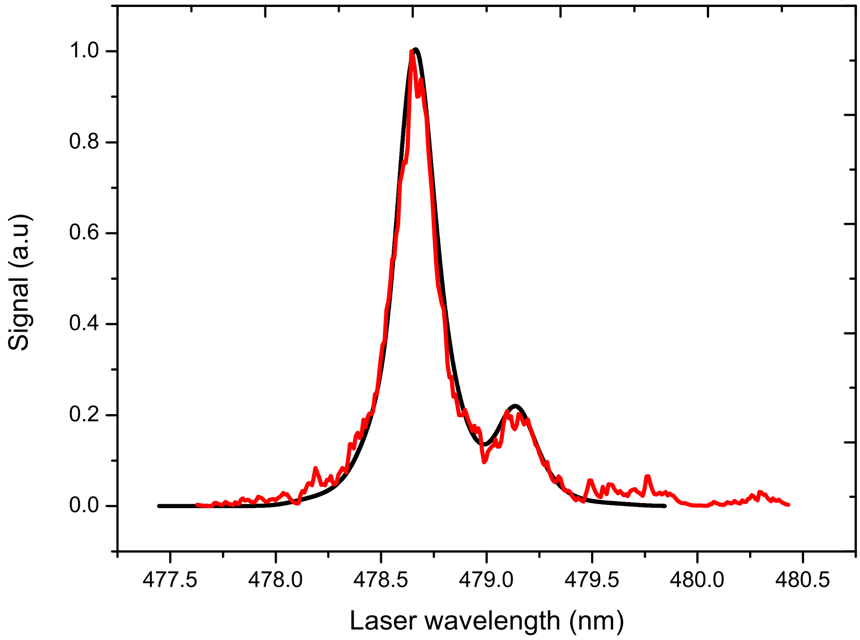

Figure 2.19: The simulated rotational contour is fitted to the experimental data using 4 % CS_2, producing a fit of 10 K.

stimulated emission constants are not available for the $^1\prod_u$ state in CS_2. In hindsight, a way to test influence of the competing processes is to plot the ion signal as a function of intensity. In the low intensity regime, the signal should be proportional to the fourth power of the intensity as four photons are required for ionisation. With increasing intensity, all of the ions in the intermediate state will be ionised, and the ion signal should be proportional to the laser intensity since only one photon is required for ionisation from the intermediate state. How much the actual measured signal deviates from this quadratic-linear behaviour would reveal the influence of stimulated and spontaneous emission. With increasing intensity the signal should become constant, indicating saturation has occurred. By determining the threshold intensity for saturation, care can be taken to operate the laser intensity well below the saturation threshold.

Another reason why the predicted temperature maybe inaccurate is because of the presence of the $^3\prod_u \leftarrow \tilde{X}^1\sum_g^+ 0_0^1$ transition, which is a symmetric stretch state and is located 23 cm^{-1} (+0.175 nm) from the $^1\prod_u\, 0_0^0$ line. It has not been included in the model as its strength is weak[143]. But it could affect the simulated spectra, decreasing the confidence in the estimates of the rotational temperature. The strength of the $^1\prod_u\, 0_0^0$ feature compared to $^3\prod_u\, 0_0^0$ is 11 % in figure 2.14, it arises due to Renner-Teller coupling. The maximum height of a $^3\prod_u\, 1_1^0 \leftarrow \sum_g^+ 0_0^0$ vibronic transition would be

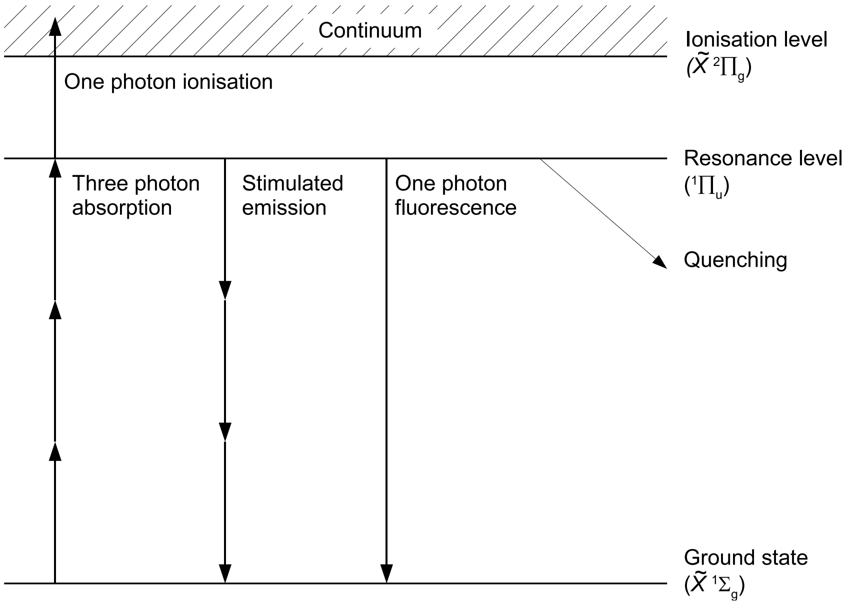

Figure 2.20: An energy diagram of the processes which can occur in absorption spectroscopy. The ion signal is created by ionisation from the intermediate level, but is also competing with stimulated emission and fluorescence. Quenching refers to the decay through collisions with other molecules.

11 %, however the Frank-Condon factors would decrease the strength of the vibronic transition further. Further assumptions such as assuming a Boltzmann distribution of the levels, assuming there are constant broadening effects, assuming Hund's case a) for the addition of angular momenta, and fitting the instrument linewidth can add up systematic errors. Cossart-Magos *et al.*[143] used 20 % CS_2 in argon and carried out unresolved rotational spectroscopy on the $(^1\prod_u) \leftarrow \tilde{X}^1 \sum_g^+ 0_0^0$ band, by modeling their band contours of just the $^1\prod_u 0_0^0$ state, a fit of 50 K was found. The bandwidth used in the simulations was 12 cm^{-1}, by inputting the same parameters into the 3-photon model described in this chapter, good agreement is found between the calculated widths. In a similar experiment, Liu *et al.* [163] has modeled resolved rotational lines and obtained rotational temperatures of around 10 K using 5 % CS_2 in argon.

2.5 Conclusion

The experimental apparatus has been described including the vacuum systems, probe and IR laser. A probe laser creates CS_2^+ ions inside a TOFMS where changes in the molecular beam velocity, due to the nonresonant IR field can be detected. These changes in TOF are converted into a velocity change which is directly related to the dipole force.

Table 2.6: Molecular beam parameters

Parameter	25 % Mixture	4 % Mixture
Velocity	498 m s^{-1}	537±22 m s^{-1}
Density	5×10^{12} cm^{-3}	8×10^{11} cm^{-3}
T_t	9.4±0.2 K	3.4±0.2 K
T_v	298±7 K	250±14 K
T_R	20 K	10 K

The molecular beam is operated in two modes with 25 % and 4 % of CS_2 seeded in argon. The molecular beam characteristics are shown in table 2.6. The velocity of the 4 % beam is measured to be 537±22 m s^{-1} and agrees well with the theoretical value of 544 m s^{-1}. The 25 % beam velocity was not measured but is estimated to have a velocity of 492 m s^{-1}. The density of the molecular beam is estimated using a theoretical equation to be 8×10^{11} cm^{-3} and 5×10^{12} cm^{-3} for the 4 % and 25 % beams respectively. The translational temperature of both molecular beams is measured by fitting a Gaussian velocity distribution to the TOF signal, yielding 3.4±0.2 K and 9.4±0.2 K. The vibrational temperature was approximated by using a Boltzmann distribution to describe the population of the vibrational levels. Little if no cooling was found, the temperatures are 250±14 K and 298±7 K respectively. These values are equal to the temperatures used in the CS_2 reservoir to create the 4 % and 25 % mixture in the molecular beam. The most difficult property to accurately calculate is the rotational temperature. Using a three-photon model of absorption for CS_2, the ${}^1\prod_u \leftarrow \tilde{X}^1 \sum_g^+ 0_0^0$ and ${}^1\prod_u \leftarrow \tilde{X}^1 \sum_g^+ 2_1^1$ bands were simulated. The fitted contours produced temperatures of 10 K and 20 K. No errors are given due to the large uncertainty from the number of approximations.

Chapter 3

A review of molecular alignment

3.1 Introduction

Molecular alignment theory is well understood[55, 99, 83] and is now used in a variety of applications such as high harmonic generation[82] and in photodissociation studies[116]. The optical dipole force has also been studied extensively[61, 188], but to date there have not yet been any experimental demonstrations of the role of molecular alignment and the dipole force created by strong nonresonant fields. The aim of this chapter is to couple the theory of molecular alignment with dipole force centre-of-mass calculations so a model can be created and applied to an experiment that explores this phenomena.

3.2 Theory

A nonresonant electric field of linearly or circularly polarised light, acting on the vibronic ground state of a linear molecule, will spatially confine the molecular axis to the electric field polarisation vector. In both cases the alignment between the molecular axis and a space fixed Z direction is quantified by the expectation value $\langle \cos^2 \theta_{l,c} \rangle$, where $\theta_{l,c}$ is the angle between the molecular axis and the Z axis. We define the Z axis to be along the polarisation vector for linearly polarised light and parallel to the propagation vector for circularly polarised light. This is illustrated in figure 3.1 a), where θ_l forms the angle between the molecular bond axis and the space fixed Z axis, which is parallel to the polarisation vector (green). Figure 3.1 b), shows θ_c is the angle between the molecular axis and the propagation direction (blue arrow). The effective Hamiltonian for the nonresonant AC Stark shift $V(t)$, for each polarisation induced by an electric field $\epsilon(t)$, is (see Introduction)

$$\begin{aligned} V_L(t) &= -\frac{1}{4}\left[\Delta\alpha \cos^2\theta_l + \alpha_\perp\right]\epsilon^2(t), \\ V_C(t) &= -\frac{1}{8}\left[\alpha_{||} + \alpha_\perp - \Delta\alpha\cos^2\theta_c\right]\epsilon^2(t), \end{aligned} \tag{3.1}$$

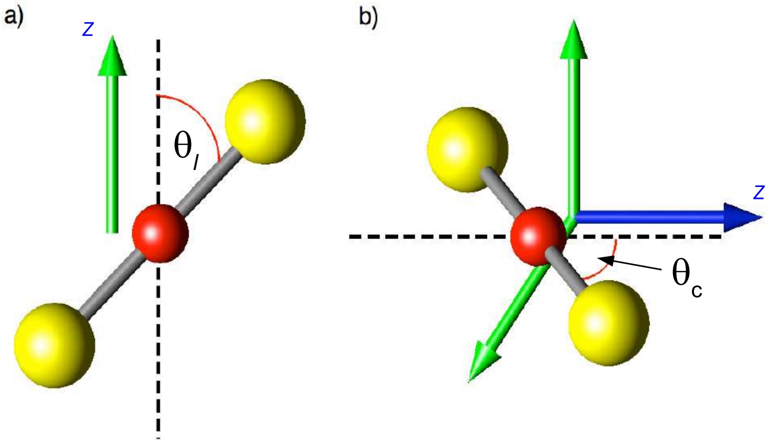

Figure 3.1: The alignment of CS_2 with linearly and circularly polarised light is shown. Linearly polarised light a), has its polarisation vector parallel to the electric field (green) in the space fixed direction Z. The alignment is quantified by θ_l. b) The Z direction for circularly polarised light is chosen to be parallel to the propagation direction (blue), but perpendicular to the plane of the radiation (green). The angle θ_c is the angle between the propagation direction (blue) and the molecular axis.

where the L & C subscripts denoted on $V(t)$, labels the Stark shift for linearly or circularly polarised light. The polarisability components $\alpha_{||}$ and $\alpha_{\perp}$, are along the bond axis and perpendicular to the axis respectively. Their values are $\alpha_{||}$=16.8×10^{-40} C m^2 V^{-1} and $\alpha_{\perp}$=6.2×10^{-40} C m^2 V^{-1}[148, 77]. The polarisability anisotropy is $\Delta\alpha = \alpha_{||} - \alpha_{\perp}$. We also define the effective polarisability as

$$\begin{aligned} \alpha_L &= \Delta\alpha \cos^2\theta_l + \alpha_{\perp}, \\ \alpha_C &= \frac{1}{2}\left[\alpha_{||} + \alpha_{\perp} - \Delta\alpha\cos^2\theta_c\right]. \end{aligned} \tag{3.2}$$

Circularly polarised light acts to confine the molecular axis to the electric field plane. The electric field "looks" the same in each direction to the molecule, producing an average of $\alpha_{||}$ and $\alpha_{\perp}$. Using linearly polarised light produces a higher effective polarisability because there is only one direction (Z) for alignment which the $\alpha_{||}$ component dominates. The maximum effective polarisabilities correspond to complete alignment between the molecule and field with $\theta_l = 0$ and $\theta_c = 90$ for linearly and circularly polarised light respectively. Putting $\cos^2\theta_l = 1$ and $\cos^2\theta_c = 0$, the maximum effective polarisability is

$$\begin{aligned} \alpha_L &= \alpha_{||}, \\ \alpha_C &= \frac{\alpha_{||} + \alpha_{\perp}}{2}. \end{aligned} \tag{3.3}$$

To calculate the alignment properties of a molecular ensemble at a rotational temperature, T_R, the expectation value, $\langle\cos^2\theta_{l,c}\rangle_{J,M}$, of a single quantum state is calculated and then averaged using a Boltzmann distribution which is used to describe the thermal population of the rotational levels. To proceed, we first calculate the expectation value, $\langle\cos^2\theta_{l,c}\rangle_{J,M}$, for each polarisation by solving the Schrödinger equation

$$i\hbar\frac{\partial}{\partial t}|\Psi_{J,M}\rangle(t) = H(t)|\Psi_{J,M}\rangle(t), \tag{3.4}$$

where $|\Psi_{J,M}\rangle(t)$ is the total rotational wave function of the molecule, and J and M are the quantum numbers for the eigenvalue of the squared angular momentum operator $\mathbf{J}^2$, and M is its projection onto the Z axis. These numbers refer to the initial rotational state being perturbed. We also note J is relabeled as $\tilde{J}$ in $|\Psi_{J,M}\rangle(t)$ to distinguish between a perturbed rotational state $\tilde{J}$, composed of the field-free states J. The Hamiltonian $H(t)$, contains the field-free Hamiltonian, H_0, of the rigid rotor, and the potential, $V_{L,C}(t)$, of the AC Stark shift

$$H(t) = H_0 + V_{L,C}(t). \tag{3.5}$$

The field-free Hamiltonian of the rigid rotor consists of the squared angular momentum operator $\mathbf{J}^2$ such that $H_0 = B\mathbf{J}^2$, where B is the rotational constant of CS_2, which is 0.109 cm^{-1}[176]. The properties of the rigid rotor equation are well known. Its solutions are the spherical harmonics[182, 183] and the eigenvalues are $J(J+1)$. The energy of rotation of the molecule is $E_J = BJ(J+1)$. Centrifugal distortion effects are not taken into account in the calculation. Molecular vibrations are also ignored. Two methods are used to determine $|\Psi_{\tilde{J},M}\rangle(t)$. In the first method, the time-dependent Schrödinger equation (TDSE) is solved by reducing it to a series of coupled first order differential equations. These equations are solved using standard numerical methods. Secondly, to confirm the results from the first method, the time-independent Schrödinger equation (TISE) is written in matrix form and subsequent diagonalization of the Hamiltonian matrix allows $\langle\cos^2\theta_{l,c}\rangle_{J,M}$ to be calculated.

3.2.1 Solving the time-dependent Schrödinger equation

More detailed descriptions are given elsewhere[125] and only a brief review is presented here. Common to both methods is the representation of the complete rotational wave function $|\Psi_{\tilde{J},M}\rangle(t)$, as a superposition of field-free rotor states $|\Psi_{\tilde{J},M}\rangle(t) = \sum_{J,M} C_{J,M}(t)|J,M\rangle$, where $C_{J,M}(t)$ are the time dependent coefficients in the expansion and $|J,M\rangle$ are the spherical harmonics. Substituting $|\Psi_{\tilde{J},M}\rangle(t)$ into equation 3.4 yields

$$i\hbar\frac{d}{dt}C_{J,M}(t) = \sum_{J',M'} C_{J',M'}(t)\langle J,M|H(t)|J',M'\rangle, \tag{3.6}$$

the matrix elements of the operator $H(t)$ are the same for linearly and circularly polarised light. For linearly polarised light the expression becomes[189, 109, 190, 191]

$$
\begin{aligned}
i\frac{d}{dn}C_{J,M}(n) = C_{J,M}(n)\left[J(J+1)-\omega_{\perp}(n)\right] \\
-\Delta\omega(n)C_{J-2,M}(n)\langle J,M|\cos^2\theta_l|J-2,M\rangle \\
-\Delta\omega(n)C_{J,M}(n)\langle J,M|\cos^2\theta_l|J,M\rangle \\
-\Delta\omega(n)C_{J+2,M}(n)\langle J,M|\cos^2\theta_l|J+2,M\rangle,
\end{aligned}
\tag{3.7}
$$

and for circularly polarised light we find

$$
\begin{aligned}
i\frac{d}{dn}C_{J,M}(n) = C_{J,M}(n)\left[J(J+1)-\omega^c_{\perp}(n)-\omega^c_{||}(n)\right] \\
+\Delta\omega^c(n)C_{J-2,M}(n)\langle J,M|\cos^2\theta_c|J-2,M\rangle \\
+\Delta\omega^c(n)C_{J,M}(n)\langle J,M|\cos^2\theta_c|J,M\rangle \\
+\Delta\omega^c(n)C_{J+2,M}(n)\langle J,M|\cos^2\theta_c|J+2,M\rangle.
\end{aligned}
\tag{3.8}
$$

Equations 3.7 and 3.8 depend on the dimensionless parameters $\Delta\omega(n) = \frac{\Delta\alpha\epsilon_0^2 f(n)}{4B}$ and $\omega_{\perp}(n) = \frac{\alpha_{\perp}\epsilon_0^2 f(n)}{4B}$. For circularly polarised light the parameters are $\Delta\omega^c(n) = \frac{\Delta\alpha\epsilon_0^2 f(n)}{8B}$ and $\omega^c_{||,\perp}(n) = \frac{\alpha_{||,\perp}\epsilon_0^2 f(n)}{8B}$. The dimensionless unit n, is defined with $n = \frac{B}{\hbar}t$ ($\frac{B}{\hbar}$=49 ps). It is used in a Gaussian envelope $f(n)$, to modulate an electric field of $\epsilon_0 = 2.746\times10^9$ V m^{-1}, corresponding to 10^{12} W cm^{-2}. Equations 3.7 and 3.8 show that a particular quantum state, $|\Psi_{\tilde{J},M}\rangle(t)$, is constructed by mixing field-free states connected via the selection rules $\Delta J = 0, \pm2$, the magnetic quantum number is conserved with $\Delta M = 0$. The selection rules mean only rotational states of even or odd J will be mixed. The mixing of the states is proportional to the matrix elements of the connected states. This interaction can be regarded as a type of Raman transition, where the nonresonant laser field interacts with the virtual states to populate the rotational levels in the vibronic ground state.

The coefficients of each quantum state were calculated in Matlab (program in Appendix) using a peak intensity of 10^{12} W cm^{-2} and a temporal pulse with shape

$$
f(n) = \exp\left(\frac{-(n-x)^2}{\sigma^2}\right). \tag{3.9}
$$

The $\frac{1}{\mathrm{e}^2}$ dimensionless width is $\sigma = 7.75$, this corresponds to a width of 0.620 ns FWHM. Adiabatic behaviour was checked by repeating the calculation for a particular state under the same conditions except with a pulse width of $\sigma = 35.4$ corresponding to 2.9 ns FWHM. Complete agreement was found between the different pulse widths.

As the rotational quantum number $\tilde{J}$ increases, the applied field is increasingly less perturbing to the natural motion of the molecule because the field-free Hamiltonian becomes large compared to the energy shift induced by the AC Stark effect. As the lowest $\tilde{J}$ state is confirmed to be adiabatic, the higher $\tilde{J}$ states will certainly be adiabatic as the rotational period decreases with increasing angular momentum. Using the time-dependent method, for each $|\Psi_{\tilde{J},M}\rangle(t)$, the initial condition of the set of equations is $C_{J,M}(0) = 1$. Typically, 27 equations were sufficient to truncate the series of equations to satisfy the condition in equation 3.10, so that at the maximum field value there is zero population in the lowest and highest J state.

$$|C_{Jmin,M}(n = x)|^2 = |C_{Jmax,M}(n = x)|^2 = 0 \tag{3.10}$$

3.2.2 The stationary Schrödinger equation

Evaluating equations 3.7 and 3.8 can take a long time to integrate on the nanosecond time scale and in order to calculate higher rotational temperatures many rotational states need to be propagated. Adiabatic time scales do not require the time-dependent Schrödinger equation as the dynamics do not depend on the temporal properties of the field. An alternative method is to make the long pulse approximation[192] which means the stationary Schrödinger equation is used

$$H|\Psi_{\tilde{J},M}\rangle = \lambda_{\tilde{J},M}|\Psi_{\tilde{J},M}\rangle, \tag{3.11}$$

where $\lambda_{\tilde{J},M}$ is the eigenvalue of the perturbed system. Following a similar procedure as above, the following equation for linearly polarised light is realized

$$\begin{aligned}\frac{\lambda_{\tilde{J},M}}{B}C_{J,M} = {} & C_{J,M}\left[J(J+1) - \Delta\omega\langle J, M|\cos^2\theta_l|J, M\rangle - \omega_\perp\right] \\ & - C_{J-2,M}\Delta\omega\langle J, M|\cos^2\theta_l|J-2, M\rangle \\ & - C_{J,M}\Delta\omega\langle J, M|\cos^2\theta_l|J, M\rangle \\ & - C_{J+2,M}\Delta\omega\langle J, M|\cos^2\theta_l|J+2, M\rangle.\end{aligned} \tag{3.12}$$

A similar expression for circularly polarised light is obtained. Equation 3.12 represents a single linear equation of a $|J, M\rangle$ state being perturbed. All of the $\tilde{J}$ state equations can be represented in a matrix as a set of linear equations obeying $\mathbf{H}|\Psi\rangle = \boldsymbol{\lambda}|\Psi\rangle$, where $\mathbf{H}$ is the Hamiltonian matrix and $\boldsymbol{\lambda}$ is a matrix of corresponding eigenvalues for each equation. The solution matrix is labeled $|\Psi\rangle$, and contains column vectors, each column vector is the solution to each row in $\mathbf{H}$. Explicitly,

$$
\begin{pmatrix}
A(0) & B(0,M) & 0 & 0 & 0 & 0 \\
C(2,M) & A(2) & B(2,M) & 0 & 0 & 0 \\
0 & C(4,M) & A(4) & B(4,M) & 0 & 0 \\
0 & 0 & C(6,M) & A(6) & \ddots & 0 \\
0 & 0 & 0 & \ddots & \ddots & B(J,M) \\
0 & 0 & 0 & 0 & C(J,M) & A(J)
\end{pmatrix}
\begin{pmatrix}
C_{0,M} & C_{0,M} & C_{0,M} & C_{0,M} & C_{0,M} & C_{0,M} \\
C_{2,M} & C_{2,M} & C_{2,M} & C_{2,M} & C_{2,M} & C_{2,M} \\
C_{4,M} & C_{4,M} & C_{4,M} & C_{4,M} & C_{4,M} & C_{4,M} \\
C_{6,M} & C_{6,M} & C_{6,M} & C_{6,M} & C_{6,M} & C_{6,M} \\
\vdots & \vdots & \vdots & \vdots & \vdots & \vdots \\
C_{J,M} & C_{J,M} & C_{J,M} & C_{J,M} & C_{J,M} & C_{J,M}
\end{pmatrix}
$$

$$
= \begin{pmatrix}
\lambda_{\tilde{0},M} & 0 & 0 & 0 & 0 & 0 \\
0 & \lambda_{\tilde{2},M} & 0 & 0 & 0 & 0 \\
0 & 0 & \lambda_{\tilde{4},M} & 0 & 0 & 0 \\
0 & 0 & 0 & \lambda_{\tilde{6},M} & 0 & 0 \\
0 & 0 & 0 & 0 & \ddots & 0 \\
0 & 0 & 0 & 0 & 0 & \lambda_{\tilde{J},M}
\end{pmatrix}
\begin{pmatrix}
C_{0,M} & C_{0,M} & C_{0,M} & C_{0,M} & C_{0,M} & C_{0,M} \\
C_{2,M} & C_{2,M} & C_{2,M} & C_{2,M} & C_{2,M} & C_{2,M} \\
C_{4,M} & C_{4,M} & C_{4,M} & C_{4,M} & C_{4,M} & C_{4,M} \\
C_{6,M} & C_{6,M} & C_{6,M} & C_{6,M} & C_{6,M} & C_{6,M} \\
\vdots & \vdots & \vdots & \vdots & \vdots & \vdots \\
C_{J,M} & C_{J,M} & C_{J,M} & C_{J,M} & C_{J,M} & C_{J,M},
\end{pmatrix}
\tag{3.13}
$$

with the equations for linearly polarised light

$$\begin{aligned} A(J) &= J(J+1) - \omega_\perp - \Delta\omega\langle J, M|\cos^2\theta_l|J, M\rangle, \\ B(J,M) &= -\Delta\omega\langle J, M|\cos^2\theta_l|J+2, M\rangle, \\ C(J,M) &= -\Delta\omega\langle J, M|\cos^2\theta_l|J-2, M\rangle. \end{aligned} \tag{3.14}$$

For circularly polarised light one uses

$$\begin{aligned} A(J) &= J(J+1) - \omega^c_\perp - \omega^c_{||} + \Delta\omega^c\langle J, M|\cos^2\theta_c|J, M\rangle, \\ B(J,M) &= +\Delta\omega^c\langle J, M|\cos^2\theta_c|J+2, M\rangle, \\ C(J,M) &= +\Delta\omega^c\langle J, M|\cos^2\theta_c|J-2, M\rangle. \end{aligned} \tag{3.15}$$

One can see that when the field is zero the system returns to its field-free state and the Hamiltonian matrix contains only $J(J+1)$ in the diagonal, which are the eigenvalues of the field-free system. The matrix $\mathbf{H}$ is diagonalized in Matlab to produce all of the coefficients for each set of equations. The magnetic quantum number M is conserved throughout the equations so the matrix must be diagonalized repeatedly for each value of M. The eigenvectors are returned in matrix form which is particularly suited to calculating all of the $\langle\cos^2\theta_{l,c}\rangle_{\tilde{J},M}$ simultaneously for all of the $\tilde{J}$ states of particular a $|M|$. The matrix must be large enough to truncate the expansion of $|\Psi_{\tilde{J},M}\rangle(t)$, but the calculation is sufficiently fast a large matrix can be solved with minimal additional computing time. Since the TDSE method can be considered to be static with each electric field value, all of the calculations are adiabatic which is useful to check results from the TDSE.

3.2.3 Matrix elements of $\langle\cos^2\theta\rangle$

The matrix elements of $\langle\cos^2\theta\rangle$ are the same for linearly and circularly polarised light and are evaluated from the recurrence relations of the associated Legendre polynomials $P^M_J(\cos^\theta)$[193, 35],

$$xP^M_J(x) = \frac{J-M+1}{2J+1}P^M_{J+1}(x) + \frac{J+M}{2J+1}P^M_{J-1}(x), \tag{3.16}$$

with $x = \cos\theta$. Applying this identity twice yields the selection rules and matrix elements of $\cos^2\theta$. The orthogonality between the spherical harmonics results in the projection along the space fixed axis to be conserved, yielding the first selection rule $\Delta M = 0$. The angular momentum selection rules are $J' = J, J \pm 2$ with the matrix elements

$$\begin{aligned}
\langle J,M|\cos^2\theta|J,M\rangle &= \frac{1}{3}+\frac{2}{3}\left[\frac{J(J+1)-3M^2}{(2J+3)(2J-1)}\right]\\
\langle J,M|\cos^2\theta|J+2,M\rangle &= \frac{1}{2J+3}\left[\frac{(J+M+2)(J+M+1)(J-M+2)(J-M+1)}{(2J+5)(2J+1)}\right]^{1/2}\\
\langle J,M|\cos^2\theta|J-2,M\rangle &= \frac{1}{2J-1}\left[\frac{(J+M)(J+M-1)(J-M)(J-M-1)}{(2J+1)(2J-3)}\right]^{1/2}.
\end{aligned} \tag{3.17}$$

In the above expressions the magnetic quantum number is always positive as the spherical harmonics depend only on $|M|$.

3.3 $\langle\cos^2\theta_{l,c}\rangle_{J,M}$ and the effects of rotational temperature

The expectation value $\langle\cos^2\theta_{l,c}\rangle_{\tilde{J},M}(n)$, which quantifies the alignment for both polarisations is evaluated from the coefficients $C_{J,M}(n)$[101, 190],

$$\begin{aligned}
\langle\cos^2\theta_{l,c}\rangle_{\tilde{J},M}(n) &= (n)\langle\Psi_{J,M}|\cos^2\theta_{l,c}|\Psi_{J,M}\rangle(n)\\
&= \sum_{J,M,J',M'} C_{J,M}(n)C^*_{J',M}(n)\langle J,M|\cos^2\theta_{l,c}|J',M'\rangle.
\end{aligned} \tag{3.18}$$

At any time n, the explicit form of $\langle\cos^2\theta_{l,c}\rangle_{\tilde{J},M}$ is

$$\begin{aligned}
\langle\cos^2\theta_{l,c}\rangle_{J,M} &= C_0C_0^*\langle J,M|\cos^2\theta_{l,c}|J,M\rangle + C_0C_2^*\langle J,M|\cos^2\theta_{l,c}|J+2,M\rangle\\
&+ C_2C_0^*\langle J,M|\cos^2\theta_{l,c}|J-2,M\rangle + C_2C_2^*\langle J,M|\cos^2\theta_{l,c}|J,M\rangle\\
&+ C_2C_4^*\langle J,M|\cos^2\theta_{l,c}|J+2,M\rangle + ...
\end{aligned} \tag{3.19}$$

At this point we note the basis set of the total wave function, which are the spherical harmonics, depend only on $|M|$ and are insensitive to the sign of the magnetic quantum number so the wave functions are identical for $\pm M$. Consequently, only positive states of M need to be calculated since $\langle\cos^2\theta_{l,c}\rangle_{\tilde{J},+M} = \langle\cos^2\theta_{l,c}\rangle_{\tilde{J},-M}$.

3.3.1 Adiabatic alignment

The rotational dynamics of the molecule in comparison to other molecular time scales can be represented by the dimensionless parameter $\hbar/B$, which is 49 ps for CS_2. The Spectra Physics laser used in the experiments, which creates the optical lens has a near-Gaussian pulse duration of 15 ns FWHM. This is much slower than the rotational dynamics of the molecule putting the alignment dynamics firmly into the

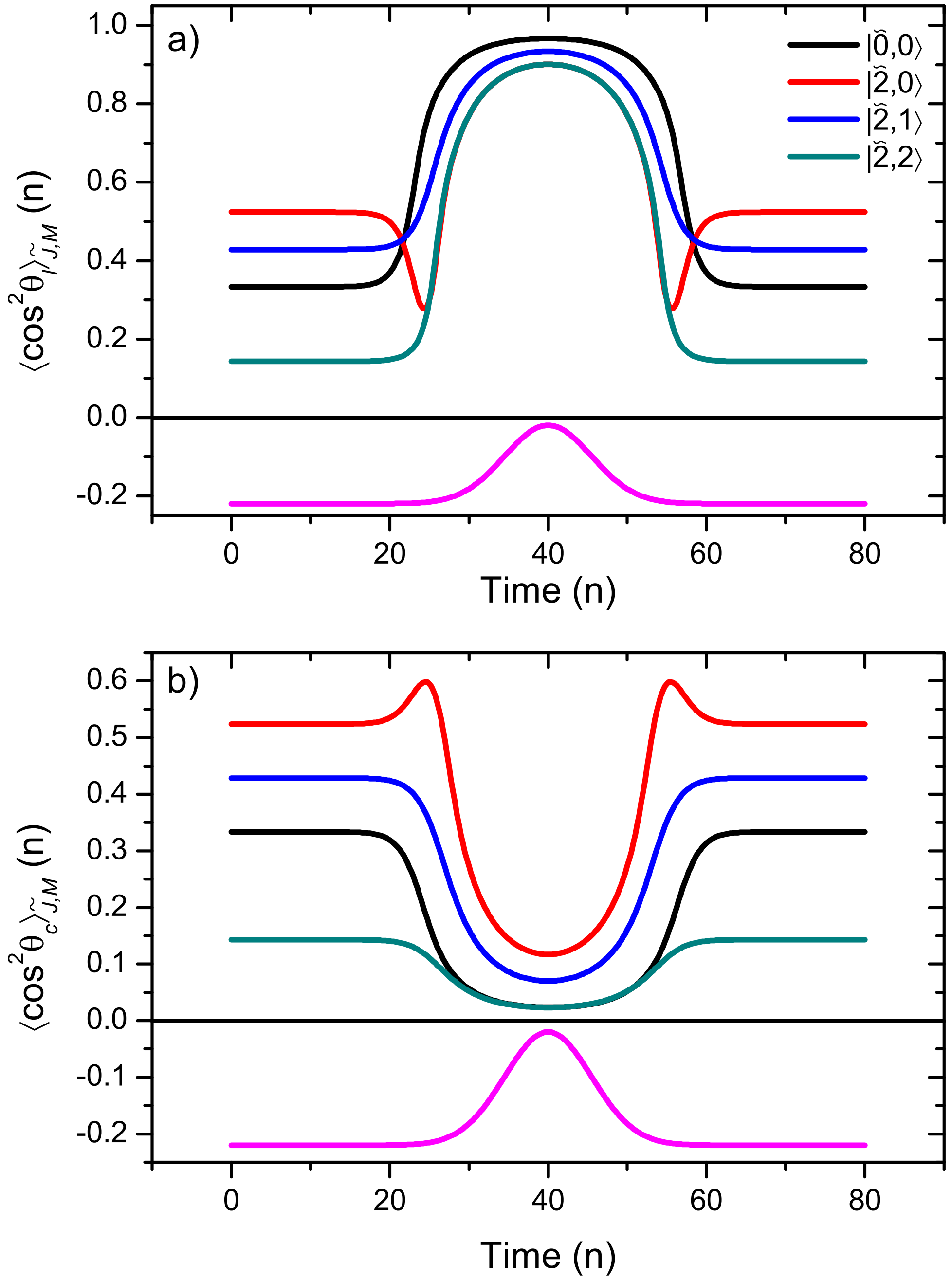

Figure 3.2: a) and b) show the expectation value for linearly and circularly polarised light for the four lowest rotational states of CS_2 aligned by a pulse with $I_0 = 10^{12}$ W cm^{-2}, and centred at $n = 40$, with e^{-2}=0.6 ns. a) For linearly polarised light the expectation value $\langle\cos^2\theta_l\rangle_{\tilde{J},M}$, is approaching 1 for the $|\tilde{0},0\rangle$ state and θ_l is close to 0° indicating that the molecular bond axis is being strongly confined to the Z axis. b) For circularly polarised light θ_c is tending toward 90°, indicating the molecule is being aligned with the electric field plane. The pulse widths are illustrated at the bottom of both graphs.

adiabatic regime. Adiabatic alignment is the creation of a rotational eigenstate in a rigid rotor that adiabatically correlates with the field-free state dressed with an electric field[194, 83, 99]. These directional states are hybrids of the field-free states and librate about the electric field polarisation vector because of the polarisability anisotropy. The molecule is free to librate about the space fixed axis like a pendulum and so adiabatic states are called pendular states. In this approximation the electric field is considered static at each point in time or space. Consequently, after the field is switched off the molecular alignment of the perturbed rotational state returns to its field-free value.

Figures 3.2 a) and b) show the adiabatic alignment of the first four rotational states of CS_2, $|\tilde{0}, 0\rangle$ (black), $|\tilde{2}, 0\rangle$ (blue), $|\tilde{2}, 1\rangle$ (red) and $|\tilde{2}, 2\rangle$ (light blue) for a linearly and circularly polarised optical field. Also shown on both figures (pink) is the electric field pulse of e^{-2} width $\sigma = 7.75$ centered at $n = 40$, with $I_0 = 10^{12}$ W cm^{-2}. Figure a) shows the $\langle \cos^2 \theta_l \rangle_{\tilde{J},M}(n)$ value is close to 1 for the centre of the pulse, indicating strong confinement between the bond axis and the Z axis. For circularly polarised light, $\langle \cos^2 \theta_c \rangle_{\tilde{J},M}(n)$ approaches 0 with $\theta_c \rightarrow 90°$. This means the molecule is aligning with the plane of the polarisation as illustrated in figure 3.1. Figures 3.2 a) and 3.2 b) also show different rotational states have different field-free values, the field-free value of the ground state is $\langle \cos^2 \theta \rangle_{0,0} = 1/3$, which arises from an orientational average over all three Euler angles. The field-free value of a complete J manifold, where the field-free values from $\pm M$ and $M = 0$ are averaged, is always $\langle \cos^2 \theta_{l,c} \rangle_J = 1/3$.

3.3.2 Nonadiabatic alignment

Nonadiabatic dynamics allow the molecular alignment to persist after the field has been turned off through rotational revivals. The electric field prepares the molecule in a coherent superposition of rotational eigenstates[189, 195] by quickly transferring a large amount of angular momentum from the optical field, creating a rotational wave packet. This process is often referred to the field giving the molecule a "kick", which sets the molecule tumbling in space. The phase differences between the mixed eigenstates cause the alignment to dephase and rephase after the field is turned off. The periodicity and size of the revivals depend on the pulse shape and the laser intensity. Although the pulse length of the IR laser used in the experiment means the molecules are adiabatically aligned, the properties of nonadiabatic behaviour are briefly illustrated here for completeness.

Figure 3.3 shows nonadiabatic alignment of the $|\tilde{0}, 0\rangle$ state calculated using the TDSE for two short optical pulses of duration $\sigma = 3$ (red) and $\sigma = 0.3$ (blue), corresponding to FWHM widths of 240 ps and 24 ps. The peak intensity is $I_0 = 10^{12}$ W cm^{-2}. In figure 3.3, the longer 240 ps pulse, is just entering the nonadiabatic regime and is considered to have "intermediate"[191] behaviour where the molecule ends up

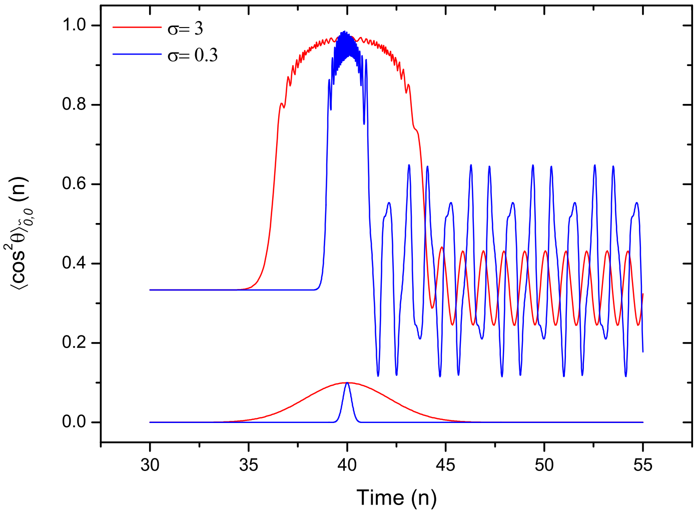

Figure 3.3: The nonadiabatic molecular alignment of the $|\tilde{0},0\rangle$ state is calculated at $I_0 = 10^{12}$ W cm^{-2} with two short laser pulses. The molecule is given a "kick" from the optical pulse which transfers angular momentum to the molecule creating a rotational wave packet. The alignment persists after the field is off due to the phase relationships between the mixed states. The pulse widths are shown at the bottom of the figure with e^{-2} reduced unit widths of $\sigma = 3$ (147 ps) (red) and $\sigma = 0.3$ (14.7 ps) (blue).

in a state which resembles the initial field-free state dressed by the field. The close amount of phase matching between the mixed eigenstates partially suppresses the rotational revivals. By contrast, the shorter 24 ps pulse produces stronger rotational revivals indicating more eigenstates have been mixed together[190].

Figure 3.4 shows the $|C_{J,M}(n)|^2$ coefficients for a molecule initially in the $|\tilde{0},0\rangle$ state during the 24 ps laser pulse. After the pulse has passed the $|C_{J,M}(n)|^2$ remain populated rather than returning to their initial values, leaving the molecule in a rotational wave packet. Eventually collisions with other molecules will return the molecule to its initial ground state.

3.3.3 Rotational temperature

The rotational temperature of the molecules is critical in determining the amount of alignment observed. The alignment quickly decreases with temperature. We assume a Boltzmann distribution of the rotational levels and the expectation value for each state, $\langle\cos^2\theta_{l,c}\rangle_{\tilde{J},M}(n)$, is summed and multiplied by the probability that state is occupied at a temperature T_R. The ensemble alignment is[196, 197]

$$\langle\cos^2\theta_{l,c}\rangle(n) = Q^{-1}\sum_J \exp\left[\frac{-BJ(J+1)}{k_b T_R}\right]\sum_{M=-J}^{J}\langle\cos^2\theta_{l,c}\rangle_{\tilde{J},M}(n), \tag{3.20}$$

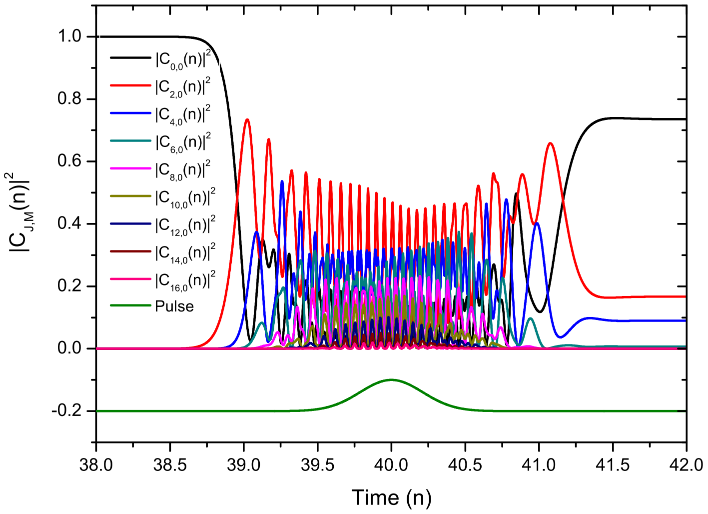

Figure 3.4: Wave packet formation through nonadiabatic alignment in the $|\tilde{0}, 0\rangle$ state is illustrated by plotting the coefficients, $|C_{J,M}(n)|^2$, of the $|\Psi_{\tilde{0},0}\rangle(n)$ expansion. A pulse of $\sigma = 0.3$ mixes the field-free states and leaves population in multiple $|C_{J,M}(n)|^2$ states rather than returning to the initial rotational state. The laser pulse is shown at the bottom of the figure.

where k_b is Boltzmann's constant, and Q is a normalization constant called the rotational partition function[161, 198],

$$Q = \sum_{J}^{J_{max}} (2J+1) \exp\left[\frac{-BJ(J+1)}{k_b T_R}\right]. \tag{3.21}$$

We can now define an ensemble alignment parameter, which will be used to calculate the properties of aligned molecules in the molecular lens. The expectation values, $\langle\cos^2\theta_{l,c}\rangle_{\tilde{J},M}(n)$, for each polarisation is averaged to produce $\langle\cos^2\theta_{l,c}\rangle$, with no J, M subscript to indicate thermal averaging has taken place. The thermally averaged effective polarisabilities are defined as

$$\begin{aligned} \bar{\alpha}_L(n) &= \Delta\alpha\langle\cos^2\theta_l\rangle(n) + \alpha_\perp \\ \bar{\alpha}_C(n) &= \frac{1}{2}\left[\alpha_{||} + \alpha_\perp - \Delta\alpha\langle\cos^2\theta_c\rangle(n)\right]. \end{aligned} \tag{3.22}$$

The dependence on the dimensionless parameter n, can be converted to intensity producing $\bar{\alpha}_{L,C}(I)$, which is more useful in simulations of the dipole force as it is a more common parameter.

Figure 3.5 shows the ensemble effective polarisabilities, $\bar{\alpha}_{L,C}(I)$, for linearly and circularly polarised light calculated using equation 3.22. The figure shows the differ-

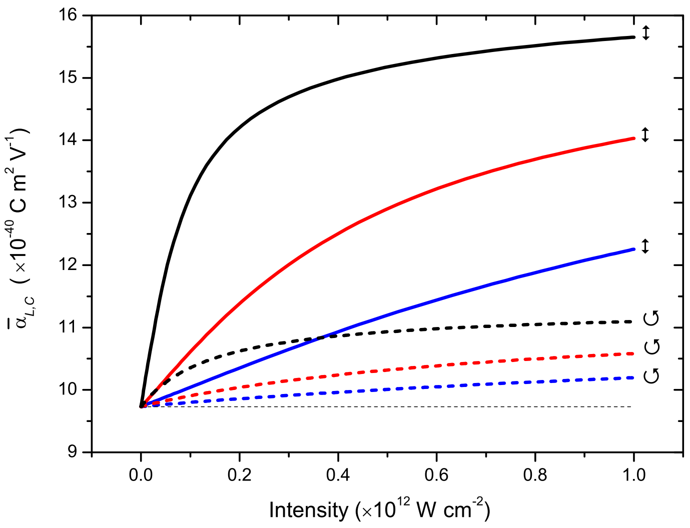

Figure 3.5: The ensemble average effective polarisability $\bar{\alpha}_{L,C}(I)$, for linearly and circularly polarised light is shown as a function of intensity. The vertical arrow indicates linearly polarised light whilst the circle arrow shows circularly polarised light. Three rotational temperatures of 2 K (black), 12 K (red), and 35 K (blue) are shown. In both cases the polarisability quickly rises and saturates with higher rotational temperatures requiring more intensity to reach saturation. The dashed line indicates the average polarisability of 9.7×10^{-40} C m^2 V^{-1}.

ence in effective polarisability between linearly (LPL) and circularly polarised light (CPL) depends on the laser intensity and on the rotational temperature. For both laser polarisations the polarisability of the molecule quickly increases and then saturates as the intensity is increased. Three temperatures are shown, 2 K (black), 12 K (red) and 35 K (blue). Higher rotational temperatures reduce the molecular alignment and increase the intensity where the effective polarisability saturates.

Figure 3.6 a) shows the effect of varying the rotational temperature T_R at a fixed intensity of 5.7×10^{11} W cm^{-2} for both laser polarisations. The results from the time-dependent Schrödinger equation (TDSE) are shown in green (LPL) and blue (CPL) up to 30 K. Also shown to 50 K are the results from the time-independent Schrödinger equation in black (LPL) and red (CPL). The agreement between the calculations for both polarisations is very good. The slightly higher TDSE curve for LPL is most likely due to cumulative errors in summing over all the states suggesting the error tolerance on the ODE solver in Matlab is not quite low enough for summing over many states. The disagreement in effective polarisability for LPL, between the TDSE and TISE calculations is 0.06 C m^2 V^{-1}, which is negligible when experimental errors are taken into account. The average polarisability α_{ave}, of CS$_2$ is shown by the dashed line. Figure 3.6 b) shows the effective polarisability for both polarisations calculated up to room temperature at 5.7×10^{12} W cm^{-2}. The decrease in expectation value of the

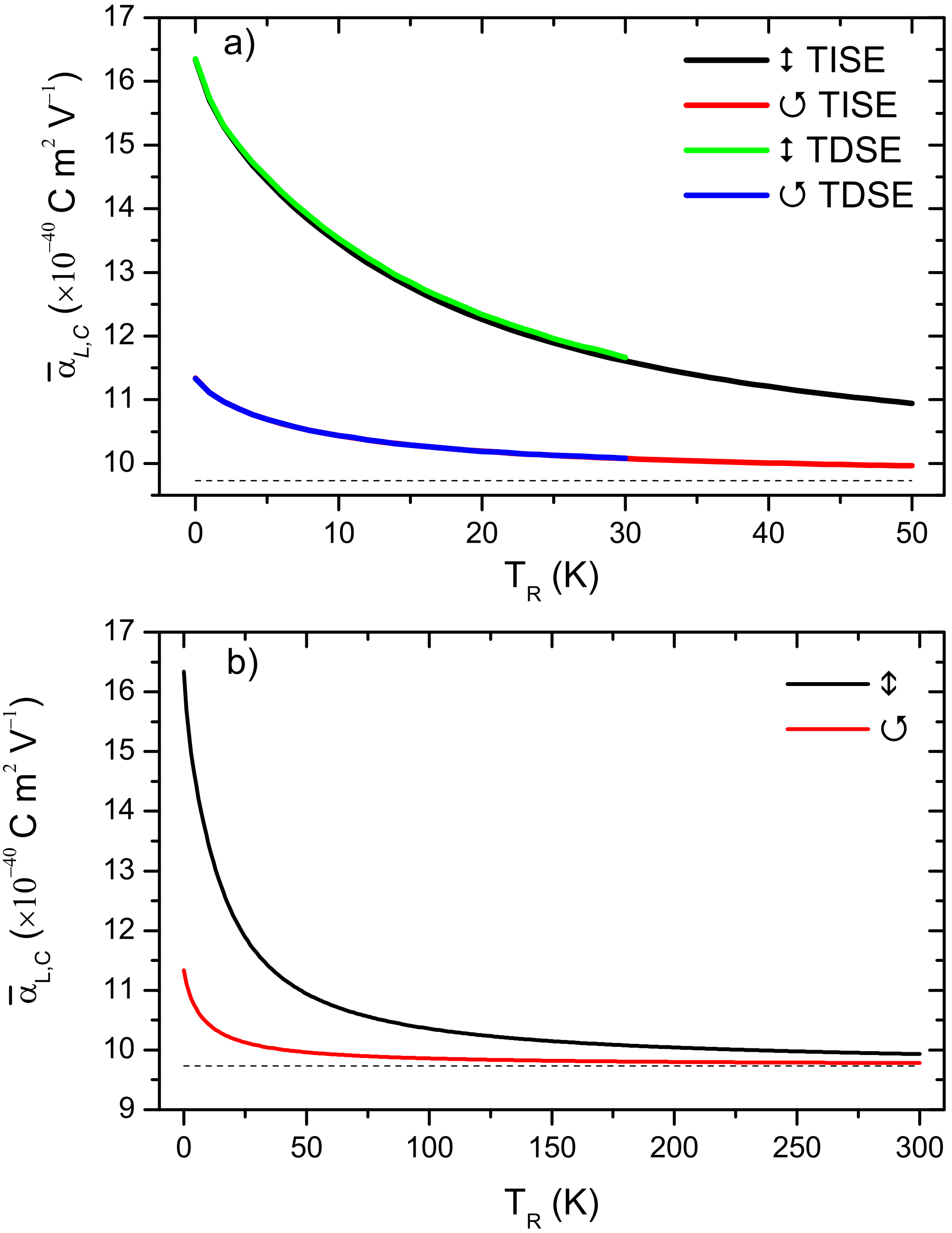

Figure 3.6: a) The effective polarisability for linearly polarised and circularly polarised light as a function of rotational temperature is plotted at an intensity of 5.7×10^{11} W cm^{-2}. The green and blue curves are calculated from the TDSE whilst the red and black curves use the TISE. Good agreement is found between the methods. At $T_R = 30$ K for linearly polarised light the difference between the methods is 0.06 C m^2 V^{-1}. b) At the same intensity the effective polarisability is plotted up to room temperature using the TISE to show the effect of using much higher rotational temperatures. The dotted line shows the average polarisability of the molecule.

ensemble with temperature is caused by the increasing rotational energy of J. The energy of the AC Stark shift becomes less comparable and cannot overcome the high rotational energy of the higher J states. Consequently, the effective polarisability decreases with $\bar{\alpha}_{L,C}(I) \rightarrow \alpha_{ave}$ at high temperatures.

3.4 The alignment-dependent dipole force

3.4.1 Model

The Stark potentials for linearly and circularly polarised light are given in equation 3.1. The Stark potential can be expressed using the intensity of the field with $\epsilon_0^2(t) = \frac{2I_0 g(t)}{c\varepsilon_0}$ and a spatial distribution $I(r)$. For both laser polarisations we find

$$V(r,t) = -\frac{g(t)}{2c\epsilon_0}\bar{\alpha}_{L,C}(I(r))I(r), \tag{3.23}$$

where $g(t)$ is the temporal profile of the intensity envelope, c and ε_0 are the speed of light and permittivity of free space respectively. The thermally averaged effective polarisability for LPL or CPL is $\bar{\alpha}_{L,C}$, and varies with intensity. By fitting a polynomial curve for multiple rotational temperatures to the calculated curves of $\bar{\alpha}_{L,C}(I)$, such as those generated in figure 3.5, an analytical form of $\bar{\alpha}_{L,C}(I)$ is generated. The effective polarisability $\bar{\alpha}_{L,C}(I)$, can now be directly inserted into classical simulations of centre-of-mass motion induced by the optical field in equation 3.23. The force on a polarisable molecule at a position r from the centre of the IR field is $F(r,t) = -\nabla V(r,t)$. From equation 3.23

$$\begin{aligned} F(r) =& \frac{1}{2c\epsilon_0}\nabla\left[\bar{\alpha}_{L,C}(I(r))I(r)\right] \\ =& \frac{1}{2c\epsilon_0}\bar{\alpha}_{L,C}(I(r))\nabla I(r) + \frac{1}{2c\epsilon_0}I(r)\nabla\bar{\alpha}_{L,C}(I(r)). \end{aligned} \tag{3.24}$$

We define a Gaussian focus, which has an e^{-2} waist radius ω,

$$I(r) = I_0 \exp\left(\frac{-2r^2}{\omega^2}\right) \tag{3.25}$$

where $r^2 = x^2 + y^2$. In our experiments in the next chapter, the force is measured along the x axis. This means the spatial derivative along the x axis is

$$\nabla I(x) = \frac{-4x}{\omega^2} I_0 \exp\left(\frac{-2x^2}{\omega^2}\right). \tag{3.26}$$

The intensity dependence of the ensemble effective polarisability is converted in one dimension along x or y to a spatial dependence through

$$\frac{d\bar{\alpha}_{L,C}}{dx} = \frac{d\bar{\alpha}_{L,C}}{dI}\frac{dI}{dx}, \tag{3.27}$$

equation 3.24 can be rewritten as a force along x or y as

$$F(x) = \frac{1}{2c\varepsilon_0}\bar{\alpha}_{L,C}(I)\nabla I(x) + \frac{1}{2c\varepsilon_0}I(x)\frac{d\bar{\alpha}_{L,C}(I)}{dI}\nabla I(x). \tag{3.28}$$

Evaluating the expression by inserting $\nabla I(x)$ and including the time dependence of the field $g(t)$, we find the alignment-dependent dipole force is

$$F(x,t) = -\frac{2xg(t)I_0}{c\epsilon_0\omega^2}\exp\left(\frac{-2x^2}{\omega^2}\right)\left[\bar{\alpha}_{L,C}(I) + \frac{d\bar{\alpha}_{L,C}(I)}{dI}\exp\left(\frac{-2x^2}{\omega^2}\right)\right], \tag{3.29}$$

where x is interchangeable with y. The resulting force is negative, this means molecular motion away from the lens is opposed. The parameter $\frac{d\bar{\alpha}_{L,C}}{dI}$, is the rate of change of effective polarisability with $I(r)$ for LPL or CPL. Figure 3.7 shows qualitatively the effect of the dipole force in the x direction for equation 3.29 along the molecular beam axis. Molecules with position $x < x_0$ are accelerated and fall into the potential well whilst molecules with position $x > x_0$, must climb the potential hill and are decelerated. The lower section of figure 3.7 shows a plot of the force with an isotropic polarisability ($\nabla\bar{\alpha}_{L,C} = 0$) to illustrate the shape of the induced velocity change as a function of position. The molecules are detected after the dipole force has been applied, and their time-of-flight is then used to determine the velocity change.

Equation 3.29 contains both the molecular alignment and centre-of-mass motion properties which are a result of the AC Stark shift. The molecular alignment occurs from the $\bar{\alpha}_{L,C}(I)$ term, whilst centre-of-mass motion results from the spatial gradients of $I(r)$ and $\bar{\alpha}_{L,C}(I)$. Equation 3.29 is a modified equation of the dipole force from other studies[188, 60, 59] where a molecular lens is formed, but alignment is not observed. This is probably due to additional longitudinal modes in the IR laser pulse (see Chapter 2). By replacing $\bar{\alpha}_{L,C}(I)$ with the isotropic polarisability of the molecule α_{ave} ($\frac{d\bar{\alpha}_{L,C}}{dI} = 0$), equation 3.29 reduces to the form used in other studies of the dipole force[188, 60, 59].

3.4.2 Implementation

The acceleration and deceleration properties of the molecular lens were simulated by 150 equally spaced particles being placed along the x axis within and outside the spatial extent of the intensity field. The particles were propagated through the laser focus in time over a duration larger than the temporal FWHM of the IR field. The

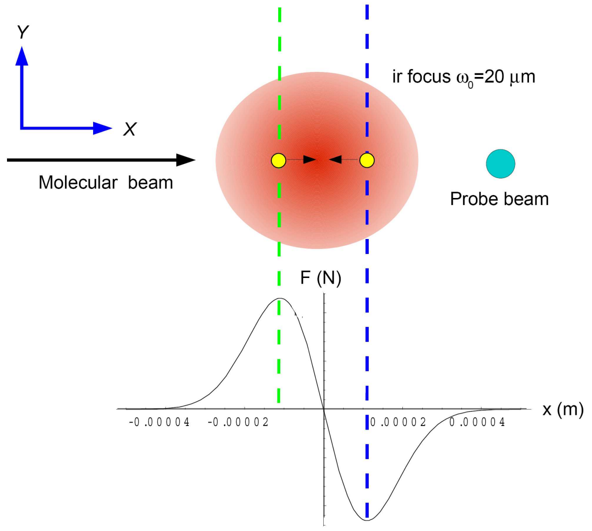

Figure 3.7: A diagram of how an IR beam can be used to apply the dipole force to neutral molecules. The plot below the IR focus shows the force through the IR focus in the x direction. Ground state molecules are high-field seeking and the Gaussian laser focus provides an attractive radial force. Molecules which are near the first dashed line (green) are accelerated toward the centre of the focus, whilst molecules near the blue dashed line are decelerated as the dipole force opposes their motion away from the laser focus.

temporal profile $g(t)$, was obtained by a fit to the experimentally measured IR pulse shape (see figure 2.6 in Chapter 2). Classical simulation of the molecular trajectories is appropriate because the de Broglie wavelength of the molecules is much less than the dimensions of the laser focus[54, 76]. The equations of motion for acceleration and position were solved for the ith particle in the x direction using the alignment-dependent dipole force in equation 3.29. The force equation is

$$\frac{dv_i(x,t)}{dt} = \frac{F_i(x,t)}{m}, \tag{3.30}$$

where v_i is the velocity of the ith particle. As $g(t)$ has a FWHM of 15 ns, and the particle velocity is 540 m s^{-1}, the molecules only travel partially through the field, resulting in a net change in velocity after the field is turned off. By solving equation 3.30 for each particle, the effect of the dipole force is mapped out by the overall velocity change imparted onto the molecule after it exits the IR field. The initial position and velocity of the particles before the IR field is switched on provides the initial conditions of the ODE solver. The induced velocity change imparted onto each particle as a function of position x, can be plotted to show the experimentally measurable effects.

3.4.3 Results

To simulate the alignment-dependent dipole force, the equations of motion were solved in Matlab for both linearly and circularly polarised light. The program is shown in the Appendix. Figures 3.8 a) and b) show the laser induced well depth and the corresponding velocity shift arising from that well depth. The parameters in a) for the potential well are for linearly polarised light with $I_0 = 7 \times 10^{11}$ W cm^{-2} and $\omega = 20$ μm. Figure 3.8 a) has no time dependence and depends only on the location of the particle to illustrate the different well depths. The time dependence of the optical field was however included in calculating the velocity changes in b). The pulse duration determines the magnitude of the velocity shift, as the longer the molecule is in the field, the greater the acceleration or deceleration. This rule applies until the field is on long enough the molecules travel all the way through the field, and consequently they will have no net perturbation due to the conservative potential. In figure 3.8 b), as expected, the well depth is enhanced by the aligned molecules, with colder molecule ensembles giving the deepest well depths. The temperatures plotted are 2 K (black), 12 K (red) and 35 K (blue). The grey dashed line indicates the well depth for isotropic molecules with α_{ave}. Compared to an isotropic molecule, the aligned molecules increase the well depth by an additional 41 K, 24 K and 13 K for the temperatures shown.

The effects from the potential well are shown in figure 3.8 b). The induced velocity change imparted to the particles at each x position in the molecular lens is shown for linearly (solid) and circularly (dashed) polarised light. The shape of the velocity change is largely unaffected by the aligned molecules, due to the dominance of the $\nabla I(x)$ term in equation 3.29. The effective polarisability $\bar{\alpha}_{L,C}(I)$, serves to enhance the magnitude of the velocity change at the regions of maximum velocity change at $x = \pm\frac{\omega}{2}$. The difference in velocity change is significant between the linear and circular laser polarisations for all three temperatures, with maximum changes of 33 %, 27 % and 20 % for 2 K, 12 K and 35 K respectively. For linear polarisation, the velocity change is increased by 20 % when the temperature is reduced from 35 K to 2 K. As the rotational temperature is increased the expectation value $\langle \cos^2 \theta_{l,c} \rangle$, tends toward the field-free value for both polarisations. This reduces the magnitude of the dipole force until at high enough temperatures ($>\approx 60$ K) the velocity shifts from linearly and circularly polarised light will be indistinguishable. For comparison, the isotropic polarisability of CS$_2$ is also plotted with $\alpha_{ave} = 9.73 \times 10^{-40}$ C m^2 V^{-1}, indicated by the grey dashed line.

As molecular alignment depends on the intensity of the field, using higher intensities would produce larger experimentally measurable velocity shifts, but the difference between LPL and CPL would not be greatly enhanced because of the saturation behaviour of the alignment dynamics.

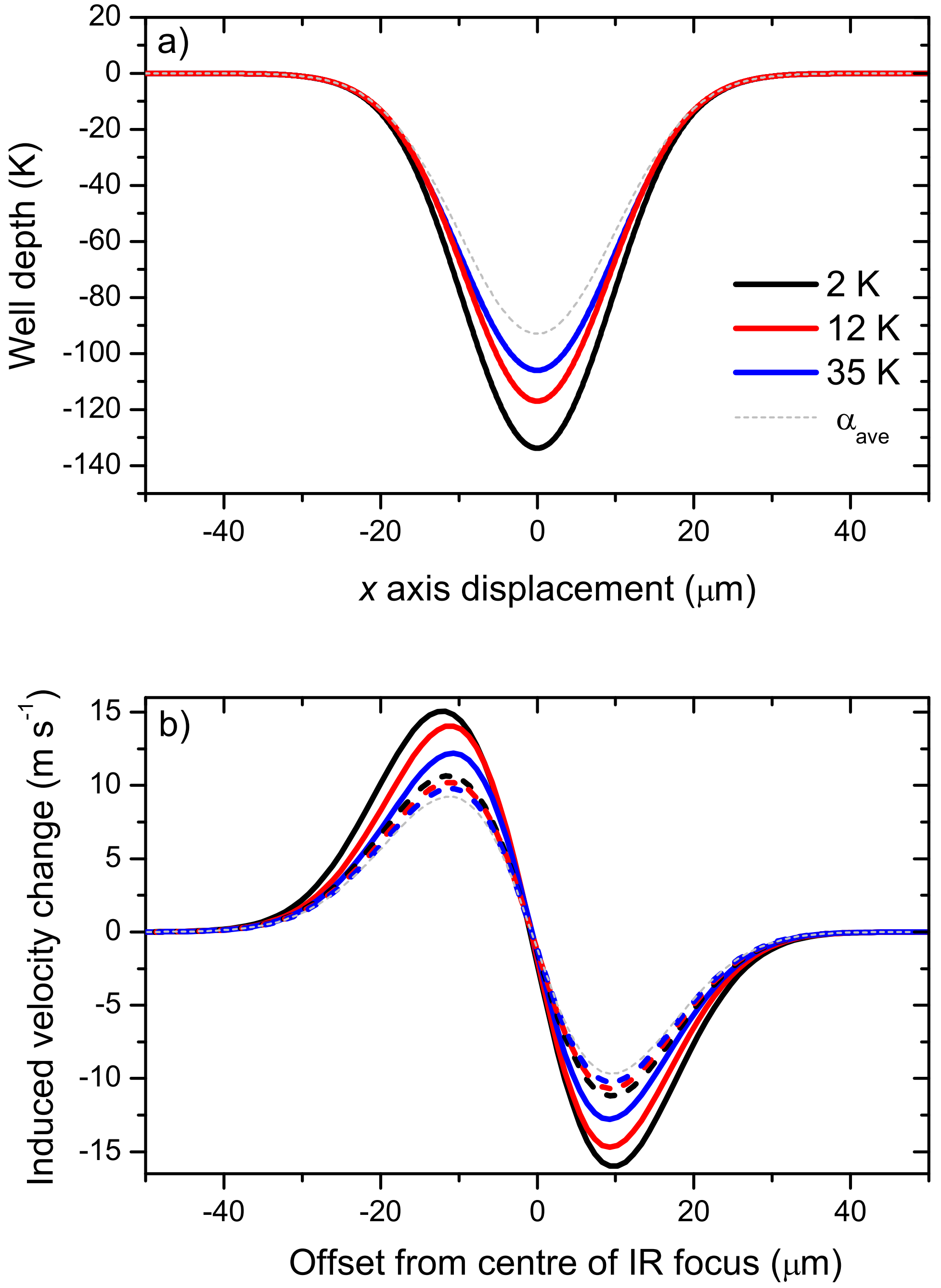

Figure 3.8: a) The well depths for linearly polarised light are shown for three rotational temperatures, 2 K (black), 12 K (red) and 35 K (blue) at an intensity of $I_0 = 7 \times 10^{11}$ W cm^{-2}, with a waist radius of 20 μm. The grey dashed line indicates the well depth for isotropic molecules with α_{ave}. b) The induced velocity change along the molecular beam axis caused by the well depth in a) is shown for the same temperatures as a). Linearly (solid) and circularly (dashed) polarised light cases are shown. The difference in velocity between the laser polarisations decreases with higher rotational temperatures. Lower rotational temperatures for circularly polarised light only modestly increase the overall dipole force compared to a molecule with α_{ave}. Whilst for linearly polarised light, from 35 K to 2 K, the force is increased by 20 %.

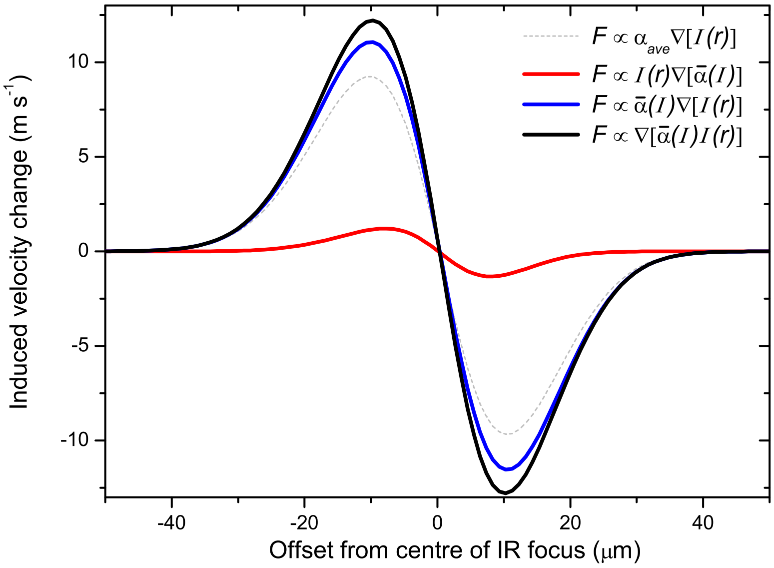

Figure 3.9: The different contributions from the alignment dependent dipole force are shown. For a peak intensity of $I_0 = 7 \times 10^{11}$ W cm^{-2}, with a waist radius of 20 μm and T_R= 35 K, the induced velocity change is enhanced by 10 % from the spatial dependence of the $\frac{d\bar{\alpha}_{L,C}}{dI}$ (red) term. The $F \propto \bar{\alpha}\nabla[I(r)]$ (blue) term contributes to the majority of the force. The sum of the contributions is also shown (black). When there are no alignment effects, α_{ave} is used with $F \propto \alpha_{ave}\nabla[I(r)]$. This is indicated by the grey dashed line.

The effect of $\frac{d\bar{\alpha}_{L,C}}{dI}$

Figure 3.9 shows the effect from the $\frac{d\bar{\alpha}_{L,C}}{dI}$ term for the conditions described in figure 3.8 with T_R= 35 K. The three curves show the velocity change by only differentiating the spatial distribution $F \propto \bar{\alpha}_{L,C}(I)\nabla[I(r)]$ (blue), the second curve (red) shows the velocity change from the spatial dependence of $\frac{\bar{\alpha}_{L,C}}{dI}$, $F \propto \nabla[\bar{\alpha}_{L,C}(I)]I(r)$. Whilst the third curve (black) shows the sum of the $\bar{\alpha}_{L,C}(I)\nabla[I(r)]$ and $\nabla[\bar{\alpha}_{L,C}(I)]I(r)$ curves, which is identical to $F \propto \nabla[\bar{\alpha}_{L,C}(I)I(r)]$. From figure 3.9, the contribution of the $\frac{d\bar{\alpha}_{L,C}}{dI}$ term is 10 % of the total velocity change. Generally, the slope of $\bar{\alpha}_{L,C}$ with respect to the intensity can contribute between 0 and 10 % of the total force. The contribution depends on the temperature and the intensity. When the field is turning on $\frac{d\bar{\alpha}_{L,C}}{dI}$ is large but the intensity is so low no centre-of-mass motion is produced. When the intensity is high enough to induce molecular motion, the alignment curve has saturated, diminishing the force $F \propto \nabla[\alpha_{L,C}(I)]I(r)$. Lower temperatures generally contribute less from $\frac{d\bar{\alpha}_{L,C}}{dI}$ since the saturation region has a lower intensity threshold. For example, at 2 K and $I_0 = 7 \times 10^{11}$ W cm^{-2}, the $\frac{d\bar{\alpha}_{L,C}}{dI}$ term contributes only 3 % of the total force.

3.5 Conclusion

The centre-of-mass motion and molecular alignment in a molecular lens created by a seeded nonresonant IR laser beam has been studied numerically. Pendular states of CS_2 are formed in the molecular lens which align with the electric field polarisation vector. The alignment characteristics of CS_2 are calculated adiabatically for each $|J, M\rangle$ state to find the expectation value $\langle \cos^2 \theta_{l,c} \rangle_{\tilde{J},M}$, for LPL and CPL. The calculated expectation values $\langle \cos^2 \theta_{l,c} \rangle_{\tilde{J},M}$, were then thermally averaged to create an intensity dependent effective polarisability $\bar{\alpha}_{L,C}(I)$, for a molecular ensemble at a temperature T_R. An analytical form of $\bar{\alpha}_{L,C}(I)$ was then used to describe the molecule's effective polarisability in the centre-of-mass problem of a molecular lens. The results show that the dipole force is proportional to the spatial gradient of the product of the effective polarisability and the intensity distribution $F \propto \nabla[\bar{\alpha}_{L,C}(I)I(r)]$. The effective polarisability $\bar{\alpha}_{L,C}(I)$, enhances the dipole force primarily at the $x = \pm\frac{\omega}{2}$ regions.

For a group of molecules traveling along the molecular beam axis, the alignment-dependent dipole force has been numerically calculated for experimental conditions. The alignment-dependent dipole force can be measured by ionisation of CS_2 in a TOFMS, which can record the induced velocity change imparted to the molecules in the molecular lens. Depending on the rotational temperature, a ≈20-30 % difference in dipole force between linearly and circularly polarised light is predicted.

Chapter 4

Measuring the effect of molecular alignment on the dipole force

4.1 Introduction

This chapter presents measurements of the dipole force on CS_2 molecules and compares these results with the theoretical predictions presented in chapter 3. The velocity induced by the dipole force is measured for linearly and circularly polarised light and the differences due to molecular alignment are compared and discussed.

In an almost identical experiment, a measurement of the dipole force between the bending vibrational mode, ν_2, of CS_2 and the linear ground state is attempted.

4.2 Method

4.2.1 Apparatus

The setup to measure the alignment-dependent dipole force and its influence on centre-of-mass motion in a molecular lens is illustrated in figure 4.1. The IR and probe beams are parallel to each other and are focussed onto the xy plane inside the TOFMS. When the probe beam creates the CS_2^+ ions via (3+1) REMPI at $\lambda = 478.63$ nm, they are repelled by the 100 V plate and collected at the MCP which is operated using -2.5 kV. The flat green arrows on the diagram indicate the direction of the dipole force due to the focussed nonresonant laser beam. Forces along the x direction cause acceleration and deceleration, whilst forces along the y axis cause focussing of the molecular beam. A 300 μm slit is placed over the MCP collector plate in order to limit ion collection to the Rayleigh range of the probe beam, this means molecules within the focal volume of the IR beam, bound by the 300 μm slit experience a constant IR intensity. This approximation means the IR intensity distribution can be represented as being only in the xy plane since $z \approx 0$.

Figure 4.2 shows a plan view of the experiment in the xz plane. The IR and probe

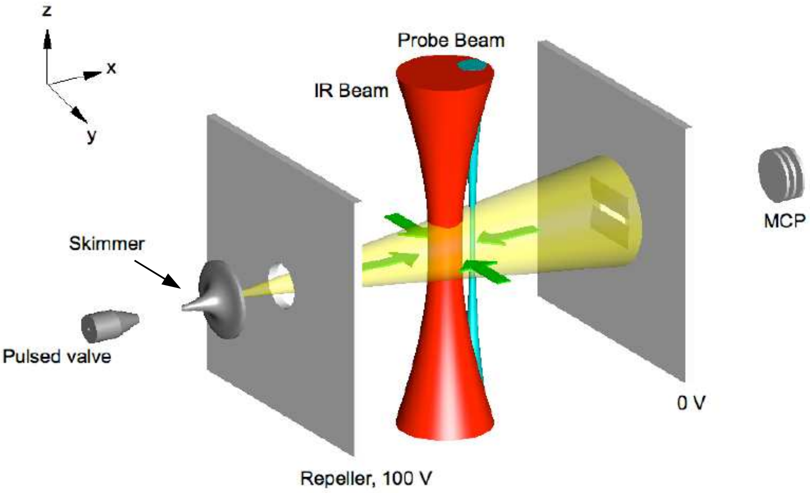

Figure 4.1: A schematic showing the molecular lens. A focussed IR beam in the xy plane creates a force in the directions indicated by the green arrows. Forces in the y direction will cause focussing of the molecular beam, whilst forces in the x direction will accelerate or decelerate the molecules before and after the lens respectively.

beams are combined by using a dichroic mirror indicated by the gray dashed line on figure 4.2. The front of the mirror is coated to reflect the probe beam at 480 nm. The IR beam travels through the back of the dichroic mirror. The parallel beams are directed into the main vacuum chamber where they intersect with a molecular beam of carbon disulphide seeded in argon. The molecular beam is operated in two modes, the first uses 450 mbar (25 %) of CS_2 whilst the second mode uses 7 mbar (4 %), both mixtures are seeded in 1.8 bar of argon. The molecular beam is skimmed through a circular 2 mm orifice before entering the main chamber, which is held below 4×10^{-7} mbar during molecular beam operation. The molecular beam velocity is approximately 492 m s^{-1} (see chapter 2 section 2.4.2) and 537±22 m s^{-1} for each respective mode of operation. The IR field was provided by a 10 Hz seeded Q-switched laser with $\lambda = 1064$ nm (Spectra Physics Quanta Ray). The probe laser beam was provided by a tunable dye laser (ND6000) pumped by the frequency tripled output of an unseeded Continuum Precision II 8000 also operated at 10 Hz. The molecular beam was pulsed at the laser repetition rate. Both lasers and the molecular beam were controlled by two Stanford Research Systems delay pulse generators (DG535).

The temporal duration of the IR and probe laser pulses had a near Gaussian profile with a FWHM width of 15 ns and 7 ns respectively. The temporal profiles were measured using a fast photodiode and 3 GHz oscilloscope. The output from the Spectra Physics laser was passed through two thin-film-polarisers (TFP) producing

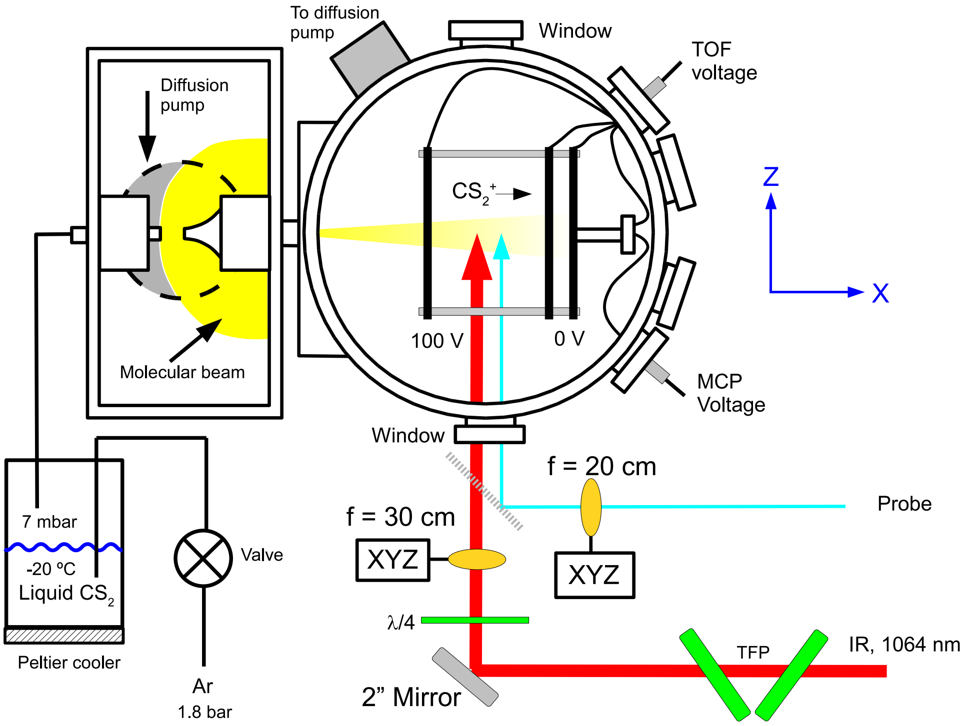

Figure 4.2: A plan view of the setup to measure the acceleration and deceleration of CS_2. The speed of the molecules is recorded by the TOF mass spectrometer which is sensitive to velocity changes along the x axis. As the IR beam is scanned along the x direction, the induced velocity change for LPL and CPL is recorded. The probe beam wave length is $\lambda = 478.650$ nm, which corresponds to the (3+1) REMPI transition $\left[\frac{1}{2}\right] np\sigma(^1\prod_u) \leftarrow \tilde{X}^1\sum_g^+$. The IR beam is passed through two thin-film-polarisers to ensure linearly polarised light. Before being focussed into the main chamber, the beam encounters a $\lambda/4$ wave-plate which is used to switch between linearly and circularly polarised light.

horizontal linearly polarised light to better than 1 part in 10^4. A $\lambda/4$ IR coated waveplate was placed before the IR focussing lens to switch between linearly and circularly polarised light. The IR intensity drops by 6 % percent in the interaction region after passage through all optics when changing from linear to circular polarisation. This is consistent with differential Fresnel reflection losses between the orthogonal components of the CPL laser beam when it encounters the back of the dichroic mirror which is at 45° to the incident beam. This effect changes the beam so that it is slightly elliptically polarised. If a molecule is completely aligned with the field polarisation vector and one of the electric field components of CPL light is reduced by 6 %, the difference in maximum effective polarisability between the slightly elliptical CPL and true CPL is < 3 %. In reality complete alignment is not realistic which reduces the difference in effective polarisability between near CPL and true CPL further. It is important however to correct for the overall intensity being 6 % lower.

The pulse energy of the IR and probe laser was 150 ± 10 mJ and 0.2 ± 0.05 mJ respectively. Each laser was focussed outside the vacuum chamber by separate plano-convex lenses mounted on xyz translation stages. The IR beam could be positioned in the x direction with a resolution of ±1 μm, all other translation directions for both lasers had a resolution of ±5 μm. Although the probe beam was also mounted on a xyz translation stage it was not moved during the experiment because this would affect the time-of-flight of the ions. The infrared laser was focussed by a 30 cm plano-convex lens to a Gaussian focus with a e^{-2} radius of 20 μm, providing a peak intensity of $5.7\pm0.3\times10^{11}$ W cm^{-2}. At this intensity no CS_2 ions were detected from nonresonant ionisation. At low frequencies the nonresonant intensity threshold can be calculated from the tunneling model of ionisation[199, 200] to be

$$I_t(\mathrm{W\ cm^{-2}}) = 4 \times 10^9 \left[\frac{I.P(\mathrm{eV})}{Z^2}\right]^4, \tag{4.1}$$

where Z is the residual charge, and $I.P$ is the ionisation potential in eV, which is 10.08 eV[143] for CS_2. The first ionisation potential is $Z = 1$ yielding a value of $I_t = 4 \times 10^{13}$ W cm^{-2}. The IR laser operates well below this intensity and care was taken to operate the laser without producing ions via nonresonant ionisation.

The dye laser was focussed through a 20 cm plano-convex lens to a waist radius of 5 μm and an intensity of 2×10^{10} W cm^{-2} which was sufficient to ionise the carbon disulphide into CS_2^+ molecular ions. The ionisation process is a (3+1) REMPI at a laser wavelength of $\lambda = 478.650$ nm, corresponding to the three photon transition $\left[\frac{1}{2}\right] np\sigma(^1\prod_u) \leftarrow \tilde{X}^1\sum_g^+$[140, 141]. As the (3+1) REMPI process requires subsequent absorption of three photons and a fourth for ionsiation, it is estimated the spatial resolution of the probe beam is approximately less than the waist radius as only the central region of the focus will have sufficient intensity to ionise the molecules. After

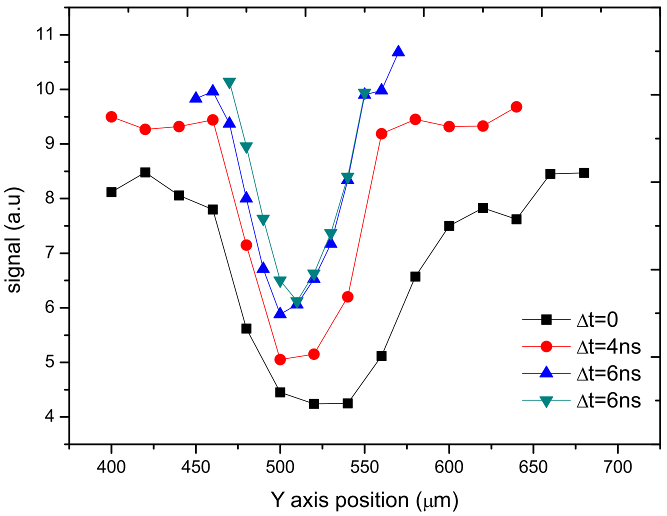

Figure 4.3: The integrated signal is shown to decrease as the vertical axis of IR laser is scanned across the probe beam, the probe beam is not moved to avoid changing the TOF of the molecules. Increased time delays between the probe and IR laser decreases the magnitude of the Stark shift, allowing greater accuracy when locating the optimum overlap.

ionisiation by the probe beam in the time-of-flight mass spectrometer, the molecular ions are repelled by a 100 V electrode and enter a field-free drift region and impact onto the MCP where the induced velocity change can be recorded. We assume the velocity of the neutral molecules is equal to the velocity of the ions. The maximum excess kinetic energy which could be transferred to the ion during ionisation is 2.2 m s^{-1}(see section 2.3.1). During ionization, electrons are preferentially ejected along the probe laser polarisation axis, which is vertical (along y) and perpendicular to the molecular beam axis. An increase of 2.2 m s^{-1} in the y direction yields a negligible change in molecular time-of-flight, minimising the effects of excess kinetic energy from the ionization process. The voltages on the plates in the mass spectrometer determine its sensitivity to velocity changes. Using lower voltages will mean the molecules are in the drift region for longer and can spread out more increasing the arrival time between faster and slower molecules. Lower voltages also mean the molecules are more susceptible to stray electric fields at the electrodes, which may artificially alter the TOF signal. The MCP is connected directly to the oscilloscope which in turn is connected using a GPIB interface to a computer where the oscilloscope traces can be recorded using Labview software. Each trace or TOF mass spectra is collected and averaged over 1200 laser shots.

4.2.2 Optimum alignment between the probe and IR beam

During the experiments the dye laser will sample the molecules after they have interacted with the nonresonant laser field. It is critical to the success of the experiment that the probe and IR beams be parallel and initially spatially overlapped. To achieve the initial alignment, the beams are aligned using a series of pin holes. After this procedure, the focussed beams are generally within 200 μm of each other. At this point the AC Stark shift from the nonresonant laser field is used as it will shift the energy levels of CS_2 out of resonance with the probe beam. This causes a drop in integrated ion signal and the magnitude of the decrease is proportional to the intensity of the IR field. If we neglect molecule alignment, the magnitude of the shift in the ground state is

$$V(r,t) = -\frac{1}{4}\alpha E^2(r,t). \tag{4.2}$$

To obtain optimum overlap between the two laser beams the integrated ion signal is minimized. By plotting the integrated ion signal in the x, y and z directions as the IR beam is scanned across the probe beam, it is possible to overlap the laser foci to within ± 2 μm. Shown in figure 4.3, using larger IR fields initially, the integrated ion signal is recorded as the IR focus is scanned in the y direction. As the overlap becomes known (black curve), the probe and IR beams are moved temporally out of synchronization to reduce the sensitivity to the Stark shift (red, blue and green curves). The scan is repeated iteratively to locate the centre of the focus. The off-centre troughs in figure 4.3 are most likely due to backlash on the translation stage as each successive scan is recorded. The shape and smoothness of the curves in figure 4.3 indicate the quality of the IR laser focus. A good quality Gaussian beam is required in dipole force experiments because the measured force is proportional to the spatial gradient of the intensity distribution and irregular or sharp potentials mean a Gaussian form of $I(r)$ cannot be assumed. Diffraction rings can present themselves in good quality laser foci and can have large spatial gradients. Care was taken to make sure the overlap was centred on the central spot and not on a diffraction ring. In figure 4.3 the probe beam has a waist radius $e^{-2} = 5$ μm, compared to the nonresonant field with $e^{-2} = 20$ μm. It is important to have a probe beam with a smaller waist radius in order to have the resolution to spatially map out the IR focus.

4.2.3 Procedure

To record the induced velocity shift applied to the molecules, the IR laser is moved along the x axis relative to the probe beam. The centre of the IR probe beam overlap defines the origin of the xy plane. To avoid a decrease in ion signal caused by the IR beam Stark shifting the molecules out of resonance, the probe beam is delayed by 70 ns. The delay means molecules perturbed by the IR field will have travelled past the

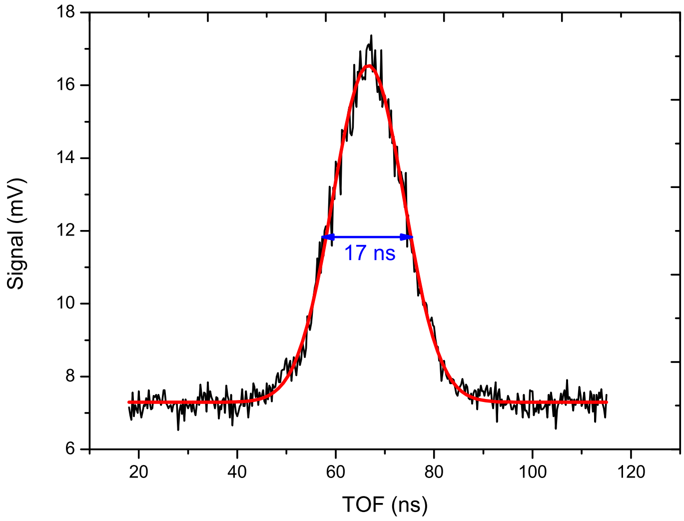

Figure 4.4: The TOF spectra of CS_2 as recorded at the oscilloscope. The translational temperature T_t of the beam is well approximated by the Gaussian FWHM width, which is 17 ns corresponding to a velocity width of 42 m s^{-1}, yielding T_t= 2.9±0.1 K.

probe beam by the time the probe beam fires. Consequently, the IR beam is moved up stream by an amount $\bar{x}_0 = vt$, where $\bar{x}_0$ is the new IR beam position, v and t are the velocity of the beam and the IR-probe beam time delay respectively. By moving the IR beam in a straight line through its new position $\bar{x}_0$, the probe beam focus, which has a smaller waist radius, will sample the induced dipole force imparted to the molecules as a function of position. The induced velocity change of the ground state molecules was recorded by incrementally increasing x through $\bar{x}_0$ along the x axis in one direction to avoid backlash on the translation stage. The $\lambda/4$ wave-plate was used to switch between LPL and CPL to record both TOF traces at each increment of x. This process was repeated three times to improve the accuracy of the results.

Figure 4.4 shows the TOF velocity profile of the 4 % CS_2 beam with no IR beam present, a Gaussian fit determines a translational temperature of 2.9 ± 0.1 K. All changes in TOF were compared against the unperturbed TOF in order to calculate the difference in TOF. This difference is later converted to an induced velocity change using the dispersion ratio calculated by Simion (see Chapter 2).

4.3 Results

Figure 4.5 shows the TOF spectra measured near $\bar{x}_0 \pm 10$ μm, these are positions of maximum dipole force for LPL (blue) and CPL (red). The reference TOF spectra is also shown (black). In figure 4.5 a), the TOF spectra were recorded at $\bar{x}_0 - 10$ μm where acceleration of the CS_2 molecules is clearly seen in the TOF spectra. Both

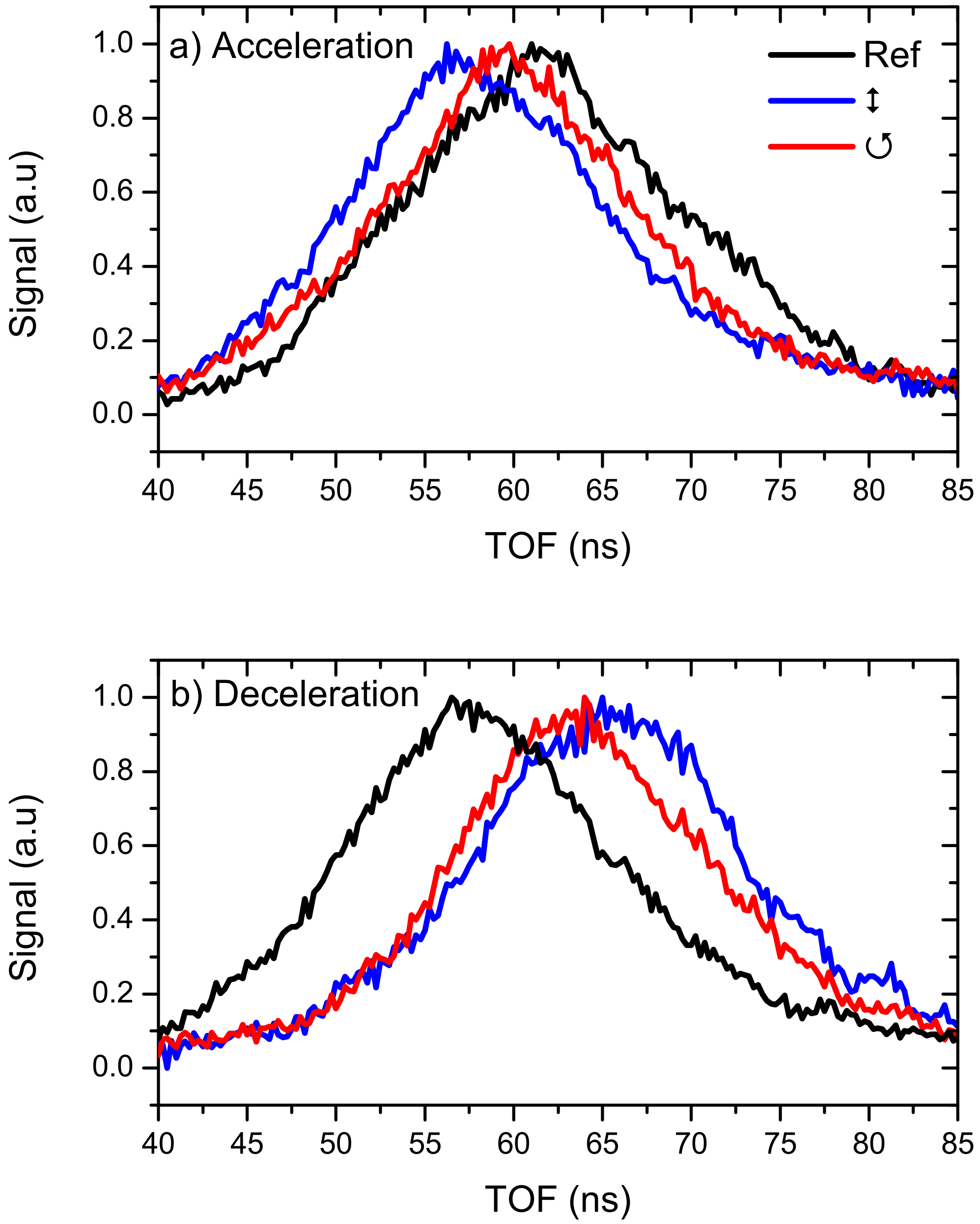

Figure 4.5: The acceleration a) and deceleration b) induced in CS_2 by the nonresonant field is shown for linearly (blue) and circularly (red) polarised light. Each trace has been normalized separately. The reference trace (black) shows the TOF when no IR field is present. In a), traces to the left of the reference trace have been accelerated and arrive earlier at the TOF mass spectrometer, similarly in b), traces to the right of the reference trace have been decelerated. In a), the velocity changes are 9.5 m s^{-1} and 5.0 m s^{-1} whilst for the deceleration shown in b), the changes are 10.6 m s^{-1} and 8.6. m s^{-1}.

LPL and CPL TOF spectra arrive earlier at the mass spectrometer compared to the reference trace. Also obvious is the difference in arrival time between LPL and CPL, indicating the dipole force is greater for linearly polarised light. In figure 4.5 b), $\bar{x}_0 + 10$ μm and the molecules are decelerated as they are traveling away from the molecular lens. This is shown by the TOF for LPL and CPL arriving at a later time compared to the reference trace. Again there is a noticeable difference between the arrival times of LPL and CPL. Figures 4.5 a) and b) were recorded at different times and using different voltages on the TOFMS, b) shows a larger difference in TOF compared to a), where the TOFMS voltage was 70 V compared with 100 V for a). To calculate the induced velocity change, the dispersion ratio for the TOFMS is used to convert TOF into changes in velocity. For the voltages given, the values are 0.4 ns/(m s^{-1}) and 0.7 ns/(m s^{-1}) for the 100 V and 70 V settings. Using these ratios and using the centre of each spectra (obtained using a Gaussian fit) to obtain the TOF, the recorded velocity change for LPL and CPL was 9.5 m s^{-1} and 5.0 m s^{-1} for acceleration, whilst in deceleration values of 10.6 m s^{-1} and 8.6 m s^{-1} were recorded. These quoted figures for CPL have been corrected for the drop in IR intensity of 6 % by increasing the velocity shift by 6 %. Although the dipole force is not directly proportional to $\nabla I(r)$ because of the $\bar{\alpha}_{L,C}(I)$ term, it is reasonable to multiply the shift by 1.06 at this moment to initially determine the velocity change from figure 4.5. The velocity change in deceleration is slightly higher because the molecules spend longer in the lens as they are being slowed.

The induced velocity change for each TOF spectra, in the region of $\bar{x}_0$ using LPL and CPL is plotted in figure 4.6 a). The experiment was repeated three times and averaged, with the error bars resulting from the average difference between successive scans at each x position. Figure 4.6 a) firstly shows the dispersion shape which is equal to the first derivative of a Gaussian spatial profile and typical of a molecular lens[59, 188]. Secondly, linearly polarised light (blue circles) clearly exerts a greater dipole force than circularly polarised light (red circles). The data for circularly polarised light has not been corrected for the 6 % drop in intensity caused by the Fresnel loss at the dichroic mirror. The solid lines are theoretical fits to the data and are calculated as follows. The induced velocity shift depends strongly on the intensity of the laser field and on the rotational temperature of the molecules. The intensity of the IR beam was measured using a CCD camera and a fast photodiode yielding intensities of $(7.6 \pm 2.3) \times 10^{11}$ W cm^{-2} for LPL and $(7.1 \pm 2.2) \times 10^{11}$ W cm^{-2} for CPL. We reduce the uncertainty in intensity by repeating the experiment using the 25 % CS_2 beam. Under these conditions the rotational temperature is sufficiently high that no alignment is observed. This is shown in figure 4.6 b), where linearly polarised light (blue circles) and circularly polarised light (red circles) have no clear difference in dipole force. From figure 4.6 b), the averaged shift in the dipole force is 7.5 m s^{-1}. Using equation 3.29 from the previous chapter, a fitted curve based on the average

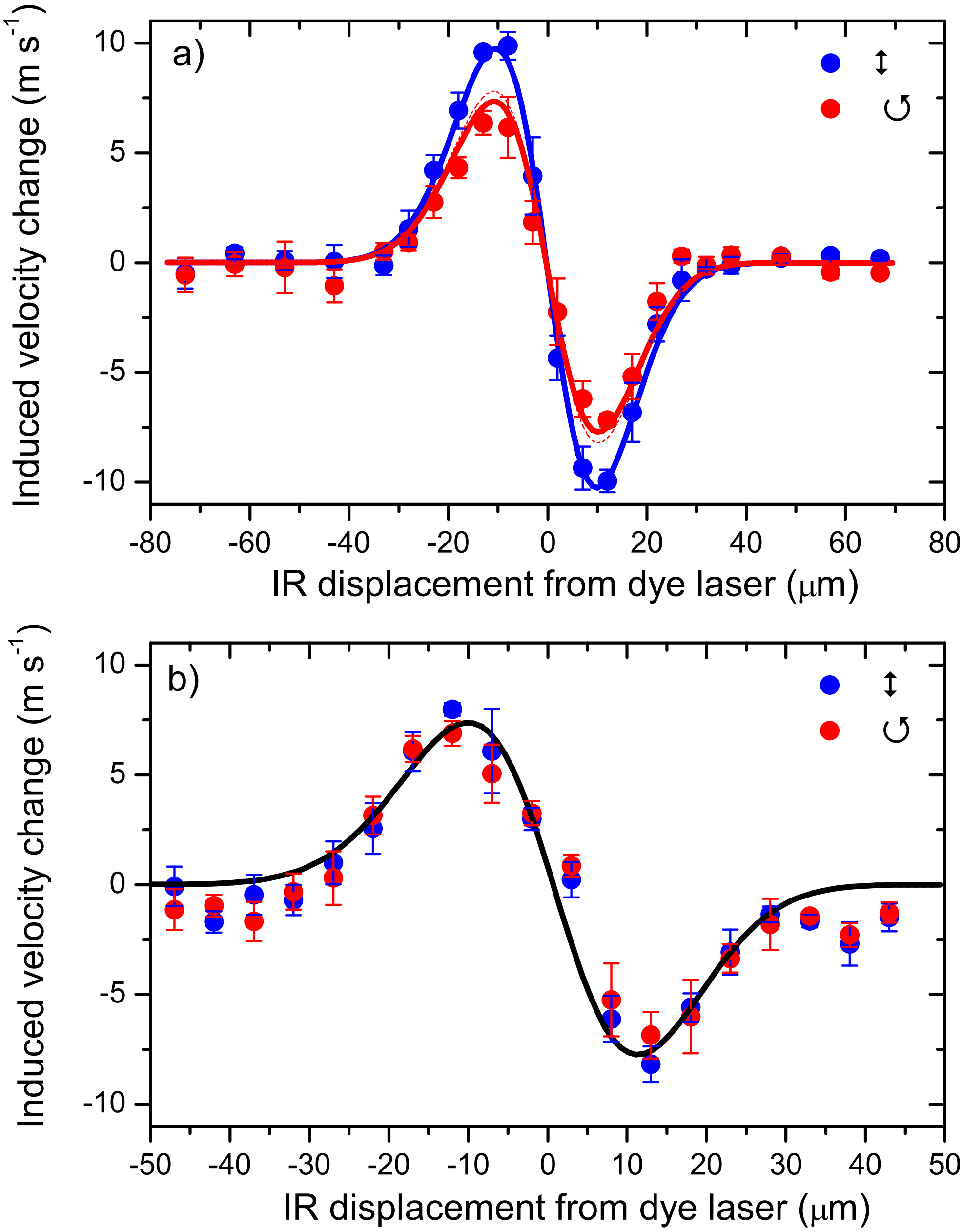

Figure 4.6: a) The difference in each TOF spectra is plotted as a function of position in the x direction through the IR focus using the 5 % CS_2 beam. The solid lines are fits based on a rotational temperature of 35 K with $I_0 = 5.7 \pm 0.3 \times 10^{11}$ W cm^{-2} and $I_0 = 5.4 \pm 0.3 \times 10^{11}$ W cm^{-2} for LPL and CPL respectively (see text). b) Under the same experimental conditions the experiment was repeated but using the 25 % CS_2 molecular beam, the solid line is a fit based on α_{ave}. For both a) and b) the induced velocity changes for LPL (blue) and CPL (red) were recorded and averaged over three scans.

polarisability of CS_2 with $\alpha_{ave} = 9.73 \times 10^{-40}$ C m^2 V^{-1} and $\frac{d\bar{\alpha}_{L,C}}{dI} = 0$, produces an intensity of $(5.7 \pm 0.3) \times 10^{11}$ W cm^{-2} and $5.4 \pm 0.3 \times 10^{11}$ W cm^{-2} for LPL and CPL respectively. Both intensities are within the experimental error of the intensity measurements made using the CCD and photodiode.

With the uncertainty in intensity reduced to ±5 %, the fit to the LPL and CPL data points in figure 4.6 a) is achieved by holding the alignment-dependent dipole force equation at the new intensity and varying the rotational temperature. This produces a best fit of 35 K, the fitting range and uncertainty in intensity mean the temperature could be as low as 33 K or as high as 45 K. The solid lines in figure 4.6 a) show the numerical model based on this temperature and for the intensity of each respective polarisation. Also shown on figure 4.6 a) is a dashed line (red) which shows the induced velocity change if the LPL and CPL beams had equal intensities. As this dashed curve is separated quite clearly from the LPL curve, this shows there is a clear difference in dipole force between LPL and CPL purely due to molecular alignment.

Using the solid curves, the maximum change in velocity imparted onto the molecules is 9.8 m s^{-1} and 7.3 m s^{-1} in acceleration and 10.0 m s^{-1} and 7.6 m s^{-1} in deceleration. The corresponding effective polarisability at 35 K is 11.4×10^{-40} C m^2 V^{-1} with $\langle \cos^2 \theta_l \rangle = 0.49$ for linearly polarised light and 10.1×10^{-40} C m^2 V^{-1} with $\langle \cos^2 \theta_c \rangle = 0.28$ for circularly polarised light. The average polarisability of a linear molecule that is not aligned by the field is 9.7×10^{-40} C m^2 V^{-1} with $\langle \cos^2 \theta_{l,c} \rangle = \frac{1}{3}$. The well depths of the optical Stark potential for the linearly and circularly polarised fields are 89 K and 74 K respectively. This produces a 25 % change in the dipole force and a 20 % change for equal beam intensities. Additionally, because the effective polarisability is now dependent on the intensity of the laser field, the dipole force is no longer directly proportional to $\nabla I(x)$. This is illustrated by the fact the difference in effective polarisability between the laser polarisations is only 12 %, but this leads to a change in force of 20 %.

The effect of the new $\frac{d\alpha_{L,C}}{dI}$ term in the alignment-dependent dipole force equation increases the rotational temperature, without the term the best fit for the rotational temperature would have been 12 K with limits of 8 and 20 K. Depending on the temperature, the $\frac{d\alpha_{L,C}}{dI}$ term can add an additional ≈10 % to the dipole force, particularly for LPL because it is more sensitive to changes in effective polarisability. The difference in dipole force in figure 4.6 a) is measured to be 25 % and the difference in intensity is 6 %, the change for constant intensity beams is 20 % rather than 19 % because of this additional polarisability term.

4.3.1 Elliptically polarised light

Shown in figure 4.7 is the induced velocity change at $x = -10$ μm, corresponding to an acceleration of the CS_2 molecules. The alignment dependent dipole force is

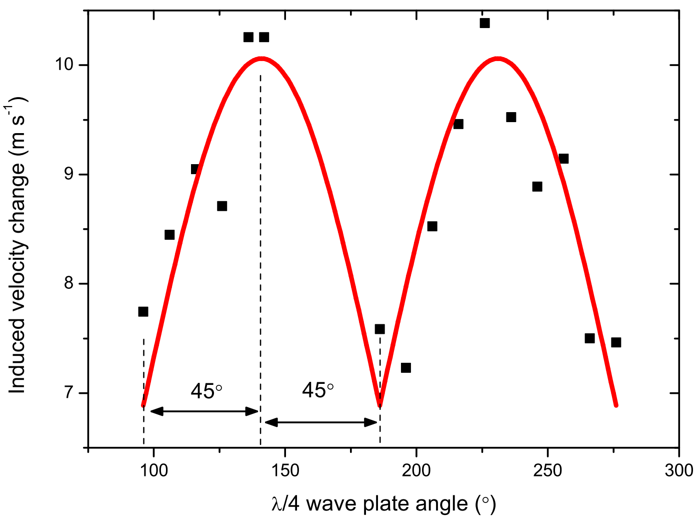

Figure 4.7: The dipole force and its dependence on the $\lambda/4$ wave-plate angle is studied. Molecules at $x = -10\ \mu$m in the IR beam are probed, this position produces maximum acceleration. The induced velocity changes are recorded as the $\lambda/4$ wave-plate is used to change from circularly to elliptically to linearly polarised light. The solid curve is a calculated approximate form of the effective polarisability as function of wave-plate angle.

plotted against the quarter wave-plate angle. CPL occurs at 96°, 186°, and 276° and LPL occurs at 141° and 231°. The solid curve shows the induced velocity change for elliptically polarised light. This was calculated by assuming complete alignment of the molecule and field for elliptically polarised light[148] to reach an expression for the effective polarisability which depends only on the angle of the wave-plate. The magnitude of the calculated $\bar{\alpha}_{eff}$ curve was then reduced to match the induced velocity change as measured in the experiment. This fitting procedure is a good approximation of the dipole force behavior for elliptically polarised light, negating the need to calculate the exact $\langle\cos^2\theta\rangle_{J,M}$ values for varying ellipticity of the light field. Two cycles of circularly to linearly to circularly polarised light are shown. Overall there is good agreement in the data except for the points around $\theta \approx 150° - 175°$ where four successive bad data points, caused by an instability in the experiment were removed.

4.3.2 Molecular lens

Although we have measured the induced velocity along the molecular beam direction in figure 4.6, the same forces are also produced in the radial direction in the xy plane. The force in the y direction acts as a cylindrical lens for the molecules[148, 188, 77, 60]. This lens is different to a conventional optical lens because it is only turned on for a

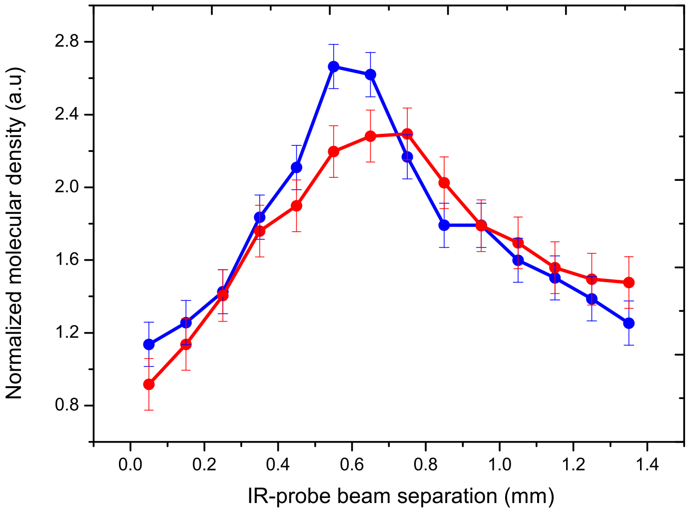

Figure 4.8: Molecular density in the focal region of the molecular optical lens. The downstream density along the x axis is determined by integrating the ionisation signal as a function of distance between IR and probe beam. Linearly polarised light (blue circles) produces a molecular optical lens with a focal length of ∼600 μm whilst circularly polarised light (red circles) has a focal length of ∼700 μm.

short time (15 ns), and therefore only molecules that are initially in the field during the pulse will be focussed. As a larger force is created for LPL, we expect the molecular lens will have a shorter focal length compared to CPL. To verify this, the relative density of molecules as they are focussed downstream along the x axis is measured for both polarisations. This is done by integrating the TOF signal, and normalizing it to the background ion signal with no IR beam present. The results are shown in figure 4.8 and plot the density as a function of the distance between the centre of IR focus and the probe beam. For each IR-probe beam separation, the temporal delay between the firing of IR and probe laser is adjusted to maximize the measured density. The distance between the center of the IR beam and probe beam where the peak molecular density occurs is defined to be the focal length of the molecular lens. Figure 4.8 indicates that a shorter focal length of ∼600 μm is produced for LPL and ∼700 μm for CPL. As the focal length is shorter for LPL, one would expect a smaller molecular focus and therefore a higher density. This effect can be seen in figure 4.8 where the peak density, normalized to the background gas density, is 21 % larger for LPL compared to CPL, indicating that the focussed molecule spot size is smaller by approximately the same amount.

In this experiment it is difficult to separate the effect of using a slightly lower intensity beam for LPL because the induced velocity change is not being measured directly. From figure 4.6 we know the difference in dipole force to be 20 %, and can reasonably assume the majority of the difference in focal lengths between LPL and CPL is due to alignment effects. This would mean we estimate the separation in focal lengths between the laser polarisations to be slightly less than ∼100 μm.

The rotational temperature and the dipole force

The rotational temperature in the 4 % CS_2 molecular beam has been estimated to be between 33 K and 45 K. In Chapter 2 the rotational temperature was calculated spectroscopically and was estimated to be 10 K and 20 K for the 4 % and 25 % CS_2 mixtures respectively. When the dipole force was measured using the 25 % molecular beam, no alignment was observed. By simulating the LPL and CPL induced velocity changes based on the alignment-dependent dipole force equation, the temperature where the separation in velocity change between the polarisations becomes unresolved is ∼60 K. This means the temperature for the 25 % beam is estimated to be atleast ∼60 K using the dipole force method. Given the assumptions in the spectroscopic estimates, when T_R is calculated spectroscopically and compared to the dipole force estimates for temperature, we conclude the spectroscopic values are unprecise.

4.4 Dipole force applied to vibrating molecules

All of the molecules considered so far have been in their ground electronic and vibrational ground state. A vibrating molecule in an electric field can change the magnitude of the induced Stark shift[201, 202, 203, 204] because the averaged geometry of the nuclear motions can change the components of the polarisability tensor. The effect of vibrations on the AC Stark shift should be examined because vibrational cooling is inefficient in supersonic expansions and molecules in the beam may remain vibrationally active and exhibit different behaviour compared to ground state molecules, introducing additional abberations into a molecular lens.

The vibrational temperature of the beam is described in section 2.4.5 and in table 2.5 of chapter 2. The vibrational temperature is calculated to be 298±7 K for the 25 % CS_2 molecular beam. From the strength of the 2^1_1 transition measured in Chapter 2 in figure 2.15 for both 25 % and 4 % mixtures of CS_2, the fraction of molecules in the $\nu_2 = 1$ bending state is calculated to be 22.6 % and 15.4 % respectively. In an experiment identical to measuring the alignment-dependent dipole force, the acceleration and deceleration of the ground state can be compared with the bending mode in CS_2. By using the 25 % CS_2 beam the dynamics are simplified as α_{ave} can be used to describe the molecule's polarisability. The signal strength of the 4 % beam was too low to allow an alignment-dependent dipole force study of the vibrational molecules. The theory required to describe the vibrational polarisability and the AC Stark interaction is beyond the scope of this thesis and a qualitative discussion on

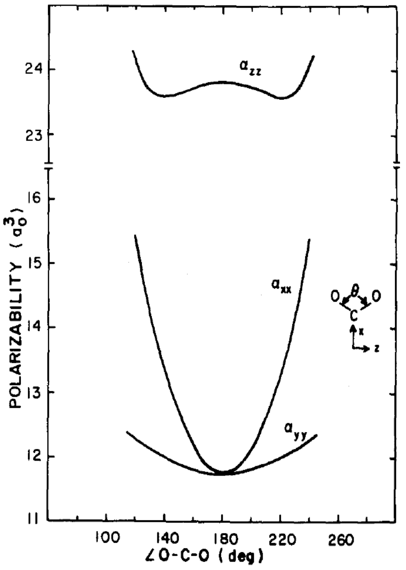

Figure 4.9: This image was taken from [205] and shows how the molecular polarisability components of the molecular polarisability tensor vary as the bond angle θ is changed for CO_2 in free space. As the angle is increased the body fixed polarisability components α_{yy} and α_{xx} are no longer equal because the molecule is being stretched into the x direction increasing the α_{xx} component. The field-free geometry of the molecule is $\theta = 180°$.

why the polarisability should be different is presented.

4.4.1 Theory

The fundamental vibrations of a triatomic molecule consist of the asymmetric stretch ν_3, symmetric stretch ν_1, and the degenerate bend ν_2. Each mode is characterized by a normal coordinate q_a, q_s and q_b[160]. As the normal coordinate is varied the polarisability components of the polarisability tensor of the molecule change because the geometry is being distorted, this is caused through vibrations or deformation by an electric field. Artificially changing the bond length or angle of a linear triatomic molecule and calculating how each component of the polarisability tensor changes with respect to the bond geometry has been performed for CO_2 by Morrison *et al.*[205]. Shown in figure 4.9 is Fig. 4 from reference [205] to illustrate how the polarisability components of a triatomic molecule change with bond angle. Morrison *et al.* also calculates the polarisability components under the symmetric and asymmetric stretch geometries.

Figure 4.9 shows how the bending angle of CO_2 in free space changes the polarisability components of the polarisability tensor. As the molecule bends, the parallel components (α_{xx} and α_{yy}) of the polarisability tensor are no longer equal and the molecule becomes an asymmetric top since $\alpha_{xx} \neq \alpha_{yy} \neq \alpha_{zz}$. If the polarisability change was large enough it would alter the induced dipole moment created by a non-resonant field, and also change the alignment dynamics if the molecular beam were sufficiently cold.

The vibrational motion of a particular mode can be approximated to be uncoupled from the other vibrational motions allowing us to express the total vibrational wave function as a product of the three modes of vibration

$$\mid \psi\rangle = \mid s, n\rangle \mid b, n\rangle \mid a, n\rangle, \tag{4.3}$$

where s, b and a refer to the symmetric stretch, bending and asymmetric stretch modes and n is the vibrational quantum number. The expectation value of the bending mode wave function is required to find the new equilibrium angle of the molecule. This expectation value can subsequently be read from a figure similar to figure 4.9 for CS_2 in order to find the required polarisability components. This has been achieved for CO_2 in the bending mode and in the asymmetric stretch[206], experimental evidence of a vibrational-state-dependent polarisability in CO_2 has also been produced through laser Stark spectroscopy[207]. Unfortunately for CS_2, no vibrational state specific calculations have been performed to determine how the bending mode affects the polarisability components. Determination of the vibrational contribution to the molecular polarisability components is often only calculated to first order in the vibrational ground state, corresponding to the zero point energy of the vibrational state. This is a vibrational correction to the polarisability when it is calculated from the electronic wave function and is generally a few percent[208, 209, 210] of the electronic polarisability. In some cases it is higher, such as lithium hydride (LiH)[211] and CHF_3[212] where the zero point vibrational contribution is calculated to be 10 % and 25 % of the total polarisability respectively. A thorough review of vibrating molecules and polarisability is presented by Bishop[202].

Field-free expression for vibrational polarisability

The static polarisability of a molecule can be expanded in a Taylor series about the equilibrium position[206]

$$\alpha(q) = \alpha_e + \alpha'(q_e)\Delta q + \frac{1}{2}\alpha''(q_e)(\Delta q^2) + \cdots \tag{4.4}$$

where $\alpha(q)$ is a polarisability component along the molecular axis xyz. The first and second polarisability derivatives[130], evaluated at the equilibrium position are labeled α' and α''. The electronic polarisability is labeled α_e and q is the normal coordinate of the vibrational mode. The contribution from each vibrational mode to the static polarisability is

$$\alpha(q) = \alpha_e + \alpha'_s q_s + \frac{1}{2}\alpha''_b q_b^2 + \frac{1}{2}\alpha''_a q_a^2 + \cdots \tag{4.5}$$

There is no first derivative of the bending and asymmetry modes[205] at the equilibrium position as the polarisability components are symmetrical about the origin. To proceed, the expectation value of the normal coordinate for the bending mode and relevant zero point corrections must calculated. The equation for the polarisability of the bending mode in CS$_2$ becomes

$$\alpha^{xx}_{010} = \alpha_e + \alpha''_b \frac{1}{2} \langle\, b, 1 \,|q^2_b|\, b, 1 \,\rangle + \alpha''_a \frac{1}{2} \langle\, a, 0 \,|q^2_a|\, a, 0 \,\rangle. \tag{4.6}$$

The subscript in α^{xx}_{010} refers to the quantum numbers of symmetric stretch, bending, and asymmetric stretch. The superscripts are the directions of the field and polarisability. Equation 4.6 includes the zero point correction from the asymmetric stretch mode. There is no zero point correction for the symmetric stretch because its expectation value is the equilibrium position. Expansion of the polarisability about the equilibrium position is useful because often the full polarisability curves shown in figure 4.9 for each mode of vibration are not known. More frequently, the first and second static polarisability equilibrium derivatives are available, as they are related to the line strengths of vibrational transitions[213, 214].

There is a problem with the procedure outlined above in that the molecule is in a strong field and consequently is not vibrating as it would in free space, thus creating a new averaged geometry and modified polarisability components[209]. The vibrational wave function becomes dependent on the electric field ϵ, such that $|\, \psi\rangle = |\, s, n, \epsilon\rangle |\, b, n, \epsilon\rangle |\, a, n, \epsilon\rangle$ should be used in evaluating the expectation value.

The vibrational polarisability of CS$_2$

Information regarding the bending mode of carbon disulphide and the contributing vibrational state polarisability is not available. The static parallel and perpendicular polarisabilities already evaluated for the 020 bending mode of CO$_2$ has two values because the parallel component of the polarisability of CO$_2$ is negative in the theoretical calculation[206] but positive when measured experimentally[207]. Both studies show that the average polarisability is increased for a positive or negative change to α_{zz}, as the $\alpha_{xx,yy}$ components are also increased. Combined with an examination of figure 4.9, in the experiment we should expect the polarisability to be greater for the vibrational state.

Dipole force

The experiment used to measure the difference in polarisability between the ground and $\nu_2 = 1$ state is identical to the experiment used to measure the alignment-dependent dipole force. A focussed nonresonant beam is used to induce acceleration and deceleration of the CS$_2$ molecules along the molecular beam axis. The first approximation was to assume the AC Stark shift experienced by a ground state molecule in a nonresonant field is the same as that of the bent molecule, such that it is only the polarisability between the states that is different. The dipole force equation along the x axis with the ground state and vibrational polarisability $\alpha_{ave}^{0,\nu}$, is

$$F(x,t) = -\frac{2g(t)x\alpha_{ave}^{0,\nu} I_0}{\varepsilon_0 c\omega^2} \exp\left(\frac{-2x^{-2}}{\omega^2}\right), \tag{4.7}$$

where ε_0 is the permittivity of free space, c is the speed of light, $g(t)$ is the laser pulse envelope and I_0 is peak intensity of the field. The average polarisability of each state is

$$\begin{aligned} \alpha_{ave}^{0} &= \frac{1}{3}\left(\alpha_{||} + 2\alpha_{\perp}\right), \\ \alpha_{ave}^{\nu} &= \frac{1}{3}\left(\alpha_{xx} + \alpha_{yy} + \alpha_{zz}\right). \end{aligned} \tag{4.8}$$

with $\alpha_{||} = \alpha_{zz}$ and $\alpha_{\perp} = \alpha_{xx} = \alpha_{yy}$ for linear molecules. We use the average polarisability because no molecular alignment was observed with 25 % CS_2.

4.4.2 Experiment

Method

In order to probe the molecules perturbed by the IR focus, the IR beam was moved in the x direction relative to the REMPI probe beam and the wavelength was switched to be in resonance with the 0_0^0 or 2_1^1 transition. This process was repeated incrementally throughout the length of IR focus along x. The experiment was carried out three times and the data was averaged. Figure 4.10 shows the ground state transition 0_0^0 and the bending to bending 2_1^1 electronic transition. The red bars on figure 4.10 show the ionisation wavelengths $\lambda_1 = 478.650$ nm and $\lambda_2 = 479.180$ nm for the ground and $\nu_2 = 1$ states. Only linearly polarised light was used to provide the IR field, and a slightly higher intensity was used in this experiment compared to the alignment-dependent dipole force experiment. A Gaussian focus of $I_0 = (9.2 \pm 2.3)\times 10^{11}$ W cm^{-2} was calculated by measuring a waist radius with e^{-2} = 15 μm and $g(t) = 15$ ns FWHM.

The TOF spectra recorded at the oscilloscope of the 0_0^0 and 2_1^1 modes are shown in figure 4.11. Each trace was recorded over 1200 laser shots and saved to a computer for analysis. In figure 4.11, the black trace shows molecules ionised with λ_1 producing ions from the 0_0^0 state whilst the red trace shows the signal from the $\nu_2 = 1$ state ionised by λ_2. The horizontal axis of the figure is offset at zero by 9.3 μs which is the drift time of the molecules. The translational temperature T_t was calculated by averaging five traces with the IR field turned off for each state, producing temperatures

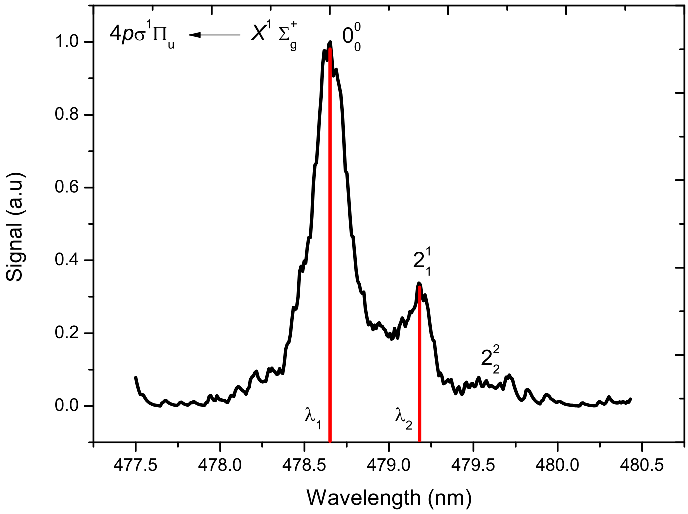

Figure 4.10: The ion signal is recorded as the dye laser is scanned in wavelength around the $\left[\frac{1}{2}\right] np\sigma(^1\prod_u) \leftarrow \tilde{X}^1\sum_g^+ 0_0^0$ transition. The red bars indicate the wavelengths $\lambda_1 = 478.650$ nm and $\lambda_2 = 479.180$ nm of the 0_0^0 and 2_1^1 transitions.

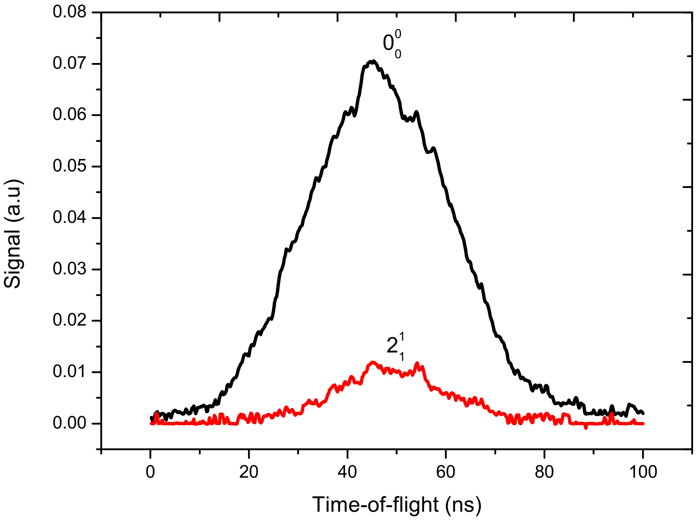

Figure 4.11: The TOF spectra for the ground (black) and $\nu_2 = 1$ (red) states are shown, each trace was averaged over 1200 laser shots. The translational temperature is 12.7±0.9 K and 10.6±0.8 K for the 0_0^0 and 2_1^1 states respectively.

of 12.7±0.9 K and 10.6±0.8 K for the 0_0^0 and 2_1^1 transitions respectively. A higher probe beam intensity was used in order to gather sufficient ions from the ν_2 state. This also increased the already strong signal from the ground state, in this situation ion repulsion in the interaction region is a concern. The ions can repulse each other distorting the TOF spectra altering measurements. However, the T_t of 12.7 K is consistent with previous measurements when using lower probe intensities and the same CS_2 mixture.

Results

Figure 4.12 shows the induced velocity change for both the 0_0^0 (blue) and 2_1^1 (red) transitions as the IR beam is traversed along the x axis. The TOF of the molecules is calculated by fitting a Gaussian line shape with the centre of the distribution being the mean TOF. The change in TOF is calculated by subtracting a reference TOF taken with no IR field present. Both curves show the characteristic acceleration and deceleration induced at the $x = \pm\frac{\omega}{2}$ positions, indicating the general shape of the force when x is varied is described by equation 4.7. The solid lines indicate the simulated curves of the dipole force from equation 4.7 fitted to the data using the α^0_{ave} (blue) and α^ν_{ave} (red). The fitted intensity to both curves is 7.3×10^{11} W cm^{-2}, which is within the experimental error of the photodiode and CCD measurements. Using $\alpha^0_{ave} = 9.7 \times 10^{-40}$ C m^2 V^{-1} to determine I_0, the λ_2 data is fitted by varying α^ν_{ave}, the best fit is $\alpha^\nu_{ave} = (7.7 \pm 2.2) \times 10^{-40}$ C m^2 V^{-1}. The large amount of error arises from the spread of points outside of the IR region which should have a zero velocity shift. Although the same averaging times were used in the alignment-dependent dipole force data, the smaller spot size of the IR focus leads to larger errors. This is because near the centre of the IR field $x = \pm5$ μm, large errors can occur because the induced velocity shift is extremely sensitive to horizontal position. The lack of stability of the experiment is illustrated in the regions were no field is applied, ($x < -30$ μm and $x > 30$ μm), where the induced velocity change should be zero. The $\nu_2 = 1$ state shows the largest scatter in the data. This is most likely to be due to the small signal from the 2_1^1 transition in the TOF spectra. With an experimental value of $\alpha^\nu_{ave} = (7.7 \pm 2.2) \times 10^{-40}$ C m^2 V^{-1}, it is concluded that the errors in this particular experiment, are too large to sufficiently resolve a difference in the polarisability of the bending mode.

Proposed optical lattice experiment

To investigate this effect further but with greater sensitivity, an optical lattice experiment[215, 216, 217] could be used and would offer two advantages; an increased dipole force and a reduction in the time required to carry out the experiment. An optical lattice experiment involves overlapping two counter-propagating laser beams at a small angle to

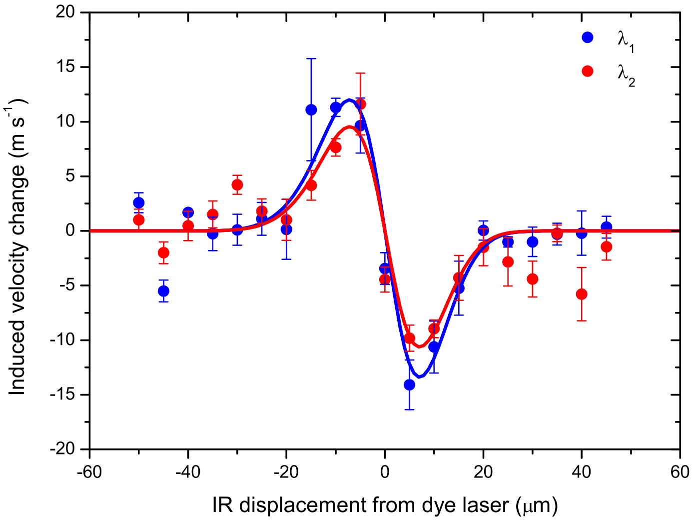

Figure 4.12: The difference in induced velocity of each TOF for both the ground state (blue) and $\nu_2 = 1$ (red) state is shown between subsequent positions along x. The solid lines indicate simulated data with $I_0 = 7.3 \times 10^{11}$ W cm^{-2} with an e^{-2} waist radius of 13 μm. The fitted polarisability of the $\nu_2 = 1$ state is $\alpha^{\nu}_{ave} = (7.7 \pm 2.2) \times 10^{-40}$ C m^2 V^{-1}.

form a standing wave. The molecular beam travels along the direction of the standing wave so the molecules become trapped by the periodic potential. Shown below are the maximum well depths for an optical lattice. Neglecting molecular alignment,

$$\begin{aligned} \text{Single focussed beam :} \quad V_0 &= \frac{\alpha_{ave}}{2\varepsilon_0 c} I_0, \\ \text{Optical lattice :} \quad V_0 &= \frac{2\alpha_{ave}}{\varepsilon_0 c} I_0. \end{aligned} \tag{4.9}$$

The symbols have their usual meanings. The maximum well depth for linearly polarised light using a single focussed Gaussian beam under the conditions described above is 102 K whilst using the same intensity a periodic lattice potential could exert a maximum well depth of 410 K, four times that of a single focussed Gaussian beam. Although the same well-depth could be obtained using a single Gaussian beam by increasing the intensity, the maximum value of I_0 is limited by the ionisation threshold of the molecules[218]. The resulting gradient of the standing wave potential is much greater compared to a focussed Gaussian beam which allows this technique to be much more sensitive to changes in molecular mass or polarisability.

Dong *et al.*[219] shows that by using an optical lattice with a frequency chirp[220], it is possible separate molecular species depending on the mass to polarisability ratio. Of interest are the simulations of CO and N_2 which have the same mass of 28 amu and are indistinguishable in mass spectroscopy. The molecules have a difference in polarisability of only 0.27×10^{-40} C m^2 V^{-1} which is typically on the order of the vibrational contribution to the polarisability[212]. The simulations by Dong *et al.* show that CO and N_2 could be detected and resolved through TOF mass spectrometry. The CO and N_2 signals were separated by 16 m s^{-1}, which is easily resolvable in our TOF mass spectrometer. These simulations show even a small difference in polarisability, which would arise from occupied vibrational states could be detected. Another advantage to the lattice technique is that data can be gathered much faster compared to the acceleration-deceleration experiment used in this thesis. Because the lattice period is too small to be spatially resolved, the whole lattice is sampled at once, decreasing the time over which data is gathered. This is opposed to spatially plotting the dipole force through the IR focus as in used in this thesis (figure 4.12),

4.5 Conclusion

4.5.1 Alignment-dependent dipole force

The centre-of-mass motion and alignment effects are examined in a molecular lens created by a seeded nonresonant IR laser beam. Pendular states of CS_2 are formed in the molecular lens which align with the electric field polarisation vector. The difference in dipole force was measured between linearly and near circularly polarised light. Maximum induced velocity changes of 10 m s^{-1} and 7.5 m s^{-1} respectively were recorded. The corresponding effective polarisability from the fitted rotational temperature of 35 K is 11.4×10^{-40} C m^2 V^{-1} with $\langle\cos^2\theta_l\rangle = 0.49$ for linearly polarised light and 10.1×10^{-40} C m^2 V^{-1} with $\langle\cos^2\theta_c\rangle = 0.28$ for circularly polarised light. The average polarisability of a linear molecule that is not aligned by the field is 9.7×10^{-40} C m^2 V^{-1} with $\langle\cos^2\theta\rangle = \frac{1}{3}$. The well depths of the optical Stark potential for the linearly and circularly polarised fields were 89 K and 74 K respectively. This produces a 25 % change in the dipole force. A 20 % change in dipole force was calculated for equal beam intensities.

The downstream density at the focus of the molecular lens was probed by measuring the ion signal for both laser polarisations. The focal lengths for linearly and circularly polarised light were found to be separated by $\sim$100 μm, although some of this difference in focal length is caused by the 6 % lower intensity for circularly polarised light.

In summary, the dipole force is relatively robust to rotational temperature where even at the relatively high $T_R = 35$ K, a 12 % difference in effective polarisability produced a 20 % difference in force. Additionally, by altering the laser polarisation, the focal length of a molecular lens can be smoothly altered.

4.5.2 Effect of vibrating molecules

In an identical experiment, the dipole force was applied to bent CS_2 molecules and the difference in force was compared between the linear ground state molecules. Using a molecular beam of $T_t \sim 12$ K, consisting of 23 % of $\nu_2 = 1$ molecules and 73 % of ground state molecules, the results showed the $\nu_2 = 1$ state had a lower average polarisability compared to the linear molecule. Despite concerns about error and the intensity dependence of the polarisability in the dipole force equation, the average polarisability of the $\nu_2 = 1$ state was found to have a value of $(7.7 \pm 2.2) \times 10^{-40}$ C m^2 V^{-1}. With this amount of error it is not possible to conclude if there is a difference in the polarisability between the ground state and first vibrational bending mode.

A method with greater experimental accuracy is proposed. An experiment involving an optical lattice would exert a much greater dipole force which would help alleviate the error and stability issues associated with measuring the dipole force in the acceleration and deceleration configuration. The enhanced sensitivity of the measured velocity changes from the optical lattice may be able to resolve very small changes in polarisability arising from occupied vibrational states.

Chapter 5

Effect of rotational states on a molecule focus

5.1 Introduction

The use of intense nonresonant laser fields allows any molecule to be manipulated via the interaction between the field and the molecule's polarisability. As molecular beams reach lower rotational temperatures[156, 155], the influence of a specific rotational quantum state and its individual effective polarisability caused by the quantized internal geometry becomes important. Molecules which have a permanent dipole moment can be manipulated through the use of carefully arranged electrodes called hexapoles. Using the hexapole, individual rotational states in the molecular beam can be spatially separated and experimented upon[50, 221, 51, 222, 223]. This achievement means experiments can be performed on pure samples of rotational quantum states. The goal in this chapter is to examine the effect of separate rotational states on the focussing properties of a molecular lens with typical experimental parameters. Two molecules are studied, CS_2 and the lighter, less polarisable molecule N_2. A comparison is made between these results.

5.2 Method

In this chapter, the influence of the dipole force on separate rotational states is examined numerically in a molecular lens experiment. A schematic of the lens and the molecular trajectories induced by the dipole force is shown in figure 5.1. The molecular beam coming from the left is attracted toward the high field region in the centre. The molecules fly through the IR field but due to the dipole force, converge at a later time to form a molecular focus. The time scales of alignment (ps) and centre-of-mass motion (μs) differ by several orders of magnitude and the internal motion of the molecule is solved separately[76]. The calculated alignment values are then inserted

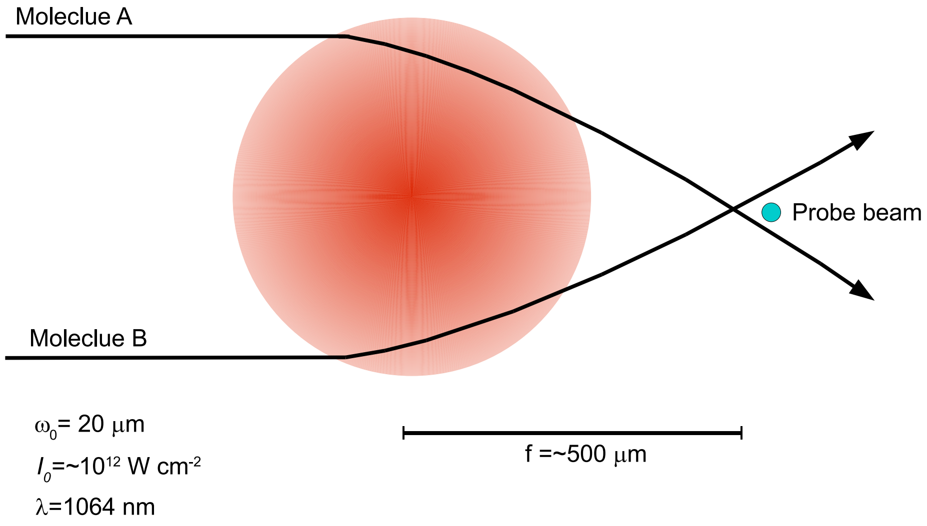

Figure 5.1: A schematic of how a single nonresonant focussed laser beam can be used to focus a molecular beam. The molecules are attracted to the high field region at the centre of the IR focus. They are then deflected causing a molecular focus downstream. Typically the focal length of such a lens is $\sim$500 μm.

into a classical simulation to calculate the trajectories of a group of randomly generated molecules in the plane of the IR focus. The molecules are given a beam velocity and translational temperature T_t, similar to the experiment in Chapter 4.

5.3 Theory

The degree of alignment a particular rotational quantum state $|J, M\rangle$ perturbed by a nonresonant field exhibits, is characterized by the expectation value $\langle\cos^2\theta\rangle_{\tilde{J},M}$, where θ is the angle between the molecular axis and a space fixed axis. The value $\langle\cos^2\theta\rangle_{\tilde{J},M}$ can be evaluated under adiabatic conditions for linearly polarised light by using a superposition of field-free rotor states $|\Psi_{\tilde{J},M}\rangle(t) = \sum_{J,M} C_{J,M}(t)|J, M\rangle$. Solving the time independent Schrödinger equation for the rigid rotor, as shown in Chapter 3, yields the coefficients $C_{J,M}(t)$ of the wave function expansion which allows the expectation value $\langle\cos^2\theta\rangle_{\tilde{J},M}$, to be calculated.

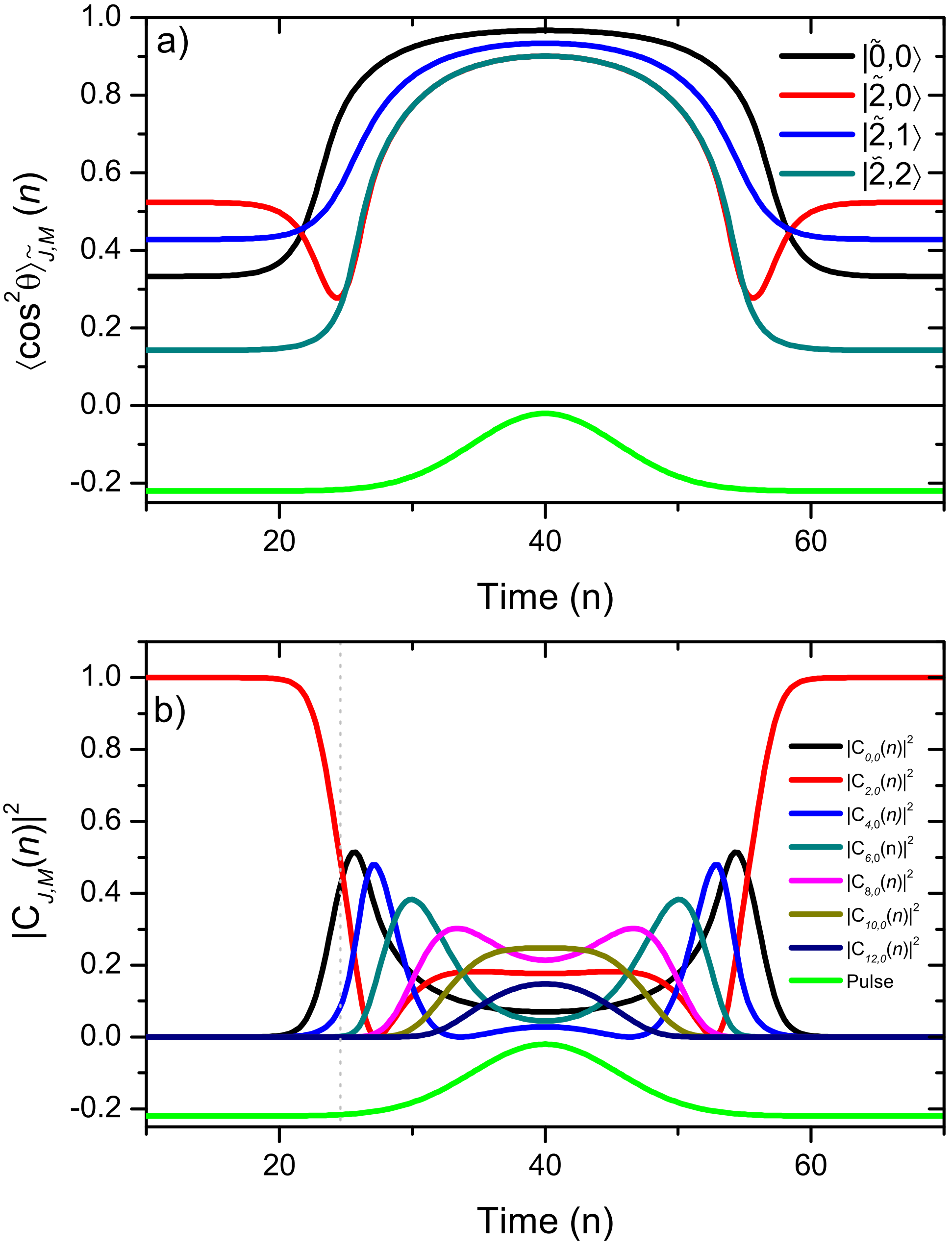

Figure 5.2: a) The expectation value of the $|\tilde{0}, 0\rangle$, $|\tilde{2}, 0\rangle$, $|\tilde{2}, 1\rangle$ and $|\tilde{2}, 2\rangle$ rotational quantum states is shown for a nonresonant pulse of linearly polarised light with $I_0 = 10^{12}$ W cm^{-2}. Individual rotational states have different field-free and field-applied expectation values. The laser pulse (green) is Gaussian with a FWHM width of 0.62 ns centred at $n = 40$, the horizontal axis is in reduced units of $\frac{\hbar}{B}$=49 ps. b) The first seven coefficients of the $\Psi_{\tilde{2},0}(n)$ quantum state are plotted as a function of time.

5.3.1 Properties of $\langle\cos^2\theta\rangle_{\tilde{J},M}$ and $\alpha_{\tilde{J},M}$

Alignment of CS_2

The calculated results for the alignment of the CS_2 molecule in a linearly polarised nonresonant electric field of intensity I_0=10^{12} W cm^{-2}, modulated by a Gaussian pulse of FWHM of 0.62 ns (green) are shown in figure 5.2. The expectation value is plotted against time in dimensionless units for the $|\tilde{0},0\rangle$ (black), $|\tilde{2},0\rangle$ (red), $|\tilde{2},1\rangle$ (blue) and $|\tilde{2},2\rangle$ (dark green) rotational states. The temporal pulse is centered at $n = 40$ in dimensionless units. The figure shows that the rotational states have different expectation values when the field is on and also when the field is off. The expectation value $\langle\cos^2\theta\rangle_{\tilde{J},M}$, can be confirmed in the high field limit through the Hellmann-Feynman theorem[224, 225]. When there is significant angular confinement of the molecular axis to the space fixed axis, the motion is considered to be that of a two-dimensional harmonic oscillator. In this regime, the high-field expectation values are[55, 226, 193]

$$\begin{aligned}\langle\cos^2\theta\rangle_{\tilde{J},M} &= 1-\frac{\tilde{J}+1}{\sqrt{\Delta\omega}} \text{ for } (\tilde{J}-|M|) \text{ even},\\ &= 1-\frac{\tilde{J}}{\sqrt{\Delta\omega}} \text{ for } (\tilde{J}-|M|) \text{ odd},\end{aligned} \tag{5.1}$$

where $\Delta\omega = \frac{\Delta\alpha\varepsilon_0}{4B}$. The high field limits are extremely useful for quick estimates of alignment of different molecules, intensities and rotational states. In figure 5.2 it can be seen the states $|\tilde{2},0\rangle$ and $|\tilde{2},2\rangle$ reach the same value of $\langle\cos^2\theta\rangle_{\tilde{J},M}$, as in the high field limit $\langle\cos^2\theta\rangle_{\tilde{J},M}$ is independent of $|M|$ and depends only on $\tilde{J}$ and the parity of $(\tilde{J}-|M|)$. This approximation breaks down with increasing $\tilde{J}$ due to the potential $V(t)$, becoming comparable to the field-free energy of the molecule. The independence of $|M|$ in the low $\tilde{J}$ states is useful as it simplifies the number of states to be calculated when modeling the downstream density in a molecular focus. Individual $|\tilde{J},M\rangle$ states of a particular $\tilde{J}$ with the same $(\tilde{J}-|M|)$ parity will have the same $\langle\cos^2\theta\rangle_{\tilde{J},M}$ and also $\alpha_{\tilde{J},M}(I)$, in the high field regions of the laser focus.

The drop in expectation value of the $|\tilde{2},0\rangle$ (shown in red in figure 5.2 a)) state, just as the field is turning on is explained by plotting the $|C_{J,M}(n)|^2$ coefficients of the wave function expansion $\Psi_{\tilde{J},M}(n) = \sum_J C_{J,M}(n)|J,M\rangle$. This will allow the contribution from each field-free $|J,M\rangle$ state to $\langle\cos^2\theta\rangle_{\tilde{2},0}(n)$ to be examined. Figure 5.2 b) shows the probabilities of each state $|C_{J,M}(n)|^2$, in the $\Psi_{\tilde{2},0}(n)$ expansion plotted against n. It can be seen the how the field mixes the rotational states and that the states are also symmetrical about $n = 40$, the centre of the IR pulse, indicating adiabatic behaviour. When the field is off, $|C_{2,0}(0)|^2 = 1$ and $J = 2$ $M = 0$ is the only state populated. As the field is switched on, indicated by the vertical grey dotted line which

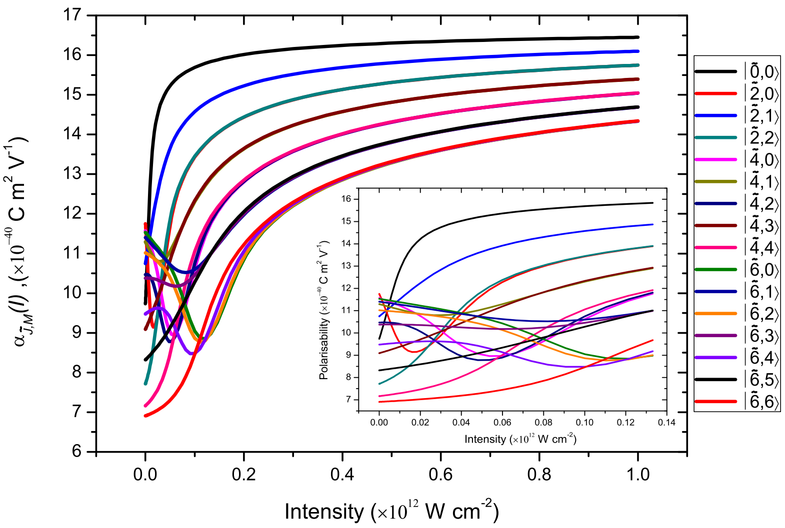

Figure 5.3: The effective polarisability for CS_2 for all quantum states up to $\tilde{J} = 6$ is shown. The effective polarisability quickly rises and then saturates. The inset graph shows the field turn-on region, where the states are only modestly perturbed from their field-free values. Also shown, as predicted by the Hellmann-Feynman theorem, is that states with the same $(\tilde{J} - |M|)$ parity have the same expectation value.

corresponds to an intensity of 2×10^{10} W cm^{-2}, the $\Psi_{\tilde{2},0}(n)$ state at the grey line is made up of three field-free rotational states $|0,0\rangle$ (black), $|2,0\rangle$ (red) and $|4,0\rangle$ (blue). The probabilities are 0.45, 0.45 and 0.1 respectively. The modulus squared of the wave function $|\Psi_{\tilde{2},0}(n)|^2$, can be approximated by equal parts of the $|0,0\rangle$ and $|2,0\rangle$ states. The expectation value of $\langle\cos^2\theta\rangle_{\tilde{2},0}(n)$ is lowered because $\Psi_{\tilde{2},0}(n)$ is taking on the field-free alignment characteristics of the $|0,0\rangle$ state, which has a lower value of $\langle\cos^2\theta\rangle_{0,0}(0) = \frac{1}{3}$ compared to $\langle\cos^2\theta\rangle_{2,0}(0) = 0.524$. This drop in expectation value before reaching the maximum value of $\langle\cos^2\theta\rangle_{\tilde{J},M}(n)$ is common to many rotational states. Of interest is at what intensity does the decrease occur and also how will it affect the motion of the molecules in a molecular lens. For the $|\tilde{2},0\rangle$ state, the decrease in $\langle\cos^2\theta\rangle_{\tilde{2},0}(I)$ occurs at $I_0 = 2 \times 10^{10}$ W cm^{-2}, the corresponding induced velocity shift in the radial direction for CS_2 is < 0.5 m s^{-1}. Thus, for low $\tilde{J}$ states in CS_2, the effects of a decrease in polarisability before the molecule reaches its maximum alignment value is negligible. Higher rotational states such as $|\tilde{14},0\rangle$ have a drop in $\langle\cos^2\theta\rangle_{\tilde{14},0}(I)$ occurring at $I = 4 \times 10^{11}$ W cm^{-2}. However, $\tilde{J} = 14$ has 29 M states and it is likely a feature specific to a particular M state will be smeared out after thermal averaging.

Effective polarisability of individual rotational states, $\alpha_{\tilde{J},M}$

Figure 5.3 shows how the effective polarisability depends on the intensity for the $|\tilde{0},0\rangle$, $|\tilde{2},1\rangle$, $|\tilde{2},0\rangle$ and $|\tilde{2},2\rangle$... up to $|\tilde{6},6\rangle$ rotational states. The polarisability is related to the expectation value by

$$\alpha_{\tilde{J},M}(I) = \left[\Delta\alpha\langle\cos^2\theta\rangle_{\tilde{J},M}(I) + \alpha_\perp\right]. \tag{5.2}$$

Each rotational state has a different $\alpha_{\tilde{J},M}$, and thus when used in a molecular lens will experience a different dipole force. Effective polarisability curves of the same $(\tilde{J}-|M|)$ parity have the same expectation value when the field has sufficient strength to satisfy the strong field approximation in the Hellman-Feynman theorem. The expectation value of the low $\tilde{J}$ states rises very quickly with intensity and saturates around 0.2×10^{11} W cm^{-2}. This means the polarisability will vary very little once the molecule has entered the regions of intensity above this value. Above this threshold is where the centre-of-mass motion begins to take effect and so we would expect the majority of the low $\tilde{J}$ states to have their effective polarisability saturated. The inset graph in figure 5.3 shows the field turn-on region where the Hellmann-Feynman high field expressions are not valid.

Nitrogen

The effective polarisability of nitrogen is shown in figure 5.4 for the first few lowest rotational states. The maximum intensity has been increased to $I_0 = 10^{13}$ W cm^{-2} to account for the lower polarisability of the molecule. The rotational constant is $B = 1.99$ cm^{-1}, with $\alpha_\parallel = 2.44\times10^{-40}$ C m^2 V^{-1} and $\alpha_\perp = 1.63\times10^{-40}$ C m^2 V^{-1}. The average polarisability is $\alpha_{ave} = 1.91\times10^{-40}$ C m^2 V^{-1}. Figure 5.4 is interesting because unlike CS_2, the rotational dynamics are not saturated at the intensities required for centre-of-mass motion induced by the dipole force. In fact, the states are only being modestly perturbed from their field-free values, consequently there is quite a large degree of variation in alignment between the rotational states. This however, is counteracted to some degree by the low polarisability anisotropy ($\Delta\alpha$) of the molecule.

M dependence of molecular alignment

The expectation value of molecules which have the angular momentum quantum number J, can have different expectation values depending on how the molecule is orientated with respect to the field. High $|M|$, ($|M| = J$) means the molecule is rotating in a plane perpendicular to $\mathbf{J}$ and has to move over a greater angular range to meet the z axis. Low $|M|$ states have the molecule rotating in a plane closer to the z axis and so for the same field strength will move closer to the z axis and exhibit greater

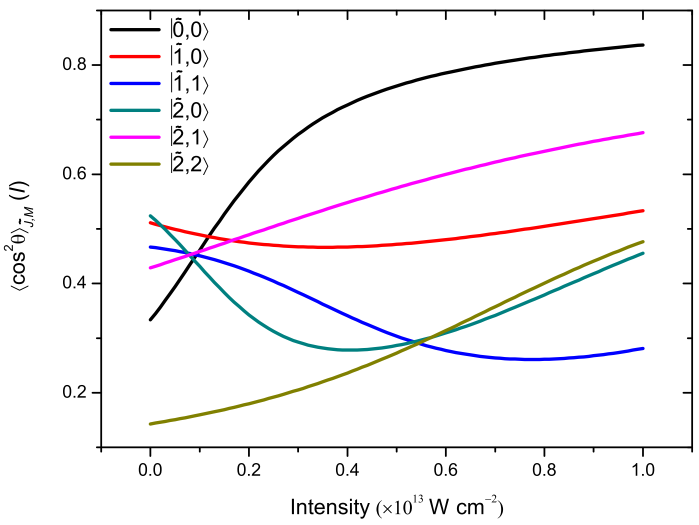

Figure 5.4: The effective polarisability of the $\tilde{J} = 0, 1, 2$ rotational states is shown up to an intensity of 10^{13} W cm^{-2} for molecular nitrogen. Due to the low polarisability of the molecule, and its lower weight, $\langle\cos^2\theta\rangle_{\tilde{J},M}(I)$ and consequently $\alpha_{\tilde{J},M}(I)$ do not saturate at the intensities used in our dipole force experiments. The resulting low field behaviour cannot be approximated using the strong field approximation yielded by the Hellmann-Feynman theorem.

alignment.

5.3.2 Dipole force

As already shown in the previous chapters, an attractive force $F(r,t) = -\nabla V(r,t)$, where $V(r,t)$ is the AC Stark shift, is created by a nonresonant optical pulse. We make a slight distinction that instead of simulating thermally averaged distributions of rotational states $\bar{\alpha}(I)$, the individual field dependent polarisabilities from specific rotational states are used, $\alpha_{\tilde{J},M}(I)$. The force in the radial direction is

$$F(\mathbf{r},t) = -\frac{2\mathbf{r}g(t)I_0}{c\epsilon_0\omega^2}\exp\left(\frac{-2\mathbf{r}^2}{\omega^2}\right)\left[\alpha_{\tilde{J},M}(I) + \frac{d\alpha_{\tilde{J},M}(I)}{dI}\exp\left(\frac{-2\mathbf{r}^2}{\omega^2}\right)\right], \tag{5.3}$$

where ϵ_0 is the permittivity of free space, $\mathbf{r}$ is the radial vector with $\mathbf{r}^2 = \hat{\mathbf{i}}x^2 + \hat{\mathbf{j}}y^2$. The experimentally measured duration of the IR pulse $g(t)$ (from Chapter 2) , is used as the time envelope. There is no z dependence on the laser intensity as in molecular lens experiments, the molecules are probed at $z = 0$ where the peak intensity occurs. The parameters $\frac{d\alpha_{\tilde{J},M}(I)}{dI}$ and $\alpha_{\tilde{J},M}(I)$, are obtained by fitting a curve to the numerically calculated expectation values $\langle\cos^2\theta\rangle_{\tilde{J},M}(I)$, for each quantum state $|\tilde{J}, M\rangle$. Fitting was performed as a function of intensity or as a function of time. The fitting function was a polynomial in intensity space or a multiple Gaussian fit in the time domain.

Typically low $\tilde{J}$ states with high alignment, which saturated rapidly, could only be fitted in the temporal domain using multiple Gaussian fits. For the Gaussian fits it is convenient to convert the temporal dependence to an intensity dependence. Fitting curves in both spaces was obtained using Origin software with a multiple Gaussian fit consisting of five or seven peaks. The polynomial fit varied from 4th to 9th order. Shown below are the equations which convert a fit in time to be dependent on intensity.

$$\begin{aligned}
&t(I) = x + \sqrt{-\sigma^2 \log I}, \\
&\alpha = \alpha_\perp + \Delta\alpha \sum_j \frac{A_j}{C\rho_j} \exp\left[\frac{-2(t(I) - \tau_j)^2}{\rho_j^2}\right], \\
&\frac{d\alpha}{dI} = \Delta\alpha \sum_j \frac{2A_j\sigma(t(I) - \tau_j)}{CI\rho_j^3\sqrt{-\log I}} \exp\left[\frac{-2(t(I) - \tau_j)^2}{\rho_j^2}\right],
\end{aligned} \tag{5.4}$$

where I is the fractional intensity ranging between 0 and 1 with units $I \times 10^{12}$ W cm^{-2}. The summation over j, accounts for multiple Gaussian functions used in fitting the effective polarisability in the x timescale, with widths ρ_j, normalization constants, A_j, and offsets, τ_j. Additionally, $C = \sqrt{\pi/2}$. The time variable, t, in the scale in which the expectation values were calculated is now defined in terms of I which can be modulated on the time scale of the centre-mass-motion $g(t)$. The polynomial fit of the effective polarisability is already in intensity space and has the form

$$\alpha_{J,M}(I) = \alpha^0_{\tilde{J},M} + \sum_j C_j I^j, \tag{5.5}$$

where $\alpha^0_{\tilde{J},M}$ is the field-free expectation value of a specific quantum state, the derivative is simply

$$\frac{d\alpha_{\tilde{J},M}}{dI} = \sum_j j\ C_j I^{j-1}. \tag{5.6}$$

Typically the agreement between the fitted curve and the calculated values for the effective polarisability and its derivative as a function of intensity was less than 1%.

5.3.3 Implementation

The focussing properties of the molecular lens were simulated by 750 000 randomly generated particles in an area of 120 μm × 120 μm encompassing the focussed beam of $\omega = 20$ μm for CS_2 and $\omega = 30$ μm for N_2. Classical simulation of the molecular trajectories is appropriate because the de Broglie wavelength of the molecules is much less than the dimensions of the laser focus[54, 76]. The equations of motion for acceleration and position were solved for the ith particle in the x and y directions using the alignment-dependent dipole force in equation 5.3.

$$\frac{dv_i(x,t)}{dt} = \frac{F_i^x(x,t)}{m} \tag{5.7}$$

where v_i is the velocity of the ith particle. By solving equation 5.7 at each spatial location in the optical field the velocity can be found, whilst the position of the molecule is found by solving the equation

$$v_i(x,t) = \frac{dx_i}{dt}. \tag{5.8}$$

The particles were given an initial velocity of 540 m s^{-1} which is similar to the velocity of the CS_2 molecular beam measured in Chapter 2. A thermal velocity distribution along the molecular beam axis x, of 3 K is also included. The initial position and velocity of the particle provides the initial conditions of the ODE solver. The particles are propagated by solving the differential equations over the duration of the laser pulse. Once the laser pulse has passed, each particle is propagated downstream by the relation $d_{x,y} = v_{x,y}t$, where $d_{x,y}$ is the x or y component of the molecule's trajectory after passing through the lens.

The nitrogen simulations were carried out under optimum conditions which mean the molecular beam was apertured such that $-\frac{\omega}{2} \leq y \leq \frac{\omega}{2}$. This has the effect of only using the region in the molecular lens where the force applied to the molecules in the y direction is approximately linear with the molecule's distance from the centre of the lens. In the N_2 simulations a translational temperature of 3 K was given to the molecules. To compensate for the lower polarisability, a peak intensity of $I_0 = 5 \times 10^{12}$ W cm^2 was used.

5.4 Results

Figure 5.5 illustrates the geometry used in the simulations. A Gaussian IR beam is focussed onto the xy plane, the coordinate origin is at the centre of the ir focus with $x_0 = y_0 = 0$. The particles are generated within the dashed square. After the position and velocity of each particle in the xy direction is calculated throughout the duration of the laser pulse, the particle motion is then propagated to an arbitrary time after the laser pulse using the relation $d_{x.y} = v_{x,y}t$, where t is the delay between the IR pulse ending and the time for the molecules to propagate downstream. Also shown in figure 5.5 is a two-dimensional contour plot in x and y of the density of the particles 0.475 μs after the IR pulse. The plot is for the randomly chosen $|\tilde{2},2\rangle$ rotational state of the CS_2 molecule. In figure 5.5, noting the difference in the x and y scales, it is apparent the molecular focus is strongly confined in the y direction compared to x. This is common to all rotational states. Due to the anharmonic shape[76] of the

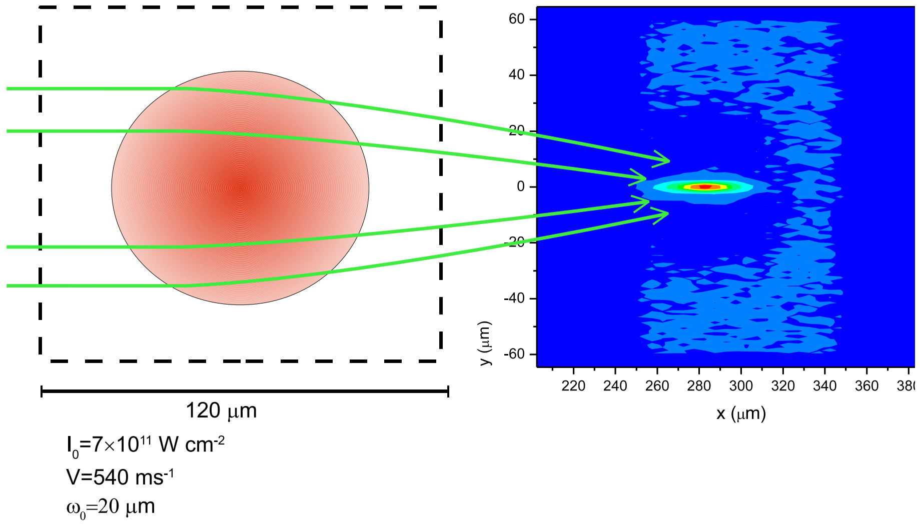

Figure 5.5: This schematic shows the IR focus with four particle trajectories drawn to represent the focussing action of the lens. The left side of the schematic shows a dashed square in which 750 000 particles are generated with random xy positions. This simulation was for CS_2 and the particles were given a velocity of $v_x = 540$ m s^{-1}, with a spread along x corresponding to $T_t = 3$ K. The right-hand side shows a xy density map of the molecular focus. Red indicates the highest density with blue indicating lower density. The position where the highest density occurs defines the focal length to be $f = 285$ μm.

potential $V(t)$ which governs the lens, molecules outside $y = \pm\omega/2$ no longer have a restoring force proportional to the distance from the centre of the lens. Consequently, molecules outside $y = \pm\omega/2$ have a longer focal length. This effect is analogous to spherical abberation[147] in conventional optics. The focal length of the lens in figure 5.5 can be defined by where the peak density occurs (red contour on density plot), which for this particular geometry and quantum state is 285 μm from the centre of the IR focus. Figure 5.6 shows a density plot of the molecular focus of the $|\tilde{2}, 2\rangle$ CS_2 state plotted in the xy plane with the z axis corresponding to the normalized particle density. The density is calculated by constructing 2d bins in the xy plane into which the particles are placed according to their xy position. The bin size is 5 μm $\times$ 1 μm for all calculations. From figure 5.6 the FWHM of the feature is 3.5 μm in the y direction.

5.4.1 N_2

Figure 5.7 shows the properties of the molecular focus for nitrogen. The lens parameters are $I_0 = 5 \times 10^{12}$ W cm^{-2} and $\omega = 30$ μm, with a molecular beam aperture

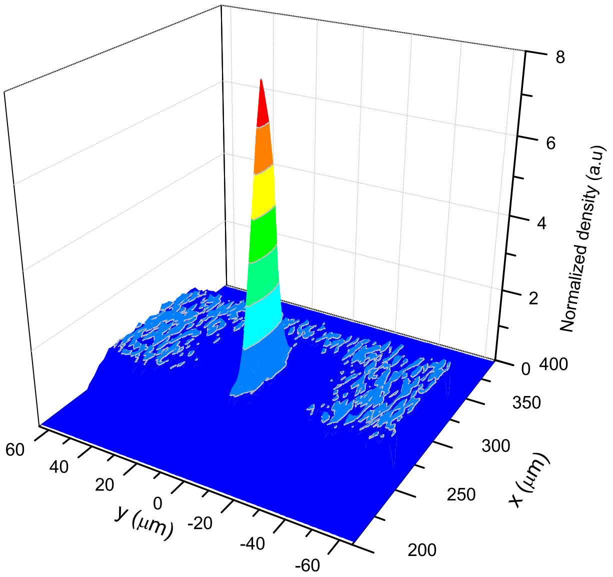

Figure 5.6: The particle density in the simulation is plotted in three dimensions to illustrate the properties of the focus. The focus is long (in x) and the areas above and below the focus (y axis) are depleted because the adjacent particles have been pushed into the centre. This simulation is for the $|\tilde{2}, 2\rangle$ quantum state and the molecular focus has a FWHM of 3.5μm.

$-\frac{\omega}{2} \leq y \leq \frac{\omega}{2}$. Figure 5.7 a) shows the density of the particles against the downstream distance for separate rotational states. The density of the particles is normalized to the average number of particles in each bin when no field is applied. The data was created by measuring the peak density and position at different delay times ranging from 0.1-2 μs. This is necessary in order to build up a density profile as a function of x, as the focussed cloud of particles travel along x. Figure 5.7 b) represents what density would be measured if each rotational level was resonant to the probe selectively. The information regarding individual $|\tilde{J}, M\rangle$ states is lost as once the molecules exit the IR field, their eigenvalues return to the field-free values, and $|M|$ becomes degenerate in the J manifold. Figure 5.7 b) also shows the downstream density for nitrogen using the average polarisability of the molecule (dark yellow). It can be seen only the $\tilde{J} = 0, 2$ states have a shorter focal length compared to the $J = 1, 3, 4$ states. Due to the low polarisability anisotropy of N$_2$, the focal length of each $\tilde{J}$ state quickly converges to the focal length for the average polarisability of the molecule. This behaviour is expected since with increasing $\tilde{J}$ the molecular alignment will decrease. Figure 5.7 c) shows the thermally averaged focus for different rotational temperatures. The focal length increases with rotational temperature which also has the effect of decreasing the molecular density. The thermal averaging is dependent on the rotational temperature of the beam and on the spin statistics of the nitrogen nuclei. Nitrogen is homonuclear and at 0 K the molecules exist entirely in the even

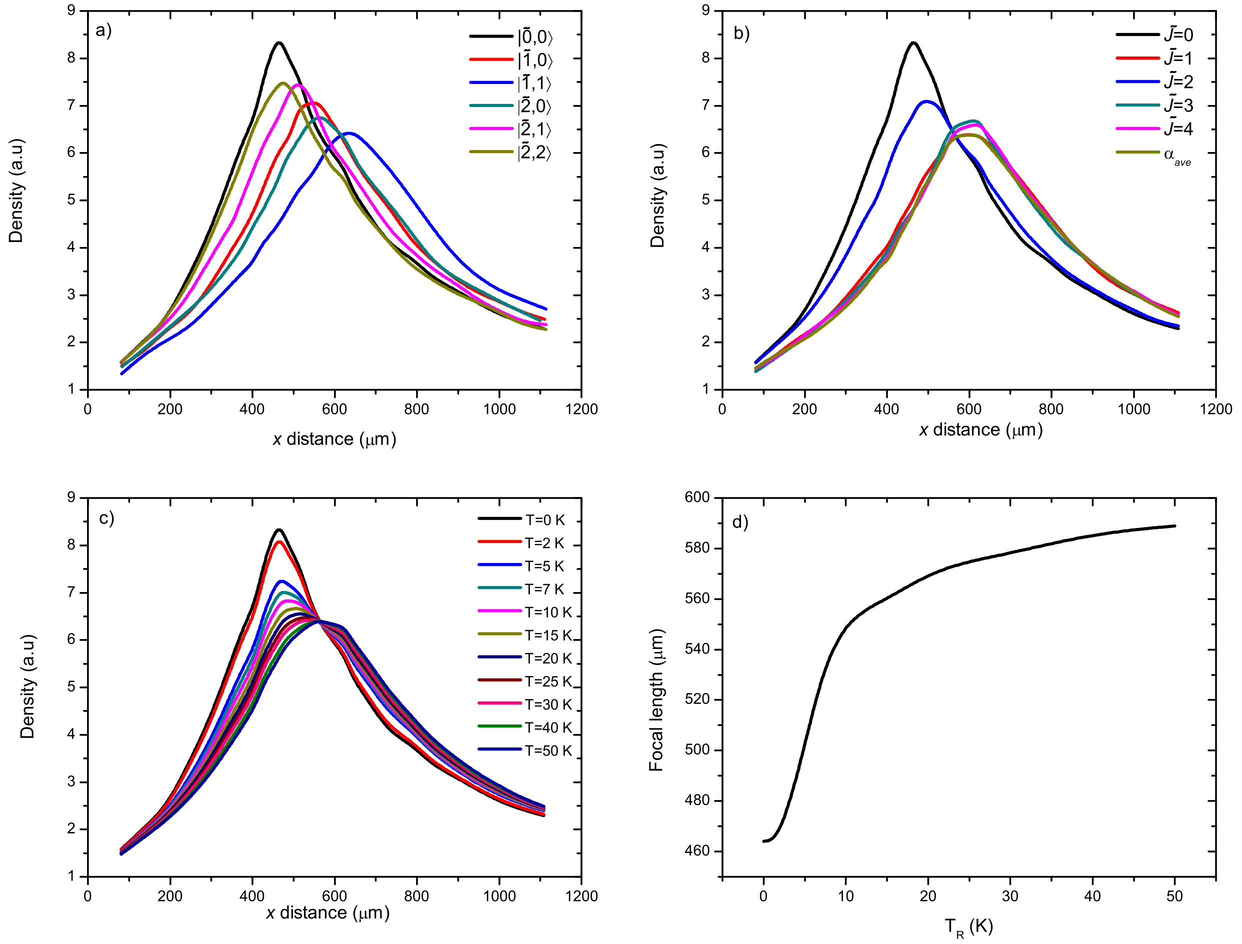

Figure 5.7: a) Shows a plot of the downstream density for individual rotational states of N_2. b) The rotational states have been averaged into their respective $\tilde{J}$ manifold. c) The thermally averaged molecular focus is shown for different rotational temperatures. d) The relationship between focal length and rotational temperature in c) is shown.

$J = 0$ state. The nitrogen nucleus has a spin of ± 1[227] and in a nitrogen molecule the nuclei spins can be aligned parallel or antiparallel to each other. Analogous to ortho and para-hydrogen, parallel spins on the nuclei mean the wave function is even allowing only $J = 0, 2, 4...$, whilst antiparallel spins allow only odd wave functions with $J = 1, 3, 5....$ In a supersonic expansion the gas is assumed to maintain its spin statistics, which are given by $(I + 1)/I$. This produces a 2:1 ratio for the rotational population of para-nitrogen to ortho-nitrogen. Figure 5.7 d) shows a plot of the focal length against rotational temperature, obtained from figure 5.7 c). It shows a quick increase in focal length owing to the rapid decrease in molecular alignment with increasing temperature. The flat region where the focal length remains approximately constant is where the molecular alignment tends toward the field-free value for the ensemble with $\langle \cos^2 \theta \rangle = \frac{1}{3}$. This means $\alpha_{\tilde{J},M}(I) \rightarrow \alpha_{ave}$.

By examining figure 5.7 c), the focal length is smoothly increased from $f \approx 460$ μm to $f \approx 580$ μm by increasing the rotational temperature. The focal length, $f \approx 580$ μm, represents the maximum focal length as it is determined by the average polarisability of the molecule. This means a difference in focal length of 120 μm is possible by taking account of the rotational temperature of the beam. The corresponding decrease in molecular density is $\approx$30 %.

5.4.2 CS$_2$

Figure 5.8 a) shows numerous rotational states of CS$_2$ which have been focussed by an IR beam with an intensity of $I_0 = 7 \times 10^{11}$ W cm^{-2}. States which exhibit a decrease in $\langle \cos^2 \theta \rangle_{\tilde{J},M}$ before saturating as shown in figure 5.3, show no difference compared to states with no drop in $\langle \cos^2 \theta \rangle_{\tilde{J},M}$ before reaching saturation. This is expected since at the intensities where the expectation values are lowered, the intensity is too low to induce centre-of-mass motion. This means only two states of odd and even parity in $(\tilde{J} - |M|)$ for each $\tilde{J}$ need to be simulated. For example, by only plotting the odd and even $(\tilde{J} - |M|)$ states for $\tilde{J} = 6$ and $\tilde{J} = 8$ such as $|\tilde{6}, 5\rangle$, $|\tilde{6}, 6\rangle$, $|\tilde{8}, 7\rangle$ and $|\tilde{8}, 8\rangle$, the behaviour of all the other $|M|$ states for $\tilde{J} = 6, 8$ is known. The average polarisability for CS$_2$ and three higher rotational states ($|\tilde{16}, 0\rangle$, $|\tilde{20}, 0\rangle$ and $|\tilde{24}, 0\rangle$) is also plotted to further explore the polarisability dependence of the particle focus. The focal length is 250 μm for the low $\tilde{J}$ states, an intermediate state $\tilde{J} = 16$, has a focal length of $\approx$350 μm, whilst the $|\tilde{20}, 0\rangle$, $|\tilde{24}, 0\rangle$ and α_{ave} states have focal lengths with $f \approx 400$ μm.

Figure 5.8 b) shows the downstream density for individual $\tilde{J}$ states until their focal lengths converge to the focal length of α_{eff}. Individual $\tilde{J}$ state behaviour was calculated by averaging the M states into the J manifold. Effectively all states up to $\tilde{J} = 10$ focus at the same position with only the relative density decreasing. This is caused by each $\tilde{J}$ state becoming increasingly difficult to saturate, eventually the saturation region exists above the intensity used to create the lens, and then the $\tilde{J}$

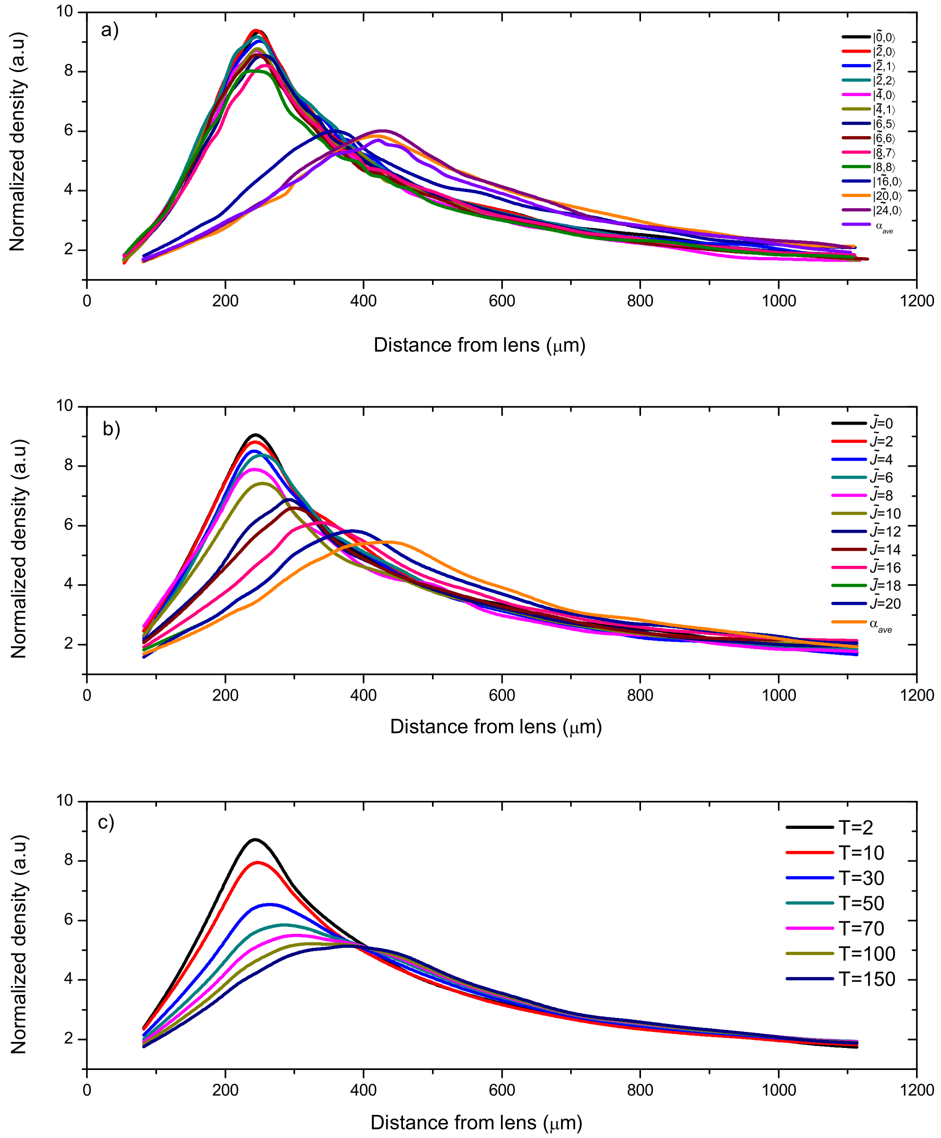

Figure 5.8: a) The density of the molecules is plotted as a function of distance from the molecular lens for CS_2 molecules with $I_0 = 7 \times 10^{11}$ W cm^{-2} and $\omega = 20$ μm. Each line is a theoretical curve for the density due to various rotational states. b) The density of each $\tilde{J}$ state, which defines an effective polarisability within the molecular lens is plotted up to $\tilde{J} = 20$. Low $\tilde{J}$ ($\tilde{J} < 12$) states have the same focal length of $f \approx 250$ μm. Some of the higher $\tilde{J}$ states ($\tilde{J} > 16$) have longer focal lengths which tend toward $f \approx 400$ μm, the focal length produced by the average polarisability. c) The thermally averaged density is shown. Lower rotational temperatures produce higher densities and shorter focal lengths.

state has effectively a field-free value. Figure 5.8 c) shows the thermally averaged downstream density from the lens over the temperature range $2 - 150$ K. Due to the low rotational constant ($B = 0.109$ cm^{-1}) and high polarisability anisotropy of CS_2, many rotational states are occupied at low temperatures making the focal length of the lens vary slowly with temperature. The focal range can vary from $f \approx 250$ μm to $f \approx 400$ μm, whilst the density will be decreased by 45 %.

5.4.3 Summary

In summary, the variation in focal length and also molecule density is caused by the alignment induced in the molecules. The molecules with higher alignment show a shorter the focal length. When a molecule has increasing rotational energy $J \to \infty$, it acts like a gyroscope and becomes harder to align with the electric field. Eventually the field-free rotational energy is so large the electric field only modestly perturbs the motion. In this circumstance, by averaging all the orientations, the molecular ensemble becomes isotropic with respect to its effective polarisability. This is why at higher temperatures the focussing properties of the lens are approximated by the average polarisability of the molecule.

5.4.4 Longitudinal velocity spread

The molecular lens may be composed into two force components, acceleration and deceleration along the molecular beam axis and focussing, which induces velocity changes perpendicular to the molecular beam axis. This means a portion of the molecules are decelerated and accelerated whilst being focussed. The effect of this force along x is decreased because of the longitudinal velocity spread. To examine this behaviour the simulations are repeated with $T_t = 0$ K. Figure 5.9 shows the focussing properties of the molecular lens for CS_2 when the molecules have a “monochromatic” velocity with $T_t = 0$ K. The density as a function of distance of the two most polarisable states $|\tilde{0}, 0\rangle$ (black) and $|\tilde{2}, 1\rangle$ (red) are plotted. The main difference between the simulations from the previous section is a large increase in density. No increase in sensitivity between the rotational states is observed because the difference in effective polarisability between the states is small at 6 %. Consequently there is very little difference between the plots. The bin size (5 μm$\times$1 μm) is kept the same for comparison with earlier figures, but it is actually too small to characterize density molecular density smoothly. Although not shown here, after the molecular beam has been focussed the molecules separate into two bunches because of the acceleration and deceleration properties of the lens. This only occurs when the molecules have had enough time to disperse, but because the focus is achieved quite quickly in time (~ 0.45 μs) and the dispersion takes much longer (>2 μs), the acceleration and deceleration effects are negligible.

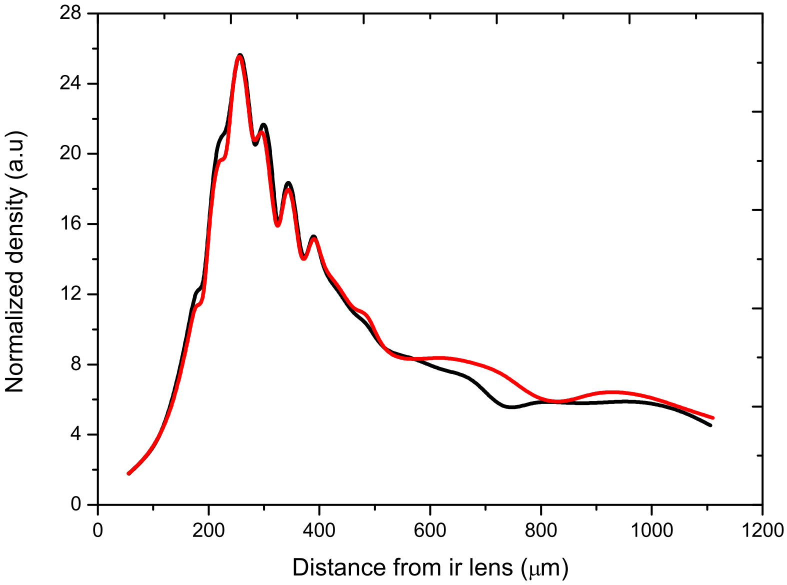

Figure 5.9: The density of CS_2 for the $|\tilde{0}, 0\rangle$ (black) and $|\tilde{2}, 1\rangle$ (red) states as a function of distance from the IR lens is plotted. The conditions are the same as figure 5.8 except with $T_t = 0$ to investigate the influence of translational temperature. The bin size is too large to measure the changes in density smoothly.

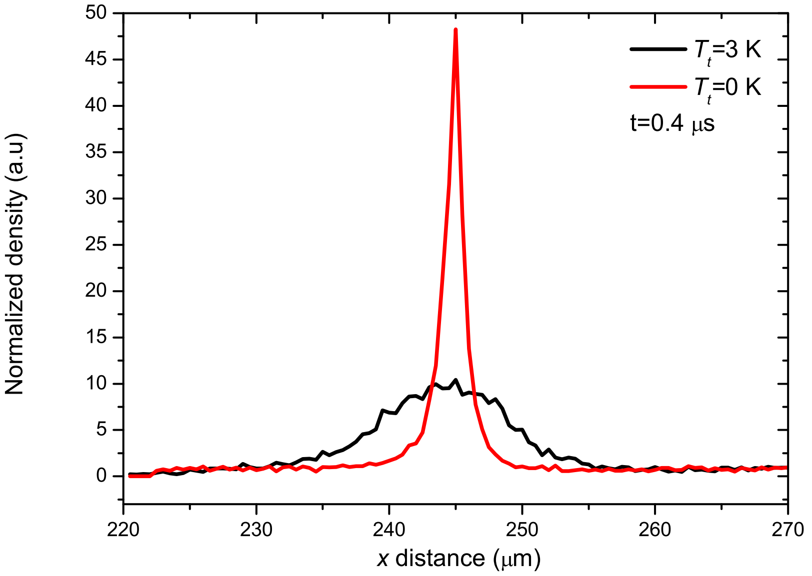

Figure 5.10: The density along the x axis at the molecular focus is shown 0.4 μs after the IR field has been turned off for $T_t = 3$ K (black) and $T_t = 0$ K (red). The longitudinal velocity spread increases the dispersion of the molecules along the x axis, decreasing the maximum density.

Figure 5.10 shows a slice through the molecular focus along the x axis for $T_t = 0$ K (red) and $T_t = 3$ K (black). The time delay after the IR field has been turned off is 0.4 μs. The particles with greater T_t spread out along the x axis decreasing the maximum density. The bin size used to count the particles was 2.5 μm × 0.5 μm along x and y respectively. Of note is that the density when molecules have $T_t = 0$ K, the molecule density is five times that when a 3 K beam is used. A larger density for the $T_t = 0$ K temperature is recorded in this graph compared to figure 5.9 because a smaller bin size has been used which has the spatial resolution along y to fully account for the particle density at the focus. Although not shown, the focal length, and width of the focus in the y direction remain unaffected, which is expected since these properties are determined by ω and I_0[188]. Thus the net effect of decreasing T_t, is to increase the overall density by reducing the spatial extent of the molecules along the x axis.

5.5 Towards molecule state selection

In this section, we explore the ability of the dipole force to spatially disperse molecules dependent on their initial rotational state. Figure 5.11 shows a schematic of a proposed setup where an aperture is placed in the molecular beam. The aperture is a 1 μm wide slit and limits the molecules to the $\omega/2$ region of the IR focus. This is where the dipole force is strongest. The aim is to deflect the molecules along the Z direction by creating a downward motion along Z away from the IR beam. As different rotational states have different polarisabilities, the force in the Z direction will differ for each rotational state. We restrict the calculations to N_2, with an intensity of 5×10^{12} W cm^{-2}, and with a Gaussian focus of $\omega = 20$ μm. A translational temperature of 3 K was used. Figure 5.12 shows simulations of the trajectories of the low rotational states in N_2 for the setup shown in figure 5.11, where the molecular beam speed is 540 m s^{-1}. The trajectories for the different rotational states were calculated as described in section 5.3. In figure 5.12 each rotational state is represented by two lines of the same colour. Each line represents a molecule at $X = 0$ distributed from $Z = 10$ μm to $Z = 11$ μm in order to create a 1 μm window. It can be seen that if the molecules propagate far enough it is possible to separate the molecules because of their different effective polarisabilities $\alpha_{\tilde{J},M}(I)$. The ground state $|\tilde{0},0\rangle$ (black), is deflected the most followed by the $|\tilde{2},1\rangle$ (red) state. This is expected as examination of the effective polarisabilities in figure 5.2 shows that the $|\tilde{2},1\rangle$ state has the next highest effective polarisability.

To acquire an idea of what proportion of the molecules will be deflected by the IR field and how closely overlapped the $|\tilde{0},0\rangle$ and $|\tilde{2},1\rangle$ states will be downstream, trajectory simulations were performed to determine the particle density. For the $|\tilde{0},0\rangle$ and $|\tilde{2},1\rangle$ rotational states, a 120 μm ×1 μm area in the ZX plane, centred at

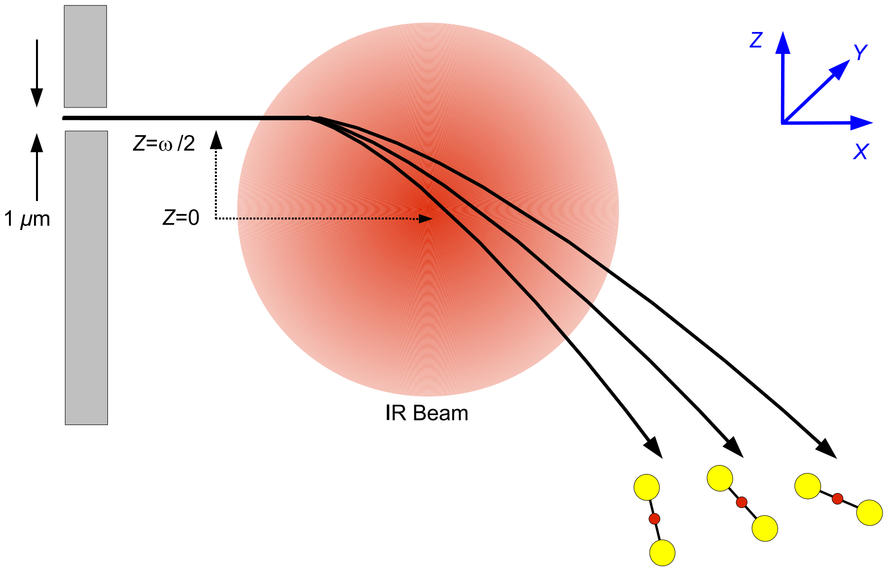

Figure 5.11: A scheme designed to separate molecules based on their effective polarisability. In the exaggerated sketch, the molecules are allowed to pass through a 1 μm aperture which limits the interaction region to $Z = \omega/2$. Depending on the effective polarisability of each rotational state, the dipole force imparts a "kick" in the Z direction, dispersing the molecules downstream. The coordinate axis are defined at the centre of the IR focus.

$X = 0$, containing 300,000 randomly generated molecules is propagated through the IR focus with the condition 10 μm $\leq Z \leq$ 11 μm. Figure 5.13 shows the results when the molecules are allowed to propagate for 10 μs after the IR field has switched off. Shown in figures 5.13 a) and b), are density plots showing the number of particles at each location defined by a 0.5 μm $\times$10 μm rectangle along Z and X respectively, for the $|\tilde{0}, 0\rangle$ and $|\tilde{2}, 1\rangle$ states. The large cloud at the top of both plots shows undeflected molecules that have simply traveled in a straight line from their starting point at 10 μm $\leq Z \leq$ 11 μm. The clouds at the bottom of a) and b) show the molecules that were in the IR field when it was switched on. These molecules have been given a downward trajectory due to the dipole force. The particles which lie between the two clouds are molecules which were at the fringes of the IR field in space in time and so receive a much weaker dipole force. The presence of these particles increases the noise in the deflected could measurement. The green lines on figures a) and b) are drawn for comparison to show the vertical separation between the deflected particle clouds for the two rotational states. The Z positions of the clouds are 167 μm and 156 μm for the $|\tilde{0}, 0\rangle$ and $|\tilde{2}, 1\rangle$ states. This yields a spatial separation along Z of 11 μm. The centre of both deflected distributions in the X direction is 5.4 mm. There is no separation between the deflected clouds along X because the molecules are traveling at the same speed. These measurements indicate the molecules must travel quite far

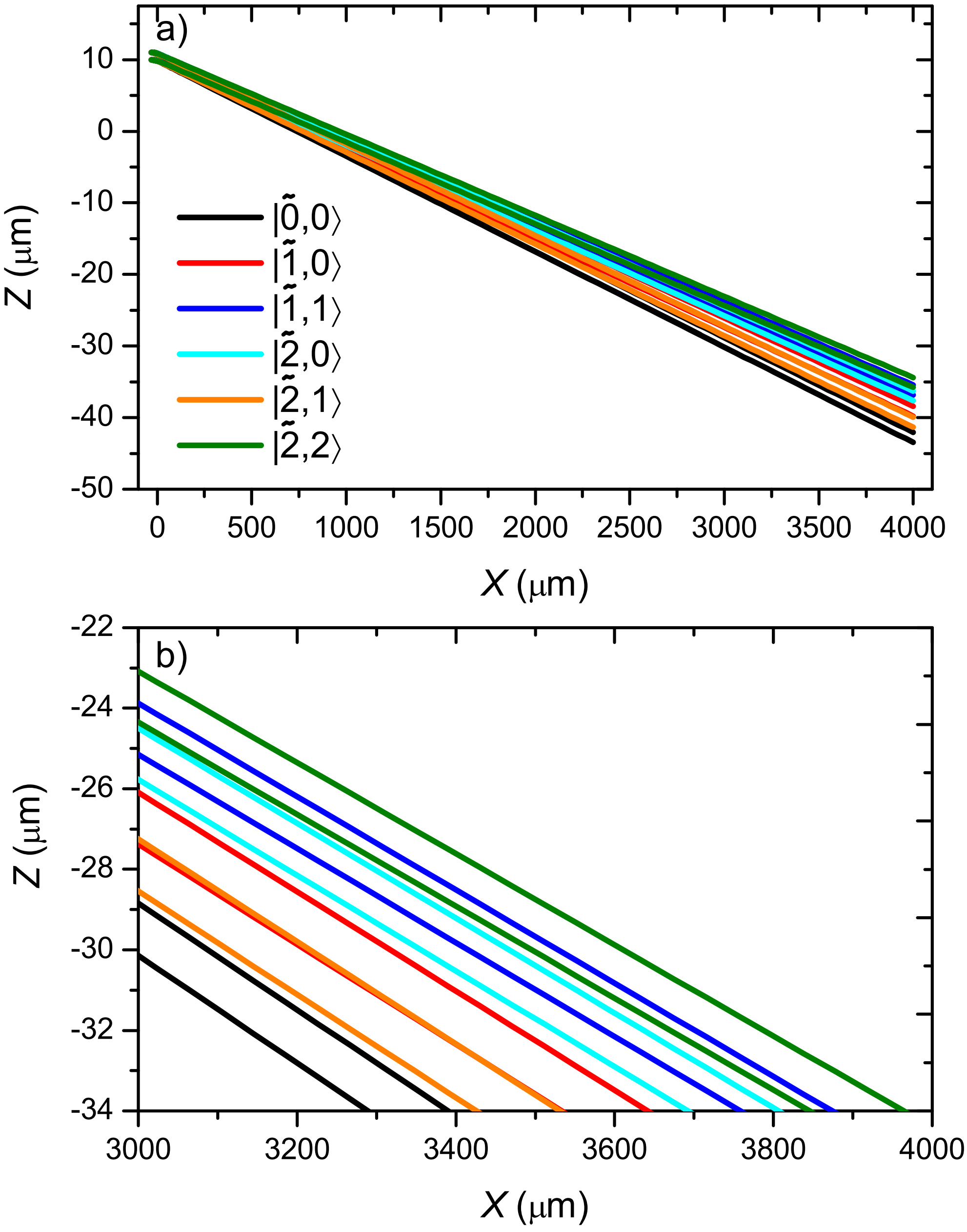

Figure 5.12: a) Shows the particle trajectories from $Z = 10$ μm and $Z = 11$ μm, both particles originate at $X = 0$ μm. The propagation time is 10 μs. Solid lines of the same colour correspond to particles of the same rotational state $|\tilde{0}, 0\rangle$ (black), $|\tilde{1}, 0\rangle$ (red), $|\tilde{1}, 1\rangle$ (blue), $|\tilde{2}, 0\rangle$ (light blue), $|\tilde{2}, 1\rangle$ (orange) and $|\tilde{2}, 2\rangle$ (olive). b) A close up of the trajectories downstream.

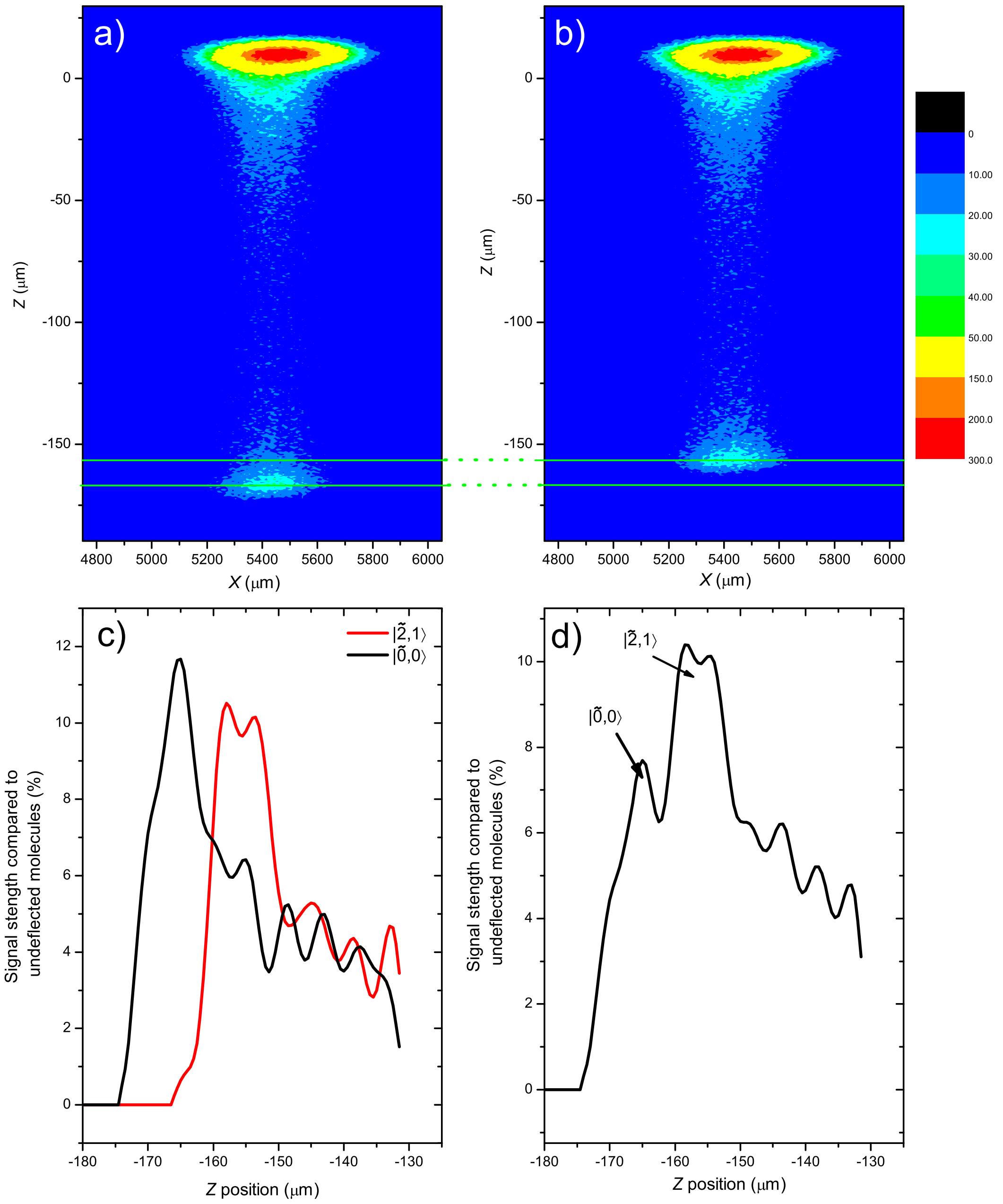

Figure 5.13: a) and b) are density profiles showing the different deflection between the $|\tilde{0},0\rangle$ and $|\tilde{2},1\rangle$ states. The particle clouds at the top of a), and b), are undeflected molecules. c) A cut in the Z direction at $X = 5430$ μm, from each plot in a) and b) is shown. d) An average of both states is shown. All graphs are for the N_2 molecule.

before they can be resolved spatially along Z. This is expected since the induced velocity along the Z direction is $\sim$ 15 m s^{-1}, whilst along X the molecular beam speed is 540 m s^{-1}.

Figures 5.13 c) and d) show the distribution of the deflected molecules by taking a cut through the density profiles in figures 5.13 a) and b) along Z at $X = 5430$ μm. The cut is through the region with the most particles. Figure 5.13 c) shows the $|\tilde{0},0\rangle$ (black) and $|\tilde{2},1\rangle$ (red) states along the Z axis where the $|\tilde{0},0\rangle$ state is the most deflected. The y axis in the figure is the percentage of molecules deflected compared to those incident on the aperture. The data in both figures has been smoothed by using a FFT low pass filter. Despite the number of particles used in the simulation, the number of particles deflected, combined with the spatial resolution required mean the deflected particle cloud was not completely smooth. However, the data is sufficient for a conclusive analysis to calculate the spatial separations between the deflected rotational states. In figure 5.13 c) the separation between the rotational states is 11 μm. By measuring the height at the centre of the distribution we find the $|\tilde{0},0\rangle$ peak is made up of 95 % $|\tilde{0},0\rangle$ particles. The background level, composed of residual particles from the $|\tilde{0},0\rangle$ state mean the $|\tilde{2},1\rangle$ peak sits on a $|\tilde{0},0\rangle$ state, background pedestal. Consequently, it is more impure than the $|\tilde{0},0\rangle$ distribution with 62 % of the particles being in the $|\tilde{2},1\rangle$ state. Figure 5.13 d) shows the average of both states in the deflected particle cloud. In these circumstances the $|\tilde{0},0\rangle$ state is still resolvable.

Figure 5.14 a) shows the $|\tilde{0},0\rangle$ (black), $|\tilde{1},0\rangle$ (red), $|\tilde{1},1\rangle$ (blue), $|\tilde{2},0\rangle$ (dark green), $|\tilde{2},1\rangle$ (pink) and $|\tilde{2},2\rangle$ (dark yellow) states of N_2 after propagating downstream for 10 μs. The ground state is deflected the most and lies on the outer most fringe of the distribution along Z. The $|\tilde{2},1\rangle$ (pink) and $|\tilde{2},2\rangle$ (dark yellow) states arrive at the same position and will be indistinguishable in space. The next deflected state is the $|\tilde{2},0\rangle$ (dark green) and $|\tilde{1},0\rangle$ (red) state, whilst the least deflected state is $|\tilde{1},1\rangle$ (blue). By comparing with the effective polarisabilities shown in figure 5.4, it can be seen that the order of arrival of the states isn't necessarily the order of decreasing effective polarisability. This is because of the influence of the $d\alpha_{J,M}/dI$ term in the dipole force equation. By examining figure 5.4 one might conclude that the $|\tilde{2},2\rangle$ state would be less deflected compared to the $|\tilde{2},1\rangle$ state, but they actually arrive at approximately the same position along Z. This is because although the $|\tilde{2},2\rangle$ state has a significantly lower value of $\alpha_{\tilde{J},M}(I)$ at 5×10^{12} W cm^{-2}, the applied dipole force is effectively the same as the $|\tilde{2},1\rangle$ state, because the $|\tilde{2},2\rangle$ state has a steeper slope in $d\alpha_{J,M}/dI$. Although the effective polarisability curves can serve as a good and general guide to evaluating the strength of the dipole force on molecules it should be remembered that it is the force that must be calculated. At this point however, by carrying out dipole force simulations the generality of the effective polarisability curves (they only depend on intensity) is lost because the experimental parameters such as beam waist and molecular beam speed must be included.

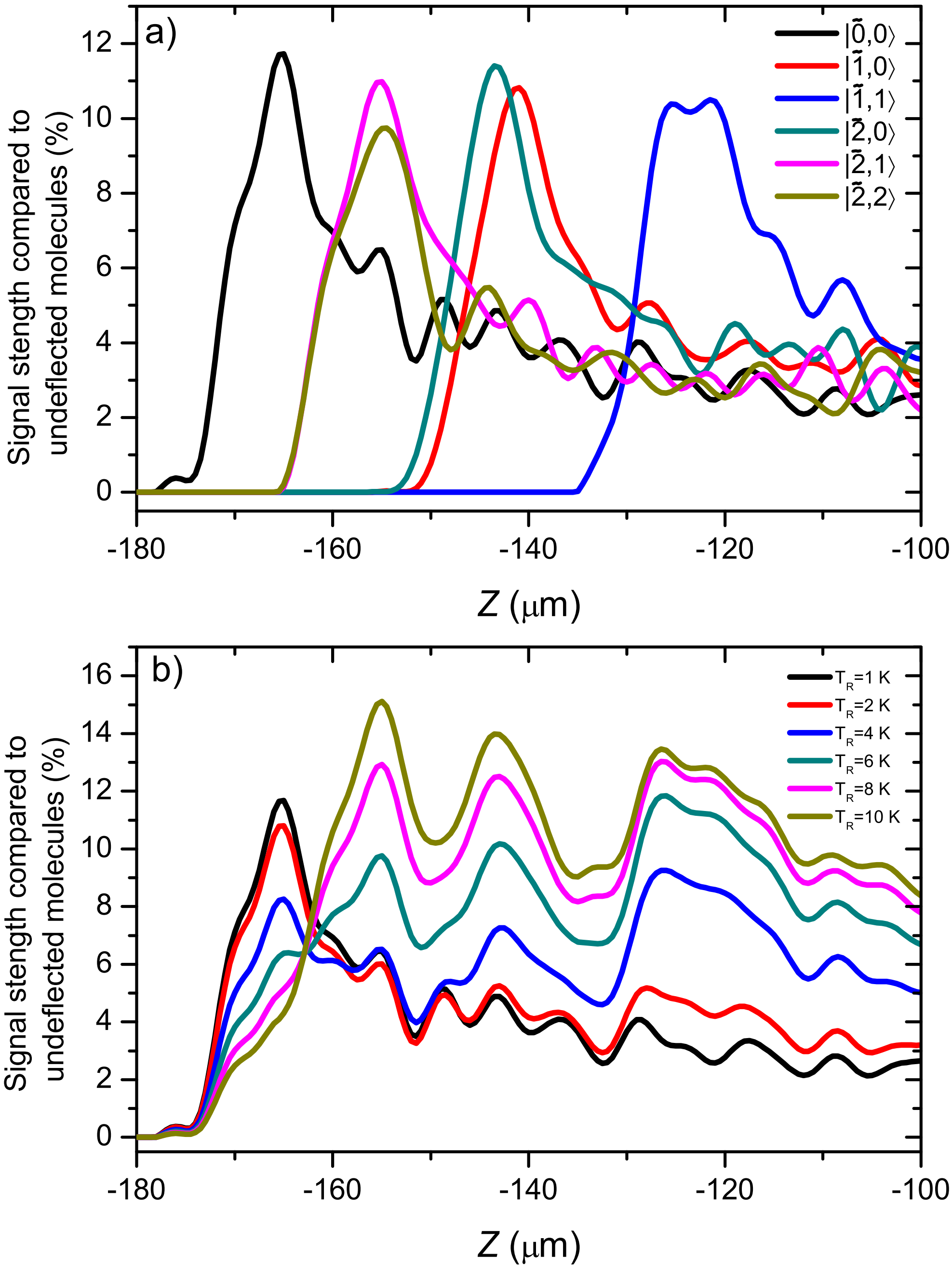

Figure 5.14: a) A cut along Z shows the spatial separation of the different rotational states $|\tilde{0},0\rangle$ (black), $|\tilde{1},0\rangle$ (red), $|\tilde{1},1\rangle$ (blue), $|\tilde{2},0\rangle$ (dark green), $|\tilde{2},1\rangle$ (pink) and $|\tilde{2},2\rangle$ (dark yellow). On average the peaks are separated by 10 μm. b) The effects from thermal averaging is shown for various temperatures 1 K (black), 2 K (red), 4 K (blue), 6 K (dark green), 8 K (pink), and 10 K (dark yellow).

Table 5.1: Rotational state composition (%) at 8 K

State	Peak		
	1	2	3
$\vert\tilde{0},0\rangle$	2.7	1.8	1.1
$\vert\tilde{1},0\rangle$	0	3.0	1.1
$\vert\tilde{1},1\rangle$	0	0	3.2
$\vert\tilde{2},0\rangle$	0	2.8	0.8
$\vert\tilde{2},1\rangle$	2.7	1.2	0.8
$\vert\tilde{2},2\rangle$	2.4	1.2	0.8

Figure 5.14 b) shows the thermally averaged distribution of the N_2 molecules for various rotational temperatures. The effects from thermal averaging are shown for the temperatures 1 K (black), 2 K (red), 4 K (blue), 6 K (dark green), 8 K (pink), and 10 K (dark yellow). Figure 5.14 b) has the same x scale as figure 5.14 a) so a comparison can be made between the figures. A feature of nitrogen is that at low temperatures the ground state is highly populated, but also due to the nuclear spin statistics the odd rotational levels have one half the strength of the even rotational states. This results in the ground state being prominent until at 6 K where the higher even states begin to dominate, where the ($|\tilde{2},2\rangle$ and $|\tilde{2},1\rangle$) and ($|\tilde{2},0\rangle$ and $|\tilde{1},0\rangle$) states are separated by $\sim$ 12 μm. The $|\tilde{1},1\rangle$ state is the least deflected and is separated from the other states by $\sim$20 μm. Figure 5.15 a) shows the deflected rotational states along the Z when they are averaged into their respective $\tilde{J}$ states. For the states shown $\tilde{J} = 0, 1, 2$, the $\tilde{J} = 0$ is deflected the most followed by $\tilde{J} = 2$ and $\tilde{J} = 1$.

Figure 5.15 b) shows the deflected rotational states and their summation at 8 K. The states shown are the same for figure 5.14 except the for a summation over all states which is indicated by an orange line. This plot shows how each rotational state contributes to the overall spatial density distribution. Table 5.1 shows the composition of each of the labeled peaks in figure 5.15 b). Of note is that states which are less deflected sit on top of the residual noise or pedestal (indicated by black arrow) left by the more deflected states. This means for less deflected states, the ripple noise from the pedestal is added together to create slightly irregular line shapes in the less deflected rotational states. In a perfect simulation, the pedestal would be completely flat and would add a constant offset to the states, but because a finite number of particles is used in the simulation there is noise added to the spectrum.

5.5.1 Density

The density of the deflected particles when normalized to the density of molecules incident on the aperture before the IR beam is $\sim$ 10 %. If a molecular beam has a density of 5×10^{12} cm^{-3} (similar to chapter 2), the total number of molecules allowed

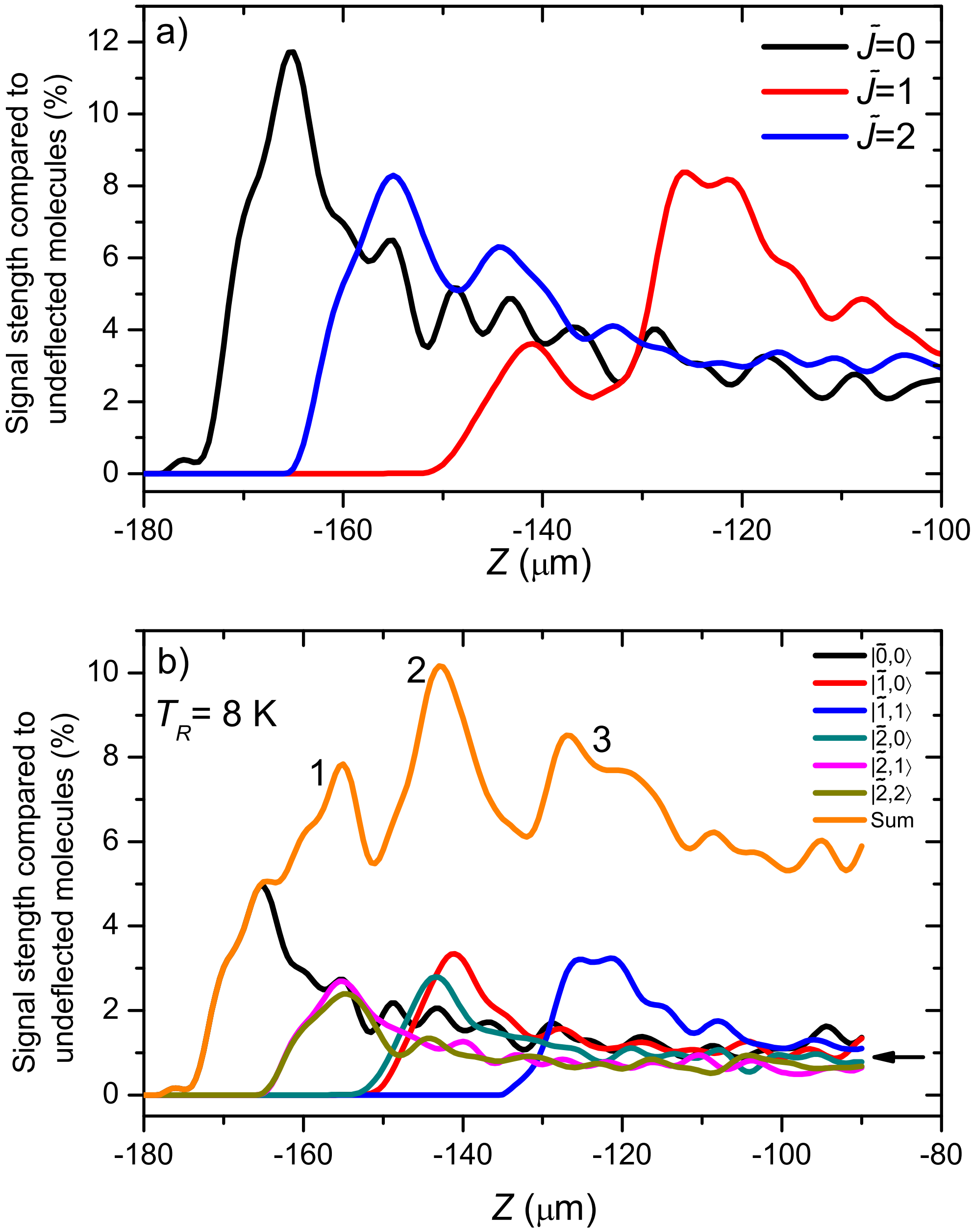

Figure 5.15: a) The deflected rotational states have been averaged into their respective $\tilde{J}$ states. b) At a rotational temperature of 8 K, each rotational state is plotted in order to show how they contribute to the overall shape of the deflected particle cloud. The states shown are $|\tilde{0},0\rangle$ (black), $|\tilde{1},0\rangle$ (red), $|\tilde{1},1\rangle$ (blue), $|\tilde{2},0\rangle$ (dark green), $|\tilde{2},1\rangle$ (pink) and $|\tilde{2},2\rangle$ (dark yellow). The sum of the states is indicated by the orange line. The composition of each of the labeled peaks is shown in table 5.1.

through a 1 μm slit would be reduced a factor of 10^4. This figure could be improved by moving the experiment closer to the molecular jet source. By moving the experiment 20 cm closer to the source, the density which we define as the number of molecules allowed though the slit and uniformly distributed in a cube with length 1 cm, would be increased by a factor of ~ 10. Since the amount of molecules deflected compared to those incident on the aperture is around 10 %, the deflected average particle density is estimated to be $\sim 5 \times 10^8$ cm^{-3}.

Although the scheme in this particular geometry does not promise great quantities of molecules or particularly large spatial separation between rotational states, it does show the alignment-dependent dipole force in principle can be used to separate molecules. By increasing the interaction times (slower molecular beam), reducing the translation temperature, or using larger electric field gradients (as in an optical lattice for example), more molecules could be dispersed.

5.6 Conclusion

The focussing properties of individual rotational states of CS_2 and N_2 molecules in a molecular lens have been examined numerically. The rotational motion of the molecules in a strong electric field was solved and then substituted into the equations of motion to analyse the focus produced by different rotational states in a molecular lens.

For nitrogen, the presence of rotational states altered the focus produced by the molecular lens. A plot of the density of the focussed molecules along the molecular beam axis showed that some of the rotational states had different focal lengths. This had the effect of making the focal length, and shape of the molecular focus dependent on the rotational temperature. From 0 K to $T_R \to \infty$, the focal length of the lens was increased from $f \approx 460$ μm by ≈ 120 μm to $f \approx 580$ μm. This represents an increase in focal length of 26 % compared to the focal length of the ground state. Due to the increase in focal length and decrease in perpendicular velocity kick applied to the molecules, the normalized molecular density was decreased by 30 %.

For CS_2, the density plot showed quantum states below $\tilde{J} = 12$ focus to effectively the same position at $f \approx 250$ μm. This is caused by the small difference in expectation value between $\tilde{J}$ states with $\tilde{J} = 0 - 12$ for the intensity used. From 0 K to $T_R \to \infty$, the rotational temperature was found to increase the focal length of the ground state from 250 μm to 400 μm, representing a 60 % increase in focal length. The normalized density was decreased by 45 %. Additionally, since the focussed molecular density for CS_2 has been decreased by 45 %, it is reasonable to assume that the area of the focal spot produced by the molecular lens has also been increased by 45 %.

The overall density was found to depend on focal length but was also heavily dependent on the translational temperature. An increase in molecular density, which would be desirable in microscopy experiments, could be achieved by decreasing the translational temperature. This would not affect the minimum spot size produced by the molecular lens.

Finally, a simple scheme was proposed to examine theoretically if it was possible to separate molecules depending on their effective polarisability. The results showed that the ground state and the next two deflected states ($|\tilde{2},2\rangle$ and $|\tilde{2},1\rangle$) were separated by 10 μm vertically 5430 μm downstream. The estimated average molecular density is 5×10^8 cm^{-3}. The practical feasibility of this experiment relies on having the experimental stability, spatial resolution and laser wavelengths available that are resonant with the rotational levels of N_2.

Chapter 6

Effect of laser pointing stability on a molecular lens

6.1 Introduction

When lasers are used to probe gases, interactions, or surfaces, for accurate results, care must be often be taken to ensure the laser is frequency and spatially stable. This chapter investigates the spatial aspect of laser stability, often referred to as laser pointing stability, and how it affects the measured molecular focus.

Laser pointing stability can decrease the spatial sensitivity of a probe laser by varying the shot-to-shot position. This has the effect of sampling data which is not fully resolved according to the focussed laser's e^{-2} width. The diagram in figure 6.1 illustrates laser pointing stability. The angle θ measures the angular displacement of the laser beam. Pointing stability is an averaged value and is generally measured over a period of an hour and measured in μrad.

The shot-to-shot variation in the laser pointing stability can increase the minimum molecular spot size achievable with a molecular lens created by a focussed laser beam. This is because the position of the molecular lens will move around in the focal plane, smearing out the focus produced by the molecular lens. In particular, simulations of focussed molecular beams[58] have shown it is possible to create nanosized structures. If we hope to create such molecular foci, the spatial extent over which the IR focussing laser beam moves from shot to shot must be taken into account.

In general, a pulsed laser will have a pointing stability ranging from 20 μrad to 60 μrad. The actual amount of spatial variation from the laser in an experiment will depend on the geometry of the experiment. This may include distance to the interaction region and the focal lengths of any lenses used. A focussing lens can reduce the effects of a small variation in input angle through the relation $x = f\theta$, where f is the focal length of the lens and θ is the angle between normal incidence to the lens and the laser beam. Thus for a 20 μrad spread of shots focussed by a 20 cm lens, one would expect the shots to land within a 4 μm range in the focal plane.

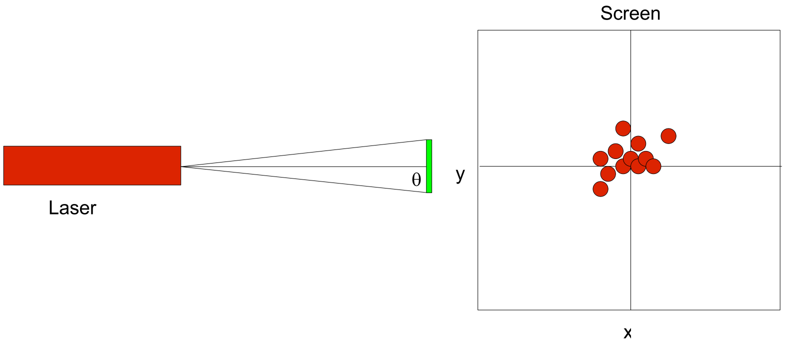

Figure 6.1: A diagram illustrating laser pointing stability. A laser beam is directed onto a screen (green slide) which records the position of each laser shot along the x and y directions. The spread of the shots in each direction can be used to define an angle θ, which describes the distribution of laser shots at the screen.

This means the shorter the focal length the smaller the spread of laser shots due to pointing stability.

There can be many factors contributing to pointing stability, air convection currents, vibrations, also heating and impurities in the gain medium can cause changes in refractive index. To minimise the effects of pointing stability in experiments, the distance between the laser and interaction region should be minimized, and extra stable optical posts should be used along with the isolation of vibrations. Electronic feedback systems[228] have had success in the past as they can actively correct for laser beam drift by using photodiodes to monitor the position of the laser beam. The photodiode voltage is then processed in a feedback circuit to control a piezo mounted steering mirror to keep the majority of the laser beam shots centred on the photodiode.

6.2 Experiment

6.2.1 Continuous wave laser

To test the feasibility of using a feedback circuit to reduce the pointing stability, a cw low power 3 mW Helium Neon laser was used in the arrangement shown in figure 6.2. A quadrant detector or quadcell (New Focus Q120), has its photodiode divided into four equal parts, top, bottom, left and right. The voltage generated from each quadrant is used to create error signals which depend on the laser beam position horizontally $X(x)$, and vertically $Y(y)$. Each voltage is normalized to the

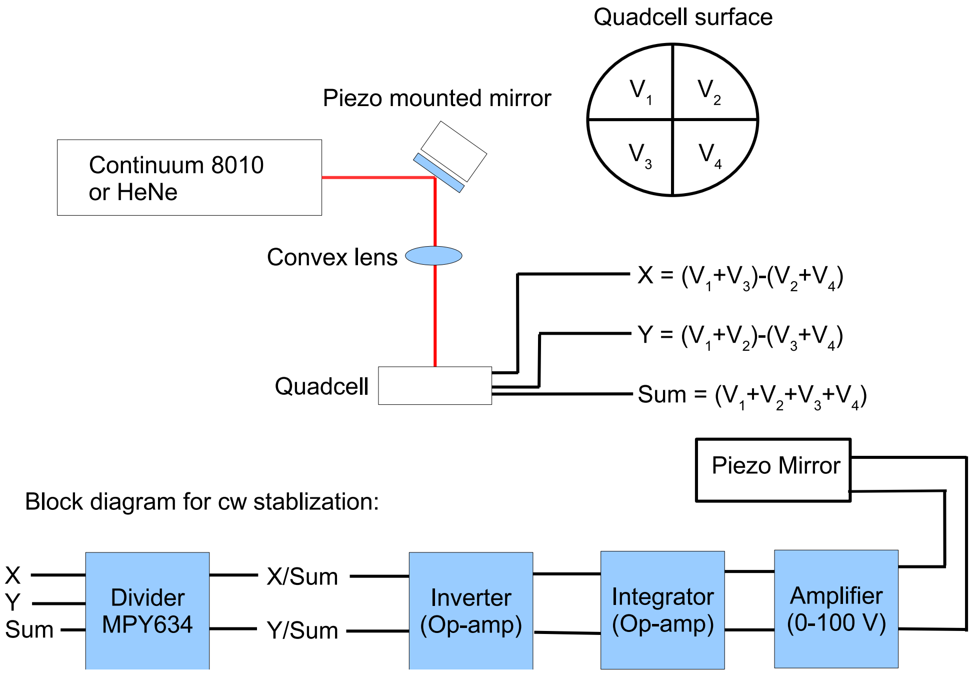

Figure 6.2: A schematic showing how the pointing stability of the cw HeNe and the pulsed Continuum laser is measured and controlled. The laser beam is focussed onto a quadcell which produces error signals depending on where the beam lands on the surface. The error signals are normalized, then passed through an inverter and an integrator and finally to an amplifier, which controls the piezo mirror to bring the laser beam back into the centre of the quadcell. Using the pulsed laser, a SR250 boxcar gated integrator was used to sample the laser pulse, which was then normalized and recorded. No active feedback stabilization was achieved for the pulsed laser.

laser intensity so fluctuations in the laser output energy do not manifest themselves as false positions on the quadcell. This is incorporated into the quadcell which has a SUM output which adds the voltage produced in each quadrant. By dividing the error signal by the SUM voltage, the error signal is independent of intensity fluctuations from the laser. The division can be done using an analogue chip from Burr-Brown, model MPY634. When the $X(x)$ and $Y(y)$ voltage signals are minimized, the laser beam is exactly in the centre of the photodiode. In figure 6.2, the HeNe laser beam after reflection from a piezo mounted mirror is focussed onto the quadcell. The quadcell is connected through a feedback circuit to the piezo actuated mirror in order to push or pull the laser beam back into the centre. Carrying out this experiment, the results showed the pointing stability in both vertical and horizontal directions was reduced to $< \pm 1$ μrad compared to ± 10 μrad with the feedback circuit turned off.

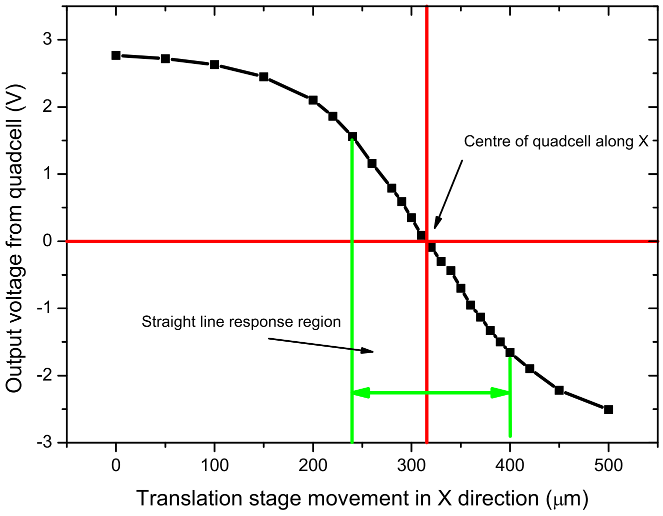

Figure 6.3: The output voltage from the gated integrator (SR250) in Volts is plotted against the translational stage movement in the horizontal direction. The red lines indicate where the error signal is zero corresponding to the centre of the quadcell at approximately 320 μm. The green lines indicate the linear response of the output voltage with translation stage movement, this range corresponds to ±80 μm.

6.2.2 Pulsed laser

Before application of the active feedback system to a pulsed laser it was necessary to first simply measure the pointing stability of a pulsed laser. The oscillator output from a Continuum Precision II 8010 Nd:YAG laser was focussed with a 1 m plano-convex lens onto the quadcell, such that 1 μrad movements would correspond to the laser spot moving 1 μm across the photodiode. The seeded output energy from the laser was 400 mJ per pulse, which was sufficiently attenuated to not damage the quadcell. To measure the pointing stability, the setup shown in figure 6.2 is modified because the quadcell no longer has a DC output but an AC output from the pulsed laser. Two boxcar gated integrators (SR250) were used to sample the laser pulse shape from the $X(x)$ and SUM outputs. The integrated AC signal was then used as the error signal. The voltage output from the boxcar was calibrated by traversing the laser beam a known amount on a translation stage. A plot of the voltage signal as the translation stage is moved is shown in figure 6.3. The translation stage had a resolution of <2 μm and the position error that resulted from error on the voltage signals from the quadcell was negligible. In figure 6.3 the voltage response is linear within a 160 μm range at the centre of the photodiode. A straight line fit in this region allows the voltage from the SR250 to be converted to position.

Figure 6.4 shows a small portion of the pointing stability data in the horizontal direction. There are two series, each was recorded for five minutes corresponding

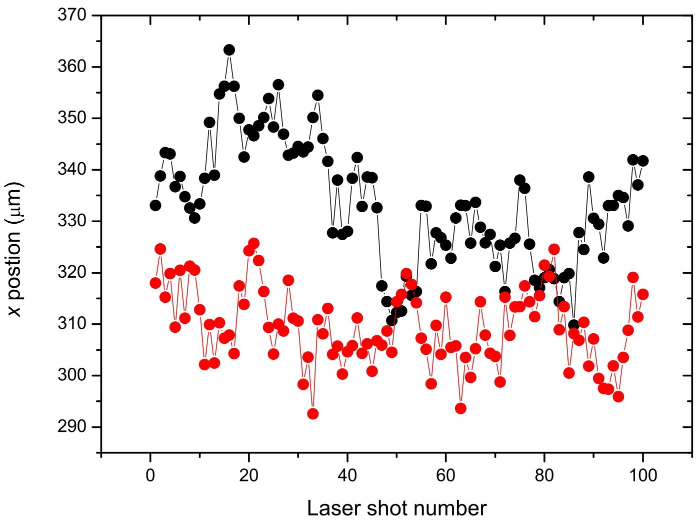

Figure 6.4: A portion of the shot-to-shot variability of the pulsed 10 Hz Continuum laser is shown, two five minute samples were recorded separated by thirty minutes. The figure shows both shot-to-shot stability accompanied by a long term drift, each data set is separated 26±10 μm.

to 3000 laser shots, the second series (red) was recorded thirty minutes after the first series (black). Each point corresponds to a single laser shot, only 100 shots are shown in figure 6.4 to avoid over crowding the graph. Figure 6.4 shows two features of pointing stability, the first is shot-to-shot stability which is how much each subsequent shot moves after the previous shot. The second feature is the long term drift of the laser which is shown by the separation of the red and black traces. The black scan compared to the red scan has moved by 26±10 μm, each distribution has a mean of 327±11 μm and 301±9 μm respectively. It can be seen that each shot can vary by $\approx \pm 20$ μm, this is an intrinsic property of the laser and active feedback would not correct this. However, as the average position of the distribution moves slowly in time, it should be possible to follow the average of the laser distribution using a modified feedback circuit. This would at least mean the average of the spatial distribution is centred on the photodiode, and experimental measurements would only be limited by shot-to-shot stability.

6.2.3 Shot-to-shot stability

To examine the shot-to-shot variability of the laser after a thirty minute warm-up period, a five minute sample was taken similar to figure 6.4, and the difference between one shot and the next was calculated. This data is subsequently binned into 1 μm bins to look at the distribution of shots that lie within an angular range. The experiment

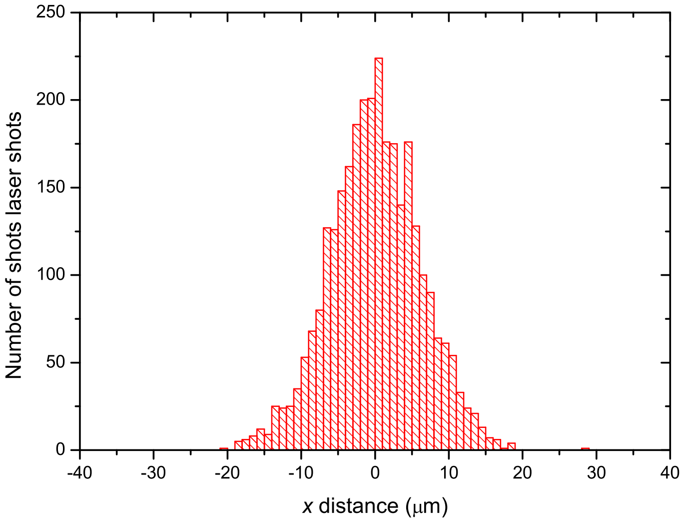

Figure 6.5: The number of shots in a five minute scan with difference in μm between subsequent shots is shown in the histogram. The data was recorded with the Continuum laser on full power and being seeded.

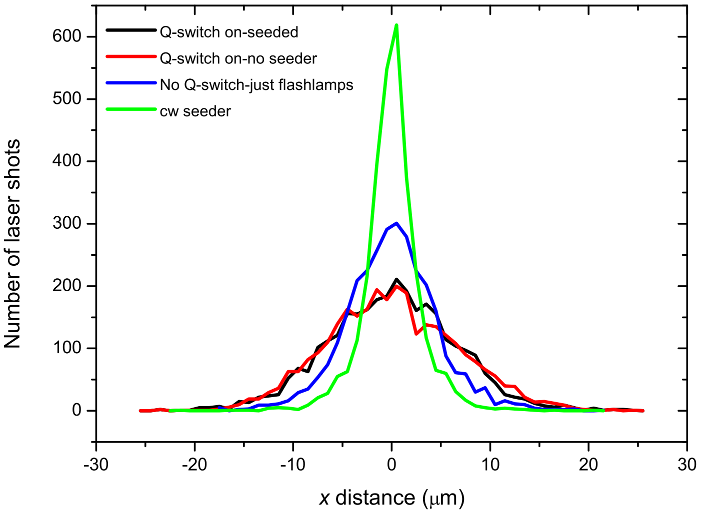

Figure 6.6: The histogram for each mode of operation of the Continuum laser is plotted as a line graph for comparison. Integrating a Gaussian fit to the data allows the percentage of points that lie within a certain angular range to be compared.

was repeated four times; with just the seeder laser operating and with the seeder on and flash lamps on but with no Q-switching. The third and fourth experiments show the laser operating at full power with the seeder on and off. A histogram of the distribution for the seeded Q-switched operation is shown in figure 6.5, the distribution is approximately Gaussian indicating randomly distributed factors are the main cause of the instability. To compare the shot-to-shot variability of each mode of operation, each histogram is plotted as a line graph and overlaid, this is shown in figure 6.6. One observes that with just the seeder operating (green), it has the narrowest distribution which is to be expected as it is a cw laser and operates under steady state conditions where as the pulsed laser does not. Turning on the flashlamps, but with no Q-switch (blue) broadens the profile, whilst finally operating in pulsed full power mode has the broadest distribution (red and black). By activating the flashlamps the gain medium is being pumped which will change its optical properties increasing instability. Additionally, the optical cavity in the pulsed laser is much larger than the seeder cavity, and so it is more susceptible to thermal effects. When the Q-switch is turned on, the laser is operating at full power, this mode has the widest pointing stability distribution as the random effects which arise from emitting a high power optical pulse will be added to those already present in the laser.

By integrating a Gaussian fit to each distribution, the limits of the integration determine how many shots lie within a specified range. Operating at full power, 30 % of shots lie within ±5 μm and 10 % of shots lie within ±1 μm. As the data was recorded over five minutes this gives an idea of how long it would take to gather 3000 shots of data within the specified angular range, this corresponds to 17 minutes and 50 minutes respectively. By recording all of the laser shots and the corresponding data to each shot during an experiment, those laser shots outside of the accuracy range could be discarded. This would leave only data which was within the specified spatial resolution. This type of analysis would have to carried out after the experiment has been performed.

6.2.4 Limiting resolution

Figure 6.7 shows a numerically calculated cut through a molecular focus in the y direction (perpendicular to the molecular beam) created by a molecular lens for CS_2 (see Chapter 5 figure 5.6). The parameters of intensity and e^{-2} width are described in the previous chapter in section 5.3. Figure 6.7 shows the calculated y axis width with no laser pointing stability averaging in black. Four widths of Gaussian FWHM 1 μm (red), 3 μm (pink), 5 μm (blue) and 10 μm (green) were used to broaden the distribution to calculate the effect of using a nonresonant laser which suffered from pointing stability. The FWHM widths calculated from figure 6.7 are 1.7 μm, 3.7 μm, 5.6 μm and 10.7 μm for each of the respective pointing stability widths. It can

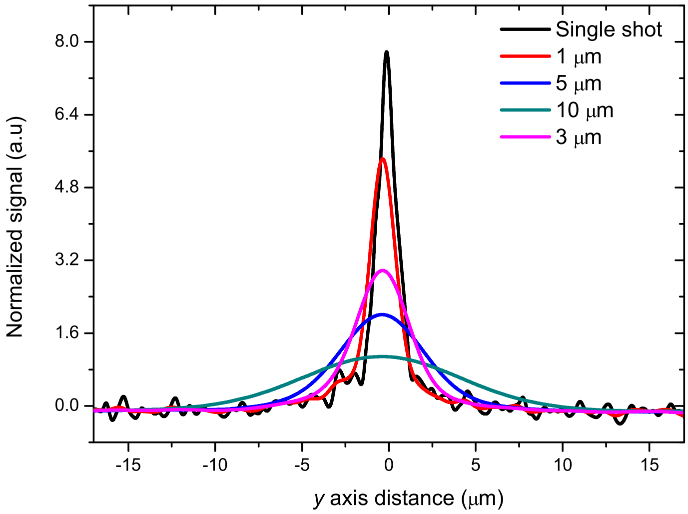

Figure 6.7: A y cut through the molecular focus of CS_2 molecules is shown when probed using a laser with increasing pointing stability. The FWHM width (black) is 1.5 μm. When the laser is given a probability distribution to represent the laser shots, defined by a Gaussian line shape with FWHM widths 1 μm (red), 3 μm (pink), 5 μm (blue) and 10 μm (green), the "measured" molecular focus FWHM increases to 1.7 μm, 3.7 μm, 5.6 μm, 10.7 μm, respectively.

be seen the overall width of each of the pointing stability values remains generally the same because the molecular focus is so narrow compared to the width of the distributions. The pointing stability distributions are normalized so that they have an area of unity to represent a probability distribution. The observed widths in figure 6.7 are calculated by a method similar to a convolution, the probability distribution is moved across the molecular focus in the y axis and the product of the calculated molecular focus and probability distribution yields the measurable signal. The results show that by having a pointing stability distribution which has a spatial extent larger than the molecular focus, the minimum spatial resolution is limited to the width of the pointing stability distribution. Additionally but equally important, is the overall signal strength is also significantly reduced as wider pointing stability distributions are used.

6.3 Conclusion

The effects of pointing stability in a molecular lens experiment have been determined numerically based on an experimental measurement of the pointing stability in a pulsed IR laser. The pointing stability can be separated into two regimes, long term drift and shot-to-shot stability. The long term drift in 10 Hz laser systems which occurs over many minutes could be corrected by using a feedback system which could average many shots and follow the mean of the laser shot distribution over time. Pulsed feedback control has been demonstrated by other researchers but only by using higher laser repetition rates[229, 230].

An analysis of the shot-to-shot variation from the laser showed it had a Gaussian distribution indicating that random factors were the main cause of the instability. To examine the effects of measuring a molecular focus created by a molecular lens which was in turn produced by a laser with pointing stability, several Gaussian distributions of various widths were used to represent the laser's pointing stability. This had the effect of decreasing the overall signal strength and placed a limit on the minimum resolution of detectable features to be approximately the width of the pointing stability distribution.

Finally, this analysis has shown it is possible to achieve a pointing stability of $< \pm 1$ μm, by eliminating laser shots which lie outside the desired accuracy range in a post experiment analysis, this would only work for microscopy type experiments and not for lithography experiments.

Chapter 7

Conclusion and future directions

In this chapter, a summary of the results from the experimental and numerical chapters is presented. Future directions and improvements are also discussed.

7.1 Summary of results

7.1.1 Theory

The centre-of-mass motion and molecular alignment induced by a molecular lens created by a seeded nonresonant IR laser beam was studied numerically. The alignment characteristics of CS_2 were calculated by solving a series of eigenvalue equations obtained from the stationary Schrödinger equation. These results were confirmed by also solving the time-dependent Schrödinger equation. Good agreement was found between the two methods. The expectation value $\langle\cos^2\theta_{l,c}\rangle_{J,M}$, for linearly and circularly polarised light was then thermally averaged to create an intensity dependent effective polarisability $\bar{\alpha}_{eff}(I)$, for a molecular ensemble at a temperature T_R. The ensemble effective polarisability $\bar{\alpha}_{eff}(I)$, was then used for linearly or circularly polarised light in simulations of the dipole force experiments.

The simulations of the dipole force involved using the effective polarisability to describe the acceleration and deceleration of molecules along the molecular beam axis caused by a molecular lens. The numerical results showed that the dipole force is significantly enhanced by the formation of pendular states. Linearly polarised light produced the strongest interaction compared to circularly polarised light. Both polarisations increased the dipole force compared to the average polarisability of the molecules. The dipole force was found to be strongly dependent on the rotational temperature since this parameter determines the number of rotational states occupied. Lower rotational states exhibit stronger alignment as the electric field confinement energy is much greater than the field-free energy of rotation. Additionally, the slope of the effective polarisability of a molecule with respect to the intensity is important as it can increase or decrease the dipole force depending on the alignment-saturation of a particular rotational state.

7.1.2 Experimental results

Alignment experiments

Using a molecular lens to measure the acceleration and deceleration of a beam of CS_2 molecules, the difference in dipole force between linearly and near circularly polarised light for a constant optical intensity, was 20 %. This was measured by recording the induced velocity change imparted to molecules which were ionised and detected by time-of-flight mass spectrometry. Maximum velocity changes of 10 m s^{-1} and 7.5 m s^{-1} were recorded for linearly and near circularly polarised light. By fitting our alignment-dependent dipole force model to the data, a rotational temperature of 35 K was found. This yielded an effective polarisability of 11.4×10^{-40} C m^2 V^{-1} with $\langle \cos^2 \theta_l \rangle = 0.49$ for linearly polarised light and 10.1×10^{-40} C m^2 V^{-1} with $\langle \cos^2 \theta_c \rangle = 0.28$ for circularly polarised light. Both values represent an increase from the field-free average polarisability of 9.7×10^{-40} C m^2 V^{-1}. The well depths of the optical Stark potential for the linearly and circularly polarised fields were 89 K and 74 K respectively. This produced a 25 % change in the dipole force and a 20 % change for equal beam intensities.

The downstream density at the focus of the molecular lens was probed by measuring the ion signal for both laser polarisations. The focal lengths for linearly and circularly polarised light were found to be separated by ~100 μm, although a small portion of this difference in focal length is attributed to the 6 % lower intensity beam for circularly polarised light. This means by altering the laser polarisation from linear to elliptically to circularly polarised light, the focal length can be smoothly altered over the ~100 μm focal range of the molecular lens.

These experimental results show that when seeded IR lasers are used to create a potential, the dipole force is no longer directly proportional to the spatial gradient of the intensity[148, 60]. This applies to all dipole force experiments and is not specific to the case of the molecular lens. The alignment-dependent dipole force was also found to be relatively robust to rotational temperature where at a relatively high temperature ($T_R = 35$ K), a 12 % difference in effective polarisability produced a 20 % difference in dipole force.

Bending mode experiment

The dipole force between the $\nu_2 = 1$ bent state of CS_2 and the linear ground state was measured. Using a molecular beam of $T_t \sim 12$ K, consisting of 23 % of $\nu_2 = 1$ molecules and 73 % of ground state molecules, the induced velocity change was recorded in acceleration and deceleration. Unfortunately, the results were not conclusive because of the large amount of error involved in the experiment. A fit to the data of the $\nu_2 = 1$ state, suggested a polarisability of $(7.7 \pm 2.2) \times 10^{-40}$ C m^2 V^{-1}. This means there is not a distinguishable difference in polarisability compared to the ground state. Further modeling and experimentation would be necessary to achieve a greater accuracy.

7.1.3 Effects of rotational states on a molecules focus

The focussing properties of individual rotational states of CS_2 and N_2 molecules in a molecular lens were simulated numerically. These molecules were chosen to compare the difference between less polarisable molecules (N_2) and highly polarisable molecules (CS_2).

For nitrogen, the presence of rotational states was found to alter the focus produced by the molecular lens. Separate rotational states were shown to have different focal lengths. Thermal averaging of the states from 0 K to 10 K showed the focal length of the molecular lens was increased by 80 μm to $f \approx 520$ μm. This represents a 26 % increase compared to the focal length of the ground state with $f \approx 460$ μm. The maximum molecule density over this temperature range was decreased by 30 %, caused by the increased population of the higher J levels, which have a lower effective polarisability and longer focal length.

For CS_2, the results showed that all quantum states below $\tilde{J} = 12$ focussed to effectively the same position at $f \approx 250$ μm. This is due to the small differences in effective polarisability between the states when perturbed by the electric field. States above $J = 14$ were found to focus at $f \approx 400$ μm, this also corresponds to the focal length produced by the average value of the polarisability for CS_2. For a significant amount of rotational states to be at or near $J = 14$, the rotational temperature would need to be approximately 40-50 K. This suggests varying the rotational temperature from 0 K to 50 K can increase the focal length of the CS_2 focus by up to 200 μm. The corresponding decrease in molecular density with this increase in focal length was 45 %.

In a separate section, a scheme was proposed to examine theoretically if it was possible to separate molecules depending on their effective polarisability. In this scheme, an aperture is placed in front of the molecular lens, limiting the molecular beam to the $+\omega/2$ region of the lens. The molecules are then deflected toward the centre of the laser beam and spread out downstream as they propagate. The downstream dispersion of the molecules depends on the effective polarisability of each rotational state. The simulations showed that the ground state and next two deflected states ($|\tilde{2}, 2\rangle$ and $|\tilde{2}, 1\rangle$) of N_2, were vertically separated by 10 μm when 5430 μm downstream from the molecular lens. As the optical field is only on for a short time, only 10 % of the molecules incident onto the aperture are deflected. The aperture in the molecular beam also reduces the amount of molecules which interact with the field and the estimated average molecular density of the deflected cloud of molecules is $\sim 10^8$ cm^{-3}.

7.1.4 Laser pointing stability

In a brief investigation, the effects of pointing stability on a molecular lens experiment were determined numerically using the results from an experimental measurement of the pointing stability of the pulsed IR laser used to form the molecular lens. The pointing stability of the IR laser was split into two regimes, short term shot-to-shot stability and long term laser beam position drift. The shot-to-shot stability refers to how much each laser shot can vary compared to the next. It was found that the distribution was well approximated by a Gaussian line-shape which describes the probability of a laser shot with spatial location x. If we define the shot-to-shot stability by a Gaussian shape which has an origin x_0, the long term drift relates to how much x_0 will move over time. Put alternatively, the probability distribution itself also moves in time, but on a much slower timescale.

A method similar to a convolution was employed to evaluate how the pointing stability in a laser which produces a molecular lens, will broaden the width of the corresponding molecule focus. A Gaussian probability distribution was used to represent the laser's pointing stability. Molecule trajectories in a molecular lens were simulated in order to determine the molecular focus formed by a laser without pointing stability. By using Gaussian line-shapes of various widths, the effect of using a laser with increasing pointing stability can be seen. Two main conclusions were drawn from the analysis, the first was that as the width of the molecular focus is often very narrow < 1 μm and the pointing stability distributions are relatively wide, > 10 μm, the resolution of detectable features in the molecular focus is limited to the width of the pointing stability distribution. This is because in general, as the molecular focus is extremely narrow compared to the pointing stability distribution of the laser, it acts in a similar fashion to a delta function, which when convolved with another function simply re-creates the original function. The second point, is that the overall signal strength is significantly reduced. By using normalised Gaussian line-shapes to represent a probability distribution, the convolved molecule focus is significantly reduced in molecular density as wider pointing stability distributions are used. For example, when a pointing stability distribution defined by a FWHM of 1 μm is used, the signal strength compared to a laser with no pointing stability is reduced by 30 %, for a FWHM of 5 μm, it is reduced by 74 %.

It was also concluded that it would be possible to actively measure which laser shots lie within a certain accuracy range during an experiment. With the lasers used in this work, it is estimated that for 3000 shots to lie within $< \pm 1$ μm of each other, it would require 30,000 shots or 50 minutes of laser shot sampling. By eliminating the data obtained from a laser shot which lies outside the desired accuracy range, the spatial resolution of the laser pointing stability can be improved. This method limits data to microscopy type measurements rather than lithography type experiments, since the analysis will be need to be done after the experiment has been carried out.

7.2 Future Directions

Future experiments and investigations could work toward realizing the deposition of molecular species onto a substrate. Even on the micron scale this would be a significant achievement. By crossing two IR beams perpendicular to each other, a convex rather than a cylindrical lens would be created. However, with decreasing molecular foci, the method of using another focussed laser beam to probe the molecular lens focus would become redundant as the maximum achievable spatial resolution of the probe laser would become comparable to the spot size of the molecular focus. Another method such as raster scanning the molecular focus with a very narrow edge would need to be implemented.

The idea of using helium atoms to probe surfaces has long been appealing because helium has a sub-nanometer de Broglie wavelength at thermal energies. It is also very sensitive to surface features because it is neutral, and has a very low energy (meV), when compared to the operating properties of an electron microscope or x-ray microscope, which operate in the 10-100 eV range. This means the helium atoms scatter elastically from the surface atoms do not penetrate into the substrate. The difficulty lies with creating a tightly focussed high density helium beam, for such studies, zonel plates[231], based on the wave nature of atoms can create helium atom images with a resolution of <2 μm[37]. The nonresonant dipole force could be used to create a helium microscope as it offers nanoscale resolution and in principle is simpler to apply, as the zonel plate methods require electron beam lithography to fabricate the plates.

Finally, using the alignment-dependent dipole force, I would like to see an experiment using the high spatial gradients of optical lattices to spatially separate rotational states in a molecular beam. This method could also be used to bring the molecules to rest, which could offer a route to nonpolar state selected cold molecules[39].

Bibliography

[1] T. Kinoshita, T. Wenger, D. S. Weiss, *Science* **305**, 1125 (2004).

[2] J. Ye, H. J. Kimble, H. Katori, *Science* **320**, 1734 (2008).

[3] T. Kinoshita, T. Wenger, D. S. Weiss, *Nature* **440**, 900 (2006).

[4] J. Doyle, B. Friedrich, R. V. Krems, F. Masnou-Seeuws, *Eur. Phys. J. D* **31**, 149 (2004).

[5] B. Damski, *et al.*, *Phys. Rev. Lett.* **90**, 110401 (2003).

[6] B. C. Sawyer, *et al.*, *Phys. Rev. Lett.* **98**, 253002 (2007).

[7] J. J. Hudsen, B. E. Sauer, M. R. Tarbutt, E. A. Hinds, *Phys. Rev. Lett.* **89**, 023003 (2002).

[8] E. R. Hudson, H. J. Lewandowski, B. C. Sawyer, J. Ye, *Phys. Rev. Lett.* **96**, 143004 (2006).

[9] M. T. Bell, A. D. Gingell, J. M. Oldham, T. P. Softley, S. Willitsch, *Farad. Dicuss.* **142**, 73 (2009).

[10] E. R. Hudson, N. B. Gilfoy, S. Kotochigova, J. M. Sage, D. DeMille, *Phys. Rev. Lett.* **100**, 203201 (2008).

[11] M. T. Bell, T. P. Softley, *Mol. Phys.* **107**, 99 (2009).

[12] A. Ashkin, *Phys. Rev. Lett.* **24**, 156 (1970).

[13] A. Ashkin, *Science* **210**, 1081 (1980).

[14] T. Seideman, *J. Chem. Phys.* **107**, 10420 (1997).

[15] M. Funk, *et al.*, *Optics Lett.* **34**, 139 (2009).

[16] C. Duefel, S. forth, C. R. Simmons, S. Dejgosha, M. D. Wang, *Nat. Meth.* **4**, 223 (2007).

[17] A. I. Bishop, T. A. Nieminen, R. Heckenberg, H. Rubinsztein-Dunlop, *Phys. Rev. Lett,* **92**, 198104 (2004).

[18] A. L. Porta, M. D. Wang, *Phys. Rev. Lett.* **92**, 190801 (2004).

[19] S. Chu, *Science* **253**, 861 (1991).

[20] D. N. Fuller, *et al.*, *Nucleic Acids Res.* **34**, 15 (2006).

[21] A. Ashkin, K. Schutze, J. M. Dziedrich, U. Euteneuer, M. Schliwa, *Nature* **348**, 346 (1990).

[22] Y. Tadir, *et al.*, *Hum. Reprod.* **6**, 1011 (1991).

[23] H. Liang, W. H. Wright, W. He, M. W. Berns, *Exp. Cell. Res.* **197**, 21 (1991).

[24] J. R. Moffit, Y. R. Chemla, S. B. Smith, C. Bustamante, *Annu. Rev. Biochem.* **77**, 205 (2008).

[25] C. N. Cohen-Tannoudji, *Rev. Mod. Phys.* **70**, 707 (1998).

[26] S. Chu, *Rev. Mod. Phys.* **70**, 685 (1998).

[27] W. D. Phillips, *Rev. Mod. Phys.* **70**, 721 (1998).

[28] H. J. Metcalf, P. van der Straten, *Laser cooling and trapping* (Springer, New York, 1999).

[29] S. L. Cornish, N. R. Claussen, J. L. Roberts, E. A. Cornell, C. E. Wieman, *Phys. Rev. Lett.* **85**, 1795 (2000).

[30] D. Meschede, H. Metcalf, *J. Phys. D: Appl. Phys.* **36**, 17 (2003).

[31] M. D. D. Rosa, *Eur. Phys. J. D* **31**, 395 (2004).

[32] T. Takekoshi, J. R. Yeh, R. J. Knize, *Op. Comm.* **114**, 421 (1995).

[33] S. Chu, J. E. Bjorkholm, A. Ashkin, A. Cable, *Phys. Rev. Lett.* **57**, 314 (1986).

[34] C. S. Adams, H. J. Lee, N. Davidson, M. Kasevich, S. Chu, *Phys. Rev. Lett.* **74**, 3577 (1995).

[35] B. J. Sussman, J. G. Underwood, R. Lausten, M. Y. Ivanov, A. Stolow, *Phys. Rev. A* **73**, 053403 (2006).

[36] R. Fulton, A. I. Bishop, P. F. Barker, *Phys. Rev. A.* **71**, 043404 (2005).

[37] T. Reisinger, B. Holst, *J. Vac. Sci. Technol. B* **26**, 2374 (2008).

[38] B. Friedrich, *Phys. Rev. A* **61**, 025403 (2000).

[39] P. F. Barker, *et al.*, *Faraday Dicuss.* (2009).

[40] S. Y. T. V. de Meerakker, H. L. Bethlem, G. Meijer, *Nature Phys.* **4**, 595 (2008).

[41] H. L. Bethlem, *et al.*, *J. Phys. B: At. Mol. Opt. Phys.* **39**, R263 (2006).

[42] J. R. Bochinski, E. R. Hudson, H. J. Lewandowski, G. Meijer, J. Ye, *Phys. Rev. Lett.* **91**, 243001 (2003).

[43] H. L. Bethlem, G. Berden, G. Meijer, *Phys. Rev. Lett.* **83**, 1558 (1999).

[44] S. Y. T. van de Meerakker, N. Vanhaecke, H. L. Bethlem, G. Meijer, *Phys. Rev. A* **73**, 023401 (2006).

[45] L. Scharfenberg, H. Haak, G. Meijer, S. Y. T. van der Meerakker, *Phys. Rev. A* **79**, 023410 (2009).

[46] S. Hoekstra, *et al.*, *Phys. Rev. A* **76**, 063408 (2007).

[47] B. C. Sawyer, *et al.*, *Phys. Rev. Lett.* **98**, 253002 (2007).

[48] J. J. Gilijamse, S. Hoekstra, S. Y. T. van de Meerakker, G. C. Groenenboom, G. Meijer, *Science* **313**, 1617 (2006).

[49] B. C. Sawyer, B. K. Stuhl, D. Wang, M. Yeo, J. Ye, *Phys. Rev. Lett.* **101**, 203203 (2008).

[50] T. D. Hain, T. J. Curtiss, *Chem. Phys. Lett.* **441**, 25 (2007).

[51] T. D. Hain, R. M. Morrison, T. J. Curtis, *J. Chem. Phys.* **111**, 6797 (1999).

[52] E. Narevicius, *et al.*, *Phys. Rev. A* **77**, 051401 (2008).

[53] E. Narevicius, *et al.*, *Phys. Rev. Lett.* **100**, 093003 (2008).

[54] T. Seideman, *Phys. Rev. A* **56**, 17 (1997).

[55] B. Friedrich, D. Herschbach, *Phys. Rev. Lett.* **74**, 4623 (1995).

[56] T. Seideman, *J. Chem. Phys.* **115**, 5965 (2001).

[57] T. Seideman, *J. Chem. Phys.* **111**, 4397 (1999).

[58] T. Seideman, *J. Chem. Phys.* **103**, 7887 (1995).

[59] B. S. Zhao, *et al.*, *J. Chem. Phys.* **119**, 8905 (2003).

[60] H. Stapelfeldt, H. Sakai, E. Constant, P. B. Corkum, *Phys. Rev. Lett.* **79**, 2787 (1997).

[61] R. Fulton, A. Bishop, P. F. Barker, *Phys. Rev. Lett.* **93**, 243004 (2004).

[62] H. Sakai, *et al.*, *J. Chem. Phys.* **110**, 10235 (1999).

[63] J. J. Larsen, H. Sakai, C. P. Safvan, I. Wendt-Larsen, H. Stapelfeldt, *J. Chem. Phys.* **111**, 7774 (1999).

[64] R. Fulton, A. I. Bishop, P. F. Barker, *Phys. Rev. A* **71**, 043404 (2005).

[65] D. Meschede, H. Metcalf, *J. Phys. D: Appl. Phys.* **36**, 17 (2003).

[66] G. Timp, R. E. Beheringer, D. M. Tennant, J. E. Cunningham, *Phys. Rev. Lett* **69**, 1636 (1992).

[67] J. J. McClelland, R. E. Scholten, E. C. Palm, R. J. Celotta, *Science* **262**, 877 (1993).

[68] R. W. McGowan, D. M. Giltner, S. A. Lee, *Optics Lett.* **20**, 2535 (1995).

[69] F. Lison, *et al.*, *App. Phys. B: Las. Opt.* **65**, 419 (1997).

[70] R. Ohmukai, S. Urabe, M. Watanabe, *App. Phys. B: Las. Opt.* **77**, 415 (2003).

[71] E. te Sligate, *et al.*, *App. Phys. Lett.* **85**, 4493 (2004).

[72] D. Egorov, T. Lahaye, W. Schöllkopf, B. Friedstrrich, J. M. Doyle, *Phys. Rev. A* **66**, 043401 (2002).

[73] P. S. Julienne, *Faraday Dicuss.* **142**, 361 (2009).

[74] G. Scoles, *Atomic and Molecular Beam Methods, Vol 1 & 2* (Oxford University Press, New York, 1988 & 1992).

[75] R. J. Gordon, L. Zhu, W. A. Schroeder, T. Seideman, *J. App. Phys* **94**, 669 (2003).

[76] T. Seideman, *J. Chem. Phys.* **106**, 2881 (1997).

[77] H. Sakai, *et al.*, *Phys. Rev. A* **57**, 2794 (1998).

[78] R. Fulton, A. I. Bishop, M. N. Schneider, P. F. Barker, *Nature Phys.* **2**, 465 (2006).

[79] R. Fulton, A. I. Bishop, M. N. Schneider, P. F. Barker, *J. Phys. B: At. Mo. Op. Phys.* **39**, S1097 (2006).

[80] P. Barletta, J. Tennyson, P. F. Barker, *Phys. Rev. A* **78**, 052707 (2008).

[81] V. Aquilanti, *et al.*, *Phys. Chem. Chem. Phys.* **7**, 291 (2005).

[82] R. Velotta, N. Hay, M. B. Mason, M. Castillejo, J. P. Marangos, *Phys. Rev. Lett.* **87**, 183901 (2001).

[83] B. Friedrich, D. Herschbach, *Chem. Phys. Lett.* **262**, 41 (1996).

[84] J. J. Larsen, I. Wendt-Larsen, H. Stapelfeldt, *Phys. Rev. Lett.* **83**, 1123 (1999).

[85] J. Itatani, *et al.*, *Nature* **432**, 897 (2004).

[86] B. Friedrich, D. P. Pullman, D. R. Herschbach, *J. Phys. Chem.* **95**, 8118 (1991).

[87] M. P. Sinha, C. D. Caldwell, R. N. Zare, *J. Chem. Phys.* **61**, 491 (1974).

[88] H. G. Rubahn, J. P. Toennies, *J. Chem. Phys.* **89**, 287 (1988).

[89] A. G. Visser, J. P. Bekooy, L. K. van der Meij, C. de Vreugd, J. Korving, *Chem. Phys.* **20**, 391 (1977).

[90] W. R. Sanders, J. B. Anderson, *J. Chem. Phys.* **88**, 4479 (1984).

[91] A. Lübbert, G. Rotzoll, F. Günther, *J. Chem. Phys.* **69**, 5174 (1978).

[92] P. R. Brooks, *Science* **193**, 11 (1976).

[93] T. Kasai, *et al.*, *Rev. Sci. Inst.* **64**, 1150 (1993).

[94] V. A. Cho, R. B. Bernstein, *J. Phys. Chem.* **95**, 8129 (1991).

[95] M. Wu, R. J. Bemish, R. E. Miller, *J. Chem. Phys.* **101**, 9447 (1994).

[96] A. Mattheus, A. Fischer, G. Ziegler, E. Gottwald, K. Bergmann, *Phys. Rev. Lett.* **56**, 712 (1986).

[97] A. F. Linskens, N. Dam, J. Reuss, *J. Chem. Phys.* **101**, 9384 (1994).

[98] T. Seideman, *Phys. Rev. Lett.* **83**, 4971 (1999).

[99] B. Friedrich, D. Herschbach, *J. Phys. Chem.* **99**, 15686 (1995).

[100] H. Stapelfeldt, T. Seideman, *Rev. Mod. Phys.* **75**, 543 (2003).

[101] M. Artamoniv, T. Seideman, *J. Chem. Phys.* **128**, 154313 (2008).

[102] J. P. Heritage, T. K. Gustafson, C. H. Lin, *Phys. Rev. Lett.* **34**, 1299 (1975).

[103] L. Fonda, N. Mankoc, M. Rosina, *Il Nuovo Cimento* **7**, 437 (1986).

[104] D. Normand, L. A. Lompre, C. Cornaggia, *J. Phys. B* **25**, 497 (1992).

[105] W. Kim, P. Felker, *J. Chem. Phys.* **104**, 1147 (1996).

[106] D. H. Parker, A. T. J. B. Eppink, *J. Chem. Phys.* **107**, 2357 (1997).

[107] F. Rosca-Pruna, M. J. J. Vrakking, *Phys. Rev. Lett.* **87**, 153902 (2001).

[108] J. J. Larsen, K. Hald, N. Bjerre, H. Stapelfeldt, *Phys. Rev. Lett.* **85**, 2470 (2000).

[109] J. G. Underwood, B. J. Sussman, A. Stolow, *Phys. Rev. Lett.* **94**, 143002 (2005).

[110] D. Daems, *et al.*, *Phys. Rev. Lett.* **95**, 063005 (2005).

[111] A. Rousée, S. Guérin, V. Boudon, B. Lavorel, O. Faucher, *Phys. Rev. A* **73**, 033418 (2006).

[112] S. Ramakrishna, T. Seideman, *Phys. Rev. A* **77**, 053411 (2008).

[113] B. J. Sussman, D. Townsend, M. Y. Ivanov, A. Stolow, *Science* **314**, 278 (2006).

[114] C. B. Madsen, *et al.*, *Phys. Rev. Lett.* **102**, 073007 (2009).

[115] M. S. Molodenskiy, O. V. Tikhonova, *Las. Phys.* **17**, 401 (2007).

[116] T. P. Rakitzis, A. van den Brom, M. H. M. Janssen, *Science* **303**, 1852 (2004).

[117] A. Sugita, *et al.*, *J. Chem. Phys.* **112**, 7095 (2000).

[118] S. Y. T. van der Meerakker, *Faraday Discuss.* **142**, 113 (2009).

[119] S. S. Viftrup, *et al.*, *Phys. Rev. Lett.* **99**, 143602 (2007).

[120] D. Pinkham, T. Vogt, R. R. Jones, *J. Chem. Phys.* **129**, 064307 (2008).

[121] V. Loriot, E. Hertz, B. Lavorel, O. Faucher, *J. Phys. B: At. Mol. Opt. Phys.* **41**, 015604 (2008).

[122] I. V. Litinyuk, *et al.*, *Phys. Rev. Lett.* **90**, 233003 (2003).

[123] M. Haas, U. D. Jentschura, C. H. Keitel, *Am. J. Phys.* **74**, 77 (2006).

[124] B. W. Shore, *The Theory of Coherent Atomic Excitation, Vol. II* (Wiley, New York, 1990).

[125] T. Seideman, E. Hamilton, *Adv. At. Mol. Opt. Phys.* **52**, 289 (2006).

[126] R. W. Boyd, *Nonlinear Optics* (Academic Press, London, 2003).

[127] A. Keller, C. M. Dion, O. Atabek, *Phys. Rev. A* **61**, 023409 (2000).

[128] F. Rosca-Pruna, M. J. Vrakking, *J. Chem. Phys.* **116**, 6579 (2002).

[129] P. S. Pershan, J. P. van der Ziel, L. D. Malmstrom, *Phys. Rev.* **143**, 574 (1966).

[130] D. A. Long, *The Raman effect* (John Wiley and Sons, 2001).

[131] D. R. Lide, *Handbook of chemistry and physics 85th edition* (CRC Press, Florida, 2004).

[132] W. C. Wiley, I. H. McLaren, *Rev. Sci. Inst.* **26**, 1150 (1955).

[133] www.simion.

[134] J. L. Wiza, *Nuclear Instruments and Methods* **162**, 587 (1979).

[135] www.elmul.com.

[136] *El-Mul detector catalgoue.*

[137] S. Couris, *et al.*, *J. Chem. Phys* **100**, 3514 (1994).

[138] E. de Hoffman, V. Stroobant, *Mass Spectrometry: Principles and Applications, 3rd Edition* (Wiley, Chichester, 2007).

[139] L. Zhang, *et al.*, *J. Chem. Phys.* **114**, 10768 (2001).

[140] J. Baker, M. Konstantaki, S. Couris, *J. Chem. Phys.* **103**, 2436 (1995).

[141] R. A. Morgan, *et al.*, *J. Chem. Phys.* **104**, 6117 (1996).

[142] www.photonicsolutions.com, www.exciton.com.

[143] C. Cossart-Magos, M. Horani, *J. Chem. Phys* **104**, 7412 (1996).

[144] W. Demtröder, *Laser Spectroscopy: Basic Concepts and Instrumentation* (Springer, New York, 2003).

[145] H. H. Telle, A. U. Urena, R. J. Donovan, *Laser Chemistry* (Wiley, New York, 2007).

[146] A. E. Siegman, *Lasers* (University Science Books, California, 1986).

[147] E. Hecht, *Optics fourth edition* (Addison Wesley, San Francisco, 2002).

[148] H. S. Chung, *et al.*, *J. Chem. Phys.* **114**, 8293 (2001).

[149] R. Campargue, *J. Chem. Phys.* **88**, 4466 (1984).

[150] H. R. Murphy, D. R. Miller, *J. Phys. Chem.* **88**, 4474 (1984).

[151] H. Pauly, *Atom, Molecule, and Cluster Beam: Cluster beams, fast and slow beams, accessory equipment and applications* (Springer, New York, 2000).

[152] R. L. Byer, M. D. Duncan, *J. Chem. Phys* **74**, 2174 (1981).

[153] F. Luo, G. C. McBane, G. Kim, C. F. Giese, W. R. Gentry, *J. Chem. Phys.* **98**, 3564 (1993).

[154] R. Resnick, D. Haliday, K. S. Krane, *Physics 4th ed.* (John Wiley & Sons Inc., New York, 1992).

[155] M. Hillenkamp, S. Keinan, U. Even, *J. Chem. Phys.* **118**, 8699 (2003).

[156] V. Kumarappan, C. Z. Bisgaard, S. S. Viftrup, L. Holmegaard, H. Stapelfeldt, *J. Chem. Phys.* **125**, 194309 (2006).

[157] S. K. Tokunga, *Production and Stark deceleration of lithium hydirde molecules* (Ph.D Thesis, Imperial College London, www8.imperial.ac.uk/content/dav/ad/workspaces/ccm/Tokunaga_thesis.pdf, 2009).

[158] H. Lefebvre-Brion, R. W. Field, *Perturbations in the spectra of diatomic molecules* (Academic, Orlando, 1986).

[159] G. Herzberg, E. Teller, *Z. Phys. Chem. B* **21**, 410 (1933).

[160] J. D. Greybeal, *Molecular spectroscopy* (McGraw-Hill, New York, 1988).

[161] G. Herzberg, *Spectra of diatomic molecules* (Academic, Orlando, 1938).

[162] R. A. Morgan, *et al.*, *Int. J. Mass Spect Ion Processes* **159**, 1 (1996).

[163] S. Liu, *et al.*, *J. Chem. Phys.* **102**, 3617 (1995).

[164] I. Fischer, *et al.*, *Chem. Phys. Lett.* **202**, 542 (1993).

[165] R. McDiarmid, J. P. Doering, *J. Chem. Phys.* **91**, 2010 (1989).

[166] D. R. Miller, R. P. Andres, *J. Chem. Phys.* **1967**, 3418 (46).

[167] S. Yamzaki, M. Taki, Y. Fujitani, *J. Chem. Phys.* **78**, 4476 (1981).

[168] C. Douketis, T. E. Gough, G. Scoles, H. Wang, *J. Chem. Phys.* **88**, 4484 (1984).

[169] K. O. Lantz, V. Vaida, *Chem. Phys. Lett.* **184**, 152 (1991).

[170] E. Riedle, T. Knittel, T. Weber, H. J. Neusser, *J. Chem. Phys.* **91**, 4555 (1989).

[171] M. N. R. Ashfold, *Molec. Phys.* **58**, 1 (1986).

[172] H. Meyer, *Chem. Phys. Lett.* **262**, 603 (1996).

[173] G. C. Nieman, *J. Chem. Phys.* **75**, 584 (1981).

[174] R. Fulton, *Heriot-Watt Univeristy, Ph. D Thesis* (2006).

[175] D. S. Kummli, H. M. Frey, S. Leutwyler, *J. Chem. Phys.* **124**, 144307 (2006).

[176] G. Herzberg, *Molecular Spectra and Molecular Structure III: Electronic spectra and electronic structure of polyatomic molecules* (Van Nostrand Reinhold, New York, 1966).

[177] H. Haken, H. C. Wolf, *Molecular Physics and Elements of Quantum Chemistry, Introduction to experiments and Theory, 2nd Ed.* (Springer, 2004).

[178] D. T. Cramb, H. Bitto, J. R. Huber, *J. Chem. Phys.* **96**, 8761 (1992).

[179] R. N. Dixon, J. M. Bayley, M. N. R. Ashfold, *Chem. Phys.* **84**, 21 (1984).

[180] M. N. R. Ashfold, R. N. Dixon, *Chem. Phys. Lett.* **93**, 5 (1982).

[181] C. Mainos, Y. L. Duff, E. Boursey, *Molec. Phys.* **56**, 1165 (1985).

[182] D. M. Brink, G. R. Satchler, *Angular Momentum* (Clarendon Press, Oxford, 1993).

[183] A. R. Edmonds, *Angular Momentum in Quantum Mechanics* (Princeton University Press, Princeton, 1996).

[184] M. N. R. Ashfold, R. N. Dixon, R. J. Stickland, *Chem. Phys.* **88**, 463 (1984).

[185] C. Cossart-Magos, H. Lefebve-Brion, M. Jungen, *Molec. Phys.* **85**, 821 (1995).

[186] W. M. McClain, *J. Chem. Phys.* **57**, 2264 (1972).

[187] H. Mori, T. Nimi, I. Akiyama, T. Tsuzuki, *Phys. Fluids* **17**, 117103 (2005).

[188] B. S. Zhao, *et al.*, *Phys. Rev. Lett.* **85**, 2705 (2000).

[189] A. B. Haj-Yedder, *et al.*, *Phys. Rev. A* **66**, 063401 (2002).

[190] E. Hamilton, *et al.*, *Phys. Rev. A* **72**, 043402 (2005).

[191] J. Ortigoso, M. Rodriguez, M. Gupta, B. Friedrich, *J. Chem. Phys* **110**, 3870 (1999).

[192] A. D. Bandrauk, Y. Fujimura, R. J. Gordon, *Laser control and manipulations of molecules* (Oxford University Press, Oxford, 2002).

[193] M. Abramowitz, I. A. Stegun, *Handbook of Mathematical Functions with Formulas, Graphs, and Mathematical Tables, 10th Ed.* (National Bureau of Standards, Washington, 1972).

[194] S. Thomas, S. Guerin, H. R. Jauslin, *Phys. Rev. A* **71**, 013402 (2005).

[195] E. Peronne, M. D. Puolsen, C. Z. Bisgaard, H. Stapelfeldt, T. Seideman, *Phys. Rev. Lett.* **91**, 043003 (2003).

[196] M. Machholm, N. E. Henriksen, *Phys. Rev. Lett.* **87**, 193007 (2001).

[197] M. Macholm, *J. Phys. Chem.* **115**, 10724 (2001).

[198] C. M. Dion, *et al.*, *Phys. Rev. A* **65**, 063408 (2002).

[199] P. B. Corkum, *et al.*, *Faraday Diss.* **113**, 47 (1999).

[200] P. Dietrich, P. B. Corkum, *J. Chem. Phys.* **97**, 3187 (1992).

[201] N. Bras, E. C. de Lara, *J. Chem. Phys.* **102**, 6990 (1995).

[202] D. M. Bishop, *Rev. Mod. Phys.* **62**, 343 (1990).

[203] S. H. Brewer, S. Franzen, *J. Chem. Phys.* **119**, 851 (2003).

[204] D. J. Malik, C. E. Dykstra, *J. Chem. Phys.* **83**, 6307 (1985).

[205] M. A. Morrison, P. J. Hey, *J. Chem. Phys.* **70**, 4034 (1979).

[206] X. J. Gu, N. R. Isenor, G. Scoles, *Phys. Rev. A* **39**, 413 (1989).

[207] W. Q. Cai, T. E. Gough, X. J. Gu, N. R. Isenor, G. Scoles, *Phys. Rev. A* **36**, 4722 (1987).

[208] M. L. Guennec, K. Evain, B. Illien, *J. Molec. Struc.* **542**, 167 (2001).

[209] M. Guerreiro, N. Bras, M. Blain, J. Leclercq, *Chem. Phys. Lett.* **274**, 315 (1997).

[210] K. H. Illinger, C. P. Smyth, *J. Chem. Phys.* **32**, 787 (1960).

[211] M. F. Costa, M. C. C. Ribeiro, *Quim. Nova* **29**, 1266 (2006).

[212] D. M. Bishop, L. M. Cheung, *J. Phys. Chem. Ref. Data* **11**, 1982 (119).

[213] G. O. Sørensen, U. G. Jørgenson, *J. Chem. Phys.* **97**, 4616 (1992).

[214] M. P. Boogaard, R. Haines, *Mole. Phys.* **41**, 1281 (1980).

[215] R. Fulton, A. I. Bishop, M. N. Schneider, P. F. Barker, *Nat. Phys.* **2**, 465 (2006).

[216] P. F. Barker, M. N. Schneider, *Phys. Rev. A* **64**, 033608 (2001).

[217] P. F. Barker, M. N. Schneider, S. M. Purcell, *Phys. Rev. A* **77**, 063409 (2008).

[218] P. Dietrich, P. B. Corkum, D. T. Strickland, M. Laberge, *Molecules in Laser Fields, edited by A. D. Bandrauk* (Dekker, New York).

[219] G. Dong, W. Lu, P. F. Barker, *J. Chem. Phys.* **118**, 1729 (2003).

[220] S. Potting, M. Cramer, C. H. Schwaib, A. Pu, P. Meystre, *Phys. Rev. A* **64**, 023604 (2001).

[221] L. Holmegaard, *et al.*, *Phys. Rev. Lett.* **102**, 023001 (2009).

[222] F. Liu, M. Jin, D. Ding, *Chin. Phys. Lett.* **23**, 1165 (2006).

[223] F. Liu, M. Jin, X. Gao, D. Ding, *Chin. Phys. Lett.* **23**, 344 (2006).

[224] B. K. Agarwal, H. Prakash, *Quantum Mechanics* (Prentice-Hall of India, New Dehli, 2004).

[225] R. P. Feyman, *Phys. Rev.* **56**, 340 (1939).

[226] T. Kanai, H. Sakai, *J. Chem. Phys.* **115**, 5492 (2001).

[227] Y. Lim, *Problems and solutions on atomic, nuclear and particle physics* (World Scientific, London, 2000).

[228] S. Graftstrom, U. Harbarth, J. Kowalski, R. Neumann, J. Noehte, *Opt. Comm.* **65**, 121 (1988).

[229] F. Breitling, R. S. Weigal, M. C. Downer, T. Tajima, *Rev. Sci. Inst.* **72**, 2 (2000).

[230] I. Yamada, K. Narihara, K. Yamauchi, H. Hayashi, *Rev. Sci. Inst.* **72**, 1 (2000).

[231] B. S. Zhao, S. A. Schulz, S. A. Meek, G. Meijer, W. Schöllkopf, *Phys. Rev. A* **78**, 010902 (2008).

Appendix

All programs were written in Matlab. The first uses the stationary Schödinger equation to diagonalize the Hamiltonian matrix to calculate $\langle \cos^2 \theta_{l,c} \rangle$.

```
function Eigenvalues
clear all;
tic
global J M g;
%t = [0:0.25:80]';
%p = length(t);
Jmax = 50;
M = 0;
J = (0:Jmax).*2;
g = length(J);

%field and molecule properties
%x = 40;
%sigma  = 60;
%k = exp(-((t(s,1)-x)^2)/(sigma));
r = [0:0.01:1]';
l = length(r);
for s=1:l
I = r(s,1)*10;%0.5763;%0.5763*
dw = I*((0.81*2.73e9^2)/(4*3.96e-23))*1e-40; %dw = dalpha*field^2/4B
wp = I*(1.63e-40*2.73e9^2)/(4*3.96e-23);
wpara = I*(2.44e-40*2.73e9^2)/(4*3.96e-23);

%Each row of matrix multiplied by column probability vector


    F1 = D(J,M);
    f1 = D(J,M).*-dw;
    %f1 = D(J,M).*dw.*0.5;
    f2 = C(J,M).*-dw-wp+A(J);
    %f2 = C(J,M).*dw.*0.5+A(J)-wp*0.5-wpara*0.5;
    f3 = B(J,M).*-dw;
    %f3 = B(J,M).*dw.*0.5;
    v1 = diag(f1,1);
    v2 = diag(f2,0);
    v3 = diag(f3,-1);
    l = length(v1);
    v1(:,l) = []; v1(l,:) = [];
    v3(:,l) = []; v3(l,:) = [];
    T = v1+v2+v3;
    [V,D] = eig(T);

    %calculate expectation value
    F2 = C(J,M);
```

```
    F3 = B(J,M);
    V1 = diag(F1,0); V2 = diag(F2,0); V3 = diag(F3,0);
    %creating diagonal matrices
        for n = 1:g
            c = V(:,n);
            B1 = (V3*c)’; c1 = c;
            B1(:,1) = [];
            c1(l-1,:) = [];
            expecB = B1*c1;
            expecC = (V2*c)’*c;
            D1 = (V1*c)’; c2 = c;
            c2(1,:) = [];
            D1(:,l-1) = [];
            expecD = D1*c2;
            E(:,n) = expecB+expecD+expecC;
        end
        E(1:1);

        k(s,1) = E(1,2);
end
data = [r k];
%save(’11’,’data’,’-ASCII’);
%1-1/(sqrt(dw))
hold on
plot(r,k)
function [a] = A(J)
a = J.*(J+1);
function [b] = B(J,M)
b = (1./((2.*J)-1)).*sqrt(((J+abs(M)).*(J+abs(M)-1).*(J-abs(M))
.*(J-abs(M)-1))./(((2.*J)+1).*((2.*J)-3)));
function [c] = C(J,M)
c =((1/3)+(2/3).*(J.*(J+1)-3.*M.^2)./(((2.*J)-1).*((2.*J)+3)));
function [d] = D(J,M)
d = (1./((2.*J)+3)).*sqrt( ((J+abs(M)+2).*(J+abs(M)+1).*(J-abs(M)+2)
.*(J-abs(M)+1))./(((2.*J)+5).*((2.*J)+1)));
```

This program does the same as above but thermally averages the expectation values to plot $\langle \cos^2 \theta_{l,c} \rangle$ as a function of rotational temperature. Both linearly and circularly polarised light cases are included.

```
function Eigenvalues
clear all;
tic
global J M g T;
Jmax = 150;
Matrix = zeros(Jmax/2,Jmax/2);
g = length(Matrix);
for Temp=1:50
%create column matrix containing J state thermal population
R = 2.16e-24; %rotational constanst
kT  = Temp*1.38e-23; %temp x boltzman
K = (0:Jmax/2-1)*2;
Q1 = ((2.*K)+1).*exp(-(R.*K.*(K+1))./kT); %Partition function
Qr = sum(Q1);
p = ((exp(-R.*K.*(K+1)./kT))./Qr)';
%field and molecule properties
dw = 0.5763*((10.6*2.73e9^2)/(4*2.16e-24))*1e-40; %dw = dalpha*field^2/4B
wp = 0.5763*(6.2e-40*2.73e9^2)/(4*2.16e-24);
wpara = 0.5763*(16.8e-40*2.73e9^2)/(4*2.16e-24);
%1-1/(sqrt(0.5763*dw))
k = 1;
m = 2;
%Each row of matrix multiplied by column probability vector
for s=1:Jmax/2
    M = s-1;
    J = (s-k:Jmax/2+s-k).*2;
    F1 = D(J,M);
    %f1 = D(J,M).*dw.*0.5;%circulary
    f1 = D(J,M).*-dw;%linearly
    %f2 = C(J,M).*dw.*0.5+A(J)-wp*0.5-wpara*0.5;%circularly
    f2 = C(J,M).*-dw-wp+A(J);%linearly
    %f3 = B(J,M).*dw.*0.5;%circulary
    f3 = B(J,M).*-dw;%linearly
    v1 = diag(f1,1);
    v2 = diag(f2,0);
    v3 = diag(f3,-1);
    l = length(v1);
    v1(:,l) = []; v1(l,:) = [];
    v3(:,1) = []; v3(1,:) = [];
    T = v1+v2+v3;
    [V,D] = eig(T);

    %calculate expectation value
    F2 = C(J,M);
    F3 = B(J,M);
    V1 = diag(F1,0); V2 = diag(F2,0); V3 = diag(F3,0);
    %creating diagonal matrices
        for n = 1:g
            c = V(:,n);
            B1 = (V3*c)'; c1 = c;
            B1(:,1) = [];
            c1(l-1,:) = [];
            expecB = B1*c1;
            expecC = (V2*c)'*c;
            D1 = (V1*c)'; c2 = c;
            c2(1,:) = [];
```

```
            D1(:,l-1) = [];
            expecD = D1*c2;
            E(:,n) = expecB+expecD+expecC;
        end
        %This section puts each row into the matrix which is then
        %multiplied by p
        if s==1
        Matrix(s,s:g) = E;
        elseif mod(s,2) == 0
               k =k+1;
               k1 = k-2;
               E(:,g-s+k:g) = [];
               Matrix(s,s-k1:g) = E;
        else
               m = m+1;
               m1=m-2;
               E(:,g-s+m:g) = [];
               Matrix(s,s-m1:g) = E;
        end

end

    %contains expec of each J (columns) and M (rows)
    h = [Matrix(1,1:g);Matrix(2:g,1:g).*2];
    %h(1:10,1:10); %displays sum of expectation value for each J. i.e
    expect(Temp,1) = Temp;
    expect(Temp,2) = sum(h)*p;%sum(h) and p both vectors

end
%expect
%save('cir50','expect','-ASCII');
plot(expect(:,1),expect(:,2))


toc
function [a] = A(J)
a = J.*(J+1);
function [b] = B(J,M)
b = (1./((2.*J)-1)).*sqrt(((J+abs(M)).*(J+abs(M)-1).*(J-abs(M))
.*(J-abs(M)-1))./(((2.*J)+1).*((2.*J)-3)));
function [c] = C(J,M)
c =((1/3)+(2/3).*(J.*(J+1)-3.*M.^2)./(((2.*J)-1).*((2.*J)+3)));
function [d] = D(J,M)
d = (1./((2.*J)+3)).*sqrt( ((J+abs(M)+2).*(J+abs(M)+1).*(J-abs(M)+2)
.*(J-abs(M)+1))./(((2.*J)+5).*((2.*J)+1)));
```

This program uses the time dependent Schödinger equation to calculate $\langle \cos^2\theta_l \rangle$ for linearly polarised light.

```
function odefun
tic
global m;
global J;
matrix = [];
J = 0;
m = 0;
tspan = [0:0.25:80];
P = zeros([14 1]);
y0 = [1;0;0;0;0;0;0;0;0;0;0;0;0;P];
error = 1e-9*[1:27];
options = odeset('RelTol',1e-11,'AbsTol',error);
%for s=7:11
%   J=2*s;
%expec = [];
%for m=0:((2*J)+18)


[t,y] = ode113(@odefun,tspan,y0,options);

data = [t abs(y(:,1)).^2 abs(y(:,2)).^2 abs(y(:,3)).^2 abs(y(:,4)).^2 ...
       abs(y(:,5)).^2 abs(y(:,6)).^2 abs(y(:,7)).^2 abs(y(:,8)).^2 ...
       abs(y(:,9)).^2 abs(y(:,10)).^2 abs(y(:,11)).^2 abs(y(:,12)).^2 ...
       abs(y(:,13)).^2 abs(y(:,14)).^2 abs(y(:,15)).^2 abs(y(:,16)).^2 ...
       abs(y(:,17)).^2 abs(y(:,18)).^2 abs(y(:,19)).^2 abs(y(:,20)).^2 ...
       abs(y(:,21)).^2 abs(y(:,22)).^2 abs(y(:,23)).^2 abs(y(:,24)).^2 ...
       abs(y(:,25)).^2 abs(y(:,26)).^2 abs(y(:,27)).^2];
       l = length(t');
       a = zeros([l 1]);
       b = zeros([l 1]);
       c = zeros([l 1]);
       for n=1:l

data2=conj(y(n,1))*y(n,2)*B(J+2,m)+conj(y(n,2))*y(n,3)*B(J+4,m) ...
      +conj(y(n,3))*y(n,4)*B(J+6,m)+conj(y(n,4))*y(n,5)*B(J+8,m) ...
      +conj(y(n,5))*y(n,6)*B(J+10,m)+conj(y(n,6))*y(n,7)*B(J+12,m) ...
      +conj(y(n,7))*y(n,8)*B(J+14,m)+conj(y(n,8))*y(n,9)*B(J+16,m) ...
      +conj(y(n,9))*y(n,10)*B(J+18,m)+conj(y(n,10))*y(n,11)*B(J+20,m) ...
      +conj(y(n,11))*y(n,12)*B(J+22,m)+conj(y(n,12))*y(n,13)*B(J+24,m) ...
      +conj(y(n,13))*y(n,14)*B(J+26,m)+conj(y(n,14))*y(n,15)*B(J+28,m) ...
      +conj(y(n,15))*y(n,16)*B(J+30,m)+conj(y(n,16))*y(n,17)*B(J+32,m) ...
      +conj(y(n,17))*y(n,18)*B(J+34,m)+conj(y(n,18))*y(n,19)*B(J+36,m) ...
      +conj(y(n,19))*y(n,20)*B(J+38,m)+conj(y(n,20))*y(n,21)*B(J+40,m) ...
      +conj(y(n,21))*y(n,22)*B(J+42,m)+conj(y(n,22))*y(n,23)*B(J+44,m) ...
      +conj(y(n,23))*y(n,24)*B(J+46,m)+conj(y(n,24))*y(n,25)*B(J+48,m) ...
      +conj(y(n,25))*y(n,26)*B(J+50,m)+conj(y(n,26))*y(n,27)*B(J+52,m);
      a(n,1)=data2;

data4=conj(y(n,2))*y(n,1)*D(J,m)+conj(y(n,3))*y(n,2)*D(J+2,m) ...
      +conj(y(n,4))*y(n,3)*D(J+4,m)+conj(y(n,5))*y(n,4)*D(J+6,m) ...
      +conj(y(n,6))*y(n,5)*D(J+8,m)+conj(y(n,7))*y(n,6)*D(J+10,m) ...
      +conj(y(n,8))*y(n,7)*D(J+12,m)+conj(y(n,9))*y(n,8)*D(J+14,m) ...
      +conj(y(n,10))*y(n,9)*D(J+16,m)+conj(y(n,11))*y(n,10)*D(J+18,m) ...
      +conj(y(n,12))*y(n,11)*D(J+20,m)+conj(y(n,13))*y(n,12)*D(J+22,m) ...
      +conj(y(n,14))*y(n,13)*D(J+24,m)+conj(y(n,15))*y(n,14)*D(J+26,m) ...
      +conj(y(n,16))*y(n,15)*D(J+28,m)+conj(y(n,17))*y(n,16)*D(J+30,m) ...
      +conj(y(n,18))*y(n,17)*D(J+32,m)+conj(y(n,19))*y(n,18)*D(J+34,m) ...
```

```
      +conj(y(n,20))*y(n,19)*D(J+36,m)+conj(y(n,21))*y(n,20)*D(J+38,m) ...
      +conj(y(n,22))*y(n,21)*D(J+40,m)+conj(y(n,23))*y(n,22)*D(J+42,m) ...
      +conj(y(n,24))*y(n,23)*D(J+44,m)+conj(y(n,25))*y(n,24)*D(J+46,m) ...
      +conj(y(n,26))*y(n,25)*D(J+48,m)+conj(y(n,27))*y(n,26)*D(J+50,m);
      b(n,1) = data4;

data1=abs(y(n,1)).^2*H(J,m)+abs(y(n,2)).^2*H(J+2,m) ...
      +abs(y(n,3)).^2*H(J+4,m)+abs(y(n,4)).^2*H(J+6,m) ...
      +abs(y(n,5)).^2*H(J+8,m)+abs(y(n,6)).^2*H(J+10,m) ...
      +abs(y(n,7)).^2*H(J+12,m)+abs(y(n,8)).^2*H(J+14,m) ...
      +abs(y(n,9)).^2*H(J+16,m)+abs(y(n,10)).^2*H(J+18,m)...
      +abs(y(n,11)).^2*H(J+20,m)+abs(y(n,12)).^2*H(J+22,m) ...
      +abs(y(n,13)).^2*H(24,m)+abs(y(n,14)).^2*H(J+26,m) ...
      +abs(y(n,15)).^2*H(J+28,m)+abs(y(n,16)).^2*H(J+30,m) ...
      +abs(y(n,17)).^2*H(J+32,m)+abs(y(n,18)).^2*H(J+34,m) ...
      +abs(y(n,19)).^2*H(J+36,m)+abs(y(n,20)).^2*H(J+38,m) ...
      +abs(y(n,21)).^2*H(J+40,m)+abs(y(n,22)).^2*H(J+42,m) ...
      +abs(y(n,23)).^2*H(J+44,m)+abs(y(n,24)).^2*H(J+46,m) ...
      +abs(y(n,25)).^2*H(J+48,m)+abs(y(n,26)).^2*H(J+50,m) ...
      +abs(y(n,27)).^2*H(J+52,m);
      c(n,1) = data1;
      end

       expec = real(a+b+c);%(:,m+1)
 matrix = [t expec];
%end
%matrix = [matrix,t,expec];
%end
       %save('comlexdata3','complex','-ASCII');
       %save('nonC','data','-ASCII');
       save('nonadiabatic3','matrix','-ASCII');
 toc
%---------------------------------------------------------------
function dydt = odefun(t,y)
global m;
global J;
F = 2.16e-24;
k = 2.73e9;
a1 = 16.8e-40;
a2 = 6.2e-40;
%a2 is perpendicular to the molecular axis while a1 is parallel to it
a3 = a1-a2;
x = 40;
sigma  = 60;
g = exp(-((t-x)^2)/(sigma));
E = a2*g*k^2*(1/(4*i*F));
E3 = a3*g*k^2*(1/(4*i*F));
l = 1/i;
dydt =
[y(1)*(l*A(J)-E-C(J,m)*E3)-D(J,m)*E3*y(2)
-B(J+2,m)*E3*y(1)+y(2)*(l*A(J+2)-E-C(J+2,m)*E3)-D(J+2,m)*E3*y(3)
-B(J+4,m)*E3*y(2)+y(3)*(l*A(J+4)-E-C(J+4,m)*E3)-D(J+4,m)*E3*y(4)
-B(J+6,m)*E3*y(3)+y(4)*(l*A(J+6)-E-C(J+6,m)*E3)-D(J+6,m)*E3*y(5)
-B(J+8,m)*E3*y(4)+y(5)*(l*A(J+8)-E-C(J+8,m)*E3)-D(J+8,m)*E3*y(6)
-B(J+10,m)*E3*y(5)+y(6)*(l*A(J+10)-E-C(J+10,m)*E3)-D(J+10,m)*E3*y(7)
-B(J+12,m)*E3*y(6)+y(7)*(l*A(J+12)-E-C(J+12,m)*E3)-D(J+12,m)*E3*y(8)
-B(J+14,m)*E3*y(7)+y(8)*(l*A(J+14)-E-C(J+14,m)*E3)-D(J+14,m)*E3*y(9)
-B(J+16,m)*E3*y(8)+y(9)*(l*A(J+16)-E-C(J+16,m)*E3)-D(J+16,m)*E3*y(10)
-B(J+18,m)*E3*y(9)+y(10)*(l*A(J+18)-E-C(J+18,m)*E3)-D(J+18,m)*E3*y(11)
```

```
-B(J+20,m)*E3*y(10)+y(11)*(l*A(J+20)-E-C(J+20,m)*E3)-D(J+20,m)*E3*y(12)
-B(J+22,m)*E3*y(11)+y(12)*(l*A(J+22)-E-C(J+22,m)*E3)-D(J+22,m)*E3*y(13)
-B(J+24,m)*E3*y(12)+y(13)*(l*A(J+24)-E-C(J+24,m)*E3)-D(J+24,m)*E3*y(14)
-B(J+26,m)*E3*y(13)+y(14)*(l*A(J+26)-E-C(J+26,m)*E3)-D(J+26,m)*E3*y(15)
-B(J+28,m)*E3*y(14)+y(15)*(l*A(J+28)-E-C(J+28,m)*E3)-D(J+28,m)*E3*y(16)
-B(J+30,m)*E3*y(15)+y(16)*(l*A(J+30)-E-C(J+30,m)*E3)-D(J+30,m)*E3*y(17)
-B(J+32,m)*E3*y(16)+y(17)*(l*A(J+32)-E-C(J+32,m)*E3)-D(J+32,m)*E3*y(18)
-B(J+34,m)*E3*y(17)+y(18)*(l*A(J+34)-E-C(J+34,m)*E3)-D(J+34,m)*E3*y(19)
-B(J+36,m)*E3*y(18)+y(19)*(l*A(J+36)-E-C(J+36,m)*E3)-D(J+36,m)*E3*y(20)
-B(J+38,m)*E3*y(19)+y(20)*(l*A(J+38)-E-C(J+38,m)*E3)-D(J+38,m)*E3*y(21)
-B(J+40,m)*E3*y(20)+y(21)*(l*A(J+40)-E-C(J+40,m)*E3)-D(J+40,m)*E3*y(22)
-B(J+42,m)*E3*y(21)+y(22)*(l*A(J+42)-E-C(J+42,m)*E3)-D(J+42,m)*E3*y(23)
-B(J+44,m)*E3*y(22)+y(23)*(l*A(J+44)-E-C(J+44,m)*E3)-D(J+44,m)*E3*y(24)
-B(J+46,m)*E3*y(23)+y(24)*(l*A(J+46)-E-C(J+46,m)*E3)-D(J+46,m)*E3*y(25)
-B(J+48,m)*E3*y(24)+y(25)*(l*A(J+48)-E-C(J+48,m)*E3)-D(J+48,m)*E3*y(26)
-B(J+50,m)*E3*y(25)+y(26)*(l*A(J+50)-E-C(J+50,m)*E3)-D(J+50,m)*E3*y(27)
-B(J+52,m)*E3*y(26)+y(27)*(l*A(J+52)-E-C(J+52,m)*E3)];

function [a] = A(J)
a = J*(J+1);
function [h] = H(J,M)
h = ((1/3)+(2/3)* (J*(J+1)-3*M^2)/(((2*J)-1)*((2*J)+3)));
function [b] = B(J,M)
b = (1/((2*J)-1))* sqrt( ((J+abs(M))*(J+abs(M)-1)*(J-abs(M))
*(J-abs(M)-1))/((((2*J)+1))*((2*J)-3)));
function [c] = C(J,M)
c =((1/3)+(2/3)* (J*(J+1)-3*M^2)/(((2*J)-1)*((2*J)+3)));
function [d] = D(J,M)
d = (1/((2*J)+3))*sqrt( ((J+abs(M)+2)*(J+abs(M)+1)*(J-abs(M)+2)
*(J-abs(M)+1))/(((2*J)+5)*((2*J)+1)));
```

This program performs the same calculation except for circularly polarised light.

```
function odefun

tic
matrix = [];
global m;
global J;
tspan = [0:0.25:80];
error = 1e-9*[1:27];
P = zeros([14 1]);
y0 = [0;0;0;0;0;0;0;0;0;1;0;0;0;P];
for n=3:6
    J=2*n;
expec = [];
for m=0:J
options = odeset('RelTol',1e-11,'AbsTol',error);

[t,y] = ode113(@odefun,tspan,y0,options);

%data=[t abs(y(:,1)).^2 abs(y(:,2)).^2 abs(y(:,3)).^2 abs(y(:,4)).^2...
%      abs(y(:,5)).^2 abs(y(:,6)).^2 abs(y(:,7)).^2 abs(y(:,8)).^2...
%      abs(y(:,9)).^2 abs(y(:,10)).^2 abs(y(:,11)).^2 abs(y(:,12)).^2...
%      abs(y(:,13)).^2 abs(y(:,14)).^2 abs(y(:,15)).^2 abs(y(:,16)).^2...
%      abs(y(:,17)).^2 abs(y(:,18)).^2 abs(y(:,19)).^2 abs(y(:,20)).^2 ...
%      abs(y(:,21)).^2 abs(y(:,22)).^2 abs(y(:,23)).^2 abs(y(:,24)).^2...
%      abs(y(:,25)).^2 abs(y(:,26)).^2 abs(y(:,27)).^2];

       l = length(t');
       a = zeros([l 1]);
       b = zeros([l 1]);
       c = zeros([l 1]);
       for n=1:l

data2=conj(y(n,1))*y(n,2)*B(J+2,m)+conj(y(n,2))*y(n,3)*B(J+4,m)...
      +conj(y(n,3))*y(n,4)*B(J+6,m)+conj(y(n,4))*y(n,5)*B(J+8,m)...
      +conj(y(n,5))*y(n,6)*B(J+10,m)+conj(y(n,6))*y(n,7)*B(J+12,m)...
      +conj(y(n,7))*y(n,8)*B(J+14,m)+conj(y(n,8))*y(n,9)*B(J+16,m)...
      +conj(y(n,9))*y(n,10)*B(J+18,m)+conj(y(n,10))*y(n,11)*B(J+20,m)...
      +conj(y(n,11))*y(n,12)*B(J+22,m)+conj(y(n,12))*y(n,13)*B(J+24,m)...
      +conj(y(n,13))*y(n,14)*B(J+26,m)+conj(y(n,14))*y(n,15)*B(J+28,m)...
      +conj(y(n,15))*y(n,16)*B(J+30,m)+conj(y(n,16))*y(n,17)*B(J+32,m)...
      +conj(y(n,17))*y(n,18)*B(J+34,m)+conj(y(n,18))*y(n,19)*B(J+36,m)...
      +conj(y(n,19))*y(n,20)*B(J+38,m)+conj(y(n,20))*y(n,21)*B(J+40,m)...
      +conj(y(n,21))*y(n,22)*B(J+42,m)+conj(y(n,22))*y(n,23)*B(J+44,m)...
      +conj(y(n,23))*y(n,24)*B(J+46,m)+conj(y(n,24))*y(n,25)*B(J+48,m)...
      +conj(y(n,25))*y(n,26)*B(J+50,m)+conj(y(n,26))*y(n,27)*B(J+52,m);
      a(n,1)=data2;

data4=conj(y(n,2))*y(n,1)*D(J,m)+conj(y(n,3))*y(n,2)*D(J+2,m)...
      +conj(y(n,4))*y(n,3)*D(J+4,m)+conj(y(n,5))*y(n,4)*D(J+6,m)...
      +conj(y(n,6))*y(n,5)*D(J+8,m)+conj(y(n,7))*y(n,6)*D(J+10,m)...
      +conj(y(n,8))*y(n,7)*D(J+12,m)+conj(y(n,9))*y(n,8)*D(J+14,m)...
      +conj(y(n,10))*y(n,9)*D(J+16,m)+conj(y(n,11))*y(n,10)*D(J+18,m)...
      +conj(y(n,12))*y(n,11)*D(J+20,m)+conj(y(n,13))*y(n,12)*D(J+22,m)...
      +conj(y(n,14))*y(n,13)*D(J+24,m)+conj(y(n,15))*y(n,14)*D(J+26,m)...
      +conj(y(n,16))*y(n,15)*D(J+28,m)+conj(y(n,17))*y(n,16)*D(J+30,m)...
      +conj(y(n,18))*y(n,17)*D(J+32,m)+conj(y(n,19))*y(n,18)*D(J+34,m)...
      +conj(y(n,20))*y(n,19)*D(J+36,m)+conj(y(n,21))*y(n,20)*D(J+38,m)...
      +conj(y(n,22))*y(n,21)*D(J+40,m)+conj(y(n,23))*y(n,22)*D(J+42,m)...
```

```
    +conj(y(n,24))*y(n,23)*D(J+44,m)+conj(y(n,25))*y(n,24)*D(J+46,m)...
    +conj(y(n,26))*y(n,25)*D(J+48,m)+conj(y(n,27))*y(n,26)*D(J+50,m);
    b(n,1) = data4;

data1=abs(y(n,1)).^2*H(J,m)+abs(y(n,2)).^2*H(J+2,m)...
    +abs(y(n,3)).^2*H(J+4,m)+abs(y(n,4)).^2*H(J+6,m)...
    +abs(y(n,5)).^2*H(J+8,m)+abs(y(n,6)).^2*H(J+10,m)...
    +abs(y(n,7)).^2*H(J+12,m)+abs(y(n,8)).^2*H(J+14,m)...
    +abs(y(n,9)).^2*H(J+16,m)+abs(y(n,10)).^2*H(J+18,m)...
    +abs(y(n,11)).^2*H(J+20,m)+abs(y(n,12)).^2*H(J+22,m)...
    +abs(y(n,13)).^2*H(24,m)+abs(y(n,14)).^2*H(J+26,m)...
    +abs(y(n,15)).^2*H(J+28,m)+abs(y(n,16)).^2*H(J+30,m)...
    +abs(y(n,17)).^2*H(J+32,m)+abs(y(n,18)).^2*H(J+34,m)...
    +abs(y(n,19)).^2*H(J+36,m)+abs(y(n,20)).^2*H(J+38,m)...
    +abs(y(n,21)).^2*H(J+40,m)+abs(y(n,22)).^2*H(J+42,m)...
    +abs(y(n,23)).^2*H(J+44,m)+abs(y(n,24)).^2*H(J+46,m)...
    +abs(y(n,25)).^2*H(J+48,m)+abs(y(n,26)).^2*H(J+50,m)...
    +abs(y(n,27)).^2*H(J+52,m);
    c(n,1) = data1;
    end
expec(:,m+1) = real(a+b+c);
end %m loop end
matrix = [matrix,t,expec];
end %J loop end
     %save('comlexdata3','complex','-ASCII');
     %save('dataJ=40)','data','-ASCII');
     save('circJ=32,40','matrix','-ASCII');
 toc
%-----------------------------------------------------------------
function dydt = odefun(t,y)
global m;
global J;
F = 2.16e-24;
k = 2.73e9;
a1 = 16.8e-40;
a2 = 6.2e-40;
%a2 is perpendicular to the molecular axis while a1 is parallel to it
a3 = a1-a2;
x = 40;
sigma  = 60;
g = exp(-((t-x)^2)/(sigma));
E1 = a1*g*k^2*(1/(8*i*F));
E2 = a2*g*k^2*(1/(8*i*F));
E3 = a3*g*k^2*(1/(8*i*F));
l = 1/i;
dydt =
 [y(1)*(l*A(J)-E1-E2+C(J,m)*E3)+D(J,m)*E3*y(2)
 B(J+2,m)*E3*y(1)+y(2)*(l*A(J+2)-E1-E2+C(J+2,m)*E3)+D(J+2,m)*E3*y(3)
 B(J+4,m)*E3*y(2)+y(3)*(l*A(J+4)-E1-E2+C(J+4,m)*E3)+D(J+4,m)*E3*y(4)
 B(J+6,m)*E3*y(3)+y(4)*(l*A(J+6)-E1-E2+C(J+6,m)*E3)+D(J+6,m)*E3*y(5)
 B(J+8,m)*E3*y(4)+y(5)*(l*A(J+8)-E1-E2+C(J+8,m)*E3)+D(J+8,m)*E3*y(6)
 B(J+10,m)*E3*y(5)+y(6)*(l*A(J+10)-E1-E2+C(J+10,m)*E3)+D(J+10,m)*E3*y(7)
 B(J+12,m)*E3*y(6)+y(7)*(l*A(J+12)-E1-E2+C(J+12,m)*E3)+D(J+12,m)*E3*y(8)
 B(J+14,m)*E3*y(7)+y(8)*(l*A(J+14)-E1-E2+C(J+14,m)*E3)+D(J+14,m)*E3*y(9)
 B(J+16,m)*E3*y(8)+y(9)*(l*A(J+16)-E1-E2+C(J+16,m)*E3)+D(J+16,m)*E3*y(10)
 B(J+18,m)*E3*y(9)+y(10)*(l*A(J+18)-E1-E2+C(J+18,m)*E3)+D(J+18,m)*E3*y(11)
 B(J+20,m)*E3*y(10)+y(11)*(l*A(J+20)-E1-E2+C(J+20,m)*E3)+D(J+20,m)*E3*y(12)
 B(J+22,m)*E3*y(11)+y(12)*(l*A(J+22)-E1-E2+C(J+22,m)*E3)+D(J+22,m)*E3*y(13)
 B(J+24,m)*E3*y(12)+y(13)*(l*A(J+24)-E1-E2+C(J+24,m)*E3)+D(J+24,m)*E3*y(14)
```

```
 B(J+26,m)*E3*y(13)+y(14)*(l*A(J+26)-E1-E2+C(J+26,m)*E3)+D(J+26,m)*E3*y(15)
 B(J+28,m)*E3*y(14)+y(15)*(l*A(J+28)-E1-E2+C(J+28,m)*E3)+D(J+28,m)*E3*y(16)
 B(J+30,m)*E3*y(15)+y(16)*(l*A(J+30)-E1-E2+C(J+30,m)*E3)+D(J+30,m)*E3*y(17)
 B(J+32,m)*E3*y(16)+y(17)*(l*A(J+32)-E1-E2+C(J+32,m)*E3)+D(J+32,m)*E3*y(18)
 B(J+34,m)*E3*y(17)+y(18)*(l*A(J+34)-E1-E2+C(J+34,m)*E3)+D(J+34,m)*E3*y(19)
 B(J+36,m)*E3*y(18)+y(19)*(l*A(J+36)-E1-E2+C(J+36,m)*E3)+D(J+36,m)*E3*y(20)
 B(J+38,m)*E3*y(19)+y(20)*(l*A(J+38)-E1-E2+C(J+38,m)*E3)+D(J+38,m)*E3*y(21)
 B(J+40,m)*E3*y(20)+y(21)*(l*A(J+40)-E1-E2+C(J+40,m)*E3)+D(J+40,m)*E3*y(22)
 B(J+42,m)*E3*y(21)+y(22)*(l*A(J+42)-E1-E2+C(J+42,m)*E3)+D(J+42,m)*E3*y(23)
 B(J+44,m)*E3*y(22)+y(23)*(l*A(J+44)-E1-E2+C(J+44,m)*E3)+D(J+44,m)*E3*y(24)
 B(J+46,m)*E3*y(23)+y(24)*(l*A(J+46)-E1-E2+C(J+46,m)*E3)+D(J+46,m)*E3*y(25)
 B(J+48,m)*E3*y(24)+y(25)*(l*A(J+48)-E1-E2+C(J+48,m)*E3)+D(J+48,m)*E3*y(26)
 B(J+50,m)*E3*y(25)+y(26)*(l*A(J+50)-E1-E2+C(J+50,m)*E3)+D(J+50,m)*E3*y(27)
 B(J+52,m)*E3*y(26)+y(27)*(l*A(J+52)-E1-E2+C(J+52,m)*E3)];

function [a] = A(J)
a = J*(J+1) ;
function [h] = H(J,M)
h = ((1/3)+(2/3)* (J*(J+1)-3*M^2)/(((2*J)-1)*((2*J)+3)));
function [b] = B(J,M)
b = (1/((2*J)-1))* sqrt( ((J+abs(M))*(J+abs(M)-1)*(J-abs(M))
*(J-abs(M)-1))/((((2*J)+1))*((2*J)-3)));
function [c] = C(J,M)
c =((1/3)+(2/3)* (J*(J+1)-3*M^2)/(((2*J)-1)*((2*J)+3)));
function [d] = D(J,M)
d = (1/((2*J)+3))*sqrt( ((J+abs(M)+2)*(J+abs(M)+1)*(J-abs(M)+2)
*(J-abs(M)+1))/(((2*J)+5)*((2*J)+1)));
```

This program calculates the induced velocity change along the molecular beam axis for various rotational states.

```
function test
clear
boltz=1.38e-23;
mass=1.66*28e-27;
temp=3;
%x = textread('Book1.txt');
%x(:,1) = (x(:,1)-94)*1e-6;
%x = textread('hotdata2.txt');
%x(:,1) = x(:,1)*1e-6-99e-6;
x = textread('vibrational.txt');
x(:,1) = (x(:,1)-245)*1e-6;
data=[];
datafin=[];
vel=[];
disp=[];
velx=[];
velz=[];
%save('newdata','x','-ASCII')
tspan = [0 70e-9];
v = 540;
for k=0:1:150

y0 = [-v,(k-50)*1e-6,0,0];

% solve the problem using ODE45
options = odeset('RelTol',1e-10,'AbsTol',[1e-10 1e-10 1e-10 1e-10]);
[T,Y] = ode45(@f,tspan,y0,options);
data=[data;Y(:,1) Y(:,2) Y(:,3),Y(:,4)];
l=length(Y(:,2));

vel=[vel;Y(l,1),Y(l,3)];
disp=[disp;Y(l,2),Y(l,4)];
velx=[velx;Y(l,4),Y(l,3)];
velz=[velz;-1*Y(l,2)/1e-6,-1*Y(l,1),];

end
%plot(velx(:,1),velx(:,2),'.')
%figure;
grid on
velz(:,2) = velz(:,2)-v;
velz(:,1) = (velz(:,1)*1e-6)-18e-6;
%max(velz(:,2))
%plot(velz(:,1),velz(:,2),x(:,1),x(:,2),'sqg',x(:,1),x(:,4),'or')
plot(velz(:,1),velz(:,2),x(:,1),x(:,2),'sqg',x(:,1),x(:,3),'or')
hold on

%save('vib','velz','-ASCII')

% % --------------------------------------------------------------------------

function dydt = f(t,y)
spotsize=30.0e-6;
%I0=0.5*1.02*1.21*1.012*0.892*2.8/1.23*.8361*1.205e16;
%t0=15e-9;
c=3e8;
e0=8.854e-12;
m=1.66*76e-27;
```

```
p = sqrt(pi/2);
t1 = 1.0977e-7-70e-9;
s1 = 1.5744e-8;
b1 = 8.3148e-9;

t2 = 1.0434e-7-70e-9;
s2 = 1.0056e-8;
b2 = 7.7952e-9;

t3 = 1.2835e-7-70e-9;
s3 = 3.8731e-8;
b3 = 3.0376e-9;
I0 = (b1/(s1*p))*exp(-2*((t-t1)/s1)^2)+(b2/(s2*p))
*exp(-2*((t-t2)/s2)^2)+(b3/(s3*p))*exp(-2*((t-t3)/s3)^2);

%NITROGEN
alpha00 = (1.89+1.177*I0-0.150*I0^2-3.525*I0^3+4.926*I0^4-2.017*I0^5)*1e-40;
alpha10 = (2.04-0.226*I0+0.409*I0^2-0.181*I0^3+0.0157*I0^4)*1e-40;
alpha11 = (2.00+0.034*I0-1.333*I0^2+1.86*I0^3-0.708*I0^4)*1e-40;
alpha20 = (2.06-0.882*I0+0.066*I0^2+3.801*I0^3-4.995*I0^4+1.948*I0^5)*1e-40;
alpha21 = (1.98+0.257*I0-0.0195*I0^2-0.037*I0^3)*1e-40;
alpha22 = (1.74+0.119*I0+0.096*I0^+0.287*I0^-0.2337*I0^4)*1e-40;

dalpha00 = (1.177-2*0.150*I0-3*3.525*I0^2+4*4.926*I0^3-5*2.017*I0^4)*1e-40;
dalpha10 = (-0.226+2*0.409*I0-3*0.181*I0^2+4*0.0157*I0^3)*1e-40;
dalpha11 = (0.034-2*1.333*I0+3*1.86*I0^2-4*0.708*I0^3)*1e-40;
dalpha20 = (-0.882+2*0.066*I0+3*3.801*I0^2-4*4.995*I0^3+5*1.948*I0^4)*1e-40;
dalpha21 = (0.257-2*0.0195*I0-3*0.037*I0^2)*1e-40;
dalpha22 = (0.119+2*0.096*I0+3*0.287*I0^2-0.2337*I0^3)*1e-40;

pa = ((2*I0*1*5e16)/(m*e0*c*spotsize^2))*exp(-2*(y(2)^2+y(4)^2)/spotsize^2)
*(alpha21+dalpha21*exp(-2*(y(2)^2+y(4)^2)/spotsize^2));
dydt = [   -pa*y(2)
            y(1)
           -pa*y(4)
            y(3)
       ];
```

This program calculates the downstream density of focussed molecules.

```
function test

clear
boltz=1.38e-23;
mass=1.66*28e-27;
temp=2;
for iter=1:100
clear
tic
data=[];
datafin=[];
ff=[];
vel=[];
disp=[];


tspan = [0 80e-9];
points=5000;
a = -15e-6; b = 15e-6;
c = -60e-6; d = 60e-6;
y = a+(b-a)*rand(points,1);
x = c+(d-c)*rand(points,1);
wtx=540+17*randn(points,1);
wty=0.3*randn(points,1);

for i=1:points

y0 = [wtx(i,1);x(i,1);wty(i,1);y(i,1)];

% solve the problem using ODE45
options = odeset('RelTol',1e-10,'AbsTol',[1e-8 1e-8 1e-8 1e-8]);
[T,Y] = ode45(@f,tspan,y0,options);
%data=[data;Y(:,1) Y(:,2) Y(:,3),Y(:,4)];
l=length(Y(:,2));

vel=[vel;Y(l,1),Y(l,3)];
disp=[disp;Y(l,2),Y(l,4)];

end
   save('Npos11','disp','-append','-ASCII');
   save('Nvel11','vel','-append','-ASCII');
   toc
end

% % ------------------------------------------------------------------------

function dydt = f(t,y)
spotsize=30.0e-6;
%I0=0.5*1.02*1.21*1.012*0.892*2.8/1.23*.8361*1.205e16;
%t0=15e-9;
c=3e8;
e0=8.854e-12;
m=1.66*76e-27;
p = sqrt(pi/2);
t1 = 1.0977e-7-80e-9;
s1 = 1.5744e-8;
A1 = 8.3148e-9;
```

```
t2 = 1.0434e-7-80e-9;
s2 = 1.0056e-8;
A2 = 7.7952e-9;

t3 = 1.2835e-7-80e-9;
s3 = 3.8731e-8;
A3 = 3.0376e-9;
I0 = (A1/(s1*p))*exp(-2*((t-t1)/s1)^2)+(A2/(s2*p))
*exp(-2*((t-t2)/s2)^2)+(A3/(s3*p))*exp(-2*((t-t3)/s3)^2);
s = 40+sqrt(-60*log(I0));

pa = 2*alpha11/(m*e0*c*spotsize^2)*I0*5e16
*exp(-2*(y(2)^2+y(4)^2)/spotsize^2) +2*dalpha11/(m*e0*c*spotsize^2)
*I0*5e16*exp(-2*(y(2)^2+y(4)^2)/spotsize^2)
*exp(-2*(y(2)^2+y(4)^2)/spotsize^2);


dydt = [   -pa*y(2)
            y(1)
           -pa*y(4)
            y(3)
       ];
```

This program calculates the CS_2 rotational spectrum using the three-photon line strengths.

```
clear all
a = ([1:80]').*2;
B = 0.109;
T = 10;
w = 0.3;
w2 = 2.3;
b = a(:,1);
c = a(:,1);
l = length(a);
for n=1:l
    if(n==1) %J=0
        a(n,2) = 0;
        a(n,3) = 0;
        a(n,4) = (a(n,1)+1)*(a(n,1)+2)-1-a(n,1)*(a(n,1)+1);
        a(n,5) = P(0,T);
        b(n,2) = 0;
        b(n,3) = 0;
        b(n,4) = P(n,T)*((b(n,1)+3)*(b(n,1)+2))/((b(n,1)+1));
        c(n,2) = 0;
        c(n,3) = 0;
        c(n,4) = 0;
        c(n,5) = 0;
        c(n,6) = 0;
        c(n,7) = 0;
        c(n,8) = P(n,T)*(15*(c(n,1)+1)*c(n,1)*(c(n,1)+2)*(c(n,1)+3)
        *(c(n,1)+4)*(c(n,1)+5))/(8*(c(n,1)+1)*(c(n,1)+2)*(c(n,1)+3)
        *((2*c(n,1))+3)*((2*c(n,1))+5));
    end

    if(n==2) %J = 2;
        c(n,2) = 0;
        c(n,3) = 0;
        c(n,4) = P(n,T)*((c(n,1)-2)*(c(n,1)-1)*(((10*c(n,1))+15)-(c(n,1)+1)
        *(c(n,1)-6)+15)^2)/(8*(c(n,1)-1)*c(n,1)*(c(n,1)+1)*((2*c(n,1)-3))
        *((2*c(n,1)+3)));
        c(n,5) = P(n,T)*(3*(c(n,1)-1)*(c(n,1)+2)*(((c(n,1)^2
        +c(n,1)+3)-15)^2)*((2*c(n,1))+1))/(4*((c(n,1)-1)*c(n,1)*(c(n,1)+1)
        *(c(n,1)+2)*((2*c(n,1))-1)*((2*c(n,1))+3)));
        c(n,6) = P(n,T)*((c(n,1)+2)*(c(n,1)+3)*((15-(10*(c(n,1))-5)-(c(n,1)
        *(c(n,1)+7))))^2)/(8*((c(n,1)*(c(n,1)+1))*(c(n,1)+2)*((2*c(n,1))-1)
        *((2*c(n,1))+5)));
        c(n,7) = P(n,T)*(5*c(n,1)*(c(n,1)+2)*(c(n,1)+3)*(c(n,1)+4)
        *(c(n,1)-3)^2)/(8*((c(n,1)*(c(n,1)+1))*(c(n,1)+2)*(c(n,1)+3)
        *((2*c(n,1))+3)));
        c(n,8) = P(n,T)*(15*(c(n,1)+1)*c(n,1)*(c(n,1)+2)*(c(n,1)+3)
        *(c(n,1)+4)*(c(n,1)+5))/(8*(c(n,1)+1)*(c(n,1)+2)*(c(n,1)+3)
        *((2*c(n,1))+3)*((2*c(n,1))+5));
        c(n,9) = (c(n,2)+c(n,3)+c(n,4)+c(n,5)+c(n,6)+c(n,7)+c(n,8)
        )/((2*c(n,1))+1);
    end
    a(n,2) = (a(n,1)-2)*(a(n,1)-3)-1-a(n,1)*(a(n,1)+1);     %N
    a(n,3) = (a(n,1)-1)*(a(n,1)-2)-1-a(n,1)*(a(n,1)+1);     %O
    a(n,4) = a(n,1)*(a(n,1)-1)-1-a(n,1)*(a(n,1)+1);         %P
    a(n,5) = 1;                                             %Q
    a(n,6) = (a(n,1)+2)*(a(n,1)+1)-1-(a(n,1)*(a(n,1)+1));   %R
    a(n,7) = (a(n,1)+3)*(a(n,1)+2)-1-(a(n,1)*(a(n,1)+1));   %S
    a(n,8) = (a(n,1)+4)*(a(n,1)+3)-1-(a(n,1)*(a(n,1)+1));   %T
```

```
    a(n,9) = P(n,T);
    if(n==1)
        b(n,2) = 0;
        b(n,3) = 0;
        b(n,4) = P(n,T)*((b(n,1)+3)*(b(n,1)+2))/((b(n,1)+1));
    else
    b(n,2) = P(n,T)*((b(n,1)-2)*(b(n,1)-1))/(b(n,1)); %P line strength
    b(n,3) = P(n,T)*((b(n,1)+2)*(b(n,1)-1)*(2*(b(n,1))+1))/(b(n,1)
    *(b(n,1)+1));           %Q line strength
    b(n,4) = P(n,T)*((b(n,1)+3)*(b(n,1)+2))/((b(n,1)+1));%R line strength
    %b(n,5) = (b(n,2)+b(n,3)+b(n,4))/(2*b(n,1)+1);
    end
        if(n>2)
        c(n,2) = P(n,T)*(15*(c(n,1)-4)*(c(n,1)-3)*(c(n,1)-2)
        *(c(n,1)-1)*(c(n,1)+1)*c(n,1))/(8*((c(n,1)-2)*(c(n,1)-1)*c(n,1)
        *((2*c(n,1))-3)*((2*c(n,1))-1)));
        c(n,3) = P(n,T)*(5*(c(n,1)-3)*(c(n,1)-2)*(c(n,1)-1)*(c(n,1)+1)
        *(c(n,1)+4)^2)/(8*((c(n,1)-2)*(c(n,1)-1)*c(n,1)*(c(n,1)+1)
        *((2*c(n,1))-1)));
        c(n,4) = P(n,T)*((c(n,1)-2)*(c(n,1)-1)*(((10*c(n,1))+15)
        -(c(n,1)+1)*(c(n,1)-6)+15)^2)/(8*(c(n,1)-1)*c(n,1)*(c(n,1)+1)
        *((2*c(n,1)-3))*((2*c(n,1)+3)));
        c(n,5) = P(n,T)*(3*(c(n,1)-1)*(c(n,1)+2)*(((c(n,1)^2
        +c(n,1)+3)-15)^2)*((2*c(n,1))+1))/(4*((c(n,1)-1)*c(n,1)
        *(c(n,1)+1)*(c(n,1)+2)*((2*c(n,1))-1)*((2*c(n,1))+3)));
        c(n,6) = P(n,T)*((c(n,1)+2)*(c(n,1)+3)*((15-(10*(c(n,1))-5)
        -(c(n,1)*(c(n,1)+7))))^2)/(8*((c(n,1)*(c(n,1)+1))*(c(n,1)+2)
        *((2*c(n,1))-1)*((2*c(n,1))+5)));
        c(n,7) = P(n,T)*(5*c(n,1)*(c(n,1)+2)*(c(n,1)+3)*(c(n,1)+4)
        *(c(n,1)-3)^2)/(8*(c(n,1)*(c(n,1)+1))*(c(n,1)+2)*
        (c(n,1)+32*c(n,1))+3));
        c(n,8) = P(n,T)*(15*(c(n,1)+1)*c(n,1)*(c(n,1)+2)*(c(n,1)+3)
        *(c(n,1)+4)*(c(n,1)+5))/(8*(c(n,1)+1)*(c(n,1)+2)*(c(n,1)+3)
        *((2*c(n,1))+3)*((2*c(n,1))+5));
                end

end
a(:,2:8) = a(:,2:8)*B;
g = linspace(-15,15,3000)'; % g is in one photon wavenumbers
l1 = length(g);
d = [];
for j=1:l1
f2 = 0;
k0 = 0;
    for n=1:l
    f = b(n,2)*((1/w)*exp(-((a(n,4)-g(j,1))/w)^2))+b(n,3)*((1/w)
    *exp(-((a(n,5)-g(j,1))/w)^2))+b(n,4)*((1/w)
    *exp(-((a(n,6)-g(j,1))/w)^2));
    f2 = f2+f;
    k = c(n,2)*((1/w)*exp(-((a(n,2)-g(j,1))/w)^2))+c(n,3)
    *((1/w)*exp(-((a(n,3)-g(j,1))/w)^2))+c(n,4)*((1/w)
    *exp(-((a(n,4)-g(j,1))/w)^2))+c(n,5)*((1/w)
    *exp(-((a(n,5)-g(j,1))/w)^2))+c(n,6)*((1/w)
    *exp(-((a(n,6)-g(j,1))/w)^2))+c(n,7)*((1/w)
    *exp(-((a(n,7)-g(j,1))/w)^2))+c(n,8)*((1/w)
    *exp(-((a(n,8)-g(j,1))/w)^2));
    k0 = k0+k;
    end
    d(j,1) = f2;
```

```
    d(j,2) = k0;

end
lin = (d(:,1)*(21/175))+(d(:,2)*(10/175));
circ = d(:,2)*(25/174);
e = [g lin circ];
%plot(e(:,1),e(:,2))

%instrument function linewidth or kernal
for n=1:l1
    k(n,1) = (1/w2)*exp(-(((g(n,1))/w2)^2));
end
x = conv(e(:,2),k);
%axis conversion
l3 = length(x);
l4 = l3-1;
for n=0:l4
    a1(n+1,1) = (((abs(min(g))+abs(max(g)))/l4)*n)+min(g);
end
a1(1,2) = ((1/((62768+a1(n,1))/3))*1/100)*1e9;
for n=2:l3
    a1(n,2) = a1(n-1,2)+0.0004;
end
X = [a1 x];
X(:,4) = X(:,3)/max(X(:,3));
j = length(X);
X(j,:) = [];
%separation given spectroscopically


X(:,2) = X(:,2)+0.35;
%read in spectra data
k1 = xlsread('thesis');
subplot(2,2,1);plot(g,e(:,2))
subplot(2,2,2);plot(g,k)
subplot(2,2,[3 4]);plot(X(:,2),X(:,4),'-k',k1(:,1),k1(:,2),'.-r');
grid on
hold on
%save('freq','a','-ASCII');
%save('strenght','b','-ASCII');
save('justsim30','X','-ASCII');
```